2022

SYNTHESIS, CHARACTERIZATION, AND ACTIVATION OF PYRIDINE DIPYRROLIDE SUPPORTED VANADIUM-NITROGEN MULTIPLE BONDS

Jordan Cruz Martinez
jcm0052@mix.wvu.edu

SYNTHESIS, CHARACTERIZATION, AND ACTIVATION OF PYRIDINE DIPYRROLIDE SUPPORTED VANADIUM-NITROGEN MULTIPLE BONDS

Jordan Cruz Martinez

Dissertation submitted to the Eberly College of Arts and Sciences

at West Virginia University

In Partial Fulfillment of the Requirements for the Degree of

Doctor of Philosophy in

Chemistry

Carsten Milsmann, Ph.D., Chair

Jeffrey Petersen, Ph.D.

Brian Popp, Ph.D.

Björn Söderberg, Ph.D.

Alan Bristow, Ph.D.

Department of Chemistry

Morgantown, West Virginia

2022

Keywords: vanadium, nitrido, imido, azide, photolysis, thermolysis

ABSTRACT

SYNTHESIS, CHARACTERIZATION, AND ACTIVATION OF PYRIDINE DIPYRROLIDE SUPPORTED VANADIUM-NITROGEN MULTIPLE BONDS

Jordan Martinez

The chemistry of coordination complexes of vanadium supported by pyridine di-pyrrolide pincer ligands was probed via the synthesis and investigation of a variety of compounds from the trivalent starting material, (^{Mes}PDP^{Ph})VCl(thf)$_2$. Under reducing conditions and subsequent addition of terpyridine, a redox transfer series (1-, 0, 1+) stemming from the neutral product (^{Mes}PDP^{Ph})V(terpy) was isolated and characterized by X-ray crystallography. The precise bond lengths, in conjunction with bulk magnetic susceptibility, allowed for a detailed study of the redox non-innocence of polypyridyl ligands in these systems.

Metathesis of the halide starting material with azide salts allowed for the isolation of [Na(18-crown-6)][(^{Mes}PDP^{Ph})V(N$_3$)$_2$(thf)], which could be thermolyzed to produce the mixed nitride/azide salt, [Na(18-crown-6)][(^{Mes}PDP^{Ph})VN(N$_3$)]. Following characterization of the resulting vanadium-nitrogen triple bond, the activation of this species with electrophilic reagents was explored. The PDP supported vanadium nitride proved a competent nucleophile toward trimethylsilyl chloride, resulting in the imido complex (^{Mes}PDP^{Ph})V(NTMS)(N$_3$). This product was then subjected to reducing conditions as a first step toward silylation-coupled electron transfer, as a model analogue for homogeneous ammonia production, resulting in the isolation of the cobaltocenium salt of the parent complex.

The vanadium-imido complex (^{Mes}PDP^{Ph})V(N-^{1}Ad)(N$_3$) was prepared by thermolysis of 1-adamantyl azide in the presence of the trivalent halide starting material, followed by metathesis

with azide salts. This product, along with [Na(18-crown-6)][(^{Mes}PDP^{Ph})VN(N_3)] and (^{Mes}PDP^{Ph})V(NTMS)(N_3), were then subjected to photolytic conditions to generate transient diradical nitrene intermediate from the decomposition of the pendant azide ligand on the d^0 V(V) metal center. Irradiation with green light lead to the generation of the intra-ligand C-H activated products [(Na(18-crown-6)][(^{Mes}PDP^{Ph}-NH)VN] and (^{Mes}PDP^{Ph}-NH)V(NTMS). Following the study of this reactivity, computations revealed an unusual lowest lying excited state, which may be responsible for a divergent deazotation mechanism for the preconceived unimolecular pathway.

In order to contrast work in this lab with the photosensitizer Zr(^{Mes}PDP^{Ph})$_2$, a new ligand was prepared and appended to a variety of early metals including titanium, zirconium, vanadium, and niobium. The pyridine di-amine (PDA) ligand scaffold was directly compared to the PDP ligand, and its reactions with metals gave several interesting products during the course of this study. However, none of these were luminescent. This result was investigated by empirical techniques and computational chemistry.

The culmination of this work is dedicated to:

Stella Ora Martinez
&
Carey Steven Martinez

Though you never got to see it. I'm sorry to have lost you.

Andrew Emilio Martinez

My son, may I make you as proud of me as I am of you.

Like all men of the Library, I have traveled in my youth; I have wandered in search of a book, perhaps the catalogue of catalogues… I venture to suggest this solution to the ancient problem: *The Library is unlimited and cyclical.* If an eternal traveler were to cross it in any direction, after centuries he would see that the same volumes were repeated in the same disorder (which, thus repeated, would be an order: the Order). My solitude is gladdened by this elegant hope.

-Borges

Acknowledgements

There was a time when I had nothing. The entirety of my life fit within the confines of my backpack. I would sleep at tables in plain view and hide from the rain under bridges and trees. Meals were coffee and cigarettes, the latter a habit which was hard to quit. Every person who helped me up from that place deserves acknowledgement here. There are many, and I will try to the best of my ability to remember.

Melba and Jacob Vargas, who opened their home to me and fed me at their table. I know you wanted me to be a kid, finish school and enjoy some kind of care-free. There was just too much that had already happened when you took me in, and I hadn't been young for a long time. Thank you for learning to support me anyway and allow me the space to find my own two feet.

Steven Martinez, my brother, who is always a phone call away. His support has been imperative to my successes. It has been my great honor to support his success in return. *Basalt* has grown from his home kitchen to weekends at the Market, and finally to his own restaurant as I finished this work. I can't express how proud I am. You inspire me every day.

Mr. Gregory "Brian" Rooper, who opened his home to a younger me without question.

Gregory "Austin" Rooper, who remains my oldest friend, who never let me go hungry, who never let me go alone, who, to this day, lifts me up in times of darkness. My debts are many.

Taylor Maddox, who's wit and charm have always made me laugh, and made Austin fall in love. I'm sorry I couldn't make the wedding, but I bought a house just down the road. I think that counts.

As a student and a scientist, I would also like to acknowledge those who taught and inspired me.

Dr. Michael Castellani and his group, who allowed me use of his lab before I ever knew what I was doing. Who allowed me creative freedom, and the freedom to fail. It was in the Castellani lab that I learned to love chemistry, that I learned to love metals, and began to ask the questions which shaped my career. Caleb Calvary, who taught me how to shake a sep funnel, and everything after that. Benjamin Coleman, who worked alongside me for many years, and who made me strive to better myself and my understanding of my work.

Dr. Jeffrey Petersen and Dr. Brian Dolinar, who taught me crystallography in theory and in practice. It became a great pleasure during my time here. I'm very proud to be the Milsmann group's first published crystallographer.

My committee members, Dr. Carsten Milsmann, Dr. Brian Popp, Dr. Jeff Petersen, Dr. Björn Söderberg, and Dr. Alan Bristow, for agreeing to help me see this through.

And of course, Dr. Carsten Milsmann, who perpetuated my creative freedom in his own lab. I am proud to have contributed to his group, though I was certainly frustrating to work with. I was never one to check in and never one to reach out. It took nearly four years before I started walking into your office to ask for opinions. Thank you for allowing me to make compounds that interested me and pursue them. Thank you for tolerating my extended silences while I gathered data and allowing me the space to organize my thoughts before presenting them to you. Thank you, a thousand times, for your patience when my life at home was falling apart.

To my group mates, whose company, comradery, and mentorship made this work possible, thank you. Dr. Yu Zhang, Dr. Brett Hakey, P. Minh. N. Do, Dylan Leary, Jose Rodriguez, Marisa Tordella, Gage Jackson, Blessing Bamisaye, and all those who come after us.

Table of Contents

List of Chemical Abbreviations

Ad or ^{1}Ad	1-adamantyl
Arg	arganine
Asp	aspartic acid
Bn	benzyl
Cp	cyclopentadienyl
dipp	2,6-diisopropylphenyl
Et	ethyl
Et_2O	diethylether
Glu	glutamic acid
His	histidine
iPr	isopropyl
L	ligand
NsLi	lithium methyl(trimethyl)silane
Me	methyl
Mes	mesityl or 2,4,6-trimethylphenyl
nBu	n-butyl
PDA	2,6-(methylanilido)pyridine
PDP	pyridine dipyrrolide
Ph	phenyl
py	pyridine
tBu	tert-butyl
thf or THF	tetrahydrofuran
TMS	trimethylsilyl
tol	toluene or para-methylphenyl
Tyr	tyrosine

List of Acronyms, Symbols, and Units

•	radical
$\{^1H\}$	proton decoupled
^{13}C	carbon-13
^1H	proton
Å	angstrom, 10^{-10} meters
avg	average
br	broad
cm^{-1}	wavenumbers or inverse centimeters
d	doublet resonance
e^-	electron
HOMO	highest occupied molecular orbital
IR	infrared spectroscopy
J	coupling constant
K	Kelvin
LUMO	lowest unoccupied molecular orbital
M	molar, moles per liter
m	multiplet in NMR
m-	meta position on an aryl ring, indicating a 1,3 relationship
MHz	megahertz, 10^6 Hertz or 10^6 s^{-1}
mmol	millimole, 10^{-3} moles
MO	molecular orbital
nm	nanometer, 10^{-9} meters
NMR	nuclear magnetic resonance
o-	ortho position on an aryl ring, indicating a 1,2 relationship
p-	para position on an aryl ring, indicating a 1,4 relationship
PCET	proton coupled electron transfer
ppm	parts per million
q	quartet resonance
rt	room temperature
s	singlet resonance or second
S	spin
t	triplet resonance
T	temperature

V	potential in mV or V
V	volt
δ	delta, chemical shift in ppm
η^n	eta, hapticity or the number, n, of contiguous atoms in a ligand bound to a metal
κ^n	kappa, denticity or the number, n, of atoms in a polydentate ligand bound to the metal
μ_B	Bohr magneton, 9.274×10^{-21} erg/G
μ_{eff}	mu effective, effective magnetic moment in Bohr magnetons
ν	frequency
χ	magnetic susceptibility
χM or χm	molar magnetic susceptibility in cm^3/mol

List of Figures

List of Tables

List of Schemes

Chapter 1: Chemistry Preceding the Oxo Wall and the Pincer Platform

1.1 Vanadium Lore

Vanadium metal was first isolated in high purity in 1927[1] by the method of Marden and Rich. It was shown to be a soft and ductile metal, capable of being easily cold worked into wire. The physical properties of the material allowed for the conclusion that vanadium was of the family of tantalum, rather than arsenic, which was of debate at the time. Since the early 1900s, the metal has seen use primarily in the production of steel alloys,[2] where 85-90% of the global consumption is allocated each year.[3] It wasn't until Ercoli and coworkers described the first paramagnetic hexacarbonyl radical, $V(CO)_6$, in 1960[4] that vanadium began to gain attention in an academic setting. In the following years, the discovery and characterization of a variety of vanadium containing proteins[5–11] compounded interest into the coordination chemistry of the early metal.

An interesting example of vanadium specific biology are vandophores. These cells contain reduced vanadium (III/IV) in highly acid media, pH ~2, bound by "tris-catechol" blood pigments called tunichromes.[6] These structures are specific to sea squirts, *ascidia nigra*, which do not have a heme-based oxygen transport mechanism. It was postulated that these vanadophores participated in reversible oxygen binding via diffusion of sea water, but this was disproved by oxygen uptake and electrochemical studies.[12] Instead, it is hypothesized that these highly reducing vanadium complexes participate in the cross-linking of cellulose, which forms the thick, rubbery tunic that is characteristic of the sea squirt.[7]

A more ubiquitous form of bio-vanadium is found in cyanobacterium.[13] While it is most common for nitrogenases (Figure 1.1) to contain a molybdenum center in the protein cofactor (FeMoco), it was discovered that these species will utilize vanadium nitrogenase in environments with low levels of molybdenum, and/or low ambient temperatures,[13] where vanadium nitrogenase

(VNase) is more efficient. Interestingly, the vanadium derivative compared to the molybdenum species acts as a better hydrogenase, where hydrogen evolution occurs concomitantly with dinitrogen reduction. VNase also produces a small amount to hydrazine as a byproduct of N_2 reduction, which is not observed in FeMo cofactor.

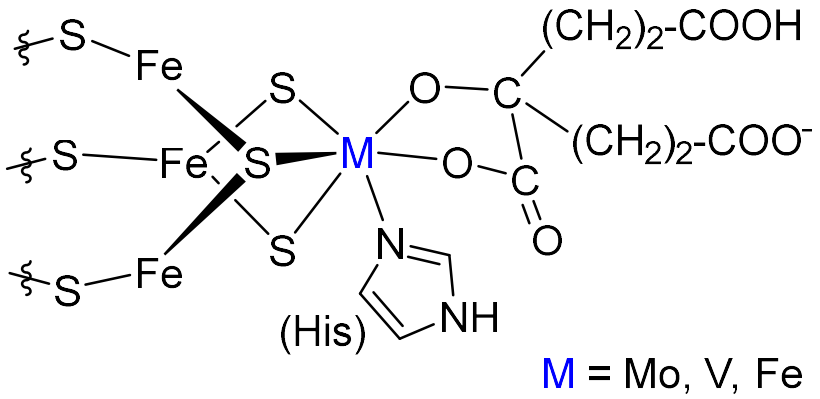

Figure 1.1: Heterometallic site in Nitrogenase Cofactor. Histidine residue reduced for clarity.

These examples of naturally developed vanadium complexes, combined with the metal's low human toxicity,[14] have inspired studies utilizing ^{51}V (I = 7/2)[15,16] and $VO^{2+}(d^1)$[17] complexes as spectroscopic probes for applications in medical procedures. These rely on the intrinsic properties of these vanadium atoms, namely their nuclear and electron spins.

For example, vanadyl insulin and maltol ligated vanadyl (Figure 1.2) have been noted for their medicinal potential as anti-diabetic agents.[18] These can be characterized by spectrophotometry, as many vanadyl complexes with a wide variety of ligand fields have been noted to absorb light in the visible and near-infrared regions. This allows for "fingerprinting" vanadyl substituted complexes as distinct from the native protein. Furthermore, d^1 vanadium centers have a non-integer spin (S = 1/2) and can be studied via electron paramagnetic resonance (EPR). Because of the single electron spin, coupled with the near 100% abundance of ^{51}V (I = 7/2), the vanadyl moiety gives an eight-line spectrum. These signals are nearly always sharp, even at room temperature, due to a

non-degenerate ground state and high lying excited states. In concert with complimentary techniques such as electron spin echo envelope modulation (ESEEM) and electron-nuclear double resonance (ENDOR), the summation of these data have been shown to give insight to binding sites per protein molecule and coordination geometry of the binding sites.[17]

Vanadium NMR has been similarly implemented in substitution studies with proteins such as apo-transferrin[16] (Figure 1.2), as the chemical shift of the nuclear spin of the vanadium is equally sensitive to its coordination environment. The intrinsic magnetic moment in the d^1 vanadyl moiety and relatively quick quadripolar relaxation makes it especially susceptible to these studies. The structural pH dependence of aqueous vanadyl is also well understood in the literature, and these data lend themselves to NMR studies of the coordinative environment of protein ligated vanadate.

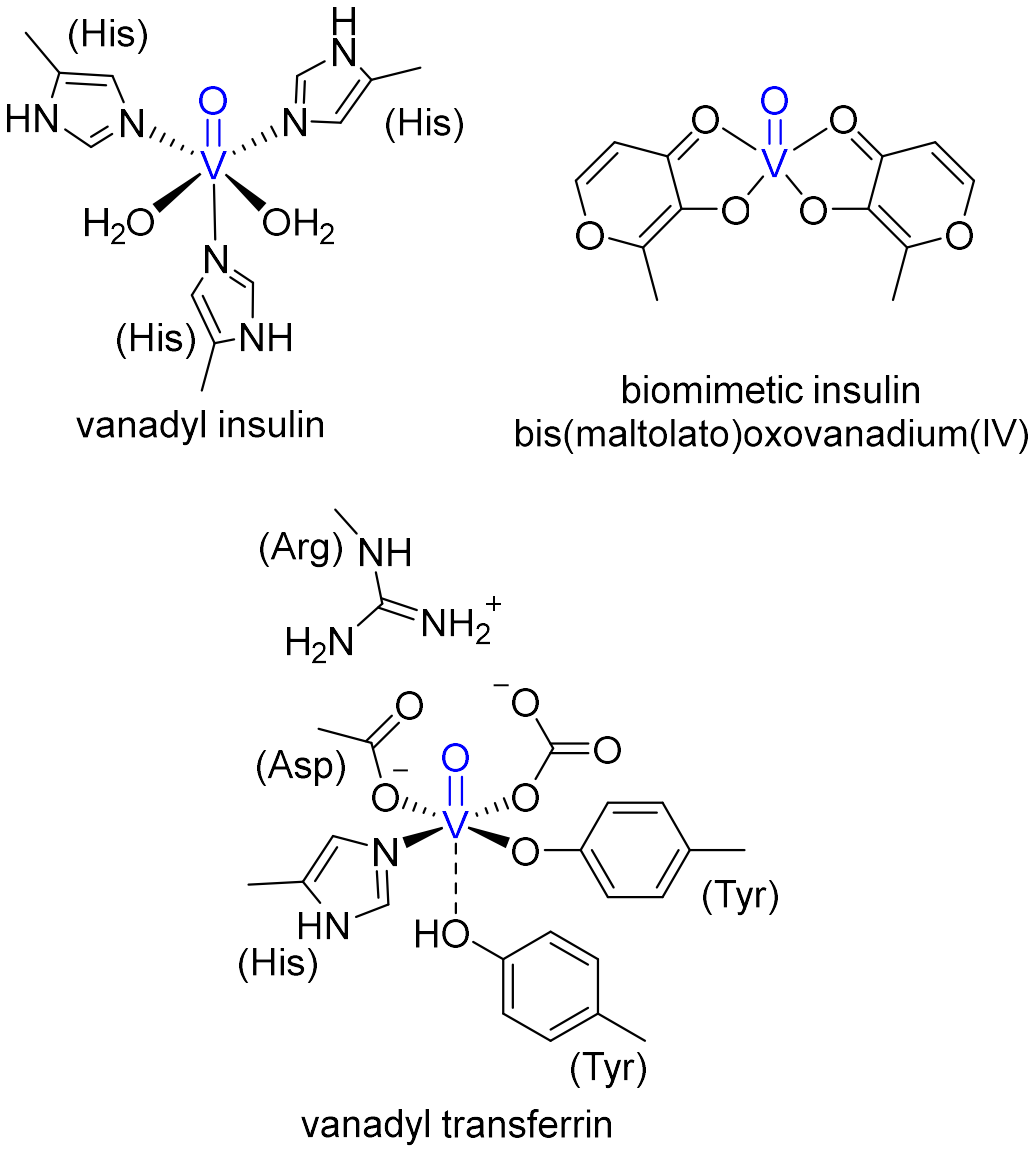

Figure 1.2: Depiction of vanadyl tagged bio-relevant structures.

Other applications of the vanadyl moiety (VO^{2+}) include biomimetic studies[7,8,19,20] outside the scope of human medicinal application. These focus on probing the structure of protein binding sites via purely synthetic models and vanadyl substituted native proteins (Figure 1.3). For example, a handful of studies[21] on mutant varieties of chloroplast F_1-ATPase have utilized EPR to observe changes in the environment about a vanadyl cofactor. By substituting amino acid residues in the protein, perturbations in EPR hyperfine coupling lend information about the inner coordination

sphere of the metal center. These data allow for understanding of the structure/activity relationships in protein structures.

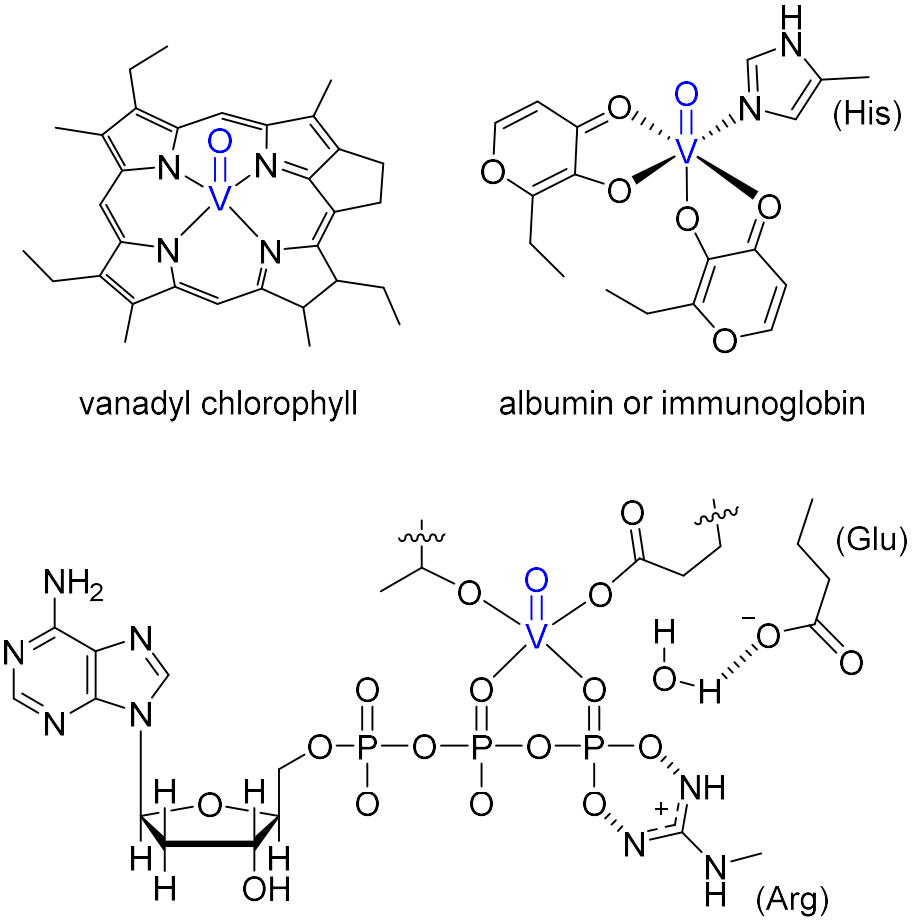

Figure 1.3: Depiction of vanadyl substituted natural products.

Another class of organic fragments of importance in biochemistry are porphyrins, which are naturally occurring compounds that have interesting and characteristic optical properties. Metalated derivatives have been studied primarily as analogues of heme-type carriers. Vanadyl petroporphyrins are most often observed as byproducts of oil refinement, where the porphyrin acts as a carrier for vanadium impurities. Some effort in this field has been applied to the separation of vanadium from these fragments to study porphyrins to better understand the maturation of crude

oil over time,[22,23] however, there are several examples of the study of their electronic structures, [20,24,25] as well as the activity of low valent vanadium(II) toward dioxygen.[26] These novel studies, decades old, serve as a foundation for the modern coordination chemistry of vanadium.

More broadly, the culmination of this work has garnered interest in the reactivity of molecules at the vanadium center, especially those with metal-heteroatom multiple bonds. Indeed, the interaction of small molecules such as dioxygen and dinitrogen, along with the production of dihydrogen, are non-trivial and valuable transformations, and the formation and cleavage of metal-ligand multiple bonds is a cornerstone of these applications. Further, the relative abundance of vanadium metal[27] is also an attractive feature in the current climate, where we as a community are pushing for more renewable technologies. The wide variety of accessible oxidation states (2^+ to 5^+), setting aside redox non-innocent ligand chemistry, also allows for multi-electron processes and charge transfer mechanisms, which may broaden the scope of their applications. In these ways, the coordination chemistry of vanadium is a rich avenue of study for fundamental chemistry in the activation of chalcogen and pnictogen bonds.

1.2 Metal – Nitrogen Multiple Bonds

Metal-ligand multiple bonds in molecular systems are of continuing interest as sources of pnictogen atoms through group transfer mechanisms,[28–30] such as metathesis of nitrene derivatives,[31,32] or stepwise activation with electrophiles.[33–37] Terminal metal nitrides have also become a target of interest in the production of ammonia[38–40] and beyond[41], as the stoichiometric splitting of dinitrogen often yields the nitride,[42] and catalytic activation has since been shown to go through nitride intermediates.[43–45] These examples, however, go through stepwise additions of protons and electrons (proton coupled electron transfer, PCET) which utilize strong Brønsted acids and an extreme excess of reducing agents. This can be attributed to the remarkable thermodynamic stability of the M≡N bond,[35] especially in the case of high valent metal centers.

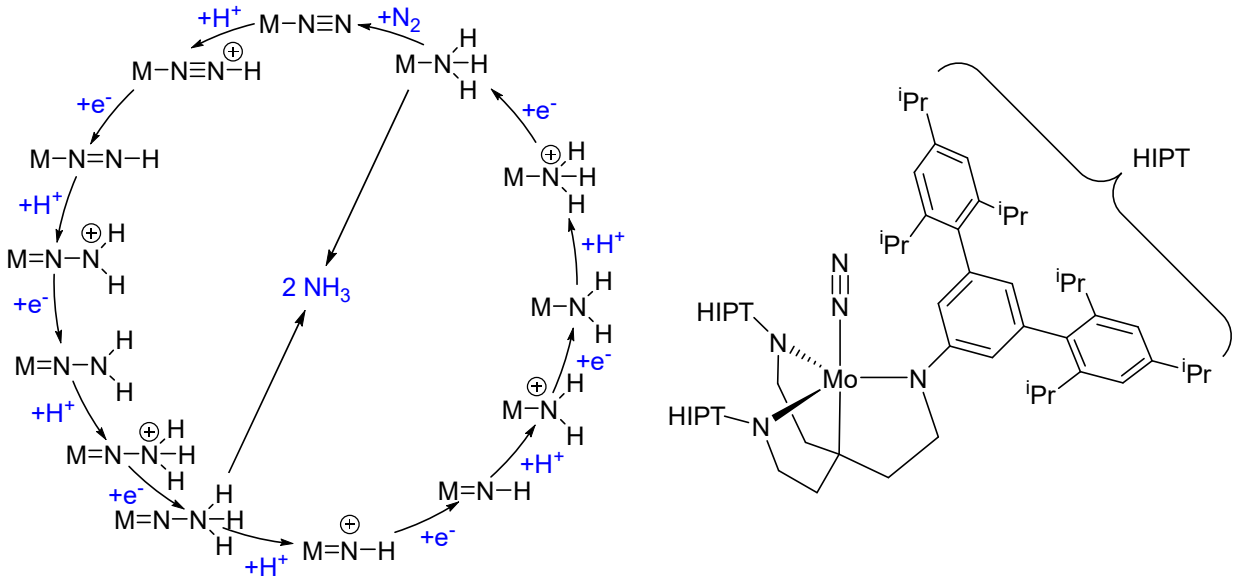

Figure 1.4: Depiction of the Schrock cycle[43] (left) and (HIPTN$_3$N)Mo(N$_2$) (right).

Indeed, the electronic structure of metal center determines the bond order and donation from the bound heteroatom. Relatively few examples of isolable late metal multiple bonds exist in the literature, where nitrene transfer can be more favorable due to ligand centered electron density.[31] This is largely due to the inability of late metals to accept electrons from the ligand in bonding

orbitals, especially at and after the d^6 arrangement in any geometry (Figure 1.5).[46] Strategies to capture intermediate species rely on steric control and/or redox non-innocent ligands as electron reservoirs. As such, some of these species possess ambiguous electronic structures, and complicated magnetic properties.

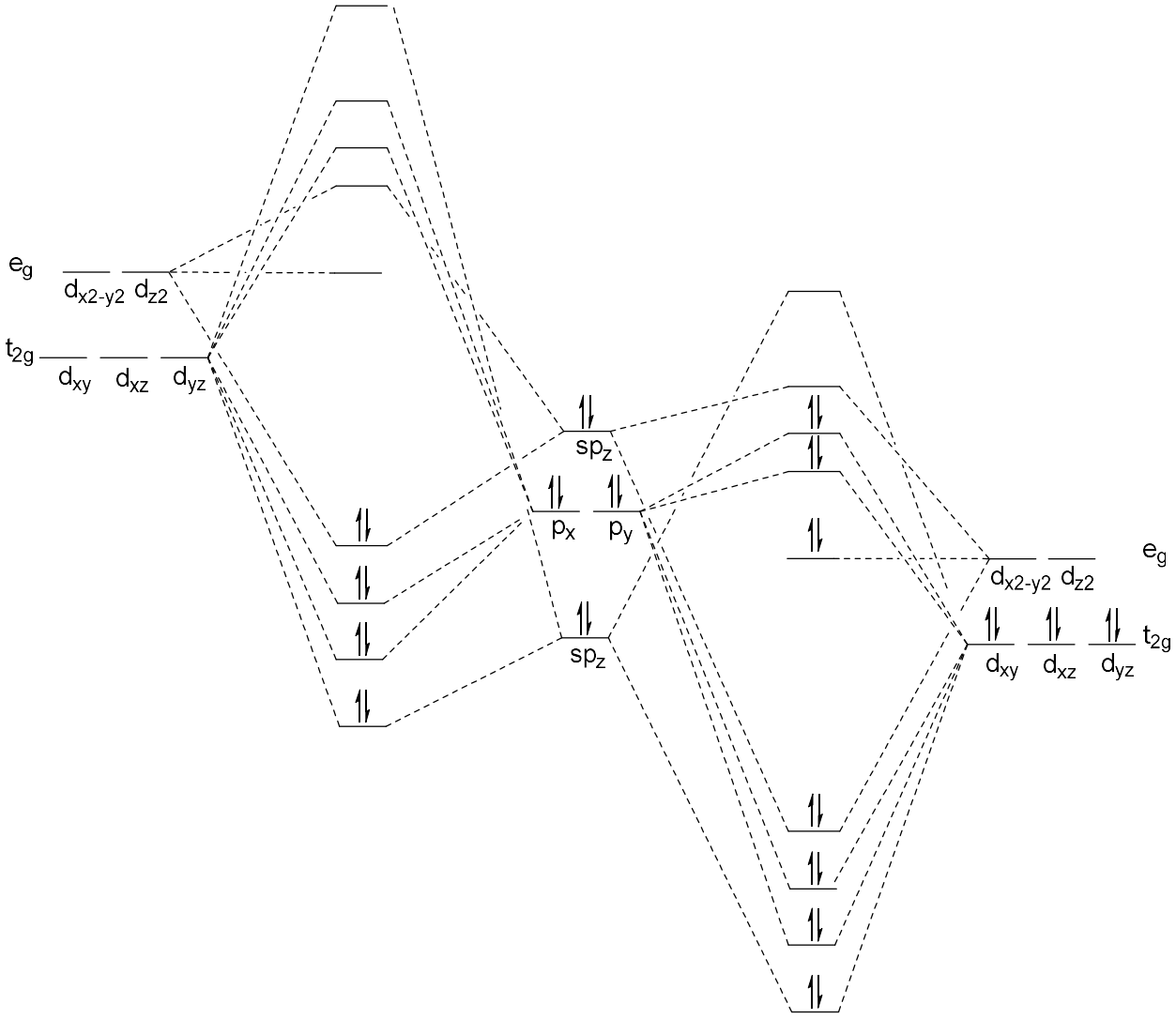

Figure 1.5: Simplified depiction of bonding and antibonding interactions between d^0 (left) or d^6 (right) metal centers and an N^{3-} ligand (center).

Simultaneously, early metal systems are readily isolable and present limited reactivity. This observation was discussed by Ballhausen and Gray in 1962 while studying the hydrated vanadyl

moiety (VO^{2+}).[47] This work followed the many biochemical studies discussed in the previous section, and set the precedent which describes metals before Group VIII as proceeding the "oxo wall" (Figure 1.6), where the energy of the metal orbitals relative to the heteroatom are markedly higher. This orbital energy difference results in π orbitals from the donor atom being readily able to satisfy the 3d-2p mixed molecular orbitals, and the lowest lying antibonding orbitals to be predominantly metal based (Figure 1.6). More generally, metals-oxo bonds to the left of this boundary are considered chemically inert; those to the right are readily reactive, and often not isolable. The Ballhausen-Gray (B-G) model for these electronic structures is still widely referenced when considering these systems and is reasonably extended to describe metal-nitrogen multiple bonds, where bond polarization is more pronounced. Strategies to coerce these stable bonds into reactivity revolves mostly around manipulating the ligand field about the M-L bond, utilizing electron rich ligands to directly affect the nucleophilicity of the heteroatom by driving electron density into multiple bonds with the metal center.

21 Sc 44.96	22 Ti 47.90	23 V 50.94	24 Cr 52.00	25 Mn 54.94	26 Fe 55.85	27 Co 58.93	28 Ni 58.70	29 Cu 63.55	30 Zn 65.41
39 Y 88.91	40 Zr 91.22	41 Nb 92.91	42 Mo 95.94	43 Tc (98)	44 Ru 101.07	45 Rh 102.91	46 Pd 106.4	47 Ag 107.87	48 Cd 112.41
71 La 138.91	72 Hf 178.49	73 Ta 180.95	74 W 183.85	75 Re 186.21	76 Os 190.2	77 Ir 192.22	78 Pt 195.09	79 Au 196.97	80 Hg 200.59

Figure 1.6: Periodic table of transition elements with the "oxo wall" denoted in red.

Generation of these metal-ligand multiple bonds are most commonly achieved through one of two pathways: the decomposition of an azide ligand, or the cleavage of dinitrogen. Both of these require starting materials with lower oxidation states, where the metal center is oxidized as a part of the reaction. Specifically for vanadium, oxidation states 2+ and 3+ can be utilized for either

mechanism. In particular, V(II) is fairly reducing, and known in the literature to activate dinitrogen,[48,49,50,51] though this oxidation state is not required.[52]

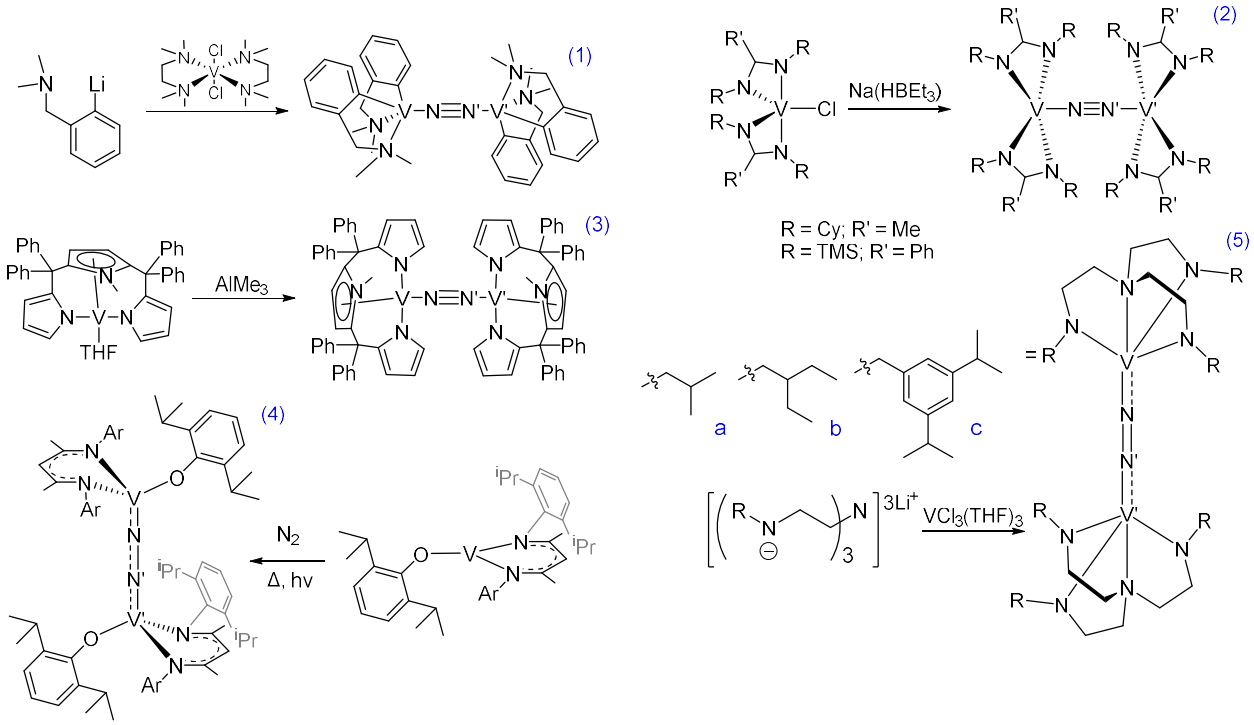

Figure 1.7: Literature examples of end-on activated dinitrogen by vanadium complexes.

Indeed, there are several examples of end-on activation, resulting in bridging dinitrogen species. These have incredible structural diversity, with a variety of ancillary ligands. These symmetric, di-nuclear species are the result of partial reductions of the N_2 unit. While these often result in a symmetric electronic structure, these examples are predominately mixed valence. In the examples of complexes 2 (V^{II}/V^{III}, μ_{eff} = 0.91 μ_B) and 3 (V^{III}/V^{IV}, μ_{eff} = 1.74 μ_B), the activated products are weakly paramagnetic, each with a magnetic moment consistent with an S = ½ ground state. This would be the result of antiferromagnetically coupled pairs of electrons on either metal across the dinitrogen unit.

Table 1.1: Summary of the relevant core bond lengths for the compounds depicted in Figure 1.7. *a*, V-V' distance calculated via 2(V-N)+(N-N') *b*, structural parameters not reported due to unreliable refraction data *c*, distances reported as an average of each ligand derivative.

See Figure 1.7	V-N (Å)	N-N' (Å)	V-V' (Å)
(1)[51,*a*]	1.833(3)	1.228(4)	4.894(calc)
(2)[49,*a*]	1.756(5)	1.235(6)	4.748(calc)
(3)[50,*a*]	1.752(6)	1.248(5)	4.752(calc)
(4)[48,*b*]	—	—	—
(5)[52,*c*]	1.774(avg)	1.208(avg)	4.755(avg)

The sole electronically symmetric paramagnetic example, complex 1 (V^{II}/V^{II}), was reported with a magnetic moment for both vanadium atoms with an effective moment of 3.47 μ_B each. Curiously, there was no overall moment reported for this species, though from these data we can infer an S = 3 ground state. From the structural data (Table 1.1) we can see that the dinitrogen bridge is most weakly activated of the paramagnetic examples, with an elongated V-N distance and contracted N-N' distance compared to the 2 and 3. Further, the fragments on either side of the μ-N_2 ligand are twisted with respect to each other by 84.2(1)˚. These may account for the lack of coupling by limited reduction of the dinitrogen unit, and low orbital overlap between metals through the N_2 bridge (Figure 1.8).

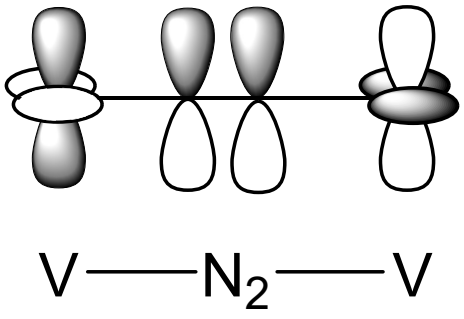

Figure 1.8: Qualitative depiction of orbital torsion of complex 1, depicted in Figure 1.7.

In contrast, complexes 4 and 5 are notably diamagnetic, S = 0, due to strong antiferromagnetic coupling effects between pairs of formally V(III) centers. Unfortunately, the diffraction data for a crystalline sample of complex 4 could not be reliably refined and cannot be analyzed by the method these data have been presented so far. However, Raman characterization of the N-N' bond was presented in both papers for both ^{14}N and ^{15}N derivatives (Table 1.2).

Table 1.2: Raman resonances for complexes 4 and 5(a, b, c), depicted in Figure 1.7. *a*, data reported as Fermi doublets. The frequency of free N_2 is given for reference.

See Figure 1.7	ν ^{14}N (cm^{-1})	ν ^{15}N (cm^{-1})	ν_{free} $^{14}N_2$ (cm^{-1})
(4)[48]	1374	1330	2358
(5a)[52]	1399	1367, 1330[a]	
(5b)[52]	1401	1369, 1331[a]	
(5c)[52]	1402	1369, 1338[a]	

These data suggest a similarity in the activation of dinitrogen between systems 4 and 5, where the structural analysis of complexes 5a, 5b, and 5c may be roughly applied to our analysis of 4. For example, during the discussion of the family of V(tren) complexes presented in their publication, Kajita and coworkers assert that the contraction of the amide donors in the trigonal plane (where the amine and N_2 are in the axial positions of a trigonal bipyramidal structure) gives evidence to the participation of π donation from the ancillary ligand in the activation of dinitrogen. If we then consider the ligands about vanadium in the Mindiola work, the phenolate ligand is much more π donating than the amide moiety. This could result in an elongation of the N_2 bond, evidenced by the lower frequency vibration that was reported (Table 1.2). The conclusions of these works were divergent in their goals, where the comparison of these species respective reactivities are not comparable. However, noted conclusions of each indicate that complex 5 is amenable to

reduction by protons and electrons to ammonia, and complex 4 does not convert to the nitride under any conditions, despite satisfying the electronic requirements for dinitrogen cleavage.

Towards the cleavage of dinitrogen, we must now consider the side-on binding mode[53–55] of N_2. There are even fewer examples of this structural motif in the literature for vanadium centered molecules. However, there appear to be a few common traits among them: strongly electron donating ligands, low valent starting materials, and products with high oxidation states. As with the end-on examples discussed above, it's no surprise that V(II) and V(III) starting materials are required to perform these transformations. These examples, however, show a more complete, if not entirely complete, reduction of dinitrogen.

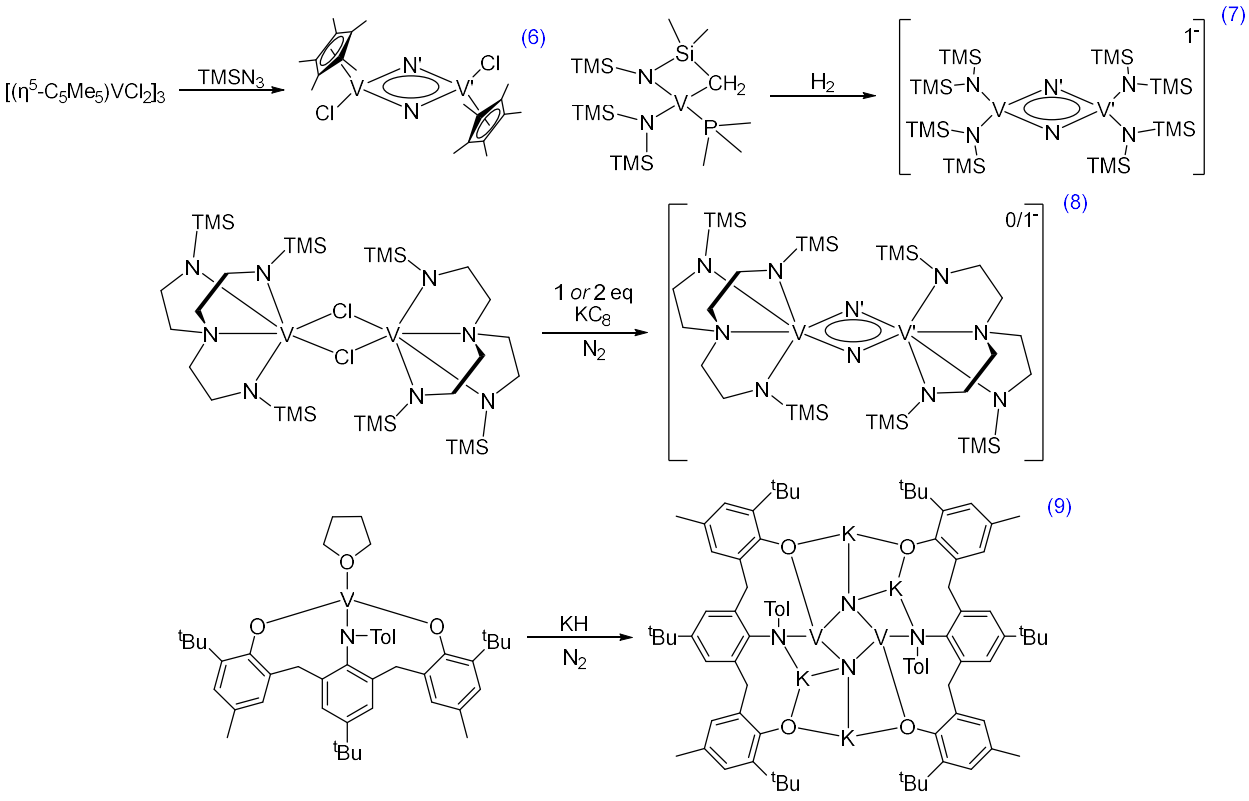

Figure 1.9: Literature examples of side-on activated dinitrogen by vanadium complexes.

As shown in Table 1.3, the N···N' interatomic separation in each example has been elongated to greater than 2.4 Å, well over double the atomic radii of a nitrogen atom (0.71 Å) and

may be considered entirely cleaved. This then leads us to investigate the apparent cleavage of dinitrogen without the release of two independent nitrides. The V-N bond distances reported here are not dissimilar to those in the examples of end-on activation (Table 1.1), suggesting a vanadium-imido double bond rather than a vanadium-nitrido triple bond. However, the angles of these associations are markedly different. In each of the end-on examples, the V-N_2-V bonds were all approximately linear, whereas here each of these V_2N_2 cores are planar and nearly square (~90˚).

Table 1.3: Summary of the relevant core bond lengths for the compounds depicted in Figure 1.8. *a*, N-N' distance calculated via V-N/sin(V-N-V'/2) *b*, crystallographically symmetric *c*, average bond lengths of V_2N_2 core.

See Figure 1.9	V-N (Å)	N-N' (Å)	V-V' (Å)
(6)[53,a]	1.771(2)[b]	2.45(calc)	2.561(1)
(7)[54]	1.773(avg)[c]	2.420(3)	2.583(1)
(8)[54], 0	1.816(avg)[c]	2.50(2)	2.632(6)
(8)[54], 1-	1.775(avg)[c]	2.44(1)	2.575(3)
(9)[56]	1.810(avg)[c]	2.550(3)	2.5682(8)

Compounds 6 and 8^0 were well characterized via NMR studies as well, as both vanadium centers in each molecule were in the 5+ oxidation state (d^0) and diamagnetic. Each of these species show an unambiguously static structure at room temperature, with no perturbation of the V_2N_2 core. Alluding to the stability of this moiety, 6 was not amenable to substitution or addition of exogenous ligands, such as phosphines or pyridine. Further, the X-type chloride ligand could be exchanged in a stepwise metathesis without changing this structure. This stability is also exemplified by complex 8^0, which was found to be redox non-innocent. Reduction with KC_8 allowed for the isolation and study of the mixed valent V^V/V^{IV} species, 8^{1-}. No further reactivity is noted for either example.

In the case of 7, the bridging dinitride was isolated as a counter anion to the trishyrido-bridged species $[\{PMe_3)_3V\}_2(\mu\text{-}H_3)]^+$ as a peculiar byproduct of an attempted hydrogenation. Studies in the absence of dinitrogen gives evidence to the capture of atmospheric N_2 by some low valent vanadium amide. However, due to the paramagnetism of the polymetallic salt, as well as inconsistencies in the reported magnetic moment, the electronic structure of any of these four vanadium atoms remains ambiguous.

A well-defined paramagnetic example, 9, exhibited an effective magnetic moment of 2.9 μ. This would suggest an S = 1 ground state, with two conceivable options for the electronic structure: V^{III}/V^{V} or V^{IV}/V^{IV}. The former would be unlikely, due to the symmetry and of the V_2N_2 core observed in the crystal structure. Under reducing conditions, the activation of dinitrogen by two transient V(II) centers via reduction by four electrons could result in a symmetric V^{IV}/V^{IV} system, however, this would not result in the cleavage of N_2, which requires six electrons. The authors posit a transient V(I) intermediate, or a mechanism which utilizes more than two vanadium centers. Further, only complex 9 has been shown to cleave dinitrogen completely into two monomeric vanadium nitrides. Aside from this example, almost all are other vanadium nitrides independently prepared from the decomposition of azide ligands[33,57,58] or nitrogen atom transfer chemistry.[59]

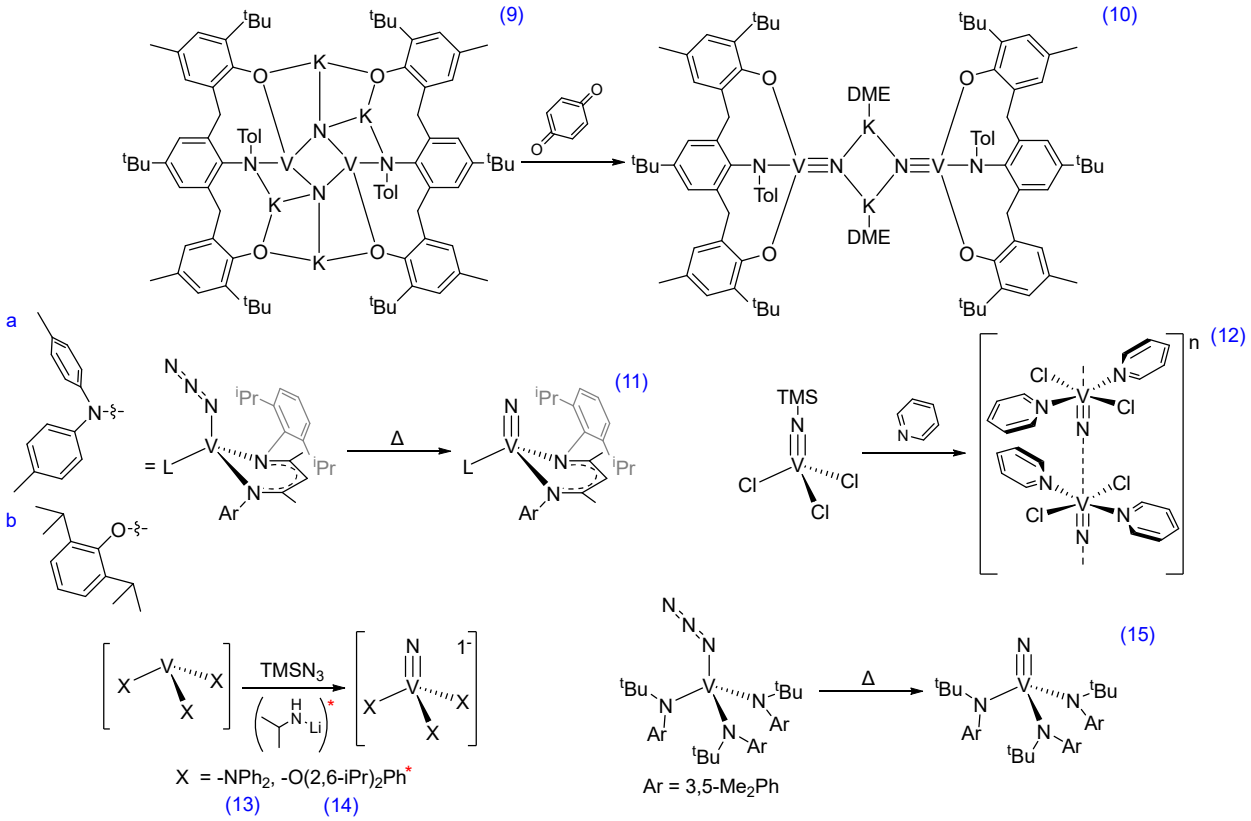

Figure 1.10: Literature examples of terminal vanadium nitrides. * denotes a second synthetic step for the specified product.

Oxidation of 9 with benzoquinone affords 10, which is dimeric in the solid state. However, NMR studies of ^{1}H, ^{15}N, and ^{51}V nuclei on the diamagnetic material give evidence to a C_s symmetric monomer in solution. This complete severance of dinitrogen to yield a vanadium(V) nitride is evidenced by the contraction of the V-N bond from ~1.8 to ~1.6 Å. This is consistent with terminal nitrides generated by alternative methods, as shown in Figure 1.10 and summarized in Table 1.4. Notably, complex 15 was not crystallographically characterized. However, further reactivity of the reported intermediate is relevant to this discussion.

In their respective publications, complexes 12 and 14 are presented as curious asides, with no further reactivity or discussion of reactivity. While they will not contribute to the discussion of the activity of vanadium-nitrogen multiple bonds, they are important to establish the parameters of the triple-bound V-N moiety as a consistent metric.

Table 1.4: Summary of relevant bond lengths depicted in Figure 1.10. a and b are notated for structures 11 in accordance with Figure 1.10.

See Figure 1.10	V-N (Å)
(10)[56]	1.591(4)
(11)[33,57,59]	1.573(2)[a], 1.565(4)[b]
(12)[60]	1.571(7)
(13)[58]	1.582(3)
(14)[61]	1.565(5)
(15)[62]	—

Each of these examples have another commonality: a high oxidation state, coupled to a low coordination number. In coordinatively unsaturated systems, significant lack of *trans*- effect with respect to the nitride ligand allows for the polarization of the V-N bond. This opens the door for electrophilic substrates at the nitrogen atom. These transformations are desirable for a variety of applications, as discussed, such as pharmaceutical chemistry and heterogeneous catalysis.

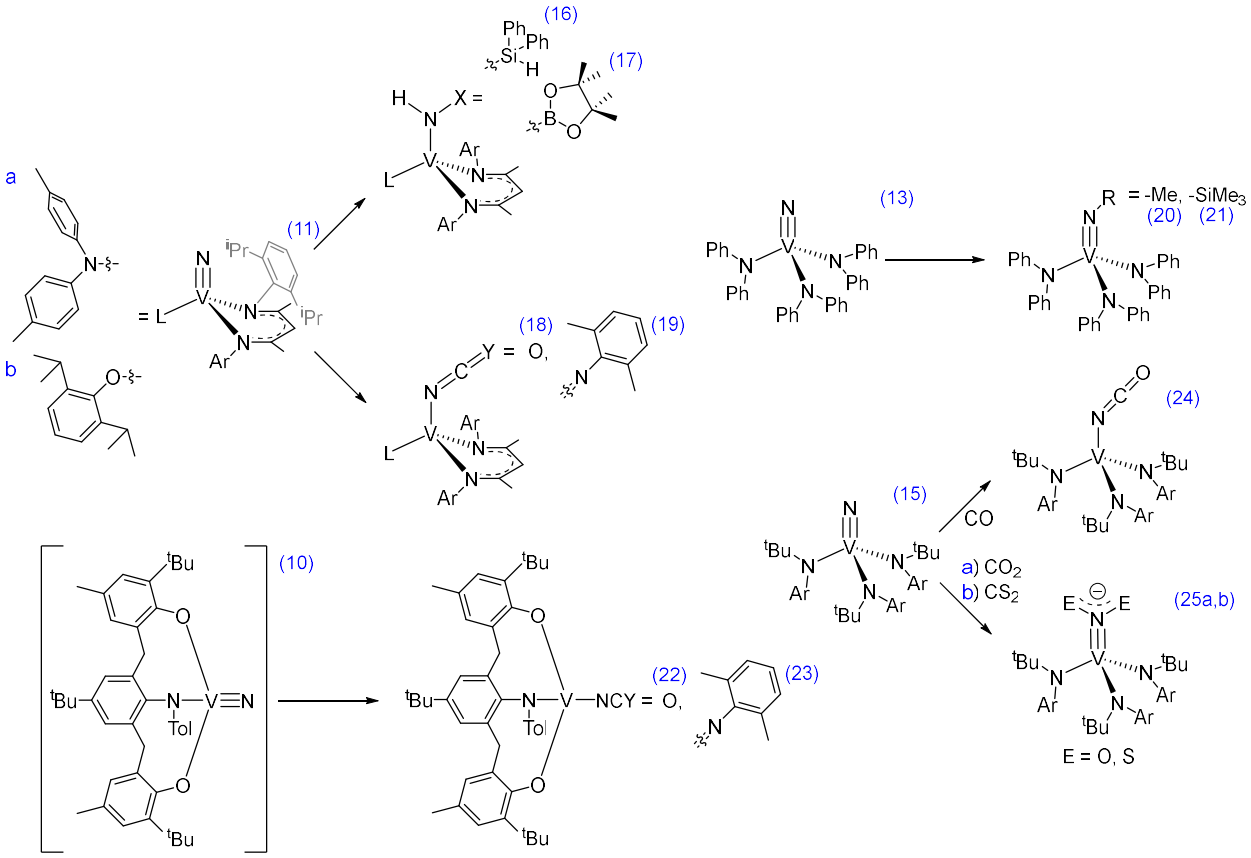

Figure 1.11: Depiction of the activation of selected V-N multiple bonds.

Due to the variability of the reactions here, direct comparison of these products is not constructive for the purpose of this discussion. This does, however, illuminate the potential for this V-N-R moiety as a target for nitrogen atom transfer chemistry. The nucleophilicity of the V-N bond is exemplified by its propensity to add to small molecules such as methyl iodide, trimethylsilyl chloride, and carbon monoxide. Complexes 20, 21, and 24 are an example of this reactivity from bulky monodentate tris-amide vanadium nitrides in a pseudo-tetrahedral coordination sphere. The one-sided bulk allows for selectivity for small molecules by discouraging dimerization of the starting materials. This functionality is furthered by 25a and 25b with the activation of highly oxidized carbon centers. The pronounced polarization of the nitride forces a

dipole upon the linear CO_2/CS_2 molecule which allows for the nucleophilic addition to carbon atom.

Indeed, heavily oxidized carbon sources such as CO and CN-R in examples 18, 19, 22, 23 and 24 are reasonably effective π acids, and are also susceptible to addition. More importantly, these reagents go on to activate the electronic structure of the vanadium-nitrogen bond via reduction of the metal center.

Table 1.5: Comparison of bond lengths of parent vanadium nitrides and activated products. Y = O, 2,6-Me_2Ph.

See Figure 1.11	11→18	11→19	10→22	10→23	15→24
V-N (Å)	1.573(2)[a]	1.573(2)[a]	1.591(4)	1.591(4)	—
V-NCY (Å)	1.9408(13)	1.938(2)	1.984(3)	1.968(3)	1.955(1)

This reduction is evidenced by the significant elongation of the metal-nitrogen bond, as well as observed paramagnetism in their respective products. Another example of the nucleophilicity of this moiety is exemplified by the transformation of 11 to products 16 and 17. Mindiola and coworkers have thoroughly studied this vanadium nitride via a series of publications,[33,57,59] where here specifically they elucidate the mechanism for the addition of boranes and silanes.[63] Though a concerted insertion of the nitride into the E-H bond is plausible, a 3-centered transition state is more common in electrophilic nitrides, where the LUMO is predominantly nitrogen based. Where this system is inverted as a more nucleophilic nitride, an initial silicon/boron adduct is more likely in this case, followed by a 1,2-H migration. This hypothesis was given evidence by an independently prepared trimethylaluminum adduct as a demonstration of the proposed nucleophilic character.

The inability to cleave the V-N bond is persistent in these examples, with the exception of 22 and 23. In the same publication as the synthesis and characterization of complexes 9 and 10,

Cummins and coworkers have demonstrated the dissociation of nitride-generated isocyanate and carbodiimide by the substitution of 2-butyne. This reaction exclusively proceeds in toluene, driven by the precipitation of potassium salts of isocyanate and carbodiimide. The alkyne adduct can then be recovered and reconstituted in toluene, regenerating the precursor to 9 (Figure 1.12). This represents a great stride toward the applicability of early metals to the activation and transfer of nitrogen atoms in unimolecular systems. The discussion of metal-ligand multiple bonds, narrowed specifically to vanadium-nitrogen bonding, encompasses a large part of this body of work (Chapter 3), and will continually be referenced as we expand upon it.

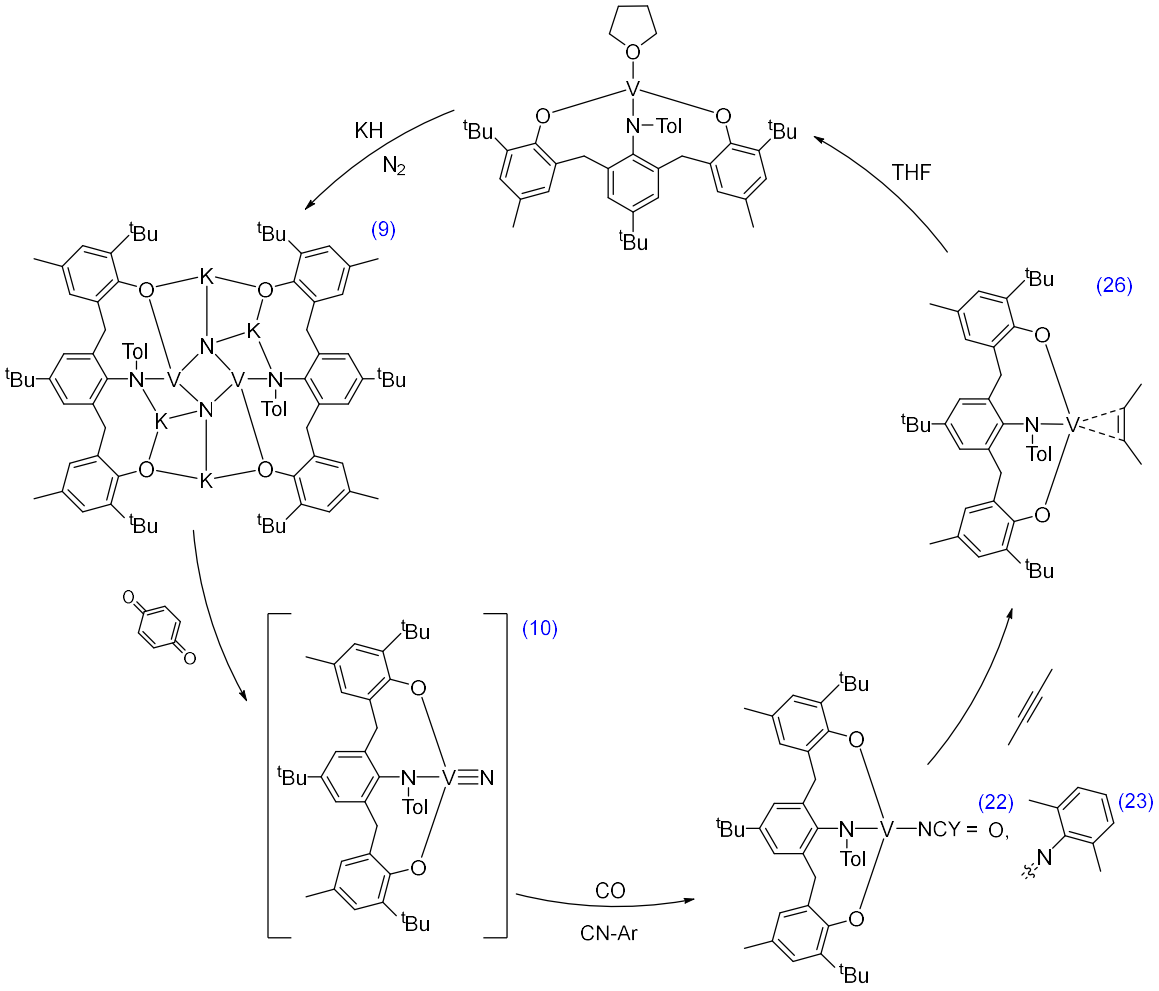

Figure 1.12: Stepwise cycle for the generation, activation, and recycling of (ONO)V≡NK.

1.3 Empty/Occupied Orbitals and the Azide Moiety

As above, activation of a nucleophilic metal-nitrogen multiple bond proceeds from an electronic state that has density centered on the heteroatom. Another mechanism by which electron density can be aggregated on nitrogen is by generating nitrenes:[64,65] a nitrogen atom which has six valence electrons, and an incomplete octet (Figure 1.13). These are incredibly reactive intermediates, and until recently,[66] have never been experimentally observed.

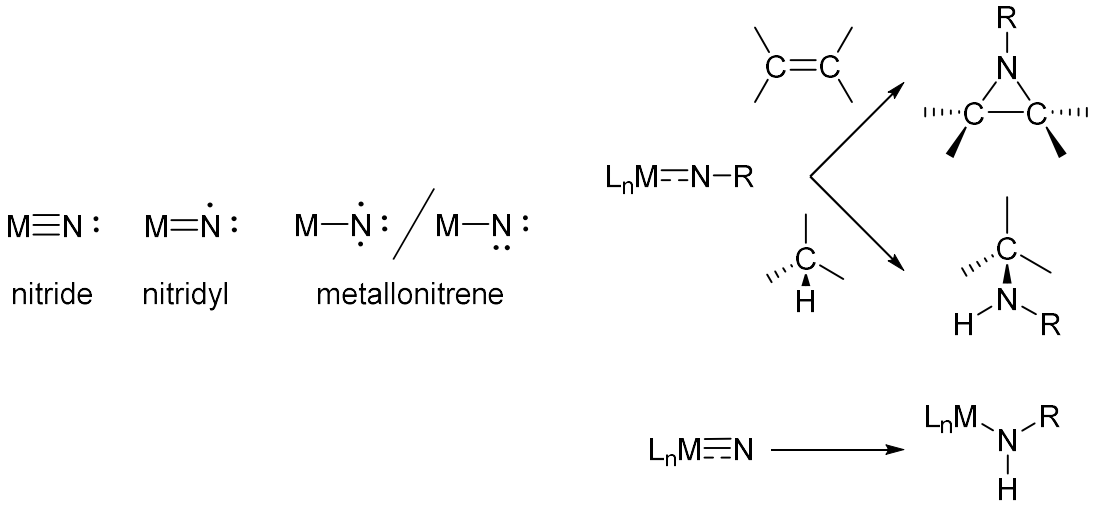

Figure 1.13: Depiction of oxidation states of terminal metal-nitrogen bonds (left), and some generalized examples of common reactivity of metal nitrenes (right).

A common method for the generation of these species is the decomposition of azides, not unlike as discussed in the generation of metal nitrides. Indeed, the oxidation of low valent metal azides by thermolysis/photolysis goes through a nitrene intermediate. However, in the case of later transition metals, where this oxidation is not always feasible, nitrenes can be directed to do powerful chemical transformations.[29,32,64,65,67–69] Examples of this have been observed with precious metals such as ruthenium,[70] osmium,[71–73] rhodium,[74] iridium,[75] and platinum,[66,76,77] as well as first row metals like iron,[78,79] cobalt,[80] nickel,[81–83] and copper.[84] High oxidation states of these metals are generally unstable, or outright inaccessible, leading to rapid reactivity of the diradical nitrogen atom.

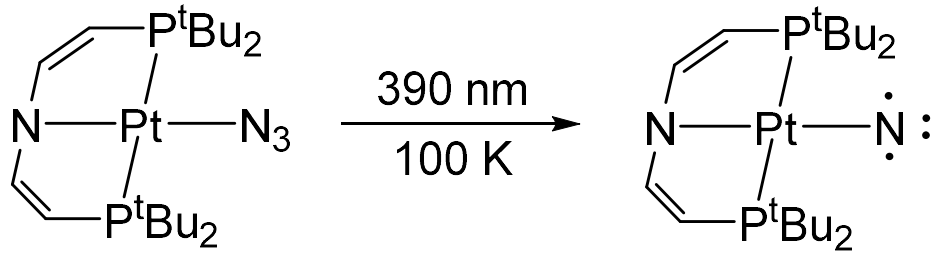

Scheme 1.1: Photolysis of (PNP)Pt(N_3).

The sole characterized metallonitrene was reported in 2020 from the lab of Sven Schneider, utilizing photocrystallography. Following the synthesis of their pincer ligated platinum azide, (PNP)Pt(N_3), a single crystal was mounted on the diffractometer and irradiated with a violet LED (390 nm) at 100 K. The diffraction was monitored for several hours, where the density in the $P\bar{1}$ space group in the void by the t-butyl substituents rose as free N_2 was released into the crystal lattice. The dinitrogen unit was located over 3 Å from the Pt-N fragment, completely separate from the freshly generated nitrene. This method goes to show the sensitivity of these intermediates, where solid state generation and characterization was required to observe this species.

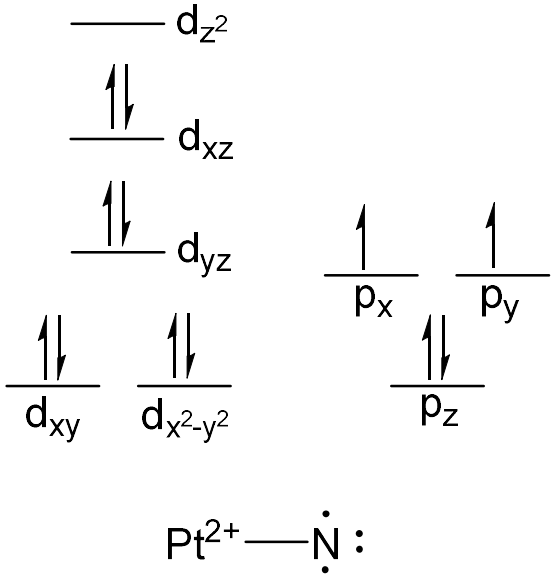

Figure 1.14: Qualitative splitting diagram for adjacent Pt(II) and diradical nitrene with and S =1 ground state.

The nitrogen radical was characterized further by superconducting quantum interference device (SQUID) magnetometry, where the azide was photolyzed at 10 K and brought to room temperature. It was observed that the susceptibility temperature product ($\chi_m T$) increased linearly under 50 K, and nearly constant between 50 and 170 K. At this temperature, the nitrene decomposed, evidenced by the rapid drop in magnetism. In the operational range of this experiment, the data are consistent with a triplet S = 1 ground state (Figure 1.15), consistent with a diradical nitrene bound to a diamagnetic, d^8 square planar Pt(II).

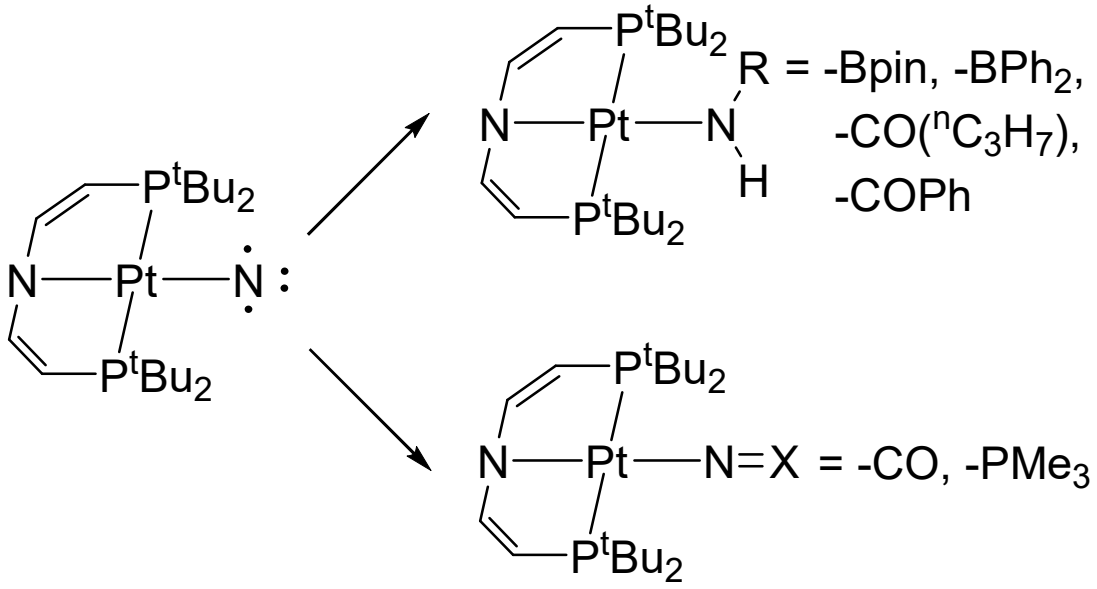

Scheme 1.2: Depiction of the substrate scope of (PNP)Pt(N), generated via *in situ* photolysis.

The reactivity of this nitrene was probed with a wide scope of substrates (Figure 1.16), where electrophiles and nucleophiles were both added to *in situ* generated nitrene. This demonstrates the ambiphilicity of the diradical, where it will serve both as a nucleophile and (for example, C-H/B-H insertion) an electrophile (via the imination of PMe_3).

These examples of intermolecular reactivity are granted by the inability of the diradical nitrogen atom to oxidize platinum(II), as well as the pincer ligand scaffold in a square planar environment, where no substituents are available for attack. This study of the metallonitrene ligand

hinges on these properties in order to impart the limited stability that has been experimentally observed. Focusing specifically on the metal center, we see how having filled d orbitals in late transition is advantages. However, we hypothesize the opposite extreme: a highly oxidized early metal as a stage for nitrene generation should also be inert to oxidation by the diradical substrate. To our knowledge, there are no published examples of this reactivity, which will be the focus of Chapter 4 of this work, where azide salts of pincer ligated vanadium(V) nitrides and neutral mixed vanadium(V) imido/azides decompose to do intramolecular C-H activation of the adjacent benzylic mesityl substituent.

1.4 References

(1) Harden, J. W.; Rich, M. N. Vanadium. *Ind. Eng. Chem.* **1927**, *19* (7), 786–788.

(2) Hamor, W. A. Current Industrial News. *J. Ind. Eng. Chem.* **1913**, *5* (8), 695–696.

(3) Yang, B.; He, J.; Zhang, G.; Guo, J. Chapter 11 - Applications of Vanadium in the Steel Industry. In *Vanadium*; 2021; Vol. 1, pp 267–332.

(4) Ercoli, R.; Calderazzo, F.; Alberola, A. Synthesis of Vanadium Hexacarbonyl. *J. Am. Chem. Soc.* **1960**, *82* (11), 2966–2967.

(5) Bruening, R. C.; Oltz, E. M.; Furukawa, J.; Nakanishi, K. Isolation and Structure of Tunichrome B-1, a Reducing Blood Pigment from the Tunicate Ascidia Nigra L. *J. Am. Chem. Soc.* **1985**, *107* (18), 5298–5300.

(6) Bruening, R. C.; Oltz, E. M.; Furukawa, J.; Nakanishi, K. Isolation of Tunichrome B-1, a Reducing Blood Pigment of the Sea Squirt, Ascidi Nigra. *J. Nat. Prod.* **1986**, *49* (2), 193–204.

(7) Bulls, A. R.; Pippin, C. G.; Hahn, F. E.; Raymond, K. N. Synthesis and Characterization of a Series of Vanadium-Tunichrome B 1 Analogues . Crystal Structure of a Tris(Catecholamide) Complex of Vanadium. *J. Am. Chem. Soc.* **1990**, No. 112, 2627–2632.

(8) Pettersen, R. C.; Alexander, L. E. The Molecular Geometry of Vanadyl Deoxophylloerythroetioporphyrin. An Analog of Chlorophyll. *J. Am. Chem. Soc.* **1968**, *90*, 3873–3875.

(9) Kneifel, H.; Bayer, E. Stereochemistry and Total Synthesis of Amavadin, the Naturally Occurring Vanadium Compound of Amanita Muscaria. *J. Am. Chem. Soc.* **1986**, *108* (11), 3075–3077.

(10) Robson, R. L.; Eady, R. R.; Richardson, T. H.; Miller, R. W.; Hawkins, M.; Postgate, J. R. The Alternative Nitrogenase of Azotobacter Chroococcum Is a Vanadium Enzyme. *Nature* **1986**, *322* (6077), 388–390.

(11) Hales, B. J.; Case, E. E.; Morningstar, J. E.; Dzeda, M. F.; Mauterer, L. A. Isolation of a New Vanadium-Containing Nitrogenase from Azotobacter Vinelandii. *Biochemistry* **1986**, *25* (23), 7351–7255.

(12) Senozan, N. M. Vanadium in the Living World. *J. Chem. Ed.* **1974**, *51* (8), 503–505.

(13) Rehder, D. Vanadium Nitrogenase. *J. Inorg. Biochem.* **2000**, *80* (1–2), 133–136.

(14) Egorova, K. S.; Ananikov, V. P. Toxicity of Metal Compounds: Knowledge and Myths. *Organometallics* **2017**, *36* (21), 4071–4090.

(15) Butler, A.; Eckert, H. ^{51}V NMR as a Probe of Vanadium (V) Coordination to Human Apotransferrin. *J. Am. Chem. Soc.* **1989**, *111* (8), 2802–2809.

(16) Butler, A.; Danzitz, M. J.; Eckert, H. ^{51}V NMR as a Probe of Metal Ion Binding in Metalloproteins. *J. Am. Chem. Soc.* **1987**, No. 109, 1864–1865.

(17) Chasteen, N. D.; Dekoch, R. J.; Rogers, B. L.; Hanna, M. W. Use of the Vanadyl (IV) Ion as a New Spectroscopic Probe of Metal Binding to Proteins. Vanadyl Insulin. *J. Am. Chem. Soc.* **1973**, *95* (4), 1301–1309.

(18) Brini, M.; Calì, T.; Ottolini, D.; Carafoli, E. *Metal Ions in Life Sciences Series*; 2013.

(19) Macor, K. A.; Czernuszewicz, R. S.; Spiro, T. G. Influence of Porphyrin Radical Type on V=O Bond Strength in Vanadyl Porphyrin Cation Radicals: Implications for Heme Protein Intermediates. *Inorg. Chem.* **1990**, No. 29, 1996–2000.

(20) Erdman, J. G.; Ramsey, V. G.; Kalenda, N. W.; Hanson, W. E. Synthesis of Properties of Porphyrin Vanadium Complexes. *J. Am. Chem. Soc.* **1956**, *78* (22), 5844–5847.

(21) Smith, T. S.; LoBrutto, R.; Pecoraro, V. L. Paramagnetic Spectroscopy of Vanadyl Complexes and Its Applications to Biological Systems. *Coord. Chem. Rev.* **2002**, *228* (1), 1–18.

(22) Bencosme, C. S.; Romero, C.; Simoni, S. Axial Interaction of Vanadyl Tetraphenylporphyrin with Lewis Bases. *Inorg. Chem.* **1985**, No. 24, 1603–1604.

(23) Rytting, B. M. K.; Singh, I. D.; Kilpatrick, P. K.; Harper, M. R.; Mennito, A. S.; Zhang, Y. Ultrahigh-Purity Vanadyl Petroporphyrins. *Energy and Fuels* **2018**, *32* (5), 5711–5724.

(24) Carter, E. A.; Goddard III, W. A. Early- versus Late-Transition-Metal-Oxo Bonds: The Electronic Structure of VO+ and RuO+. *J. Phys. Chem.* **1988**, No. 92, 2109–2115.

(25) Walker, F. A.; Hui, E.; Walker, J. M. Electronic Effects in Transition Metal Porphyrins. I. The Reaction of Piperidine with a Series of Para- and Meta-Substituted Nickel (II) and Vanadium (IV) Tetraphenylporphyrins. *J. Am. Chem. Soc.* **1975**, *97* (9), 2390–2397.

(26) Poncest, J.-L.; Barbe, J.-M.; Guilard, R.; Oumous, H.; Lecomte, C.; Protas, J. Vanadium (II) Porphyrin Complexes. *J. Chem. Soc., Chem. Commun.* **1982**, *1* (24), 1421–1422.

(27) Odom, A. L.; McDaniel, T. J. Titanium-Catalyzed Multicomponent Couplings: Efficient One-Pot Syntheses of Nitrogen Heterocycles. *Acc. Chem. Res.* **2015**, *48* (11), 2822–2833.

(28) Munhá, R. F.; Zarkesh, R. A.; Heyduk, A. F. Group Transfer Reactions of d^0 Transition Metal Complexes: Redox-Active Ligands Provide a Mechanism for Expanded Reactivity. *J. Chem. Soc. Dalt. Trans.* **2013**, *42* (2), 3751–3766.

(29) Halfen, J. A. Recent Advances in Metal-Mediated Carbon-Nitrogen Bond Formation Reactions: Aziridination and Amidation. *Curr. Org. Chem.* **2005**, *9*, 657–669.

(30) Degennaro, L.; Trinchera, P.; Luisi, R. Recent Advances in the Stereoselective Synthesis of Aziridines. *Chem. Rev.* **2014**, *114*, 7881–7929.

(31) Eikey, R. A.; Abu-Omar, M. M. Nitrido and Imido Transition Metal Complexes of Groups 6-8. *Coord. Chem. Rev.* **2003**, *243* (1–2), 83–124.

(32) Berry, J. F. Terminal Nitrido and Imido Complexes of the Late Transition Metals. *Comments Inorg. Chem.* **2009**, *30* (1–2), 28–66.

(33) Tran, B. L.; Krzystek, J.; Ozarowski, A.; Chen, C. H.; Pink, M.; Karty, J. A.; Telser, J.; Meyer, K.; Mindiola, D. J. Formation and Reactivity of the Terminal Vanadium Nitride Functionality. *Eur. J. Inorg. Chem.* **2013**, No. 22–23, 3916–3929.

(34) Cozzolino, A. F.; Silvia, J. S.; Lopez, N.; Cummins, C. C. Experimental and Computational Studies on the Formation of Cyanate from Early Metal Terminal Nitrido Ligands and Carbon Monoxide. *Dalt. Trans.* **2014**, *43* (12), 4639–4652.

(35) Smith, J. M. Reactive Transition Metal Nitride Complexes. In *Progress in Inorganic Chemistry*; 2014; pp 417–474.

(36) Grant, L. N.; Pinter, B.; Kurogi, T.; Carroll, M. E.; Wu, G.; Manor, B. C.; Carroll, P. J.; Mindiola, D. J. Molecular Titanium Nitrides: Nucleophiles Unleashed. *Chem. Sci.* **2017**, *8* (2), 1209–1224.

(37) Silvia, J. S.; Cummins, C. C. Two-Electron Reduction of a Vanadium(V) Nitride by CO To Release Cyanate and Open a Coordination Site. *J. Am. Chem. Soc.* **2009**, *131* (2), 446–447.

(38) Askevold, B.; Nieto, J. T.; Tussupbayev, S.; Diefenbach, M.; Herdtweck, E.; Holthausen, M. C.; Schneider, S. Ammonia Formation by Metal-Ligand Cooperative Hydrogenolysis of a Nitrido Ligand. *Nat. Chem.* **2011**, *3* (7), 532–537.

(39) Zhang, S.; Zhao, Y.; Shi, R.; Waterhouse, G. I. N.; Zhang, T. Photocatalytic Ammonia Synthesis: Recent Progress and Future. *EnergyChem* **2019**, *1* (2), 100013.

(40) Li, M.; Huang, H.; Low, J.; Gao, C.; Long, R.; Xiong, Y. Recent Progress on Electrocatalyst and Photocatalyst Design for Nitrogen Reduction. *Small Methods* **2019**, *3* (6).

(41) Kim, S.; Loose, F.; Chirik, P. J. Beyond Ammonia: Nitrogen-Element Bond Forming Reactions with Coordinated Dinitrogen. *Chem. Rev.* **2020**, *120* (12), 5637–5681.

(42) Forrest, S. J. K.; Schluschaß, B.; Yuzik-Klimova, E. Y.; Schneider, S. Nitrogen Fixation via Splitting into Nitrido Complexes. *Chem Rev* **2021**, *ASAPs*.

(43) Yandulov, D. V.; Schrock, R. R. Catalytic Reduction of Dinitrogen to Ammonia at a Single Molybedum Center. *Science* **2003**, *301* (July), 76–79.

(44) Schrock, R. R. Catalytic Reduction of Dinitrogen to Ammonia by Molybdenum: Theory versus Experiment. *Angew. Chemie Int. Ed.* **2008**, *47* (30), 5512–5522.

(45) Buford, R. J.; Fryzuk, M. D. Examining the Relationship between Coordination Mode and Reactivity of Dinitrogen. *Nat. Rev. Chem.* **2017**, *1*, 1–13.

(46) Dahl, J. P.; Flint, C. D.; Gray, H. B.; Henriksen, N. E.; Hocking, R. K.; Lancaster, K. M.; Moller, K. B.; Palmer, J. H.; Solomon, E. I.; Trogler, W. C.; Winkler, J. R. Molecular Electronic Structures of Transition Metal Complexes. In *Structure and Bonding*; Mingos, D. M. P., Ed.; Springer International Publishing, 2012; pp 142–215.

(47) Ballhausen, C. J.; Gray, H. B. The Electronic Structure of the Vanadyl Ion. *Inorg. Chem.* **1962**, *1* (1), 111–122.

(48) L. Tran, B.; Pinter, B.; J. Nichols, A.; T. Konopka, F.; Thompson, R.; Chen, C.-H. H.; Krzystek, J.; Ozarowski, A.; Telser, J.; Baik, M.-H. H.; Meyer, K.; J. Mindiola, D.; Tran, B. L.; Pinter, B.; Nichols, A. J.; Konopka, F. T.; Thompson, R.; Chen, C.-H. H.; Krzystek, J.; Ozarowski, A.; Telser, J.; Baik, M.-H. H.; Meyer, K.; Mindiola, D. J.; L. Tran, B.;

Pinter, B.; J. Nichols, A.; T. Konopka, F.; Thompson, R.; Chen, C.-H. H.; Krzystek, J.; Ozarowski, A.; Telser, J.; Baik, M.-H. H.; Meyer, K.; J. Mindiola, D.; Tran, B. L.; Pinter, B.; Nichols, A. J.; Konopka, F. T.; Thompson, R.; Chen, C.-H. H.; Krzystek, J.; Ozarowski, A.; Telser, J.; Baik, M.-H. H.; Meyer, K.; Mindiola, D. J. A Planar Three-Coordinate Vanadium(II) Complex and the Study of Terminal Vanadium Nitrides from N_2: A Kinetic or Thermodynamic Impediment to N-N Bond Cleavage? *J. Am. Chem. Soc.* **2012**, *134* (31), 13035–13045.

(49) Berno, P.; Hao, S.; Minhas, R.; Gambarotta, S. Dinitrogen Fixation versus Metal-Metal Bond Formation in the Chemistry of Vanadium(II) Amidinates. *J. Am. Chem. Soc.* **1994**, *116* (16), 7417–7418.

(50) Vidyaratne, I.; Crewdson, P.; Lefebvre, E.; Gambarotta, S. Dinitrogen Coordination and Cleavage Promoted by a Vanadium Complex of a σ,π,σ-Donor Ligand. *Inorg. Chem.* **2007**, *46* (21), 8836–8842.

(51) Edema, J. J. H.; Meetsma, A.; Gambarotta, S. Divalent Vanadium and Dinitrogen Fixation: The Preparation and X-Ray Structure of $(\mu\text{-}N_2)\{[(o\text{-}Me_2NCH_2)C_6H_4]_2V(Py)\}_2(THF)_2$. *J. Am. Chem. Soc.* **1989**, *111* (17), 6878–6880.

(52) Kokubo, Y.; Yamamoto, C.; Tsuzuki, K.; Nagai, T.; Katayama, A.; Ohta, T.; Ogura, T.; Wasada-Tsutsui, Y.; Kajita, Y.; Kugimiya, S.; Masuda, H. Dinitrogen Fixation by Vanadium Complexes with a Triamidoamine Ligand. *Inorg. Chem.* **2018**, *57* (19), 11884–11894.

(53) Haddad, T. S.; Aistars, A.; Ziller, J. W.; Doherty, N. M. Symmetrically Bridged Dimeric Vanadium Nitrido Compounds. Synthesis and Characterization of $[(\eta\text{-}C_5Me_5)V(N)Cl]_2$. *Organometallics* **1993**, *12* (7), 2420–2422.

(54) Berno, P.; Gambarotta, S. Reaction of a Vanadium(III) Amide with H_2: Isolation and Characterization of a Polynuclear Mixed-Valence Polyhydrido-Nitrido Complex. *Angew Chem. lni. Ed. Engi* **1995**, *34* (7), 822–824.

(55) Bates, V. M. E.; Clentsmith, G. K. B.; Cloke, F. G. N.; Green, J. C.; Jenkin, H. D. L. Theoretical Investigation of the Pathway for Reductive Cleavage of Dinitrogen by a Vanadium Diamidoamine Complex. *Chem. Commun.* **2000**, No. 11, 927–928.

(56) Ishida, Y.; Kawaguchi, H. Nitrogen Atom Transfer from a Dinitrogen-Derived Vanadium Nitride Complex to Carbon Monoxide and Isocyanide. *J. Am. Chem. Soc.* **2014**, *136* (49), 16990–16993.

(57) Tran, B. L.; Pink, M.; Gao, X.; Park, H.; Mindiola, D. J. Low-Coordinate and Neutral Nitrido Complexes of Vanadium. *J. Am. Chem. Soc.* **2010**, *132* (5), 1458–1459.

(58) Song, J. I.; Gambarotta, S. Preparation, Characterization, and Reactivity of a Diamagnetic Vanadium Nitride. *Angew. Chemie - Int. Ed. English* **1996**, *35* (19), 1258–1263.

(59) Tran, B. L.; Singhal, M.; Park, H.; Lam, O. P.; Pink, M.; Krzystek, J.; Ozarowski, A.; Telser, J.; Meyer, K.; Mindiola, D. J. Reactivity Studies of a Masked Three-Coordinate Vanadium(II) Complex. *Angew. Chemie Int. Ed.* **2010**, *49* (51), 9871–9875.

(60) Critchlow, S. C.; Lerchen, M. E.; Smith, R. C.; Doherty, N. M. Vanadium Nitride Linear Chain Polymers and Monomers. Synthesis and Structures of $[V(\mu\text{-}N)Cl_2(Py)_2]\infty$ and $V(N)Cl_2(Quin)_2$. *J. Am. Chem. Soc.* **1988**, *110* (24), 8071–8075.

(61) Henderson, R. A.; Janas, Z.; Jerzykiewicz, L. B.; Richards, R. L.; Sobota, P. Vanadium Phenoxide Complexes with Oxide, Nitride or Hydrazide Co-Ligands: Preparation and Crystal Structures of $[V(OC_6H_3Pri_2\text{-}2,6)\ 3NLi(C_4H_8O)_3]$, $[\{VO_2(OC_6H_3Pri_2\text{-}2,6)_2\}_2\{\mu\text{-}Li(C_4H_8O)_2\}_2]$. *Inorg. Chim. Acta* **1999**, *285* (2), 178–183.

(62) Brask, J. K.; Fickes, M. G.; Sangtrirutnugul, P.; Durà-Vilà, V.; Odom, A. L.; Cummins, C. C. Niobium and Vanadium Iminophosphinimide Complexes. *Chem. Commun.* **2001**, *1* (17), 1676–1677.

(63) Thompson, R.; L. Tran, B.; Ghosh, S.; Chen, C.-H.; Pink, M.; Gao, X.; J. Carroll, P.; Baik, M.-H.; J. Mindiola, D. Addition of Si–H and B–H Bonds and Redox Reactivity Involving Low-Coordinate Nitrido–Vanadium Complexes. *Inorg. Chem.* **2015**, *54* (6), 3068–3077.

(64) SIMA, J. Photochemistry of Azide-Moiety Containing Inorganic Compounds. *Coord. Chem. Rev.* **2006**, *250* (17–18), 2325–2334.

(65) Dequirez, G.; Pons, V.; Dauban, P. Nitrene Chemistry in Organic Synthesis: Still in Its Infancy? *Angew. Chemie Int. Ed.* **2012**, *51* (30), 7384–7395.

(66) De Bruin, B.; Hunger, D.; Würtele, C.; Slageren, J. Van. A Platinum(II) Metallonitrene with a Triplet Ground State. *Nat. Chem.* **2020**, *12*, 1054–1059.

(67) Park, Y.; Kim, Y.; Chang, S. Transition Metal-Catalyzed C-H Amination: Scope, Mechanism, and Applications. *Chem. Rev.* **2017**, *117* (13), 9247–9301.

(68) Suarez, A. I. O.; Lyaskovskyy, V.; Reek, J. N. H.; Van Der Vlugt, J. I.; De Bruin, B. Complexes with Nitrogen-Centered Radical Ligands: Classification, Spectroscopic Features, Reactivity, and Catalytic Applications. *Angew. Chemie Int. Ed.* **2013**, *52* (48), 12510–12529.

(69) Kuijpers, P. F.; van der Vlugt, J. I.; Schneider, S.; de Bruin, B. Nitrene Radical Intermediates in Catalytic Synthesis. *Chem. Eur. J.* **2017**, *23* (56), 13819–13829.

(70) Long, A. K. M.; Timmer, G. H.; Pap, J. S.; Snyder, J. L.; Yu, R. P.; Berry, J. F. Aryl C-H Amination by Diruthenium Nitrides in the Solid State and in Solution at Room

Temperature: Experimental and Computational Study of the Reaction Mechanism. *J. Am. Chem. Soc.* **2011**, *133* (33), 13138–13150.

(71) Brown, S. N. Insertion of a Metal Nitride into Carbon-Carbon Double Bonds. *J. Am. Chem. Soc.* **1999**, *121* (41), 9752–9753.

(72) Crevier, T. J.; Mayer, J. M. Insertion of an Osmium Nitride into Boron-Carbon Bonds. *Angew. Chemie Int. Ed.* **1998**, *37* (13–14), 1891–1893.

(73) Williams, D. S.; Meyer, T. J.; White, P. S. Preparation of Osmium(II) Nitrosyls by Direct Oxidation of Osmium(VI) Nitrides. *J. Am. Chem. Soc.* **1995**, *117* (2), 823–824.

(74) Xu, H.; Zhang, X.; Ke, Z.; Zhao, C. A Theoretical Study of Dirhodium-Catalyzed Intramolecular Aliphatic C–H Bond Amination of Aryl Azides. *RSC Adv.* **2016**, *6* (35), 29045–29053.

(75) Schöffel, J.; Rogachev, A. Y.; George, S. D. B.; Burger, P. Isolation and Hydrogenation of a Complex with a Terminal Iridium-Nitrido Bond. *Angew. Chemie Int. Ed.* **2009**, *48* (26), 4734–4738.

(76) Ronconi, L.; Sadler, P. J. Unprecedented Carbon-Carbon Bond Formation Induced by Photoactivation of a Platinum(IV)-Diazido Complex. *Chem. Commun.* **2008**, No. 2, 235–237.

(77) Hennig, H.; Ritter, K.; Chibisov, A. K.; Görner, H.; Grevels, F. W.; Kerpen, K.; Schaffner, K. Comparative Time-Resolved IR and UV Spectroscopic Study of Monophosphine and Diphosphine Platinum (II) Azido Complexes. *Inorg. Chim. Acta* **1998**, *271* (1–2), 160–166.

(78) Scepaniak, J. J.; Young, J. A.; Bontchev, R. P.; Smith, J. M. Formation of Ammonia from an Iron Nitrido Complex. *Angew. Chemie Int. Ed.* **2009**, *48* (17), 3158–3160.

(79) Hakey, B. M.; Darmon, J. M.; Akhmedov, N. G.; Petersen, J. L.; Milsmann, C. Reactivity of Pyridine Dipyrrolide Iron(II) Complexes with Organic Azides: C-H Amination and Iron Tetrazene Formation. *Inorg. Chem.* **2019**, *58* (16), 11028–11042.

(80) Grant, L. N.; Carroll, M. E.; Carroll, P. J.; Mindiola, D. J. An Unusual Cobalt Azide Adduct That Produces a Nitrene Species for Carbon-Hydrogen Insertion Chemistry. *Inorg. Chem.* **2016**, *55* (16), 7997–8002.

(81) Ghannam, J.; Sun, Z.; Cundari, T. R.; Zeller, M.; Lugosan, A.; Stanek, C. M.; Lee, W. T. Intramolecular C-H Functionalization Followed by a [2σ + 2π] Addition via an Intermediate Nickel-Nitridyl Complex. *Inorg. Chem.* **2019**, *58* (11), 7131–7135.

(82) Vreeken, V.; Siegler, M. A.; De Bruin, B.; Reek, J. N. H.; Lutz, M.; Van Der Vlugt, J. I. C-H Activation of Benzene by a Photoactivated NiII(Azide): Formation of a Transient Nickel Nitrido Complex. *Angew. Chemie Int. Ed.* **2015**, *54* (24), 7055–7059.

(83) Laskowski, C. A.; Miller, A. J. M.; Hillhouse, G. L.; Cundari, T. R. A Two-Coordinate Nickel Imido Complex That Effects C−H Amination. *J. Am. Chem. Soc.* **2011**, *133* (4), 771–773.

(84) Cundari, T. R.; Dinescu, A.; Kazi, A. B. Bonding and Structure of Copper Nitrenes. *Inorg. Chem.* **2008**, *47* (21), 10067–10072.

Chapter 2: Low Valent Complexes of Vanadium

2.1 Properties of d^2 and d^3 Complexes

Coordinatively saturated structures with V(II) and V(III) centers have been studied primarily for their novel electronic structures and low energy electronic transitions. Examples of these are polypyridyl complexes (Figure 2.1), such as $[V(bpy)_3]^{2+}$ and $[V(phen)_3]^{2+}$,[1,2] are ubiquitous in the literature as isostructural analogues of well-known and well-studied ruthenium photosensitizers.[3–8] These are renowned in the literature for their applications in light promoted reactions, such as photoredox catalysis. These methods boast greener conditions for valuable products in organic synthesis, however, have a significant limitation; ruthenium is a precious metal. The cost of ruthenium metals is not scalable to industrial methods due to its low natural abundance.[9] Much effort has been put into understanding the photophysical properties of these metal polypyridyls, as well as related complexes in order to overcome this technological barrier.

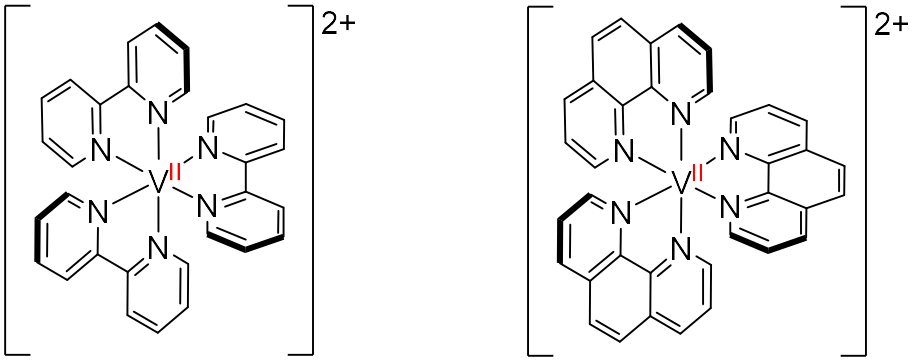

Figure 2.1: Depiction of selected polypyridyl vanadium (II). Counterions omitted for clarity.

A study by Maverick and coworkers[2] directly compared the physical properties and photophysics of both $[V(bpy)_3]^{2+}$ and $[V(phen)_3]^{2+}$ to their ruthenium analogues, both of which have broad absorption features in the visible region between 400 nm and 800 nm. Neither, however, are emissive down to 77 K. Most notable in their findings was that the trivalent oxidation

products were unstable, though reversible on a cyclic voltammetry timescale, and that the lowest energy transitions had contributions from d-d and MLCT transitions. These excited states were studied by transient absorption spectroscopy and were shown to have lifetimes of 500 ± 100 ps and 1.8 ± 0.2 ns for $[V(bpy)_3]^{2+}$ and $[V(phen)_3]^{2+}$, respectively. These photophysical properties led them to the conclusion that the d-d and MLCT contributions to the lowest excited states are mostly exclusive, and do not mix appreciably. The lack of luminescence is attributed by the authors to an unobserved broad, low energy fluorescence from a quartet metal-to-ligand charge transfer (^{4}MLCT) state, or energy loss from intersystem crossing into a low-lying doublet.

Several decades later, these properties were revisited by Rappé and Damrauer[10] utilizing ultra-fast transient absorption spectroscopy to further clarify the decay mechanisms following electronic transitions. They concluded that both are excited to a quartet metal-to-ligand charge transfer excited state which rapidly interconverts to a mixed ^{2}MLCT/^{2}MC excited state. This transition would account for the lack of emission as the doublet states would be lower in energy than the quartet states, where the rate of non-radiative decay outcompetes phosphorescence. They assert that this transition allows for the relatively long lifetime (~1 ns) they observe, and that there is potential for early metal polypyridyls for applications in photoredox catalysis.

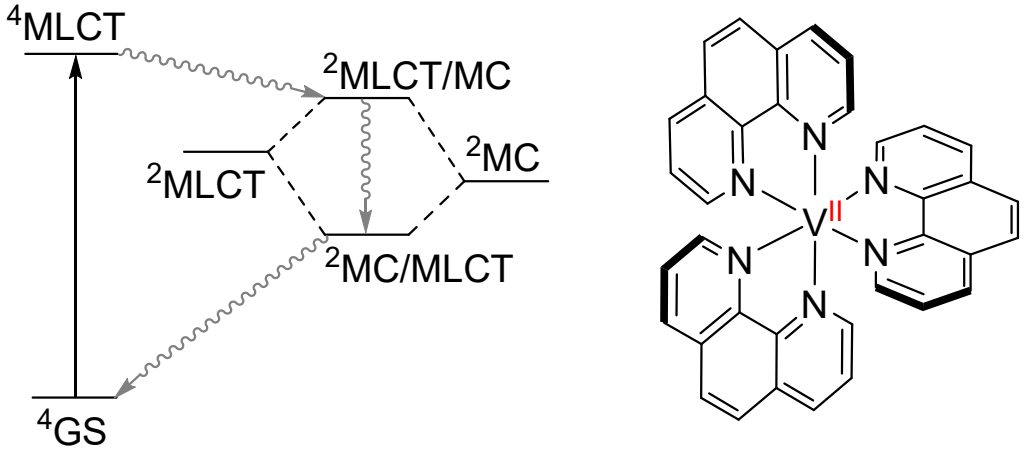

Figure 2.2: Qualitative depiction of electronic transitions in vanadium polypyridyls.

This work was followed by several publications from the lab of Karl Wieghardt.[11–14] The electronic structures of a handful of vanadium polypyridyls in a variety of oxidation states were studied by spectroscopy and calculated by density functional theory (DFT).[15,16] In 2011, they focused on applying broken symmetry solutions for crystallographically characterized M-bpy radicals, in order to establish a relationship between the contraction of the aryl-aryl bond and the resulting electronic properties. Of an exhaustive list of organometallic compounds, an electron-transfer series of three derivatives (0, +1, +2) of decamethylvanadocene bipyridine were modelled.[11]

According to this study, the reported ground states of the neutral, cationic, and di-cationic species were S = ½ (V^{III}/bpy$^{\bullet}$), S = 0 or 1 (V^{III}), and S = ½ (V^{IV}), respectively, where the cation's electronic ground state remains ambiguous. The di-cation, however, displayed an eight-line EPR characteristic of d^1 V^{IV}, and is assigned its ground state with no uncertainty. The crystal structures for this family of complexes showed a typical aryl-aryl bond length for neutral bipyridine in the case of both cationic species. However, there was significant contraction with respect to the neutral complex. This observation, along with the S = ½ ground state, gives evidence to a bipyridine radical coupled antiferromagnetically to d^2 V^{III}, leaving one spin unpaired centered on the metal. These rationalizations were then modelled by DFT, where unrestricted Kohn-Sham solutions of both cationic species were in excellent agreement with experimental data. The neutral species was subjected to a broken symmetry 2,1 calculation. The Mulliken population analysis yielded a spin density of 2:1, with a ground state of S = 0.45, as anticipated by the empirical data. The technically possible bpy^{-1}, S_V = 0 solution was ruled out due to the ring slippage observed both in the crystal structure and reproduced by the calculation.

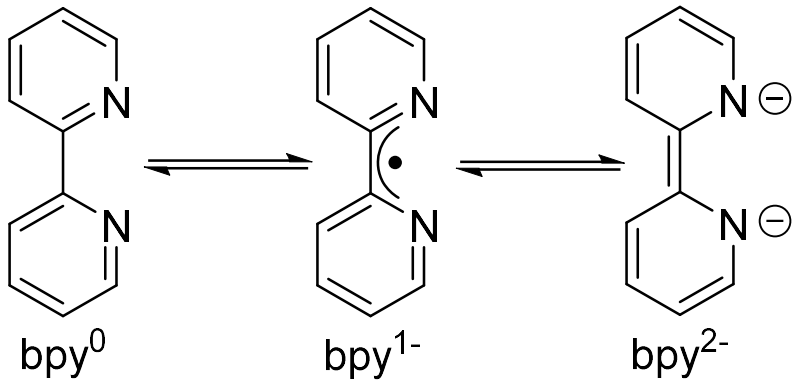

Figure 2.3: Electron-transfer series for 2,2'-bipyridine.

This was followed by the synthesis and characterization the homoleptic $[V(^{t}bpy)_3]^z$ electron-transfer series (z = 3+, 2+, 0, 1-) by Bowman, Sproules, and Wieghardt.[13] The magnetic properties of these complexes along with computational data was used to verify the origin of the observed spin states, summarized in Table 2.1. It is important to note that structural data of these complexes was not available, as single crystals could not be obtained. A single structure of the neutral complex exists in the literature, however, it only had quality enough to establish connectivity for the coordination environment local to the vanadium center.

Table 2.1: Electron-transfer series for vanadium tris-$^{t\text{-}Bu}$bipyridine.

	S	μ_{eff}	Simplified structure
$[V(^{t}bpy)_3]^{1-}$	0	-	$V^{II}(bpy^{\bullet})_3$
$[V(^{t}bpy)_3]^{0}$	1/2	1.80 μ_B	$V^{II}(bpy^{\bullet})_2(bpy^{0})$
$[V(^{t}bpy)_3]^{2+}$	3/2	3.84 μ_B	$V^{II}(bpy^{0})_3$
$[V(^{t}bpy)_3]^{3+}$	1	2.80 μ_B	$V^{III}(bpy^{0})_3$

The monocation could not be isolated due to rapid disproportionation to the neutral and dicationic species, respectively. Calculations show a Mulliken spin population that has the radical character delocalized over all the ligands, except in the case of the monocationic species. The

tendency to localize may justify the rapid electron transfer to more stable configurations. Further, cyclic voltammetry gave no evidence for isolable 2- or 3- states, and the 1- species was too sensitive for exhaustive study. The magnetic susceptibility for each of these species was recorded in the solid state and found to be largely temperature independent.

Another study by the Wieghardt group included vanadium bis-terpyridine[14] to expand upon this study of complexes exhibiting ligand non-innocence with low valent metal centers. Using a standard preparation of these materials, where the trivalent chloride is stirred over sodium amalgam in the presence of ligand, an interesting product was formed. The bis-ligand species had a ground state of S = ½ with two doubly reduce terpyridine ligands, tpy^{2-}, and the origin of paramagnetism a single d electron on V^{IV}. This is likely an example of reductively induced oxidation, where radical terpyridine ($tpy^{\bullet}$) removed an electron form the vanadium valence shell; in order to reach an antiferromagnetically coupled diamagnetic anion, the ligand facilitated an intramolecular electron transfer. This prompted the authors to put forward a revision of formalism, from "low-valent" to "highly reduced." These examples illustrate the depth of diversity in the electronic structures of vanadium polypyridyls, where novel states can be studied in order to develop more sustainable chemistry such as photoredox catalysis.

2.2 Synthesis and Characterization of (^{Mes}PDP^{Ph})VCl(thf)$_2$

The ligand precursor, H$_2$^{Mes}PDP^{Ph}, (2,6-bis(5-(2,4,6-tri-methylphenyl)-3-phenyl-1H-pyrrol-2-yl)pyridine, was previously reported by our group,[17,18] but the preparation has since been modified. From 2,6-pyridinedialdehyde and the chalcone derivative, 1- (2,4,6-trimethylphenyl)-3-phenyl-2-propen-1-one, the intermediate pyridyl tetraketone was isolated by filtration and washed with cold ethanol. This was then heated to reflux with NH_4OAc in glacial acetic acid.[19] This method improves the yield of the cyclization step and improves the ease of purification. Under a nitrogen atmosphere, the ligand was then readily deprotonated with (trimethylsilyl)methyllithium in anhydrous tetrahydrofuran to yield a dark solution with pronounced green luminescence. After thirty minutes, this was added to a stirring solution of VCl_3THF_3. Immediately upon addition, the color of the reaction mixture turns from pale pink to deep red. After stirring overnight, the crude material was reduced to dryness *in vacuo* and rigorously triturated with toluene and pentane, taken in a minimal amount of toluene, and filtered with Celite to remove any dissolved chloride salts. Slow evaporation of the solution affords crystalline material in 98% yield.

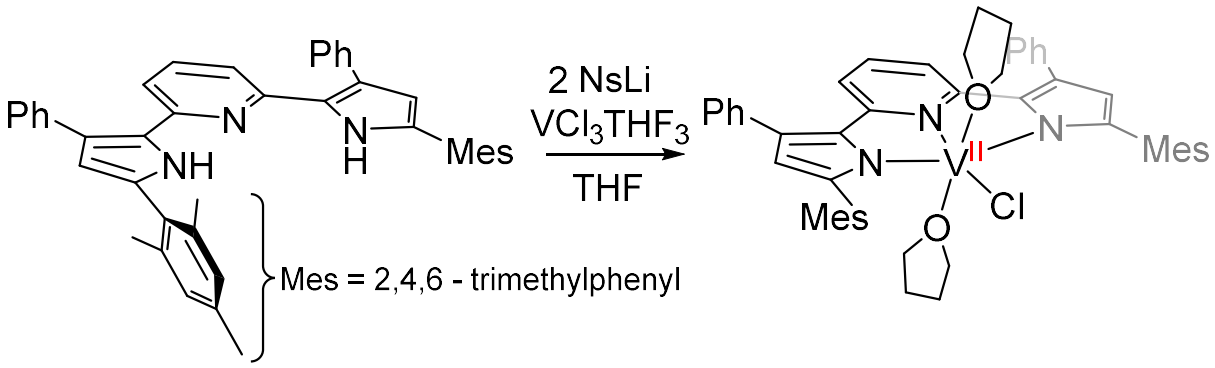

Scheme 2.1: Synthesis of (^{Mes}PDP^{Ph})VCl(thf)$_2$.

Due to the paramagnetism of this material, routine NMR characterization is not accessible. While the results of an ^{1}H NMR experiment are not informative to the structure or symmetry of

the compound, they are useful as a fingerprint for the pure material in future reactions. As such, the ^{1}H NMR spectrum in C_6D_6 shows several paramagnetically broadened resonances[20] from 25 ppm to -30 ppm. The magnetic moment of this species, 2.52 μ_B, was measured via Evan's method.[21] The deviation from the spin-only value (2.83 μ_B) from an S = 1, d^2 V^{III} center can be rationalized by unquenched orbital angular momentum in a C_{2v} symmetric ligand field.[22]

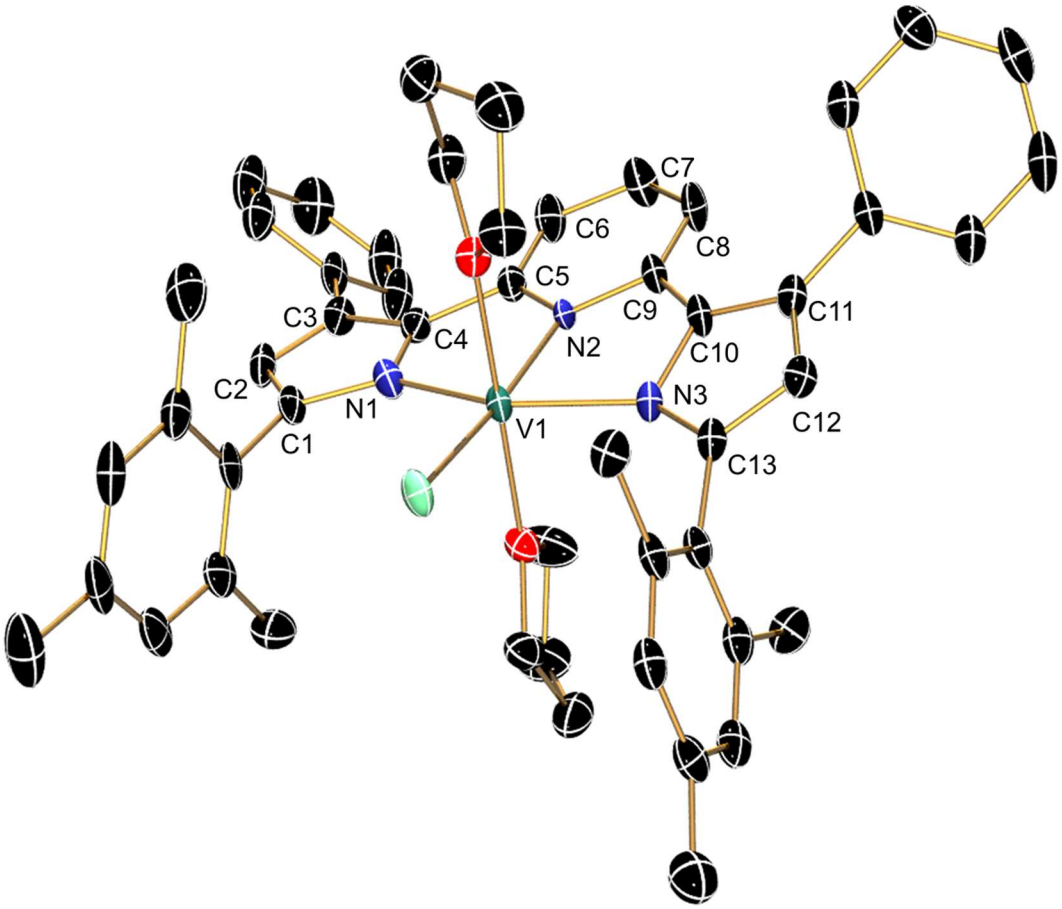

Figure 2.4: ORTEP generated crystal structure of (^{Mes}PDP^{Ph})VCl(thf)$_2$ displayed at 50% probability. Hydrogen atoms and co-crystallized solvent are excluded for clarity.

In order to determine the absolute structure of this product, single crystals were grown by slow diffusion of pentane into a concentrated toluene solution of the complex at -35 °C. The structure of (^{Mes}PDP^{Ph})VCl(thf)$_2$ was verified by X-ray crystallography (Figure 2.4), indicating a C_{2v} symmetric octahedral structure with *trans*- THF ligands in the apical positions. A summary of

relevant bond lengths can be found in Table 2.2, indicating dative pyrrolide-vanadium bonds, a coordinative pyridine-vanadium bond, and a redox neutral overall PDP^{2-} ligand.[23]

As with the NMR experiment, further characterization of ($^{Mes}PDP^{Ph}$)$VCl(thf)_2$ was performed as a baseline for subsequent species. To this effect, the infrared absorption spectrum (Appendix A2.2), taken in anhydrous KBr, was collected. Though this spectrum appears unremarkable, the window between 1800 cm^{-1} – 1600 cm^{-1} shows an important and distinct absence of resonances. This will aid in the determination of nitrogen-nitrogen multiple bonds in later complexes, where we would expect to see signals. UV-visible spectroscopy was also performed by the same reasoning.

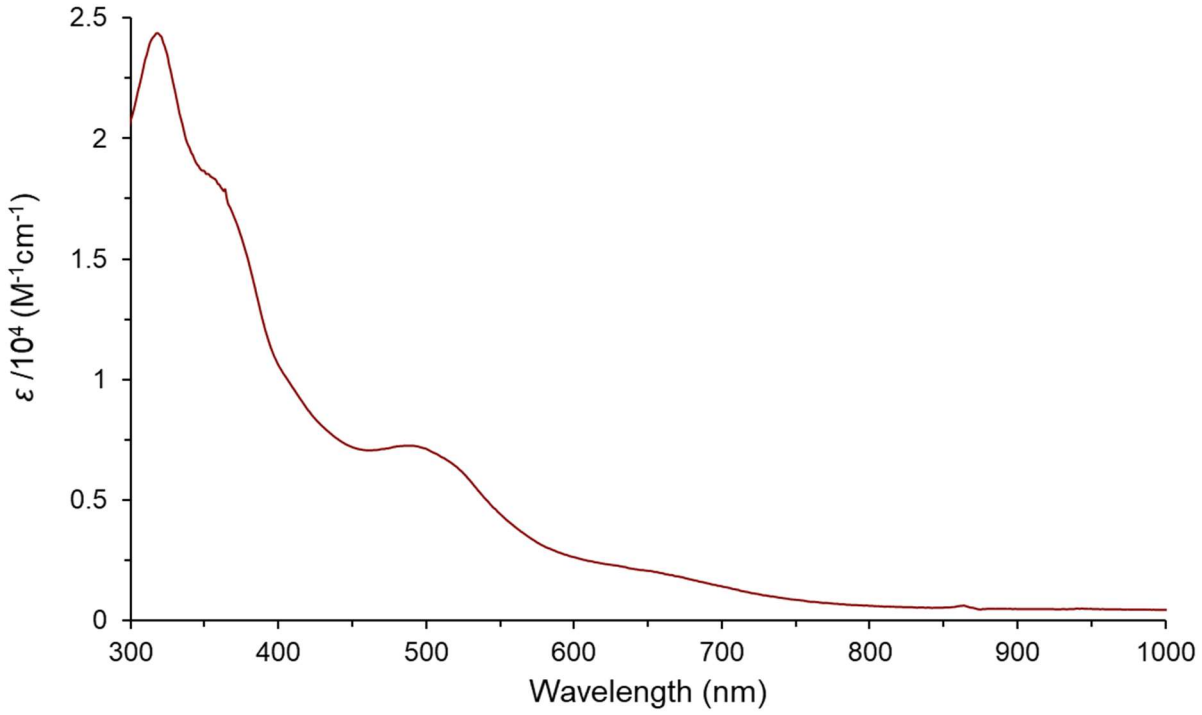

Figure 2.5: UV-visible spectrum of ($^{Mes}PDP^{Ph}$)$VCl(thf)_2$ in fluorobenzene.

The highly colored complex was taken in fluorobenzene at a concentration of 1×10^{-5} M. Fluorobenzene was chosen as the solvent for this material due to the potential for lability of the THF ligands. The most coherent feature in the visible region has a peak maximum at 490 nm,

which tapers well into the visible region past 700 nm. The plateauing around 650 nm may be indicative of another peak maximum but is unresolved. Probing either feature via fluorometry did not yield any observable emission at room temperature.

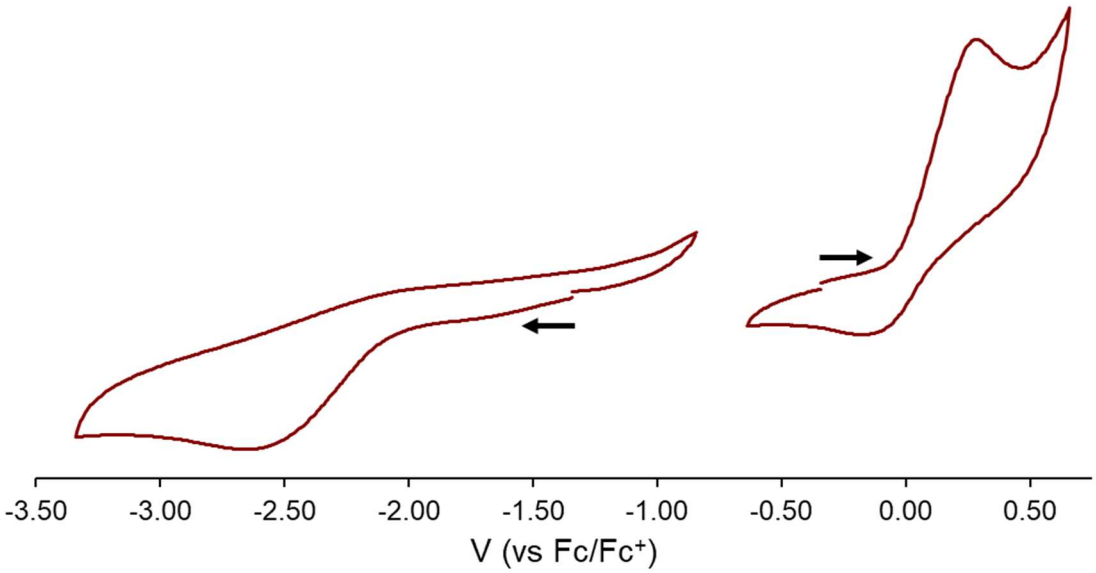

Figure 2.6: Two cyclic voltammograms of (^{Mes}PDP^{Ph})VCl(thf)$_2$ in 1,2-difluorobenzene at a scan rate of 200 mV/s. Separate voltammograms are presented to give clarity to the first irreversible events.

Cyclic voltammetry of the complex was performed in 1,2-difluorobenzene, utilizing tetrabutylammonium hexafluorophosphate as an electrolyte. This solvent was selected in order to try and mitigate the lability of the THF ligands, which appeared to have been ineffective from the resulting spectrum (Figure 2.6). There were no fully reversible events recorded from -3.50 V to 1.50 V versus ferrocene, though the event just after 0.00 V depicts what may be some reversibility. The lack of reversibility could not be overcome with increasing scan rate and may be attributed to the rapid exchange of solvent, or other minor structural rearrangements. Evidence of the tetrahydrofuran exchange was given by the synthesis of the *trans*-pyridine complex, (^{Mes}PDP^{Ph})VCl(py)$_2$.

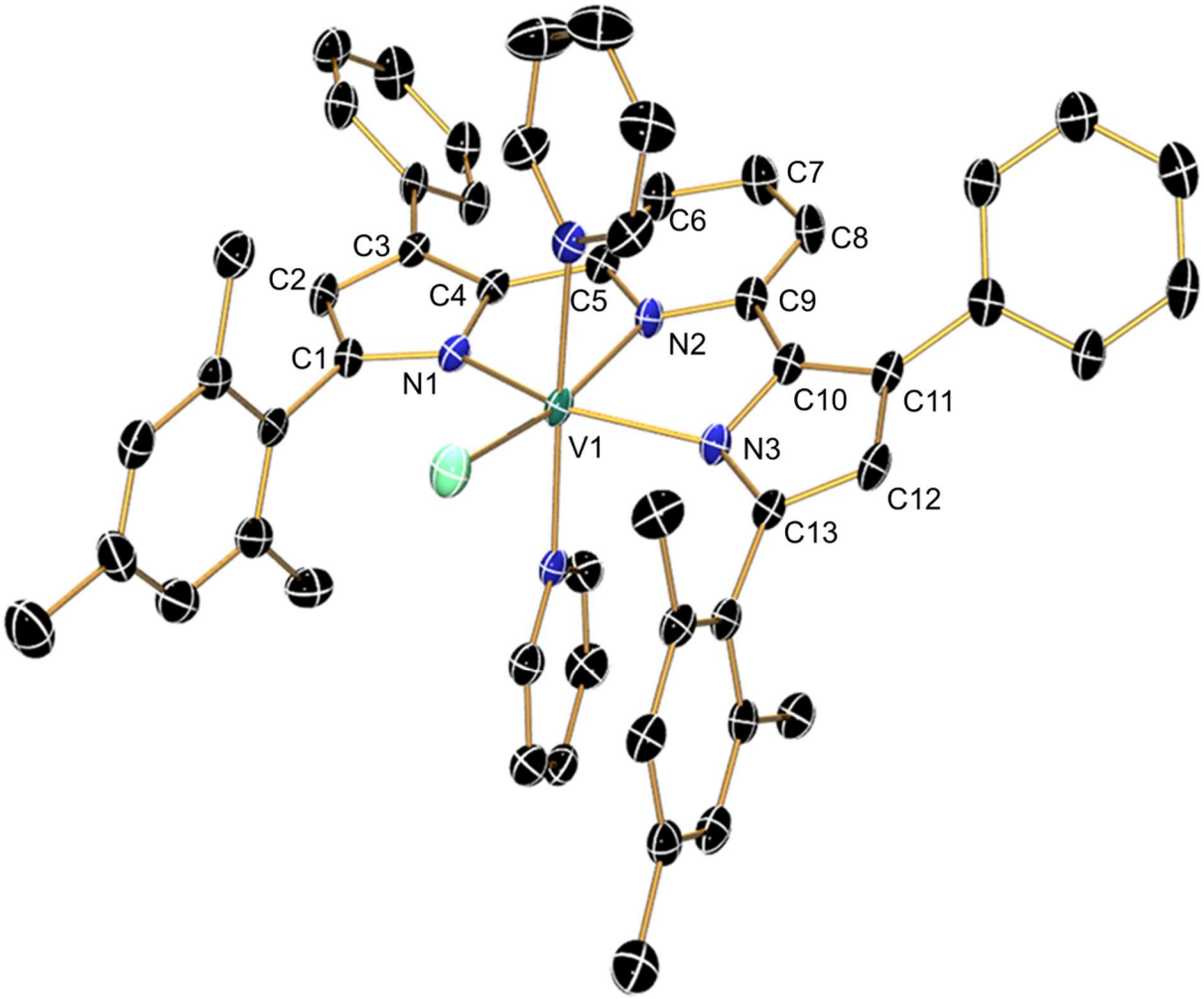

Figure 2.7: ORTEP generated crystal structure of (^{Mes}PDP^{Ph})VCl(py)$_2$ displayed at 50% probability. Hydrogen atoms are excluded for clarity.

The previously described THF adduct was dissolved in pyridine and stirred briefly before the pyridine solvent was removed under vacuum. Recrystallization by vapor diffusion of pentane into a concentrated solution of toluene gave quality single crystals which were subjected to X-ray diffraction. The crystal structure solved in a triclinic $P\bar{1}$ cell, with one molecule in the asymmetric unit. Though the unit cell was nearly identical to that of (^{Mes}PDP^{Ph})VCl(thf)$_2$, the disordered toluene could not be reliably modelled and was squeezed with the aid of the program PLATON[24] prior to the final structural refinement. No further characterization was performed on this species, which was treated as a novel derivative of a known compound.

2.3 Reduction to (^{Mes}PDP^{Ph})V(thf)$_3$ and Ligand Substitution

At room temperature, (^{Mes}PDP^{Ph})V(thf)$_3$ was prepared via reduction of (^{Mes}PDP^{Ph})VCl(thf)$_2$ with sodium amalgam in tetrahydrofuran, where the product was isolated as a dark red powder in 85% yield.

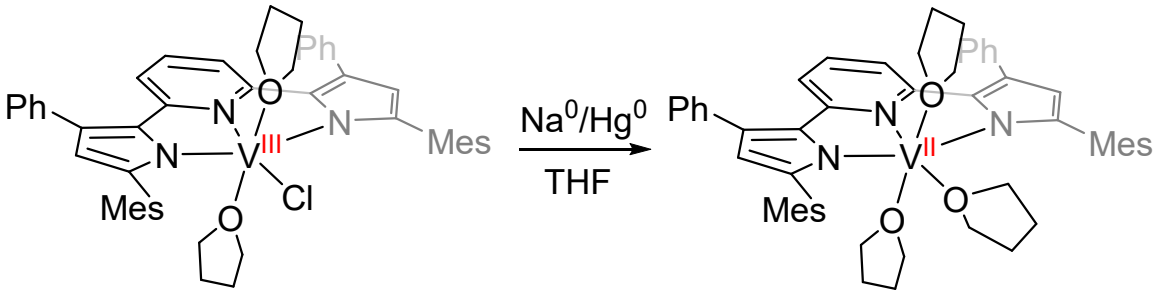

Scheme 2.2: Synthesis of (^{Mes}PDP^{Ph})V(thf)$_3$.

The structure of the neutral (^{Mes}PDP^{Ph})V(thf)$_3$ species was confirmed by X-ray diffraction. The crystal data solved in a triclinic $P\bar{1}$ cell with one molecule in the asymmetric unit, concomitant with a molecule of toluene which was nicely ordered.

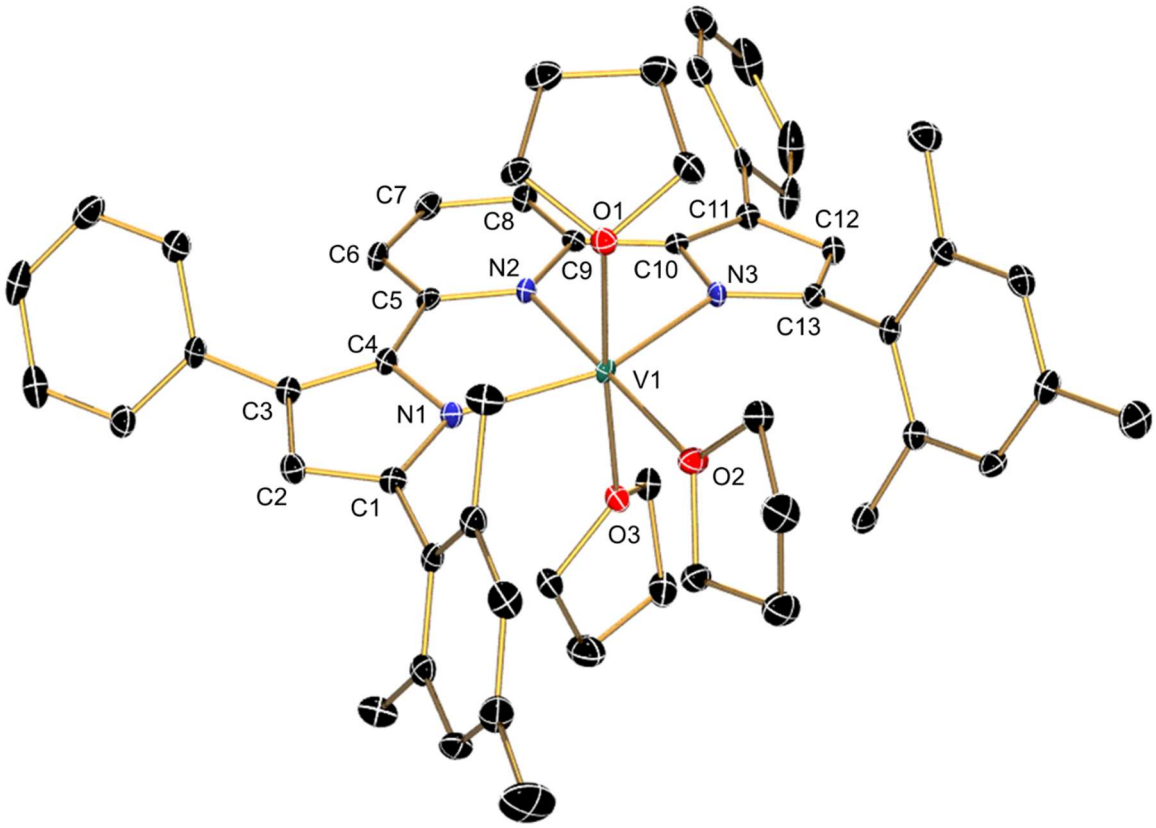

Figure 2.8: ORTEP generated crystal structure of (^{Mes}PDP^{Ph})V(thf)$_3$ displayed at 50% probability. Hydrogen atoms and co-crystallized solvent are excluded for clarity.

Due to the redox non-innocence of pyridine di-pyrrolides, careful consideration of the bond lengths of the PDP^{2-} ligand was performed. Specifically, the bonds within the central pyridine were investigated for an elongation of the nitrogen-carbon bonds N2 – C5/C9, as well as carbon-carbon bonds C7 – C6/C8. These would occur simultaneously with the contraction of carbon-carbon bonds C5 – C6 and C8 – C9. This would indicate a reduction of the ligand with an organic radical centered on the 4 position of the pyridine ring (C7), as observed in the cases of chromium and molybdenum bis-PDP species.[23] The direct comparison of bond lengths of the redox non-innocent PDP ligand is presented in Table 2.2, where expected bond lengthening is denoted in red, and bond contraction is denoted in blue.

Table 2.2: Bond lengths of the pyridine di-pyrrolide ligand of neutral coordination complexes of vanadium.

length (Å)	(^{Mes}PDP^{Ph})VCl(thf)$_2$	(^{Mes}PDP^{Ph})V(thf)$_3$	(^{Mes}PDP^{Ph})V(terpy)
V1-N1	2.080(4)	2.195(2)	2.1038(16)
V1-N2	2.073(4)	2.068(2)	2.098(2)
V1-N3	2.075(4)	2.1747(18)	2.1103(16)
N1-C1	1.374(6)	1.364(3)	1.363(3)
C1-C2	1.377(7)	1.387(4)	1.387(3)
C2-C3	1.421(7)	1.400(3)	1.408(4)
C3-C4	1.402(7)	1.409(3)	1.403(3)
N1-C4	1.398(6)	1.392(3)	1.385(3)
C4-C5	1.442(7)	1.452(3)	1.448(3)
N2-C5	1.358(6)	1.360(3)	1.358(3)
C5-C6	1.397(7)	1.402(4)	1.395(4)
C6-C7	1.386(8)	1.385(3)	1.385(3)
C7-C8	1.393(7)	1.380(3)	1.392(3)
C8-C9	1.395(8)	1.393(3)	1.395(4)
N2-C9	1.356(6)	1.358(3)	1.365(3)
C9-C10	1.448(7)	1.453(3)	1.444(3)
N3-C10	1.390(7)	1.394(3)	1.388(3)
C10-C11	1.407(7)	1.409(3)	1.402(3)
C11-C12	1.401(7)	1.401(3)	1.408(4)
C12-C13	1.388(8)	1.388(3)	1.386(3)
N3-C13	1.379(6)	1.362(3)	1.365(3)

An in-depth discussion of the bond lengths relating to the terpyridine ligand will be presented in the following sections containing that redox series. This comparison of neutral species

shows no real deviation (within error) in bond lengths on the redox active PDP moiety, specifically in the central pyridine ring.

In order to further investigate the electronic structure of (^{Mes}PDP^{Ph})V(thf)$_3$, paramagnetic ^{1}H NMR spectroscopy was attempted in benzene-d_6. Two broad signals were observed at δ 9.39 ppm and δ 3.39 ppm, which is likely paramagnetically shifted tetrahydrofuran. This spectrum is distinct from the V(III) starting material but is otherwise uninformative to its structure. The magnetic moment of the bulk material was determined by the Evan's Method[21] to be 3.79 μ_B, slightly under the spin only value for three unpaired (S = 3/2) electrons of 3.88 μ_B. This deviation is likely due to g values lower than 2, commonly associated in vanadium species, and unquenched angular orbital momentum contributions.

With the observation of an S = 3/2 ground state, two possible electronic structures were considered. In the event of a ligand centered reduction (V^{III}/d^2; PDP$^{\bullet}$), the ground state would require ferromagnetically coupled ligand radical(s),[23] which are highly unlikely in coordination complexes such as this due to orbital overlap. When we consider the results of the structural analysis, we may confidently assign the unpaired spins solely on the metal center (V^{II}/d^2; PDP^0). Cyclic voltammetry was performed in order to probe the redox events that may be accessible from this starting material.

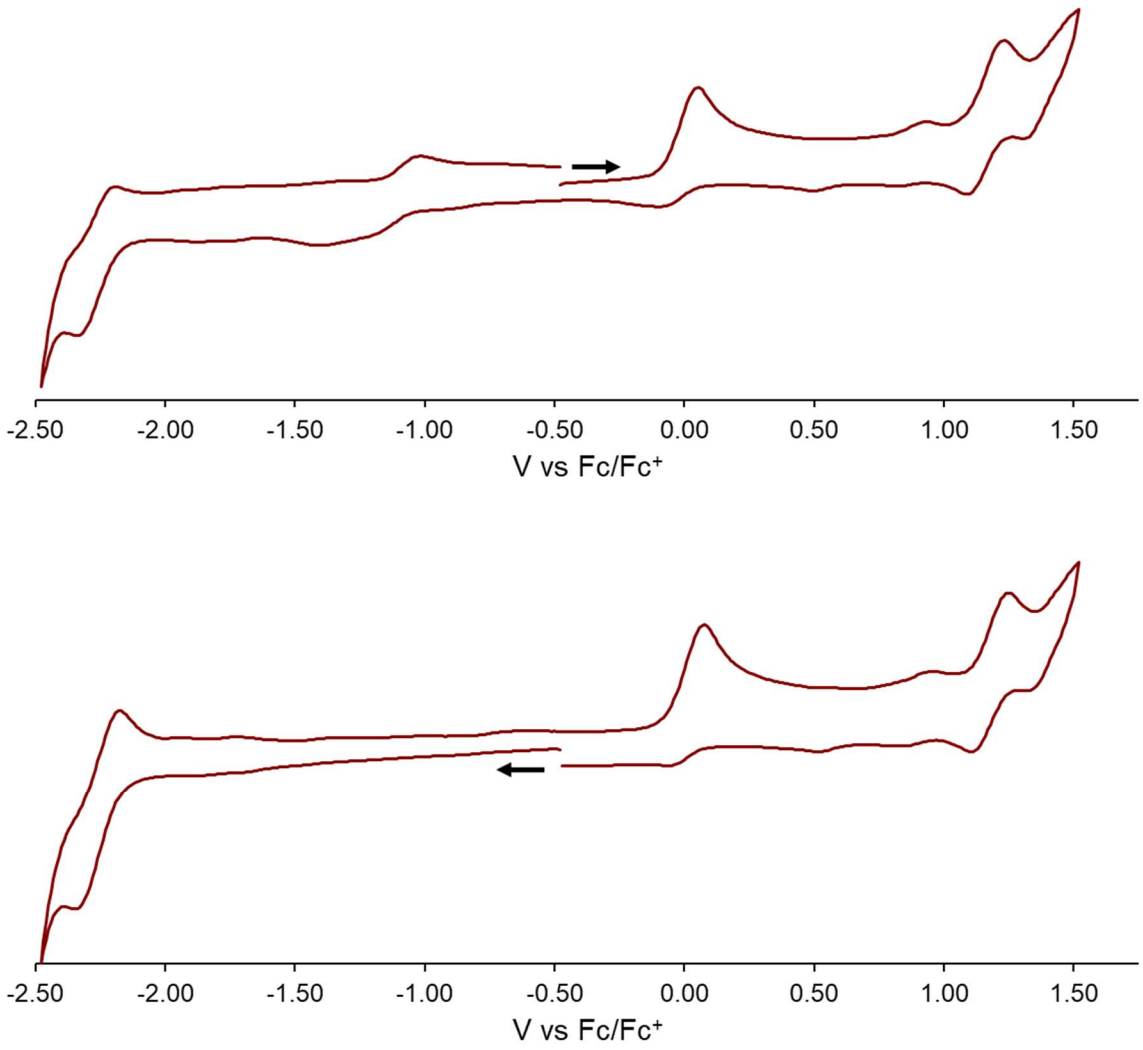

Figure 2.9: Two cyclic voltammograms of (^{Mes}PDP^{Ph})V(thf)$_3$ in tetrahydrofuran, each at a scan rate of 200 mV/s from the same origin.

The voltammogram of (^{Mes}PDP^{Ph})V(thf)$_3$ shows that speciation of intermediates is dependent upon the direction of the applied current. Proceeding towards more positive potentials, there appears to be a small concentration of an ambiguous event centered at -1.18 V (Figure 2.9, top spectrum). However, from the same origin, the same wave does not appear when first probed in the negative direction, where all other features are present. The region after 0.50 V is ambiguous, and seemingly multifaceted. If the event at 0.12 V is irreversible as it appears, it may be attributed

to another species than the target analyte, or perhaps the oxidation of the PDP ligand, which is known to be an unclean transformation. In order to determine the source of the minor, direction dependent event, the event at 0.12 V was isolated from the same origin (~ -0.5 V) and the electrochemical behavior determined out to -2.50 V. After several cycles at varying scan rates, the following spectra were recorded (Figure 2.10).

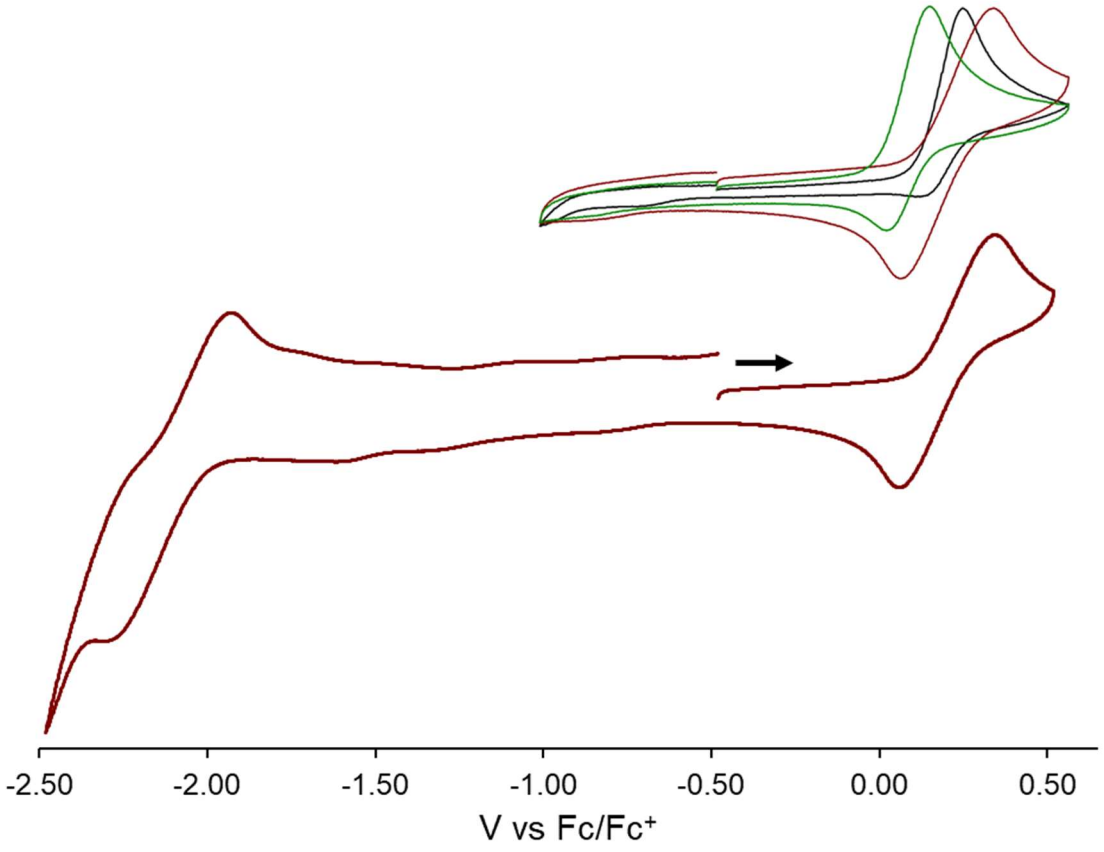

Figure 2.10: Cyclic voltammogram of selected redox events of (^{Mes}PDP^{Ph})V(thf)$_3$ at a scan rate of 1250 mV/s. Inset: variable scan rates of the same event; black at 50 mV/s; green at 200 mV/s; red at 1000 mV/s.

These experiments lead to the conclusion that the intermediate species does not result from the isolated wave (previously at 0.12 V). It is also noted here that this event becomes more reversible at higher scan rates, centered on 0.23 V. This scan rate dependency lends evidence to a relatively quick molecular rearrangement, where a chemical transformation occurs rapidly after

electron transfer. The event centered at -2.23 V is likely centered on the PDP ligand, which can reversibly accept electrons at very low potentials.[23] While the possibility for this event to correspond to a V^{II}/V^{I} couple is nonzero, it is certainly zero adjacent, and a much less likely result.[25]

These data suggest the lability of the tetrahydrofuran ligands impedes clean electrochemical reversibility, as noted for the bis-tetrahydrofuran ligated V^{III} chloride complex (Figure 2.6). In order to combat this, a terpyridine substituted derivative was prepared. A multi-dentate and redox non-innocent ligand was proposed to suffer less from speciation issues in solution and allow for study of intramolecular electron transfer as discussed in the Introduction of this Chapter.

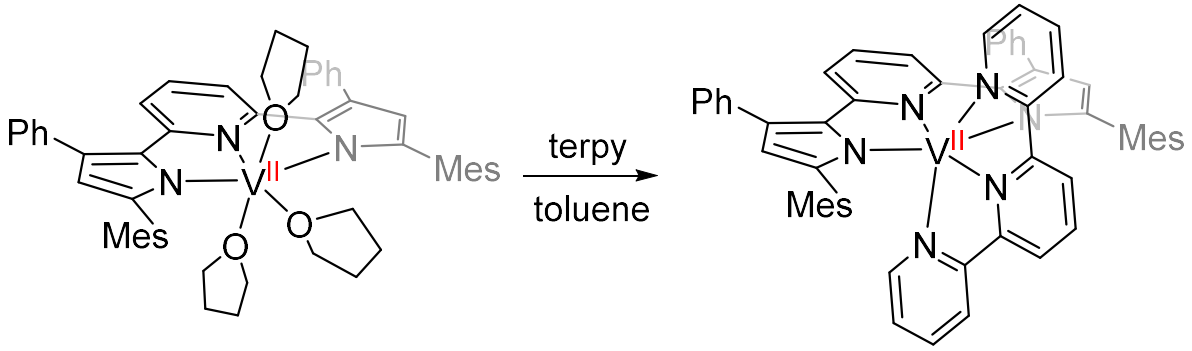

Scheme 2.3: Synthesis of (^{Mes}PDP^{Ph})V(terpy).

The substitution of (^{Mes}PDP^{Ph})V(thf)$_3$ was carried out in toluene with an equivalent of terpyridine. The reaction mixture darkened immediately upon the addition of the polypyridyl ligand and was stirred at room temperature for at least an hour to ensure complete conversion. Following trituration with pentane to remove residual solvent, the black solids were isolated in 92% yield.

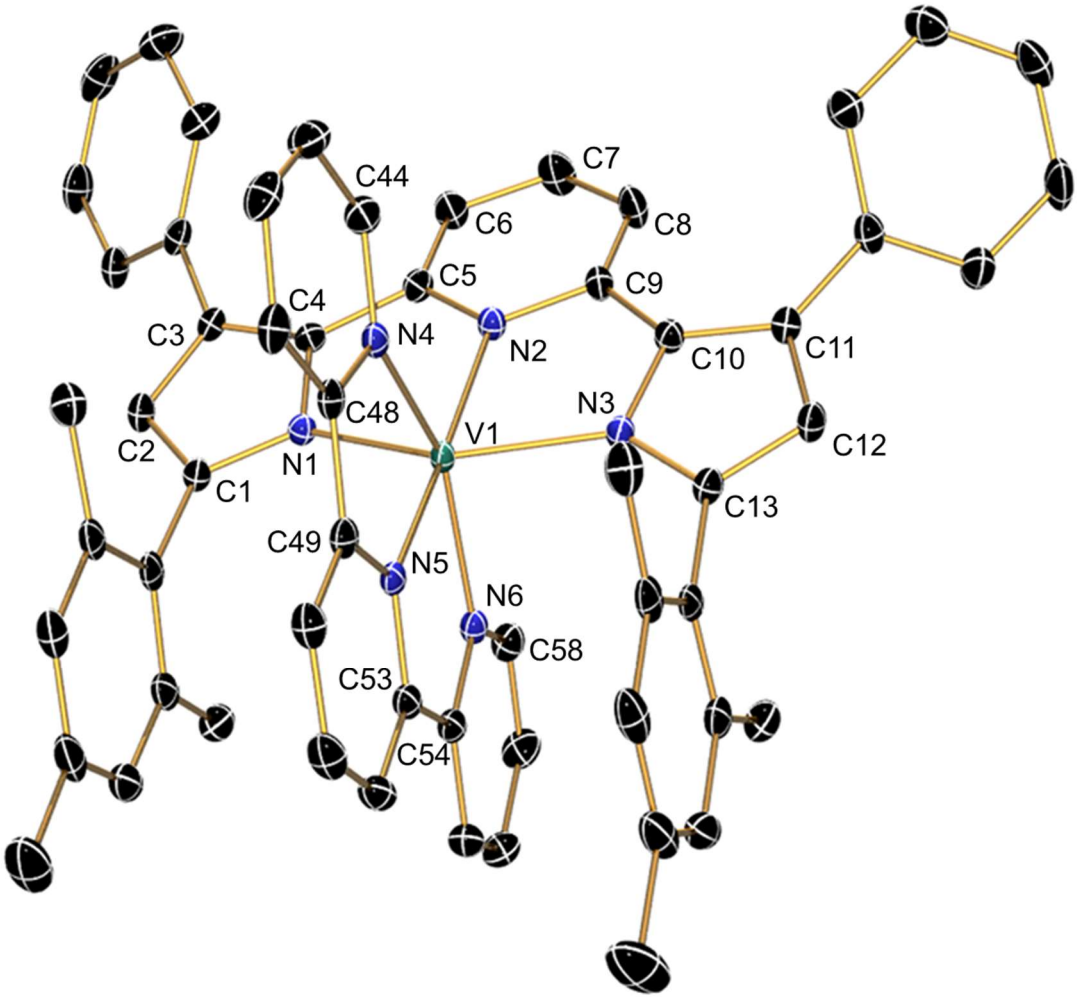

Figure 2.11: ORTEP generated crystal structure of (^{Mes}PDP^{Ph})V(terpy) displayed at 50% probability. Hydrogen atoms and co-crystallized solvent are excluded for clarity.

Single crystals of (^{Mes}PDP^{Ph})V(terpy) were grown from vapor diffusion of pentane into a concentrated solution of toluene at -45 ˚C. The complex crystallized in a triclinic $P\bar{1}$ cell, with two molecules in the asymmetric unit and 2.5 equivalents of toluene. The lack of counterions gives evidence to a neutral vanadium (II) complex with neutral PDP^{2-} and terpyridine^{0} ligands. Lists of the relevant bond lengths are given in Tables 2.3 and 2.4, where the latter also pertains to a discussion of the associated electron-transfer series.

In order to solidify our assessment of the electronic structure of this species, the paramagnetic product was characterized by ^{1}H NMR spectroscopy in benzene-d_6 with no

expectations of structural information. There were more signals than that of the starting material, which had only two attributed to THF; however, none were able to be related to each other by integration due to the diffuse intensity and the inconsistent number of peaks deterred the determination of a structural relationship. The magnetic moment was determined by Evan's Method[21] to be 3.68 μ_B, just under the spin only value for S = 3/2 (3.88 μ_B). This is relatively unchanged from the starting material, which was determined to be metal centered d^3 V^{II} with an effective moment of 3.79 μ_B.

To elucidate the stable redox configurations of this neutral molecule, cyclic voltammetry was performed. Preceding this experiment, an open circuit potential (OCP) was carried out to identify the resting potential of the neutral material.

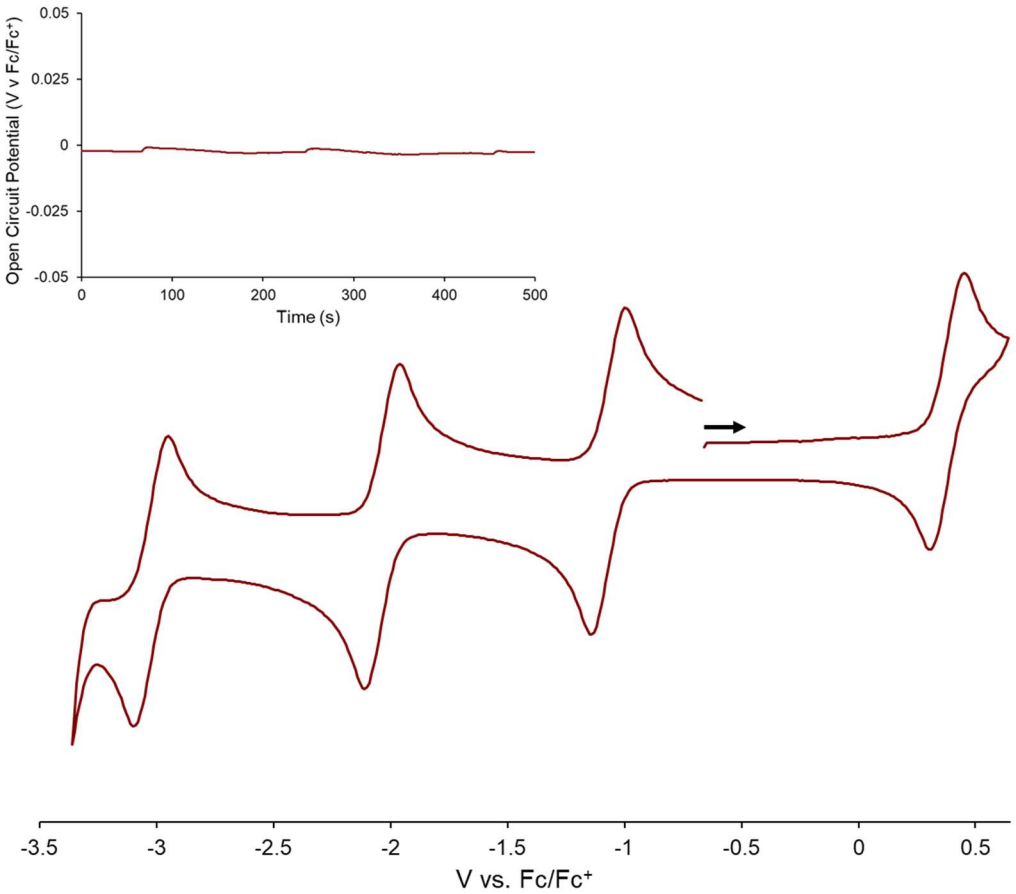

Figure 2.12: Cyclic voltammogram of (^{Mes}PDP^{Ph})V(terpy) in tetrahydrofuran at a scan rate of 200 mV/s. Inset: open circuit potential of (^{Mes}PDP^{Ph})V(terpy) in tetrahydrofuran.

As shown in Figure 2.12, the resting potential of the neutral compound was found to be -0.02 V. These data allowed for the assignment of events at more negative potentials to be reductions, and the more positive, oxidations. The oxidative event centered on 0.39 V is likely a V^{II}/V^{III} couple, which we anticipated to be readily accessible. Further, when compared to that of the tri-tetrahydrofuran ligated analogue, the oxidative potential is more positive, which is consistent with the substitution of these solely σ donors with a π accepting ligand. The three reductive events at -1.07 V, -2.02 V, and -3.02 V have a variety of potential structures. Considering the starting material which had a sole reductive event at very low potentials (-2.23 V), the addition of two more reversible waves gives good evidence to these including terpy$^{\bullet-}$, terpy^{2-}, and PDP^{1-}.

In order to validate this hypothesis, attempts were made to synthesize and isolate this electron-transfer series.

2.4 Electron-Transfer Series of (^{Mes}PDP^{Ph})V(terpy): 1-, 0, 1+

Oxidation of (^{Mes}PDP^{Ph})V(terpy) with ferrocenium tetraphenylborate at room temperature was performed overnight in tetrahydrofuran. There was no obvious change in color, or precipitation of solids. The reaction mixture was reduced to dryness under vacuum, and the solids triturated with pentane. The product was largely insoluble in toluene, which was then used to wash away any remaining ferrocenium salts. The remaining solids were reconstituted in THF and recrystallized by layering with pentane at -45 C° to further purify the material. The black crystalline solid was isolated in 86% yield.

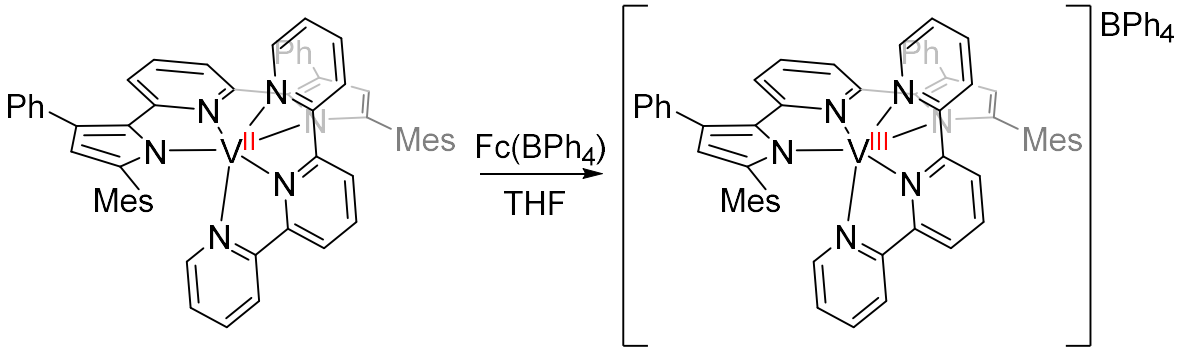

Scheme 2.4: Synthesis of [(^{Mes}PDP^{Ph})V(terpy)]$^{1+}$.

A ^{1}H NMR experiment in deuterated methylene chloride quickly showed the product to be completely NMR silent, with no signals outside of residual solvent. Following this experiment, the magnetic susceptibility was probed by Evan's Method[21], giving an effective magnetic moment of 2.60 μ_B. This is consistent with an S = 1 spin state with two unpaired spins either on vanadium, or a V^{IV} center ferromagnetically coupled with a ligand radical. Considering the starting material, a neutral V^{II} complex, this suggests the former: an oxidation at vanadium from d^3 to d^2, with antiferromagnetically coupled spins consistent with Hund's rules of maximum multiplicity.

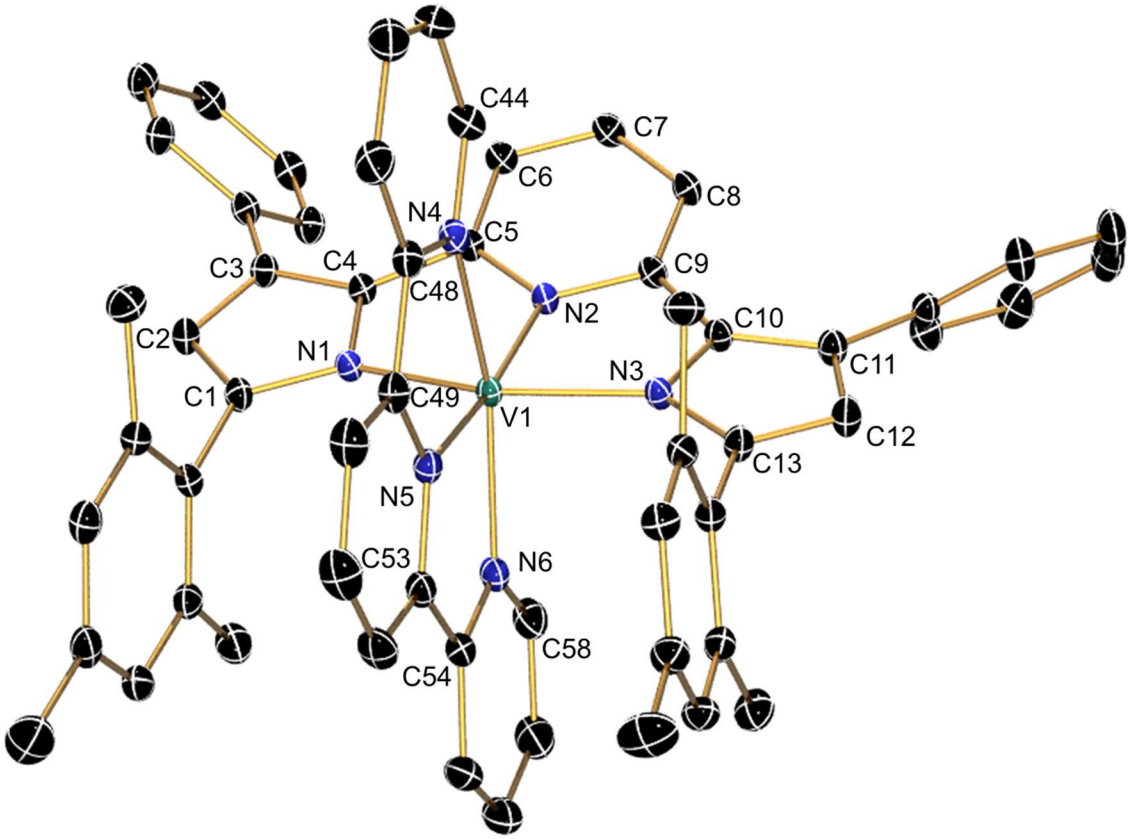

Figure 2.13: ORTEP generated crystal structure of [(^{Mes}PDP^{Ph})V(terpy)](BPh$_4$) displayed at 50% probability. Hydrogen atoms, co-crystallized solvent, and counterion are excluded for clarity.

Single crystals were grown from vapor diffusion of pentane into a concentrated solution of methylene chloride. The dark black parallelopipeds were solved in a monoclinic Cc cell with one molecule (with counterion) in the asymmetric unit. Two solvent molecules were also present in the lattice, which refined nicely with minimal disorder. The structural details of this molecule will be part of a larger discussion of the comparison of this series.

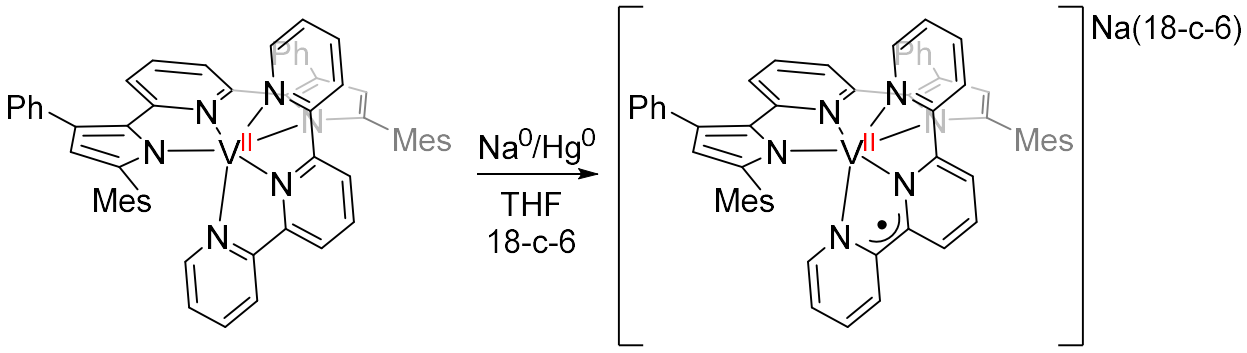

Scheme 2.5: Synthesis of $[(^{Mes}PDP^{Ph})V(terpy)]^{1-}$.

Reduction of $(^{Mes}PDP^{Ph})V(terpy)$ with sodium amalgam in THF was performed at room temperature for no less than 30 minutes. Because the reduction potential under these conditions (~2.3 V vs Fc/Fc^{+})[26] exceeds the potential of the first wave, and also the second, the reaction was not allowed to go longer than four hours. This was in effort to relegate speciation of the products to the singly reduced molecule. The product, $Na[(^{Mes}PDP^{Ph})V(terpy)]$, was isolated in 66% yield.

The products of this reaction were also NMR silent, much like the oxidized derivative. The magnetic moment (determined by Evan's Method[21]) was calculated to be 2.40 μ_B, in rough agreement with a S = 1 spin state (μ_{SO} = 2.83 μ_B). Considering this reaction from the V^{II}/d^3 starting material, the addition of another electron would yield four spins on this molecule. This gives three possible magnetic structures: S = 2, S = 1, and S = 0.

Due to the lack of diamagnetic signals in the NMR spectrum, we can rule out S = 0 immediately. This leaves two options S = 2, 1 as options, with four unpaired spins or a paired spin with two unpaired spins. Considering the S = 2 solution, there are two possible structures: four unpaired spins on vanadium, or ferromagnetically coupled V^{II} (d^3) and ligand radical. These structures would be incredibly unfavorable, where V^{I} is too highly reducing to have a potential of -1.07 V (via CV), and ferromagnetic coupling between directly bound paramagnets is rarely observed. Empirical data suggests an S = 1 solution (μ_{eff} = 2.40 μ_B), where there is either three

unpaired spins on vanadium antiferromagnetically coupled to a ligand radical, or a single unpaired spin on vanadium ferromagnetically coupled to a ligand radical. The latter solution, however, is both in violation of Hund's rules, as well as depends on ferromagnetically coupled paramagnets. This leads to the assignment V^{II}/d^3 L^1, where the ligand radical remains ambiguous. This will be investigated via structural characterization in comparison to the other members of this series.

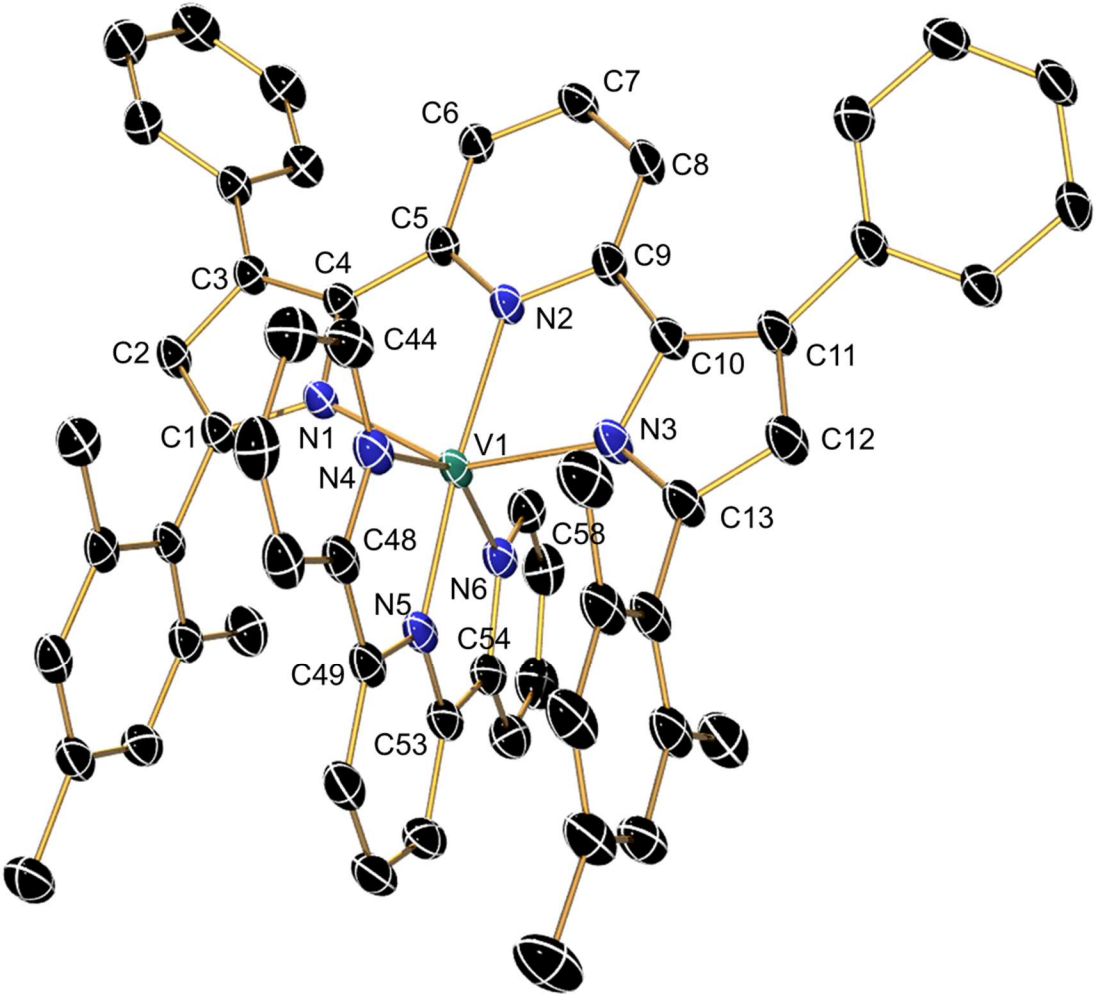

Figure 2.14: ORTEP generated crystal structure of [Na(18-crown-6)][(^{Mes}PDP^{Ph})V(terpy)] displayed at 50% probability. Hydrogen atoms, co-crystallized solvent, and counterion are excluded for clarity.

In response to issues with poor diffraction of single crystals of the sodium salt, an equivalent of 18-crown-6 was added. From a vapor diffusion of pentane into concentrated THF at

-45 ˚C, this allowed for the isolation well-ordered solids, which resolved in a triclinic $P\bar{1}$ cell. A single ionic pair is present in the asymmetric unit, as well as two molecules of disordered THF. The crown about the sodium atom is also disordered but was able to be restrained to two major positions.

In an effort to characterize the rest of the electron-transfer series, reductions were attempted with several equivalents of sodium naphthalenide (-3.10 V vs Fc/Fc^{+}),[26] as well as gross excess of potassium graphite (~3 V vs Fc/Fc^{+}). However, there was no success in these attempts to isolate the remainder of this family of compounds. Regardless, the neutral, oxidized, and reduced complexes are available for comparison. Here, the structural characterization in support of the empirical magnetic properties will solidify our assessment of their electronic structures. First attention was given to the PDP ligand (Table 2.3), which was not anticipated to behave as an electron reservoir where a terpyridine ligand is also available.

Table 2.3: Bond lengths of the pyridine di-pyrrolide ligand of the isolable species of the ($^{Mes}PDP^{Ph}$)V(terpy) electron-transfer series.

length (Å)	($^{Mes}PDP^{Ph}$)V(terpy)	[($^{Mes}PDP^{Ph}$)V(terpy)]$^{1+}$	[($^{Mes}PDP^{Ph}$)V(terpy)]$^{1-}$
V1-N1	2.1038(16)	2.0325(15)	2.112(2)
V1-N2	2.098(2)	2.0408(15)	2.107(2)
V1-N3	2.1103(16)	2.0432(15)	2.119(2)
N1-C1	1.363(3)	1.382(2)	1.360(3)
C1-C2	1.387(3)	1.389(3)	1.395(3)
C2-C3	1.408(4)	1.423(3)	1.409(3)
C3-C4	1.403(3)	1.390(3)	1.411(3)
N1-C4	1.385(3)	1.403(2)	1.385(3)
C4-C5	1.448(3)	1.448(3)	1.453(3)
N2-C5	1.358(3)	1.361(2)	1.362(3)
C5-C6	1.395(4)	1.397(2)	1.401(3)

C6-C7	1.385(3)	1.392(3)	1.391(4)
C7-C8	1.392(3)	1.397(3)	1.389(4)
C8-C9	1.395(4)	1.395(2)	1.400(4)
N2-C9	1.365(3)	1.358(2)	1.369(3)
C9-C10	1.444(3)	1.448(2)	1.449(3)
N3-C10	1.388(3)	1.405(2)	1.390(3)
C10-C11	1.402(3)	1.391(3)	1.412(3)
C11-C12	1.408(4)	1.423(2)	1.409(4)
C12-C13	1.386(3)	1.388(3)	1.395(4)
N3-C13	1.365(3)	1.376(2)	1.365(3)

The pyridine dipyrrolide ligands bound on the neutral and reduced species, respectively, appear to be relatively unchanged with respect to each other. While considering the reduction of the neutral molecule, that leaves the metal center and terpyridine ligand as potential wells for the extra electron. As the intermolecular bond lengths of the PDP ligand itself are not markedly contracted in any case, we can assume that a change in the oxidation state of the pincer stays the same under all of these conditions.

However, there is a clear contraction of the vanadium-N_{PDP} bonds in the oxidized molecule. This may be evidence of increased σ and π donation into a more Lewis acidic metal center, consistent with a transition from V^{II} to V^{III}. Indeed, when compared to the V-N_{PDP} bonds of the ($^{Mes}PDP^{Ph}$)VCl(thf)$_2$ starting material (2.080(4) Å, 2.073(4) Å, 2.075(4) Å; Table 2.2), it appears that [($^{Mes}PDP^{Ph}$)V(terpy)](BPh$_4$) is more akin to a V^{III} coordination complex. Further, as no such contraction is observed in the reduced species, we conclude that the vanadium center does not undergo a redox event, leaving terpyridine as the likely electron reservoir.

Table 2.4: Bond lengths of the terpyridine ligand of the isolable species of the (^{Mes}PDP^{Ph})V(terpy) electron-transfer series.

length (Å)	(^{Mes}PDP^{Ph})V(terpy)	[(^{Mes}PDP^{Ph})V(terpy)]$^{1+}$	[(^{Mes}PDP^{Ph})V(terpy)]$^{1-}$
V1-N4	2.1092(16)	2.1383(16)	2.087(2)
V1-N5	2.015(2)	2.0477(15)	1.954(2)
V1-N6	2.127(2)	2.0988(17)	2.083(2)
C44-N4	1.346(4)	1.339(2)	1.358(4)
C48-N4	1.364(3)	1.360(2)	1.379(3)
C48-C49	1.458(4)	1.477(3)	1.440(4)
C49-N5	1.356(2)	1.343(2)	1.393(3)
C53-N5	1.358(3)	1.349(2)	1.395(4)
C53-C54	1.470(3)	1.477(3)	1.432(4)
C54-N6	1.357(3)	1.361(2)	1.386(3)
C58-N6	1.345(2)	1.341(2)	1.366(3)

Following the analysis, the terpyridine ligand was considered for its contributions (Table 2.4). Whereas there is no observed significant structural differences associated with the terpy ligand for the neutral and oxidized species, as anticipated, the corresponding distances within the terpy ligand of the reduced species [(^{Mes}PDP^{Ph})V(terpy)]$^{-}$ anion are markedly changed. The bonds between the nitrogen and carbons on either side are elongated, while the carbon-carbon linkages between the rings are contracted. This indicates a delocalization of electron density across the terpyridine ligand, as is precedented by the literature.[12,14]

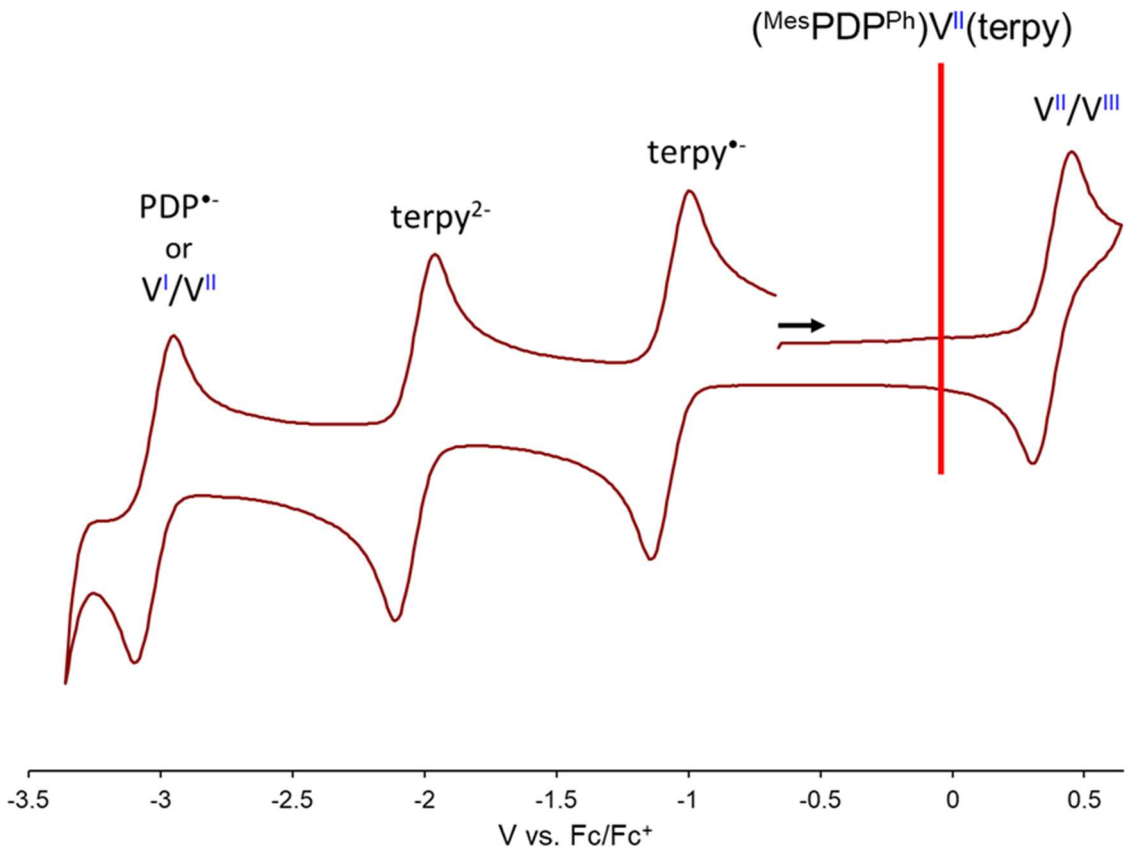

Figure 2.15: Cyclic voltammogram of (^{Mes}PDP^{Ph})V(terpy) in tetrahydrofuran at a scan rate of 200 mV/s, with reversible events tentatively assigned.

The culmination of these data resulted in the assignments depicted in Figure 2.15. While low potential electrochemically stable states (2-, 3-) show clean reversibility, they have yet to be isolated. We could attribute this to the noted instability for some analogous species reported in the literature, as previously discussed.[13] While these electronic configurations are stable on a cyclic voltammetry timescale, they may simply not have a lifetime long enough to support characterization.

2.5 Conclusions

The preparation of the V(III) starting material (^{Mes}PDP^{Ph})VCl(thf)$_2$ was straightforward, robust, and easily scalable. Reduction of (^{Mes}PDP^{Ph})VCl(thf)$_2$ yielded (^{Mes}PDP^{Ph})V(thf)$_3$, a formally V(II) coordination complex whose electronic structure showed no evidence of delocalization with the bound redox non-innocent PDP ligand. This was evidenced with a combination of X-ray structural characterization and magnetic susceptibility measurements, which assigned the three unpaired spins (S = 3/2) solely on the vanadium atom. Substitution of the tetrahydrofuran ligands with terpyridine yielded the neutral polypyridyl species (^{Mes}PDP^{Ph})V(terpy). This complex was similarly characterized to its starting material; however, the electrochemistry of this species showed a much cleaner, more reversible series of redox events. Attempts to generate the electron-transfer series (1+, 0, 1-, 2-, 3-) based on these properties gave only two more isolable species, [(^{Mes}PDP^{Ph})V(terpy)]$^+$ and [(^{Mes}PDP^{Ph})V(terpy)]$^-$.

The oxidation product is consistent with our expectations, where the V(II)/V(III) couple is facile and its products readily isolable and both redox non-innocent ligands, PDP and terpyridine, do not participate in the oxidation of the molecule. Further, V-N bond lengths with the electron-rich PDP ligand are contracted, which indicated an increase in Lewis acidity at vanadium. The single reduction product had an S = 1 ground state at room temperature. The results of the crystallographic analysis of the reduced product clearly demonstrated delocalization of a ligand radical across the terpyridine ligand. This broken symmetry allowed for antiferromagnetic coupling between the ligand and the metal center, leaving two unpaired spins at vanadium. While reduction to the 2- and 3- products was not accessible, this result may be consistent with the sensitivity observed in the homoleptic [V(^{t}bpy)$_3$]^z electron-transfer series (z = 3+, 2+, 0, 1-) reported by Bowman, Sproules, and Wieghardt.[13] The highly reduced terpyridine ligand on d^3

V(II) may result in intra/inter-molecular electron transfer due to the inaccessibility of e_g metal orbitals and the reduction potential of $(tpy)^{2-}$, leading to the recovery of $[(^{Mes}PDP^{Ph})V(terpy)]^-$ and intractable byproducts.

2.6 Experimental Procedures

General Considerations. All air- and moisture-sensitive manipulations were carried out using standard Schlenk line and cannula techniques or in an MBraun inert atmosphere drybox containing an atmosphere of purified nitrogen. Solvents for air- and moisture- sensitive manipulations were dried and deoxygenated using a Glass Contour Solvent Purification System and stored over 4 Å molecular sieves. All solids were dried under high vacuum in oven-dried glassware in order to bring into the glovebox. Deuterated benzene (C_6D_6) for NMR spectroscopy was distilled from sodium. Deuterated methylene chloride (CD_2Cl_2) for NMR spectroscopy was distilled from CaH_2. All solids that were prepared in outside of the box were dried under high vacuum in oven-dried glassware before use in inert atmosphere. Metal halides were purchased and used without further purification.

Physical and Computational Measurements. Nuclear magnetic resonance (NMR) experiments were performed at 400 MHz on a 400-MR DD2 Agilent instrument. All chemical shifts are reported relative to tetramethylsilane with residual solvent proton signal as a secondary standard. Deuterated benzene was distilled from sodium metal and stored over 4 Å molecular sieves. Deuterated methylene chloride was distilled from CaH_2 and stored of 4 Å molecular sieves. Splitting in ^1H NMR studies is notated by: s = singlet, d = doublet, t = triplet, sept = septet, b = broad, m = multiplet or combinations thereof.

Single crystals were prepared for X-ray diffraction in the glovebox by coating with previously degassed polyisobutylene oil (Sigma-Aldrich). These were then picked with a nylon loop (MiTeGen) and mounted to the goniometer head of a Bruker AXS D8 Venture fixed-chi X-ray diffractometer in a cold stream of dry nitrogen. The instrument features a Triumph

monochromator, a Mo Kα radiation source (λ = 0.71073 Å), and a PHOTON 100 CMOS detector. Utilizing the APEX3[27] software package, data was collected, processed with SAINT+, and subjected to absorption correction via SADABS/TWINABS. The space group were determined with XPREP and solved using intrinsic phasing (SHELXL[28]) before refinement with Olex2.[29] Structures are represented at 50% probability thermal ellipsoids via ORTEP-3.

Cyclic voltammetry was recorded under nitrogen atmosphere in anhydrous tetrahydrofuran using NBu_4PF_6 as an electrolyte and referenced to ferrocene/ferrocenium$^+$. Set up included a Gamry Interface 1000 electrochemical workstation in a single compartment cell utilizing a three-electrode system: a glassy carbon working electrode, platinum sheet as the counter electrode, and coiled silver wire as a quasi-reference electrode. All spectra were taken at a rate of 200 mVs^{-1} in 5 mV steps unless otherwise indicated.

UV-visible and emission spectra were acquired via Shimadzu UV-1800 spectrophotometer and RF-5301 PC spectrofluorophotometer, respectively. Samples were prepared in the glove box under nitrogen in either dry benzene or tetrahydrofuran in J-Young adapted quartz cuvettes.

Density functional theory (DFT) and time-dependent density functional theory (TD-DFT) calculations were performed with the ORCA[30,31] program package. Each were carried out at the B3LYP level of theory. Calculated orbitals were plotted using the program Gabedit.[32]

Safety Considerations. Azides are known to be toxic, energetic materials which can decompose violently under pressure, at high temperature, or when irradiated with light. While no incidents occurred during the course of this work, all manipulations involving sodium azide and azide containing products were carried out under nitrogen in the glovebox. Controlled decomposition of

azide moieties (via thermolysis or photolysis) were performed under nitrogen in sealed Schlenk tubes behind a blast shield.

(^{Mes}PDP^{Ph})VCl(thf)$_2$ – In the glovebox, a 20 mL scintillation vial was charged with 363 mg (0.61 mmol) $H_2{}^{Mes}$PDP^{Ph} and a magnetic stir bar, followed by 10 mL of THF. The ligand was deprotonated with 117 mg (1.24 mmol) of (trimethylsilyl)methyllithium and stirred at room temperature for 30 minutes. During that time, a 100 mL round bottom flask was charged with 257 mg (0.69 mmol) $VCl_3(thf)_3$, a magnetic stirrer, and 20 mL of THF. The fluorescent $Li_2{}^{Mes}$PDP^{Ph} solution was added to the pale pink VCl_3 solution dropwise at room temperature with good stirring. The color immediately darked to a near black, opaque red upon addition, and was allowed to stir overnight. The resulting reaction mixture was reduced to dryness under vacuum, then triturated successively with toluene and pentane. The crude material was then taken in a minimum amount of toluene and filtered with Celite on a medium porosity frit. Slow evaporation of the toluene solution in a 20 mL scintillation vial under gentle vacuum afforded 554 mg (0.60) mmol, 98%) black/red crystalline solid. An equivalent of co-crystallized toluene is accounted for in the calculation of the yield of these solids. $\mu_{eff} = 2.52\ \mu_B$. ^{1}H NMR (400 MHz, C_6D_6) δ 21.97, 15.24, 8.38, 8.37, 8.05, 5.36, 5.17, 3.34, 2.68, 2.47, 1.37, 1.14, -9.27, -28.12 ppm. Anal. Calcd. for $C_{51}H_{53}ClN_3O_2V + C_7H_8$: C, 75.84; H, 6.69; N, 4.57. Found: C, 75.66; H, 6.61; N, 4.54. Elemental analysis was submitted from a sample obtained via slow diffusion of pentane into toluene, which co-crystallizes in the lattice; these results reflect a correction for solvent molecules.

(^{Mes}PDP^{Ph})V(thf)$_3$ – In the glovebox, an excess of 0.5 w/w% Na^0/Hg^0 amalgam was prepared in a 100 mL round bottom flask and covered with tetrahydrofuran from 2.7 g of elemental mercury and

16 mg (0.70 mmol, 10 eq) of sodium metal. In several small portions, sodium was added to slowly stirring mercury, so that the fine gray powder that is expelled from the amalgam was contained by the solvent. After the addition was complete, 50 mg (0.06 mmol) of (^{Mes}PDP^{Ph})VCl(thf)$_2$ was added in THF and stoppered with a ground glass plug. The resulting mixture was stirred vigorously for an hour at room temperature, maximizing the surface area of the Na^0/Hg^0 amalgam by dispersion in solvent. The reaction mixture was decanted, the amalgam washed with THF, and these combined organic solutions filtered over Celite on a medium porosity glass frit. The solution was dried under vacuum and triturated with pentane. The resulting solids were then taken in toluene and filtered with Celite to remove residual halide salts. Evaporation of the solvent and trituration with pentane afforded a fine red powder (44 mg, 0.05 mmol, 85%) of the pure material. μ_{eff} = 3.79 μ_B. ^{1}H NMR (400 MHz, C_6D_6) δ 9.39, 3.39 ppm. Crystals suitable for X-ray diffraction were grown from vapor diffusion of pentane into toluene at -45 ˚C.

(^{Mes}PDP^{Ph})V(terpy) – In the glovebox, 38 mg (0.04 mmol) (^{Mes}PDP^{Ph})V(thf)$_3$ and 10 mg (0.04 mmol) terpyridine was added to a minimal amount of toluene. Upon addition of solvent, the deep red color of the starting material darkened to black. The mixture was stirred at room temperature for an hour, filtered through a pipette with Celite over a glass plug, and reduced to dryness. Trituration of the black solids with pentane afforded 36 mg (0.04 mmol, 92%) of the pure material. μ_{eff} = 3.68 μ_B. Crystals suitable for X-ray diffraction were grown from vapor diffusion of pentane into toluene at -45 ˚C.

[(^{Mes}PDP^{Ph})V(terpy)](BPh$_4$) – In the glovebox, 49 mg (0.06 mmol) of the neutral (^{Mes}PDP^{Ph})V(terpy) starting material was added to a 20 mL scintillation vial in ~5 mL of

tetrahydrofuran. With good stirring, 30 mg (0.06 mmol, 1.1 eq) of ferrocenium tetraphenylborate was added in a minimal amount of THF. The reaction mixture was capped and stirred at room temperature overnight before reducing to dryness under vacuum. The black solids were washed with toluene, as they were not particularly soluble in aromatic solvents. The reaction product was reconstituted in THF and filtered through a pipette with Celite over a glass plug yielding 64 mg (0.05 mmol, 86%) black powder. $\mu_{eff} = 2.60\ \mu_B$. Crystals suitable for X-ray diffraction were grown from vapor diffusion of pentane into dichloromethane at -45 ˚C.

Na[(^{Mes}PDP^{Ph})V(terpy)] – In the glovebox, an excess of 0.5 w/w% Na^0/Hg^0 amalgam was prepared in a 100 mL round bottom flask and covered with tetrahydrofuran from 4.4 g of elemental mercury and 30 mg (1.30 mmol, 15 eq) of sodium metal. In several small portions, sodium was added to slowly stirring mercury, so that the fine gray powder that is expelled from the amalgam was contained by the solvent. After the addition was complete, 80 mg (0.09 mmol) (^{Mes}PDP^{Ph})V(terpy) was added in THF and stoppered with a glass plug. The resulting mixture was stirred vigorously for two hours at room temperature, maximizing the surface area of the Na^0/Hg^0 amalgam by dispersion in solvent. The reaction mixture was decanted, the amalgam washed with THF, and these combined organic solutions filtered over Celite on a medium porosity glass frit. The solution was dried under vacuum and triturated with pentane. The resulting solids were then taken in toluene and filtered with Celite. Evaporation of the solvent and trituration with pentane afforded 54 mg (0.06 mmol, 66%) black solids. $\mu_{eff} = 2.40\ \mu_B$. Crystals suitable for X-ray diffraction were grown from vapor diffusion of pentane into tetrahydrofuran at -45 ˚C.

2.7 References

(1) Guenter, A. Concerning the Molecular Structure of Tris-(2,2'-Bipyridine)Vanadium(0) as Well as Isomorphous Ti(0) and Cr(0) Complexes. *Z. Chem.* **1962**, 182–187.

(2) Shah, S. S.; Maverick, A. W. Photophysics and Photochemistry of 2,2'-Bipyridine and 1,10-Phenanthroline Complexes of Vanadium(II). *Inorg. Chem.* **1986**, *25* (11), 1867–1871.

(3) Wenger, O. S. Proton-Coupled Electron Transfer with Photoexcited Metal Complexes. *Acc. Chem. Res.* **2013**, *46* (7), 1517–1526.

(4) Chergui, M. Ultrafast Photophysics of Transition Metal Complexes. *Acc. Chem. Res.* **2015**, *48* (3), 801–808.

(5) Yoon, T. P.; Ischay, M. A.; Du, J. Visible Light Photocatalysis as a Greener Approach to Photochemical Synthesis. *Nat. Chem.* **2010**, *2* (7), 527–532.

(6) Yeh, A. T.; Shank, C. V.; McCusker, J. K. Ultrafast Electron Localization Dynamics Following Photo-Induced Charge Transfer. *Science* **2000**, *289* (5481), 935–938.

(7) Prier, C. K.; Rankic, D. A.; MacMillan, D. W. C. Visible Light Photoredox Catalysis with Transition Metal Complexes: Applications in Organic Synthesis. *Chem. Rev.* **2013**, *113* (7), 5322–5363.

(8) McCusker, J. K. Femtosecond Absorption Spectroscopy of Transition Metal Charge-Transfer Complexes. *Acc. Chem. Res.* **2003**, *36* (12), 876–887.

(9) Odom, A. L.; McDaniel, T. J. Titanium-Catalyzed Multicomponent Couplings: Efficient One-Pot Syntheses of Nitrogen Heterocycles. *Acc. Chem. Res.* **2015**, *48* (11), 2822–2833.

(10) Dill, R. D.; Portillo, R. I.; Shepard, S. G.; Shores, M. P.; Rappé, A. K.; Damrauer, N. H. Long-Lived Mixed ^{2}MLCT/MC States in Antiferromagnetically Coupled d^3 Vanadium(II)

Bipyridine and Phenanthroline Complexes. *Inorg. Chem.* **2020**, *59* (20), 14706–14715.

(11) Scarborough, C. C.; Wieghardt, K. Electronic Structure of 2,2′-Bipyridine Organotransition-Metal Complexes. Establishing the Ligand Oxidation Level by Density Functional Theoretical Calculations. *Inorg. Chem.* **2011**, *50* (20), 9773–9793.

(12) Bowman, A. C.; Sproules, S.; Wieghardt, K. Electronic Structures of the $[V(Tbpy)_3]z$ (z = 3+, 2+, 0, 1-) Electron Transfer Series. *Inorg. Chem.* **2012**, *51*, 3707–3717.

(13) Bowman, A. C.; England, J.; Sproules, S.; Weyhermu, T.; Wieghardt, K. Electronic Structures of Homoleptic [Tris(2,2′-Bipyridine)M]. *Inorg. Chem.* **2013**, *52* (c).

(14) Wang, M.; Weyhermüller, T.; England, J.; Wieghardt, K. Molecular and Electronic Structures of Six-Coordinate "Low-Valent" $[M(^{Me}bpy)_3]^0$ (M = Ti, V, Cr, Mo) and $[M(Tpy)_2]^0$ (M = Ti, V, Cr), and Seven-Coordinate $[MoF(^{Me}bpy)_3](PF_6)$ and $[MX(Tpy)_2](PF_6)$ (M = Mo, X = Cl and M = W, X = F). *Inorg. Chem.* **2013**, *52* (21), 12763–12776.

(15) Hohenberg, P.; Kohn, W. Inhomogeneous Electron Gas. *Phys. Rev.* **1964**, *136* (3B), B864–B871.

(16) Kohn, W.; Sham, L. J. Self-Consistent Equations Including Exchange and Correlation Effects. *Phys. Rev.* **1965**, *140* (4A), 1133–1138.

(17) Zhang, Y.; Lee, T. S.; Petersen, J. L.; Milsmann, C. A Zirconium Photosensitizer with a Long-Lived Excited State: Mechanistic Insight into Photoinduced Single-Electron Transfer. *J. Am. Chem. Soc.* **2018**, *140* (18), 5934–5947.

(18) Hakey, B. M.; Darmon, J. M.; Zhang, Y.; Petersen, J. L.; Milsmann, C. Synthesis and Electronic Structure of Neutral Square-Planar High-Spin Iron(II) Complexes Supported by a Dianionic Pincer Ligand. *Inorg. Chem.* **2019**, *58* (2), 1252–1266.

(19) Kuwano, R.; Kashiwabara, M.; Ohsumi, M.; Kusano, H. Catalytic Asymmetric Hydrogenation of 2,3,5-Trisubstituted Pyrroles. *J. Am. Chem. Soc.* **2008**, *130* (3), 808–809.

(20) Gerothanassis, I. P.; Tsanaktsidis, C. G. Nuclear Electric Quadrupole Relaxation. *Concepts Magn. Reson.* **1996**, *8* (1), 63–74.

(21) Evans, D. F. The Determination of the Paramagnetic Susceptibility of Substances in Solution by Nuclear Magnetic Resonance. *J. Chem. Soc.* **1959**, No. 0, 2003–2005.

(22) Figgis, B. N.; Hitchman, M. A. *Ligand Field Theory and Its Applications*; 2000.

(23) Gowda, A. S.; Petersen, J. L.; Milsmann, C. Redox Chemistry of Bis(Pyrrolyl)Pyridine Chromium and Molybdenum Complexes: An Experimental and Density Functional Theoretical Study. *Inorg. Chem.* **2018**, *57* (4), 1919–1934.

(24) Spek, A. L. Single-Crystal Structure Validation with the Program PLATON. *J. Appl. Crystallogr.* **2003**, *36* (1), 7–13.

(25) Reardon, D.; Conan, F.; Gambarotta, S.; Yap, G.; Wang, Q. Life and Death of an Active Ethylene Polymerization Catalyst. Ligand Involvement in Catalyst Activation and Deactivation. Isolation and Characterization of Two Unprecedented Neutral and Anionic Vanadium(I) Alkyls. *J. Am. Chem. Soc.* **1999**, *121* (40), 9318–9325.

(26) Connelly, N. G.; Geiger, W. E. Chemical Redox Agents for Organometallic Chemistry. *Chem. Rev.* **1996**, *96* (2), 877–910.

(27) Bruker. *APEX3 User Manual*; 2016.

(28) Sheldrick, G. M. Crystal Structure Refinement with SHELXL. *Acta Crystallogr. Sect. C Struct. Chem.* **2015**, *71* (Md), 3–8.

(29) Dolomanov, O. V.; Bourhis, L. J.; Gildea, R. J.; Howard, J. A. K.; Puschmann, H.

OLEX2: A Complete Structure Solution, Refinement and Analysis Program. *J. Appl. Cryst.* **2009**, No. 42, 339–341.

(30) Neese, F. The ORCA Program System. *Wiley Interdiscip. Rev. Comput. Mol. Sci.* **2012**, *2* (1), 73–78.

(31) Neese, F. Software Update: The ORCA Program System, Version 4.0. *Wiley Interdiscip. Rev. Comput. Mol. Sci.* **2017**, *8* (1), e1327.

(32) Allouche, A. R. Gabedit - A Graphical User Interface for Computational Chemistry Softwares. *J. Comput. Chem.* **2011**, No. 32, 174–182.

Chapter 3: High Valent Vanadium Nitrides and Nucleophilicity

3.1 Metal – Ligand Bond Polarization

In pursuit of the synthesis of ammonia from homogenous catalysts, there are now several examples of utilizing trimethylsilyl electrophiles as a surrogate for protons under more mild reaction conditions, yielding tris(trimethylsilyl)amine (TMS_3N). This product is readily hydrolyzed to give ammonia, and the byproduct, trimethylsilanol, can be recovered and recycled.[1] Alternative design strategies which give this reactivity have recently been presented in the literature. Mindiola and coworkers have shown that terminal titanium nitrides supported by bulky bidentate phosphine anilido ligands in a C_{2v} symmetric square pyramid can activate a variety of electrophiles, including silyl derivatives.[2] They attribute the observed nucleophilicity to the difference in Pauling electronegativity of d^0 Ti^{4+} and N^{3-}, giving a highly polarized ionic bond. This, as well as the tetrahedral geometry, is proposed to be critical to the stability of the molecule, eliminating the potential *trans*- effect with respect to the nitride ligand.

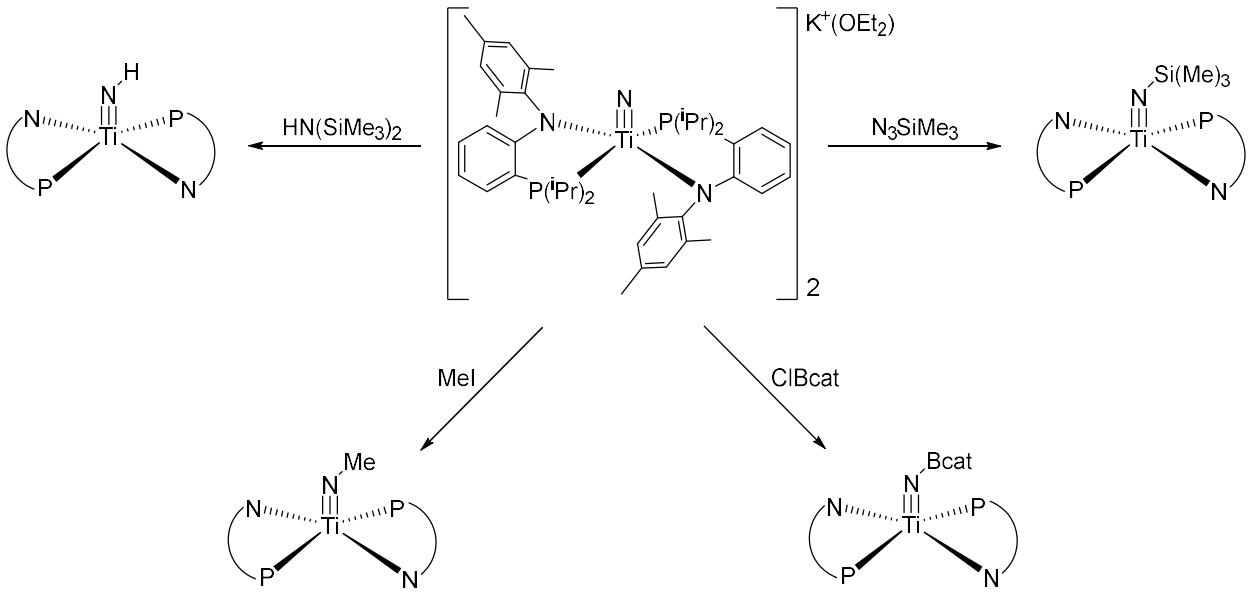

Figure 3.1: Scope of reactivity for $[(PN)_2Ti{\equiv}N]K$ with selected electrophiles.

Further, mechanistic studies of molybdenum nitrides by the Schrock group have repeatedly shown the advantage of a wide range of accessible oxidation states, a sterically controlled coordination sphere, and non-coordinating proton sources.[3–7] Under similar conditions, work by Chirik and Knowles has also presented (sal^{t}Bu)MnN as competent toward the production of ammonia via a visible light driven PCET mechanism, going from Mn(V) to Mn(II).[8] The application of a photoredox catalyst to drive their reaction is a marked advance in these types of systems, especially as we continue to push toward sustainability.[9,10]

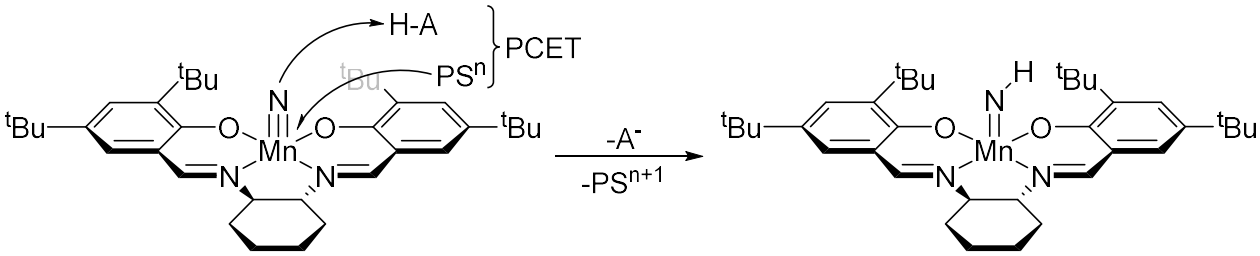

Figure 3.2: Depiction of the first proton coupled electron transfer step for the visible light mediated reduction of (sal^{t}Bu)MnN to ammonia.

By these examples, we see that tuning the nucleophilicity of the M-N fragment is non-trivial and highly dependent on the ligand coordination environment. As discussed in Chapter 1.2, each of these early metal systems leans on the boundary of the oxo wall, where the stereotypical reactivity of the nitride moiety can be pushed more easily into an activated electronic structure. The wide range of oxidation states available to group 5 and 6 metals, specifically, is desirable in designing reactions which require stepwise electrophilic additions and electron transfers.

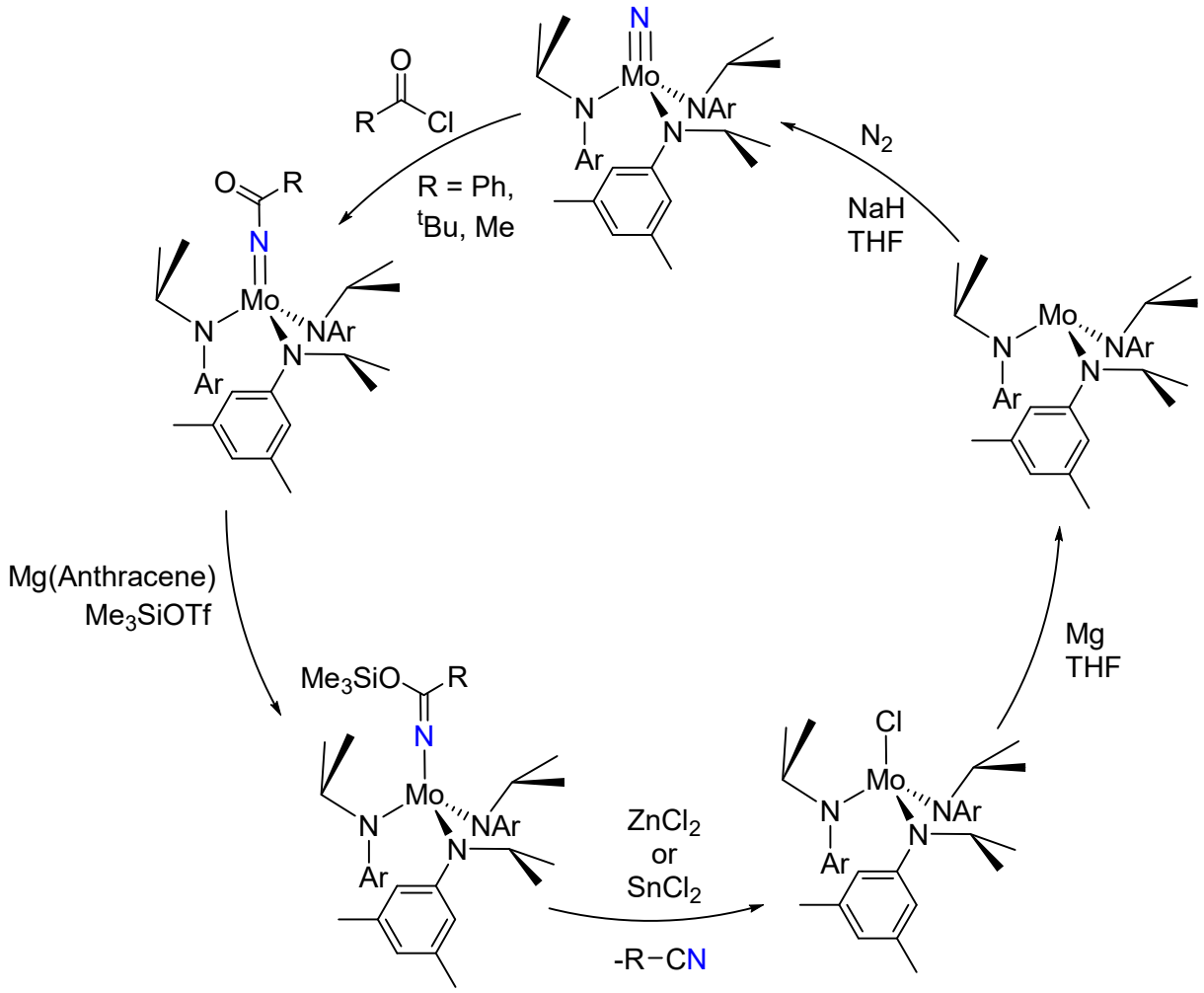

Figure 3.3: Depiction of the nucleophilic addition of (N[^{t}Bu]Ar)$_3$MoN to acyl chlorides, followed by reduction to organic nitriles. The nitride is shown in blue for ease of tracking the release of the organic products.

For example, Cummins and coworkers reported[11] a psuedotetrahedral molybdenum nitride generated from the cleavage of dinitrogen capable of nitrogen atom incorporation into organic nitriles. The first step of this reaction does not proceed in the absence of an additive Lewis acid such as pyridine or Me_3Si^+, a strong electrophile. The limited nucleophilicity of the nitride was attributed to the steric crowding of the terminal t-butyl substituents of the anilido ligands. Discussion of these reactivity followed the phenyl derivative of this scheme (Figure 3.3), where generation of the acylated species was followed by chemical reduction with magnesium

anthracene, a two-electron donor. This promoted a formal reduction of molybdenum from Mo^{VI} (d^0) to Mo^{IV} (d^2). The resulting ketimide was characterized by X-ray crystallography, confirming the bond orders between Mo-N (1.828(2) Å) and C-N (1.280(2) Å) to be roughly 1 and 2, respectively, with a nearly linear arrangement from Mo-N-C of 171.0(1)˚. Computational data supported the favorability of this orientation, where the HOMO of this complex has significant back-bonding from the molybdenum center to the π* orbital of the ketimide ligand. Application of a non-oxidizing Lewis acid ($ZnCl_2$ or $SnCl_2$) allows for the release of the nitrile product and generation of $(N[^tBu]Ar)_3MoCl$, which can be reduced with Mg^0 to the $Mo^{III}(N[^tBu]Ar)_3$ starting material.

Indeed, this work demonstrated a synthetic cycle which resulted in the manipulation of three nitrogen triple bond moieties (N≡N → Mo≡N → C≡N) at a single molybdenum site utilizing a variety of formal oxidation states at the metal center from 6+ to 3+. This Group 6 example of this reactivity is isoelectronic with the Group 5 moiety, where M≡N fragment in the 5+ oxidation state is d^0 and may proceed through M^{III} (d^2) and M^{II} intermediates (d^3). Single electron transfers which are native to first row transition metals make vanadium a viable target for these systems over niobium, which has been demonstrated to more likely form bridged structures.[12–14]

These reports and relative earth abundance of vanadium metal[15] have inspired this work, where we explore the combination of these design principles in an effort to activate a pincer-supported vanadium-nitrogen triple bond. With our electron-rich pincer ligand,[16,17] we explore the thermolysis of a bis-azide vanadium(III) pincer [Na(18-crown-6)][($^{Mes}PDP^{Ph}$)$V(N_3)_2$(thf)] which yields the mixed nitride/azide [($^{Mes}PDP^{Ph}$)VNN_3] sodium 18-crown-6 salt. The subsequent addition of trimethylsilylchloride yields a neutral imido/azido complex accompanied by the

precipitation of sodium chloride. The neutral species can be further reduced to a V(IV) salt, which is characterized by X-ray crystallography as a decamethylcobaltocenium contact ion pair.

3.2 Synthesis and Characterization of [(^{Mes}PDP^{Ph})V(N_3)$_2$(thf)]X
X = Na(18-crown-6), P(Ph)$_4$

The bis-azide salt, [Na(18-crown-6)][(^{Mes}PDP^{Ph})V(N_3)$_2$(thf)], was prepared by metathesis of (^{Mes}PDP^{Ph})VCl(thf)$_2$ with excess sodium azide in THF in the presence of an equivalent of 18-crown-6. The order of addition is not relevant to the reaction, which is quite robust. The reaction mixture was stirred overnight at room temperature before being filtered through a plug of Celite and reduced to dryness. Similar to the preparation of the halide starting material, described in Chapter 2, the crude product is treated with toluene and pentane, taken in toluene, and filtered again through Celite to remove dissolved salts.

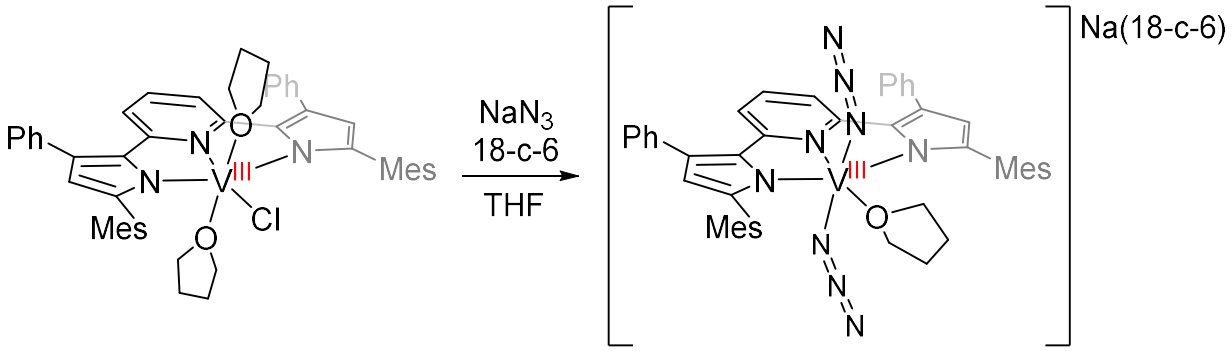

Scheme 3.1: Synthesis of [Na(18-crown-6)][(^{Mes}PDP^{Ph})V(N_3)$_2$(thf)].

The product is less soluble in toluene, but equally as dark red as the precursor. The solvent was removed to give an amorphous red powder in > 90% yield. Preparative recrystallization via layering pentane on a concentrated solution of THF at -35 ℃ gives long flexible planks, decolorizing the mother liquor with virtually no loss of yield. A selection of these were found to be suitable for x-ray diffraction. For the purpose of this discussion, these structural data and characterization proceeds the spectroscopic data, as the connectivity of these atoms cannot be established by NMR, IR, or UV-vis due to the product's intrinsic paramagnetism.

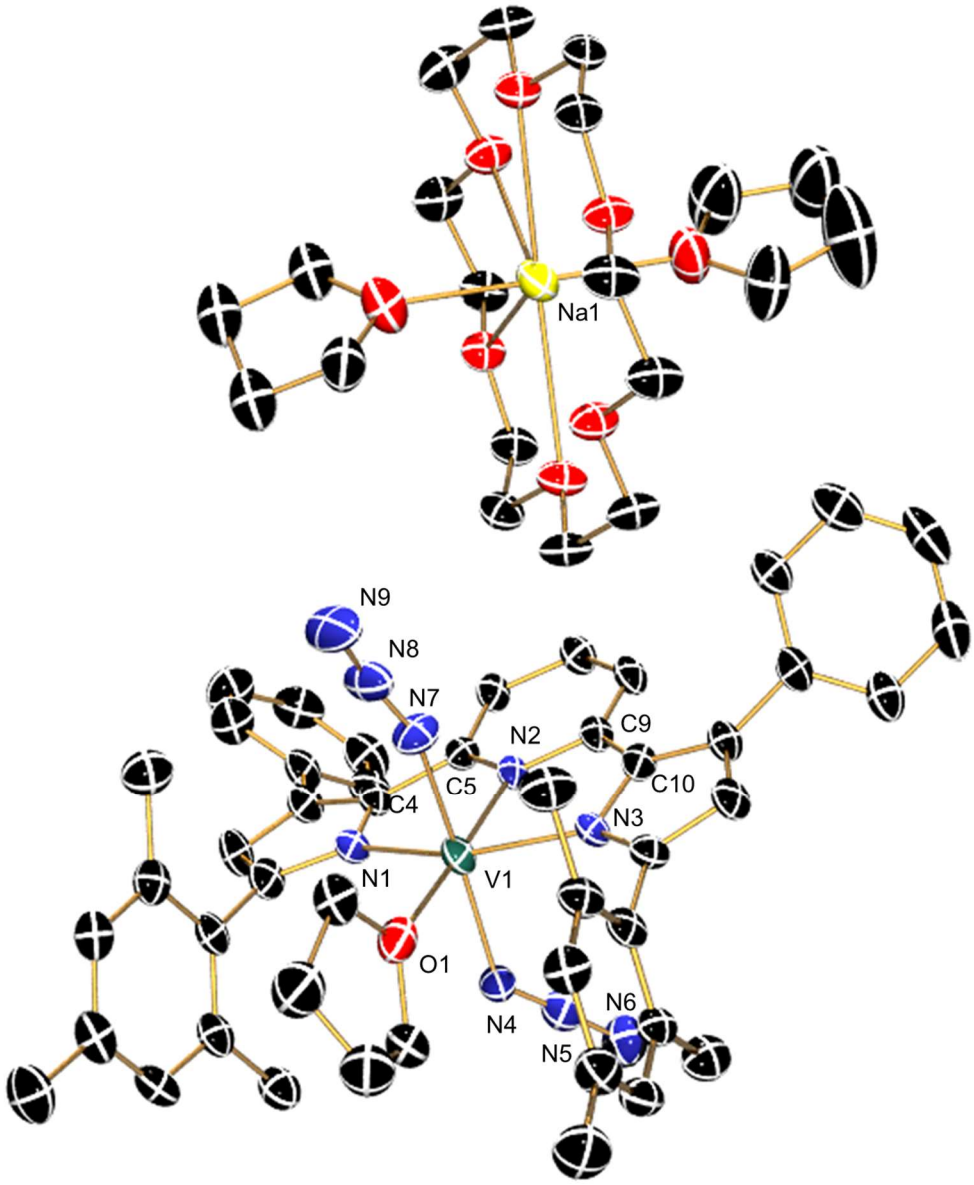

Figure 3.4: ORTEP generated crystal structure of [Na(18-crown-6)][(^{Mes}PDP^{Ph})V(N_3)$_2$(thf)] displayed at 50% probability. Hydrogen atoms and co-crystallized solvent are excluded for clarity.

The solvent separated ion pair resolved with 1.5 molecules in the asymmetric unit in a monoclinic C2/c cell, along with two molecules of co-crystallized tetrahydrofuran. Some disorder of solvent molecules and a slight wagging of the terminal end of an azide ligand were able to be nicely modeled. Recrystallization of the red powder product from toluene/pentane afforded a different crystalline morphology.

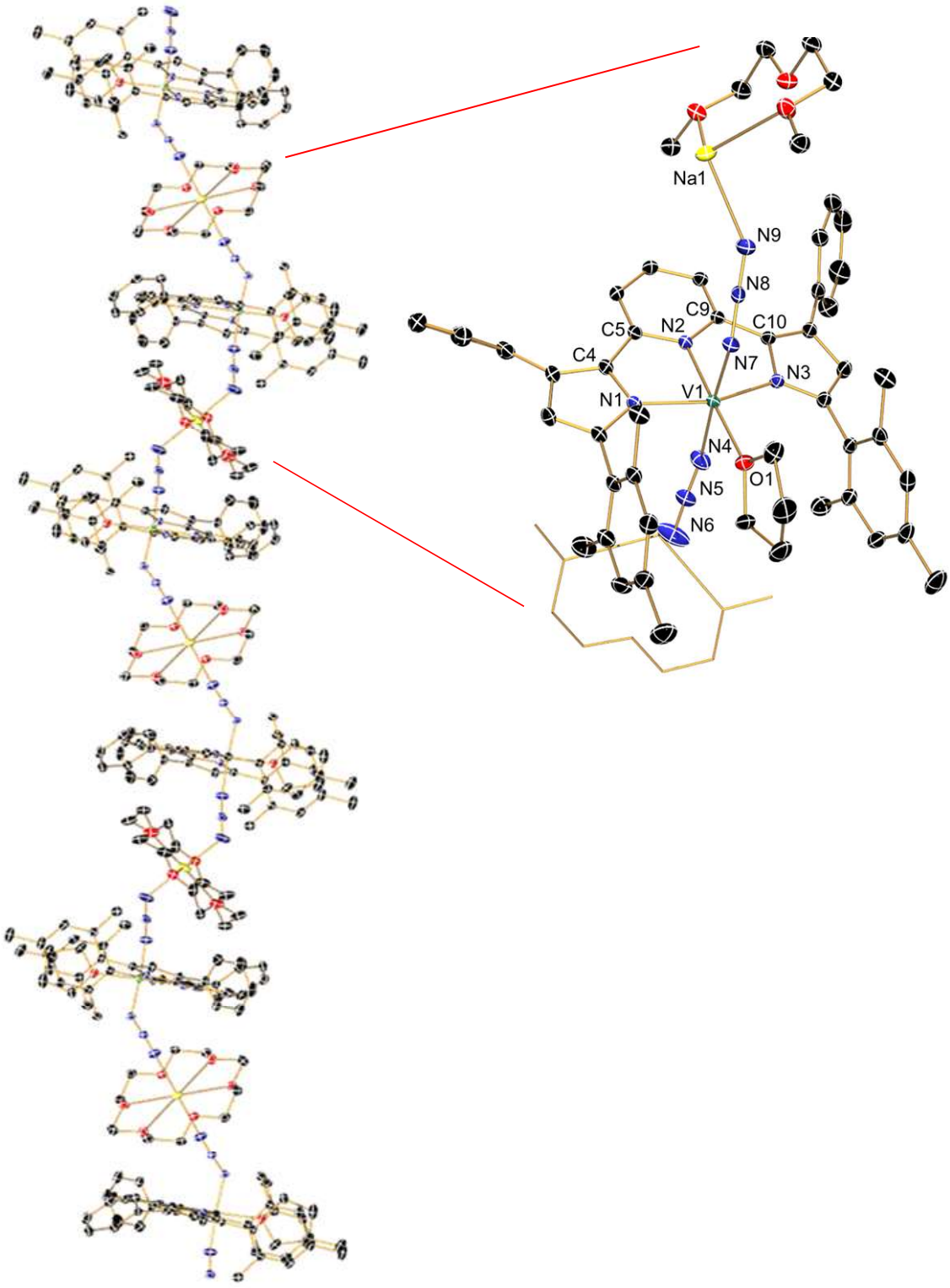

Figure 3.5: ORTEP generated crystal structures of [Na(18-crown-6)][(^{Mes}PDP^{Ph})V(N_3)$_2$(thf)] displayed at 50% probability. Hydrogen atoms and co-crystallized solvent are excluded for clarity, and half of the crown ether depicted in wireframe (right).

From concentrated benzene, a vapor diffusion of pentane at room temperature gave the structures depicted in Figure 3.5. The crystalline polymer solved in a triclinic $P\bar{1}$ cell along with 1.5 equivalents of disordered benzene. The molecule solved along the screw axis, where half of the sodium crown is situated upon the terminal end of either azide ligand. The structures of the ion separated pair and crystalline polymer are not appreciably different from each other; a summary of their relevant bond lengths is given in Table 2.1.

Table 3.1: Direct comparison of the crystalline morphologies of [Na(18-crown-6)][(^{Mes}PDP^{Ph})V(N_3)$_2$(thf)]. *a*, average bond length where N9 is disordered over two positions. *b*, average bond length of N6-Na1 and N9-Na1.

length (Å)	[Na(18-crown-6)][(^{Mes}PDP^{Ph})V(N_3)$_2$(thf)]	
	ion pair	polymer
N1-V1	2.096(4)	2.0851(10)
N2-V1	2.046(3)	2.0411(11)
N3-V1	2.087(3)	2.0917(11)
N1-C4	1.395(5)	1.3953(15)
C4-C5	1.431(5)	1.4454(17)
N2-C5	1.360(5)	1.3577(13)
N2-C9	1.351(5)	1.3565(16)
C9-C10	1.462(5)	1.4533(13)
N3-C10	1.384(5)	1.3942(16)
N4-V1	2.011(5)	2.0224(11)
N4-N5	1.174(8)	1.1600(14)
N5-N6	1.173(9)	1.1599(16)
N7-V1	2.009(5)	2.0288(10)
N7-N8	1.141(9)	1.1991(12)
N8-N9	1.23[a]	1.1540(13)
N6,9-Na1	—	2.461[b]

The bond lengths of the PDP backbone show no significant change from the previously characterized halide starting material, indicating no change in formal oxidation state. The azide ligands, *trans*- to each other in the apical positions, show reasonable dative bond lengths with respect to vanadium. The N-N bond lengths are roughly equivalent, indicating a symmetric electronic structure, except in the case of N8-N9 in the solvent separated ion pair. This terminal bond is lengthened considerably and disordered over two positions. This is likely due to the lack of sodium stabilization, as is present in the crystalline polymer. These data allow for the confident assignment of spectral properties to this species and gives meaning to further characterization.

The d^2 V^{III} complex yields a paramagnetic ^{1}H NMR spectrum, with broad resonances from 35 to -40 ppm. The spectrum is not informative to the structure of the molecule, as we would anticipate, but is distinct from the starting material. The solution magnetic moment via Evan's method[18] (2.56 μ_B) was consistent with an S = 1 ground state and the previously isolated (^{Mes}PDP^{Ph})VCl(thf)$_2$. Deviation from the spin-only value is likely a result of unquenched spin orbit coupling and a g tensor value of less than 2.

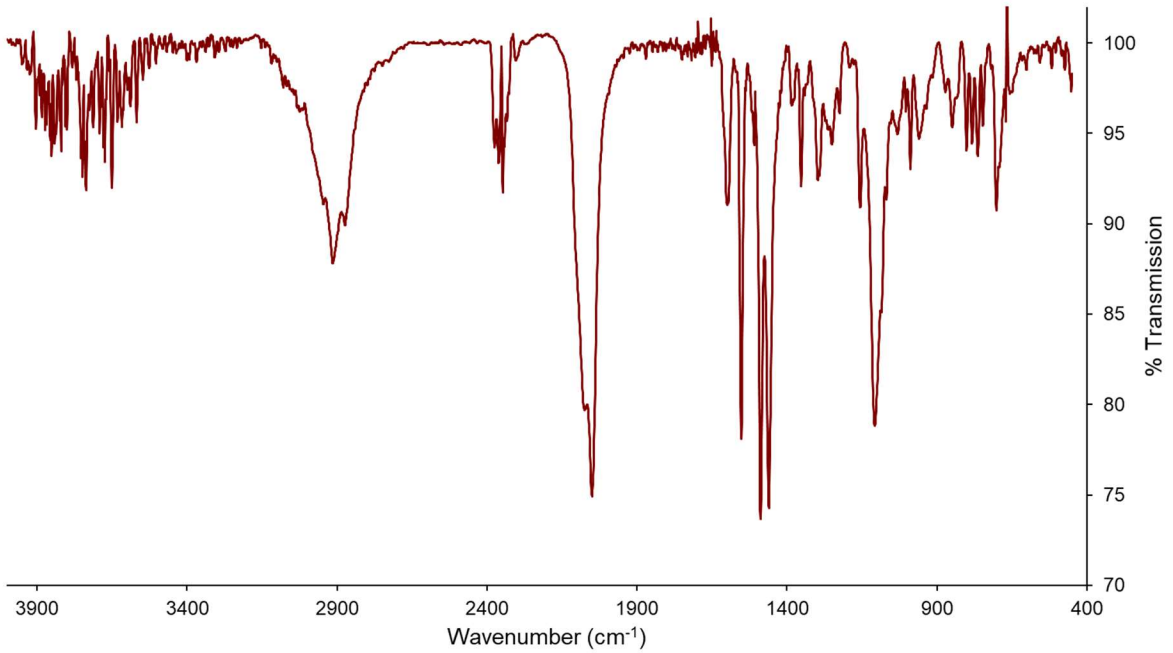

Figure 3.6: Infrared spectrum of [Na(18-crown-6)][(^{Mes}PDP^{Ph})V(N_3)$_2$(thf)] in KBr matrix.

Infrared spectroscopy of the product was performed on a sample ground in dry potassium bromide in an agate mortar and pestle. The analyte in KBr matrix shows a strong asymmetric band with two major peak maxima at 2080 cm^{-1} and 2050 cm^{-1} (Figure 3.6), indicating the presence of one or more azide ligands. These bands are consistent with asymmetric and symmetric N-N stretching modes of the azide moiety in the solid state, which are both IR active under C_{2v} symmetry. Both are inconsistent with sodium azide impurity (2140 cm^{-1}).[19]

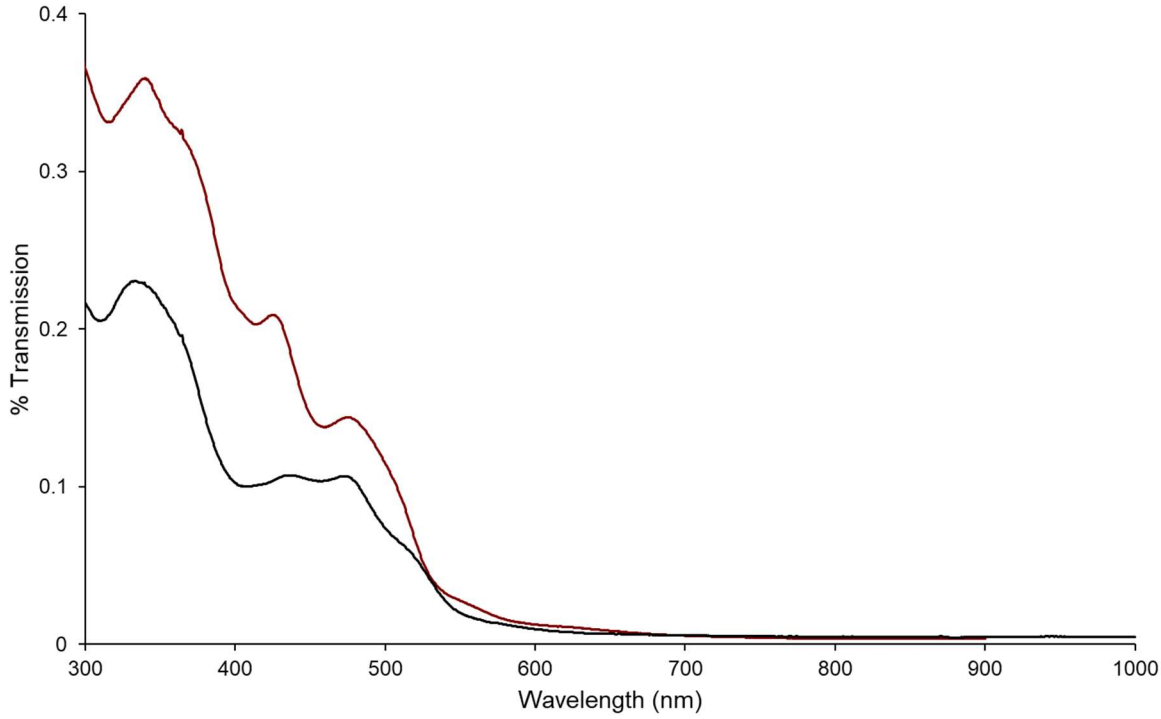

Figure 3.7: UV-visible spectrum of [Na(18-crown-6)][(^{Mes}PDP^{Ph})V(N_3)$_2$(thf)] in benzene (red) and in tetrahydrofuran (black), independently prepared.

The absorption spectrum of the bis-azide salt was taken in both benzene and THF. Though major differences were not anticipated, as major differences would indicate markedly different electronic structures, this was performed to investigate the solvation of the coordination complex. From these data, there is unlikely to be any difference in speciation dependent on the solvent, as it appears that these transitions are largely unchanged. Further, there appears to be no significant solvatochromism, where the energies of intramolecular electronic transitions are stabilized/destabilized as a function of polarity.

Preparation of the potassium analogue of this material was also pursued by the utilization of potassium azide, however, the generated material is indistinguishable from the sodium derivative. The major distinction over the course of this work is that single crystals of the potassium salts could not be generated in good quality, leaving the absolute structure of these analogues ambiguous. As a result, later reactions with these materials were not pursued.

In order to solve issues with the solubility of products discussed in Chapters 3 and 4, the tetraphenylphosphonium salt of [(^{Mes}PDP^{Ph})V(N_3)$_2$(thf)] was prepared and characterized. Similar to the sodium-crown bis-azide, (^{Mes}PDP^{Ph})VCl(thf)$_2$ was added to THF with an excess of sodium azide, now in the presence of an equivalent of (Ph_4P)Cl and stirred overnight.

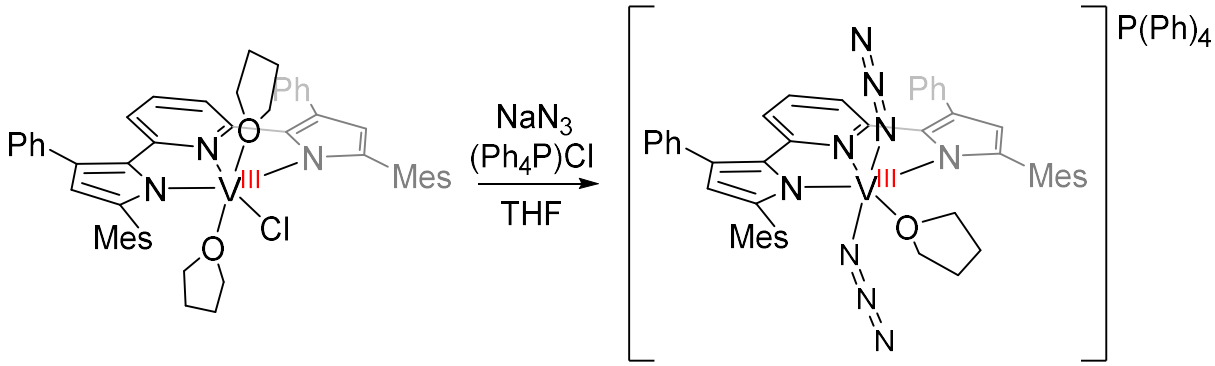

Scheme 3.2: Synthesis of [(^{Mes}PDP^{Ph})V(N_3)$_2$(thf)]PPh_4.

However, solubility of the products in toluene was minimal, which removed several steps from the work up. Considering the size, shape, and charge of the (Ph_4P) cation, we presume this not to interfere with our reaction, as sodium chloride should be much less soluble as an ionic pair in ethers, and precipitate selectively from the reaction mixture. Due to these solubility properties, recrystallization from non-polar media was not feasible. It has been demonstrated that single crystals are isolable from vapor diffusion of pentane into tetrahydrofuran, however, none have diffracted farther than $2\theta = 25^{\circ}$; efforts to obtain a solid-state structure remain unsuccessful.

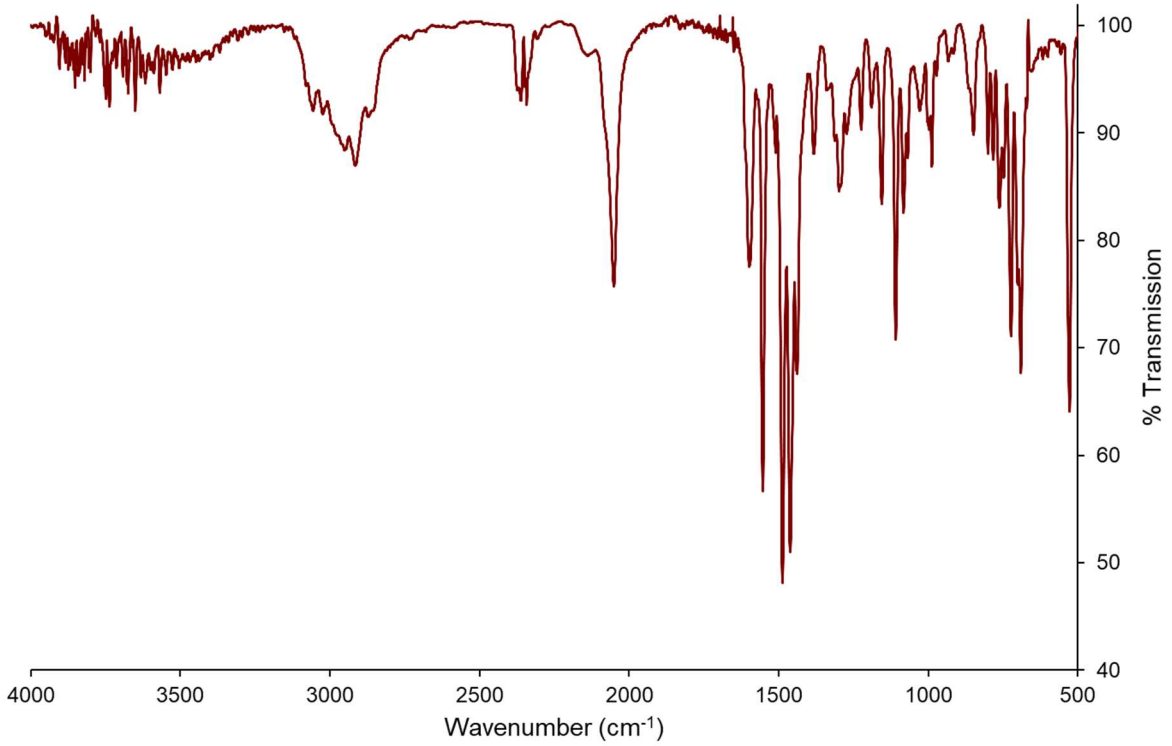

Figure 3.8: IR spectrum of [(^{Mes}PDP^{Ph})V(N_3)$_2$(thf)]PPh_4 in KBr matrix.

Spectroscopic characterization of the title complex was performed as for the previous examples. Infrared spectroscopy identified a large stretch at 2051cm^{-1}, consistent with the one of the azide stretching modes. Broadening observed toward the middle of this band is likely a shoulder belonging to the second stretching mode. NMR data continues to be uninformative for this paramagnetic species, though the Evan's Method magnetic susceptibility in methylene chloride-d_2 was measured (2.65 μ_B) and found to be comparable to the previously characterized sodium crown analogue (2.56 μ_B), consistent with an S = 1 system.

3.3 Synthesis and Characterization of [(^{Mes}PDP^{Ph})V≡N(N_3)]X
X = Na(18-crown-6), P(Ph)$_4$

Following the syntheses of the [(^{Mes}PDP^{Ph})V(N_3)$_2$(thf)]$^-$ anion, selective thermolysis of the bis-azide salts at 120 °C in C_6D_6, toluene, or on larger scales, toluene/THF, cleanly converts to the nitride, [(^{Mes}PDP^{Ph})VN(N_3)]. Thermolysis does not proceed under 100 °C. The resulting solution was a brighter red than the preceding species, and diamagnetic.

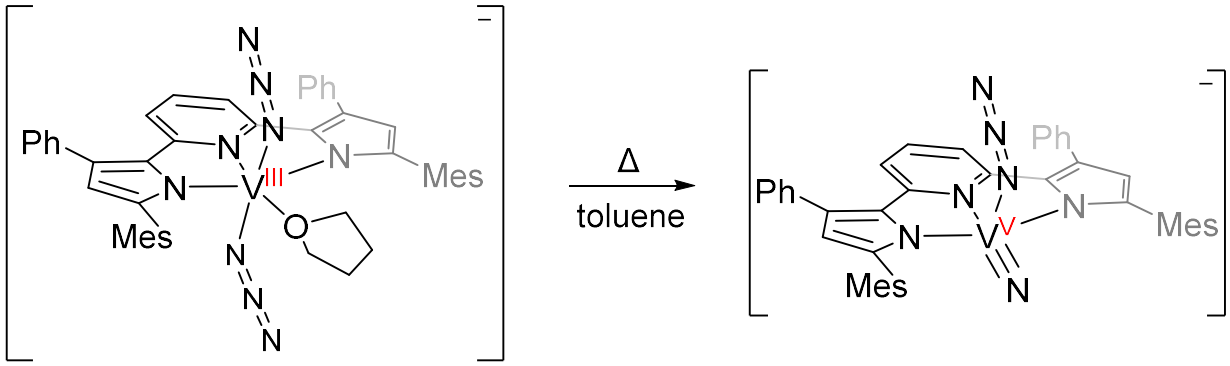

Scheme 3.3: Synthesis of [(^{Mes}PDP^{Ph})VN(N_3)]$^-$ anion. Counterions may be either [Na(18-crown-6)] or [P(Ph)$_4$].

The ^{1}H NMR spectrum (Figure 3.9) in deuterated methylene chloride shows three singlet resonances (A, B, and C) indicative of equivalent 6H methyl groups on the mesityl moiety of the ancillary ligand, which alludes to a top-bottom inequivalent, C_s symmetric molecule. This solvent was selected due to limited solubility in benzene, so that concentrations of analyte were reasonably high for ^{13}C NMR measurements. The singlet attributed to 18-crown-6 stands alone at δ 3.54 ppm (D), representing 24 protons. The last stand-alone peak at δ 6.08 ppm (E) integrates just under 2H, consistent with the protons on the backbone of the pyrrole.

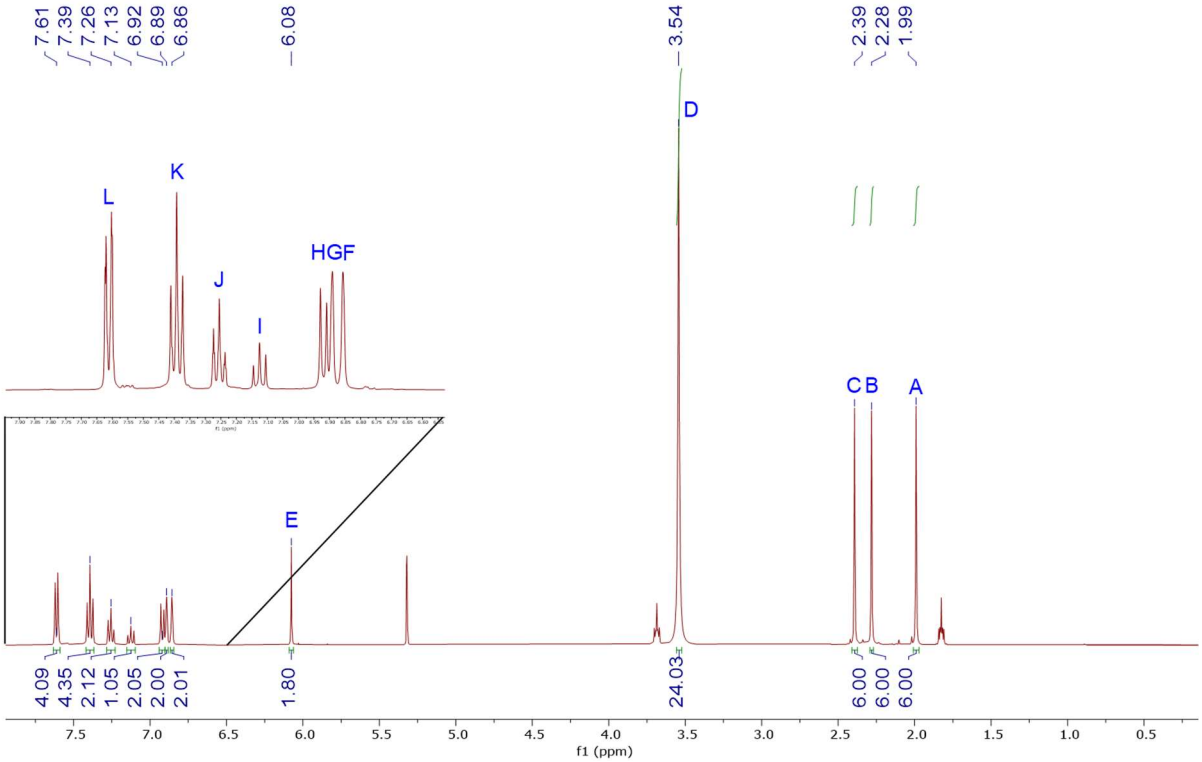

Figure 3.9: ^{1}H NMR spectrum of [Na(18-crown-6)][(^{Mes}PDP^{Ph})VN(N_3)] in methylene chloride-d_2. The region between δ 7.0 ppm and 6.5 ppm is expanded for clarity. Peak labels are given in blue.

The aromatic region of the spectrum is relatively clear, with minimal overlap. The signals at δ 7.26 (dt, 4H), 7.39 (t, 4H), 7.61 (tt, 2H) ppm show a slight roofing effect, as well as a small amount of 4J coupling between these peaks labeled J, K, and L (J = 1.5 Hz). The peak coupling on K is not well resolved, however, correlated NMR (Figure 3.10) shows a consistent pattern with J and L. These data are consistent with the phenyl rings on the back side of the PDP ligand. The remaining triplet and doublet, I and H, respectively, also display a gentle roofing (J = 7.9 Hz) and integrate in a 1:2 ratio. Their coupling relationship was reaffirmed by COSY NMR spectroscopy, with a clear off-diagonal peak. These cumulative data suggest the indicated protons belong to the pyridine backbone.

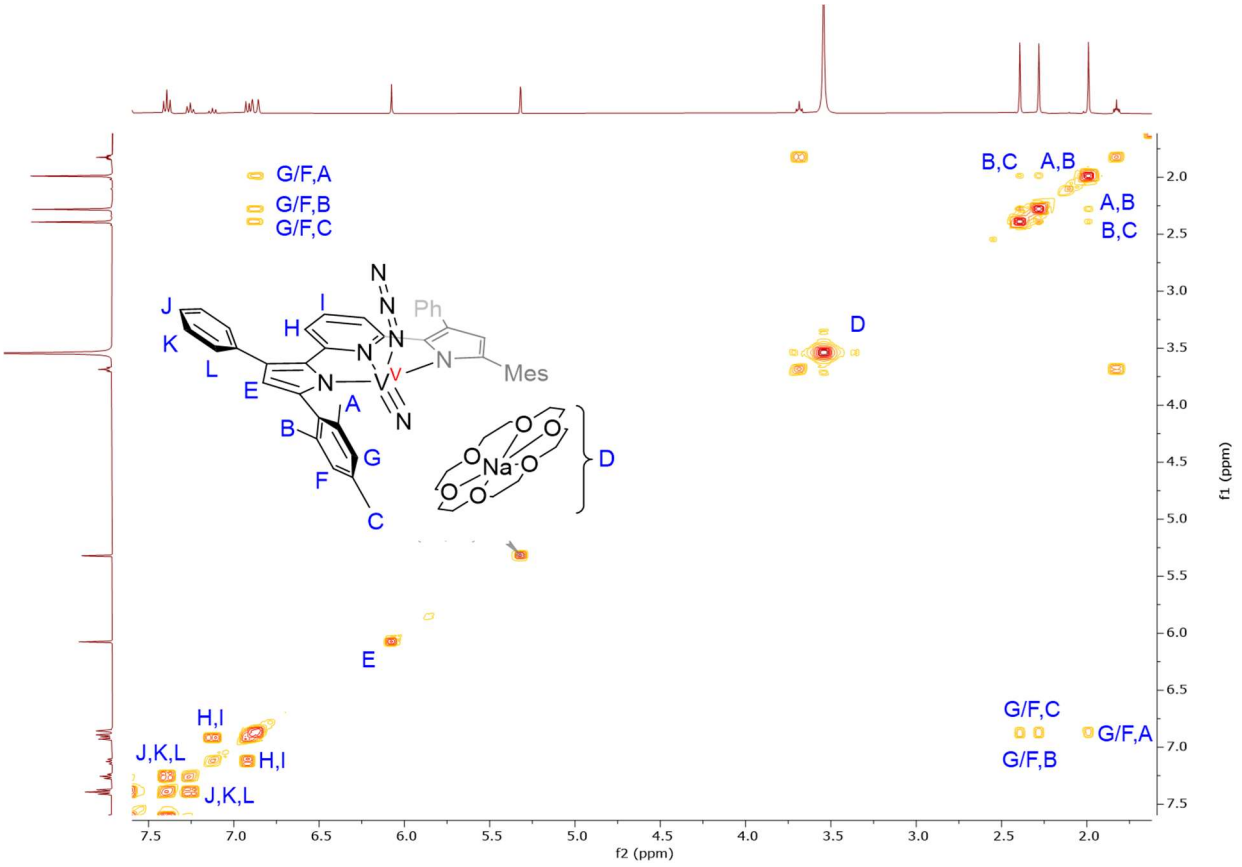

Figure 3.10: (HH) COSY NMR spectrum of [Na(18-crown-6)][(^{Mes}PDP^{Ph})VN(N_3)] in methylene chloride-d_2, where coupled signals on the off-diagonal are labelled according to the inset structure, consistent with those in Figure 3.9.

The signals G and F are closely related and appear almost as a doublet, where their similar chemical shift is due to their similar chemical environment. On the basis of an evaluation of the COSY NMR spectrum (Figure 3.10), we assert that these are the aryl protons on either side of the mesitylene fragment on the front of the PDP ligand. The two-dimensional spectrum shows relatively strong 4J coupling from these aryl protons to the methyl group protons on the mesitylene fragment, further confirming this assignment.

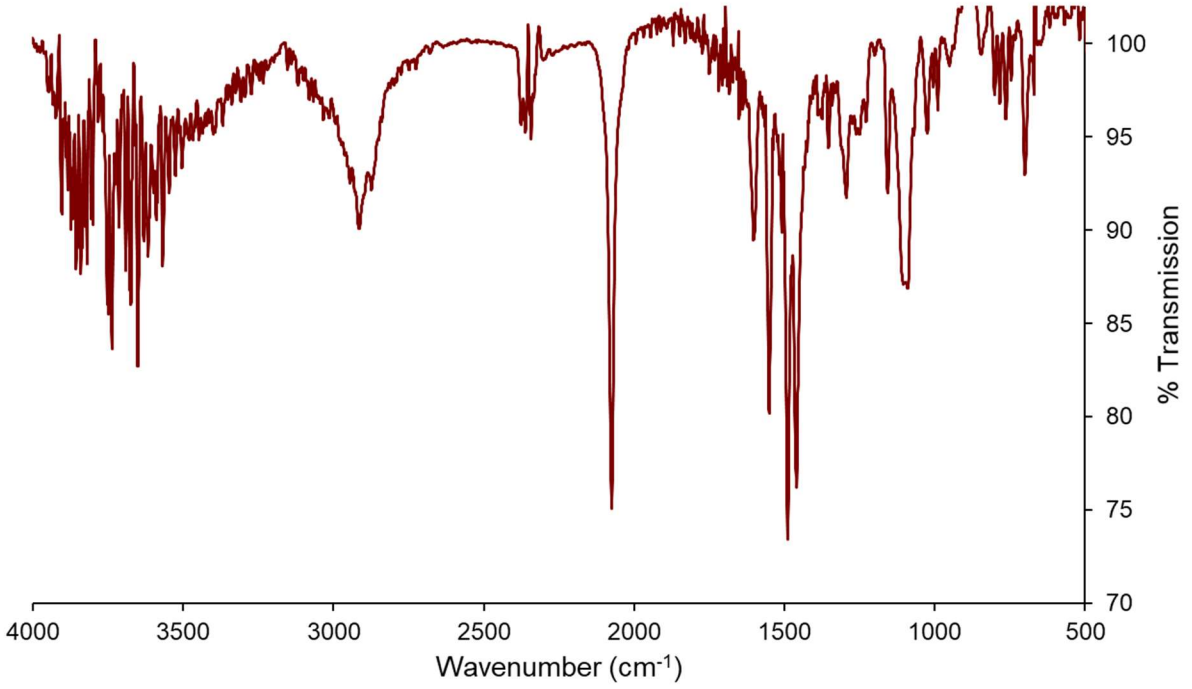

Figure 3.11: Infrared spectrum of [Na(18-crown-6)][(^{Mes}PDP^{Ph})VN(N_3)] in KBr matrix.

In order to investigate the nitrogen-based ligands on the [(^{Mes}PDP^{Ph})VN(N_3)]$^-$ anion, infrared spectroscopy was performed from pelleted KBr. This spectrum (Figure 3.11) revealed a strong singlet at 2075 cm^{-1} which is markedly sharper and more symmetric than the bis-azide precursor. A strong band also appears at 1108 cm^{-1}, which can be attributed to the V≡N stretching frequency.[20] Spectroscopic characterization of the analogous tetraphenylphosphonium salt can be found in Appendix A, to avoid data redundancy.

The structure of [Na(18-crown-6)][(^{Mes}PDP^{Ph})VN(N_3)] was further confirmed by X-ray crystallographic analysis (Figure 3.12). Single crystals were grown from slow diffusion of pentane into toluene at -35 °C, resolving half the molecule in a monoclinic cell ($P2_1/m$) about a screw axis in the unique *b* direction. Interestingly, this also results in a pseudo-coordination polymer in the *a* direction, where the terminal nitride orients itself toward the sodium crown capping the azide ligand, separated by 4.201(6) Å. The affinity for the terminal nitride to orient toward a Lewis acid

may be a preliminary indication of the nucleophilicity of this moiety. Further, the direct interaction of the azide ligand with the sodium cation is not unlike the of [Na(18-crown-6)][(^{Mes}PDP^{Ph})V(N_3)$_2$(thf)], which showed similar behavior when grown from aromatic solvents. It appears to be that the coulombic interaction with the terminal end of the dative azide ligand consistently binds the apical positions of sodium 18-crown-6 in the absence of other ligands in the solid state.

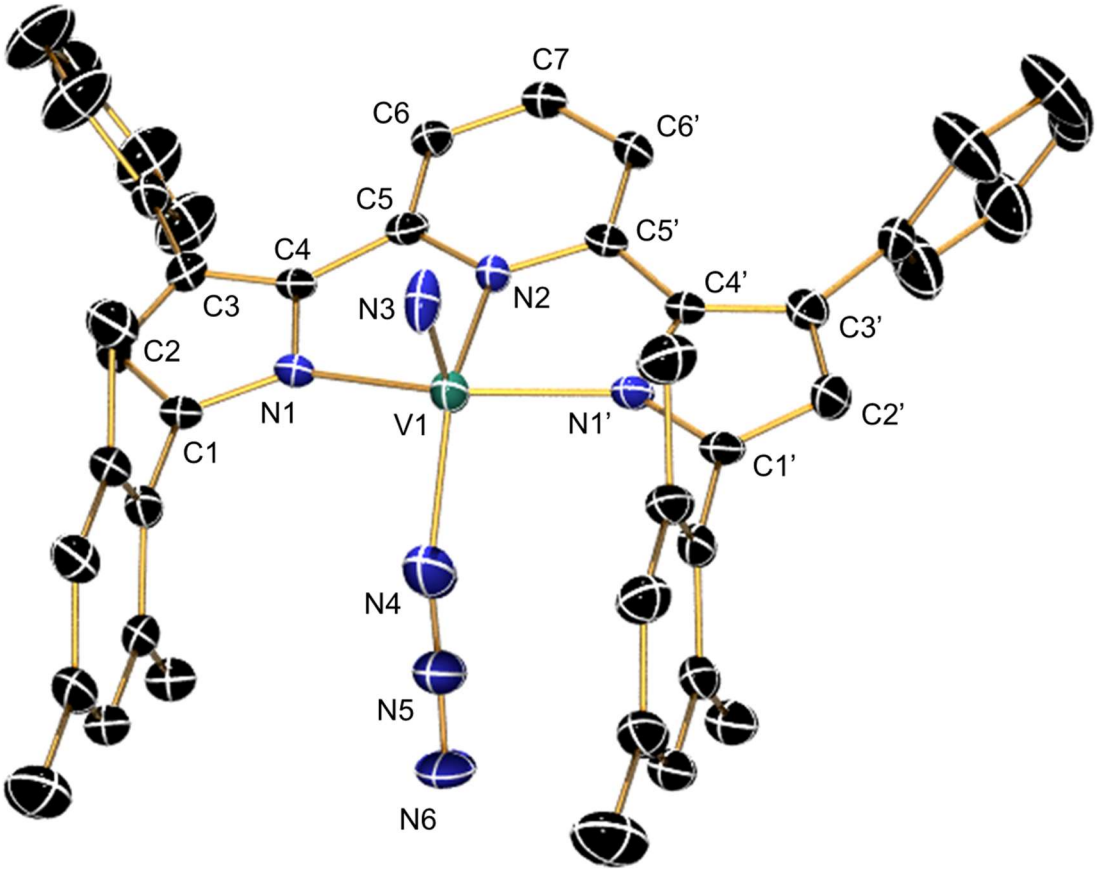

Figure 3.12: ORTEP generated crystal structure of [Na(18-crown-6)][(^{Mes}PDP^{Ph})VN(N_3)] displayed at 50% probability. Hydrogen atoms, co-crystallized solvent, and counterion are excluded for clarity.

As only half of the molecule is refined in the asymmetric unit, half of the molecule was generated by the symmetry relationship +x, 3/2-y, +z. The vanadium-pincer bond distances of the diamagnetic complex were contracted compared the V^{III} precursor, as we would have anticipated

(Table 2.1) due to the increased Lewis acidity and smaller ionic radius of the V^V ion. Despite this, the angle of chelation is only marginally affected. This product of the two-electron oxidation is expected to have a closed shell electronic structure with no metal centered electrons, however, there is a non-zero potential for an antiferromagnetically coupled V^{IV}/PDP$^{\bullet}$ electronic structure. As a result, careful consideration of the X-ray crystal structure analogous to our work with low-valent vanadium PDP ligands was carried out.

Table 3.2: Comparison of PDP bond lengths between [(^{Mes}PDP^{Ph})V(N$_3$)$_2$(thf)]$^-$ and [(^{Mes}PDP^{Ph})VN(N$_3$)]$^-$. *a*, symmetry generated positions of the relationship (+x, 3/2-y, +z).

length (Å)	[Na(18-crown-6)] [(^{Mes}PDP^{Ph})V(N$_3$)$_2$(thf)]	[Na(18-crown-6)] [(^{Mes}PDP^{Ph})VN(N$_3$)]
V1-N1	2.0851(10)	2.030(3)
V1-N2	2.0411(11)	2.027(6)
V1-N3	2.0917(11)	2030(3)*a*
N1-C1	1.3633(16)	1.353(5)
C1-C2	1.3931(15)	1.371(6)
C2-C3	1.4090(18)	1.393(6)
C3-C4	1.4030(15)	1.374(6)
N1-C4	1.3953(15)	1.373(6)
C4-C5	1.4454(17)	1.426(6)
N2-C5	1.3577(13)	1.349(5)
C5-C6	1.4010(16)	1.376(6)
C6-C7	1.3893(18)	1.376(5)
C7-C8	1.3929(15)	1.376(5)*a*
C8-C9	1.3999(17)	1.376(6)*a*
N2-C9	1.3565(16)	1.349(5)*a*
C9-C10	1.4533(13)	1.426(6)*a*
N3-C10	1.3942(16)	1.373(6)*a*
C10-C11	1.4033(16)	1.374(6)*a*

C11-C12	1.4163(17)	1.393(6)[a]
C12-C13	1.3887(19)	1.371(6)[a]
N3-C13	1.3688(14)	1.353(5)[a]

As a result of this analysis, these data suggest no activation of the PDP ligand backbone. In combination with the diamagnetic properties of the vanadium nitride, this leads to the confident assignment of the 5+ oxidation state. Further comparison of these structures with respect to metal-nitrogen bonds reveals a slight activation of the azide ligand.

Table 3.3: Comparison of V-N and N-N bond lengths between $[(^{Mes}PDP^{Ph})V(N_3)_2(thf)]^-$ and $[(^{Mes}PDP^{Ph})VN(N_3)]^-$. *a*, average lengths between either azide ligand. *b*, average length over two disordered positions.

length (Å)	[Na(18-crown-6)] $[(^{Mes}PDP^{Ph})V(N_3)_2(thf)]$	[Na(18-crown-6)] $[(^{Mes}PDP^{Ph})VN(N_3)]$
V1-Nα	2.0256[a]	1.926(10)
Nα-Nβ	1.1796[a]	1.245(12)
Nβ-Nγ	1.1570[a]	1.137(12)
Nγ-Na1	2.461[b]	2.349(9)
V≡N	—	1.615(4)

From thermolysis of the $[(^{Mes}PDP^{Ph})V(N_3)_2(thf)]^-$ starting material, the V≡N bond was determined to be 1.615(4) Å. The remaining azide ligand on the product, $[(^{Mes}PDP^{Ph})VN(N_3)]^-$, presents a contraction of the vanadium-azide bond of ~0.1 Å with respect to the bis-azide starting material. This is concomitant with an elongation of the Nα-Nβ bond by the same margin. The increased Lewis acidity of the V^V ion may be responsible for this electronic structure rearrangement of the azide ligand, where electron density is drawn away from bonding π orbitals, weakening the homoatomic nitrogen association. This would also account for the closer

association of Nγ with sodium, where Nγ would have more ionic character opposite the contracted Nα-Nβ bond.

The tetraphenylphosphonium derivative, [(^{Mes}PDP^{Ph})VN(N_3)][P($Ph)_4$], was also characterized by NMR spectroscopy, though its crystal structure has not been determined.

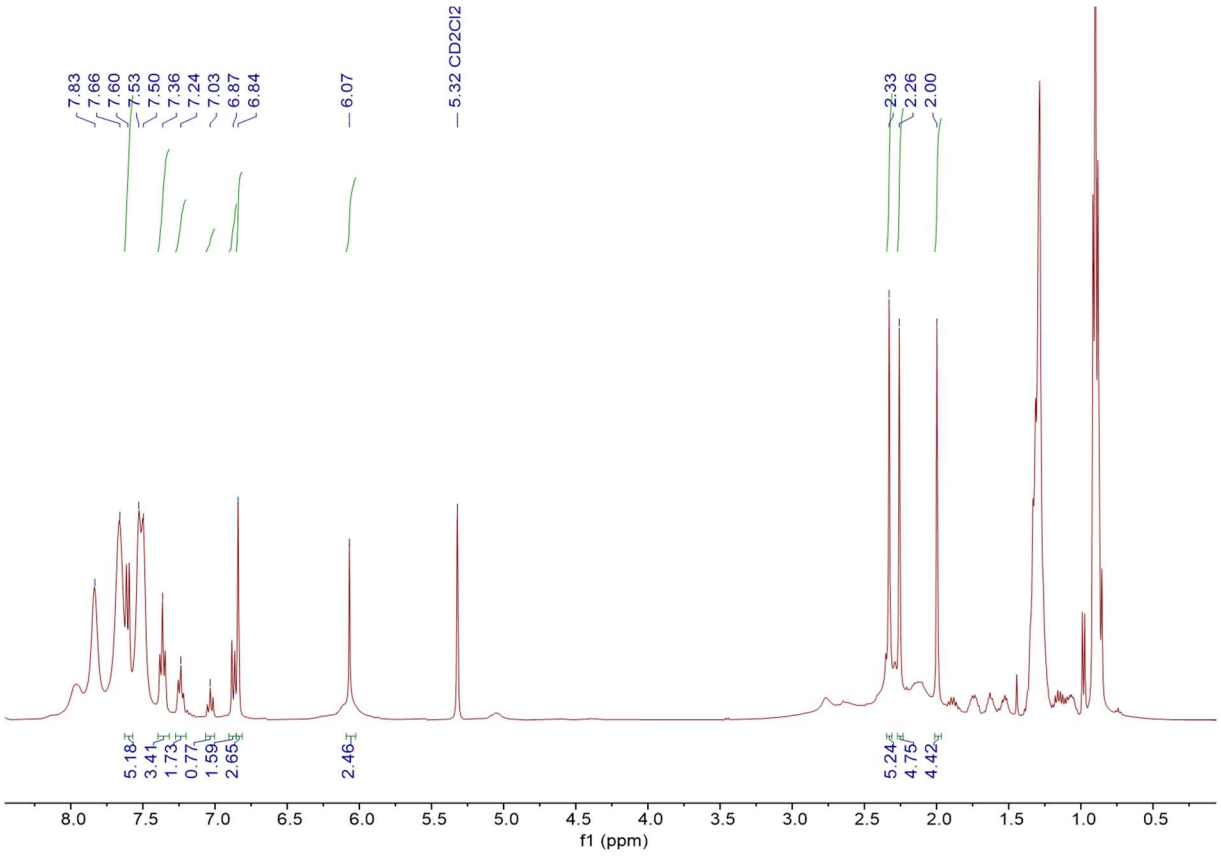

Figure 3.13: ^{1}H NMR spectrum of [(^{Mes}PDP^{Ph})VN(N_3)][P($Ph)_4$] in methylene chloride-d_2.

The counterion, in a 1:1 ratio with the nitride, should have 3 aromatic resonances with a cumulative integration of 20H. However, these are not well resolved in this spectrum. This is likely due to the unrestricted molecular movement of the cation in solution, which have coalesced these signals into the broad features > δ 7.5 ppm. Despite this, and the residual pentane, the features of this species are as expected, where solution state measurements of these salts should not be incredibly unique with respect to each other. In order to further solidify this assessment, correlated spectroscopy was also performed.

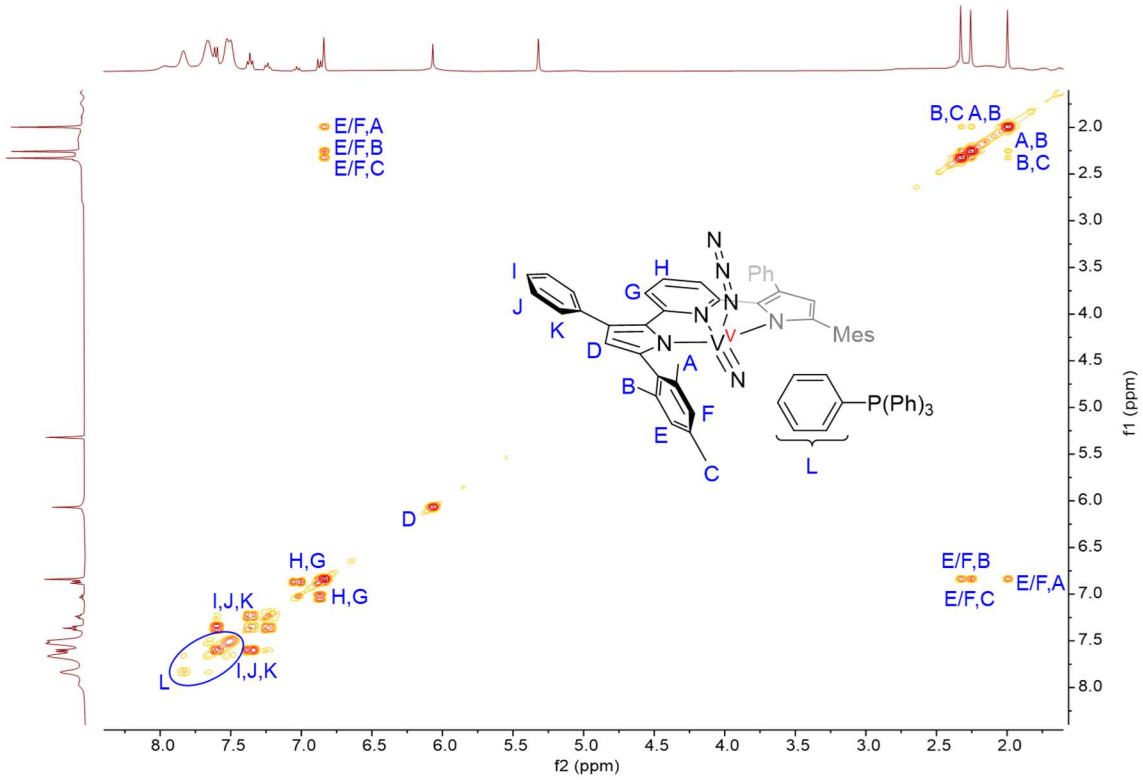

Figure 3.14: (HH) COSY NMR spectrum of [(^{Mes}PDP^{Ph})VN(N_3)][$P(Ph)_4$] in methylene chloride-d_2, where coupled signals on the off-diagonal are labelled according to the inset structure, consistent with those in Figure 3.13.

The coupling patterns between the aliphatic and aromatic regions are analogous to those reported for the Na(18-crown-6) cation derivative of the vanadium nitride, as we would anticipate. Further, the coupling associated with the phenyl substituents of the counterion do comprise the broad features > 7.5 ppm as we anticipated based on the 1D experiment. While these data are reproductions of an established system, this species provides synthetic flexibility for future work.

3.4 Activation of [Na(18-crown-6)][(^{Mes}PDP^{Ph})V≡N(N_3)] with TMS-Cl

Following the preparation of the nitride/azide salt, subsequent addition of excess trimethylsilyl chloride to the terminal nitride complex in toluene solution at 120 °C cleanly yields the neutral trimethylsilyl imido species. While no formal temperature dependent study was performed, it should be noted that the reaction does not proceed at room temperature. The solid material was isolated by removing the solvent and under vacuum. Residual 18-crown-6 was removed with several washes of pentane, and salts precipitated in toluene. The crown ether has been shown to be difficult to reliably separate from the product, and often appears in NMR spectra of otherwise pure material. An alternative synthesis of this product will be reported in Chapter 4, however, its characterization is reported below.

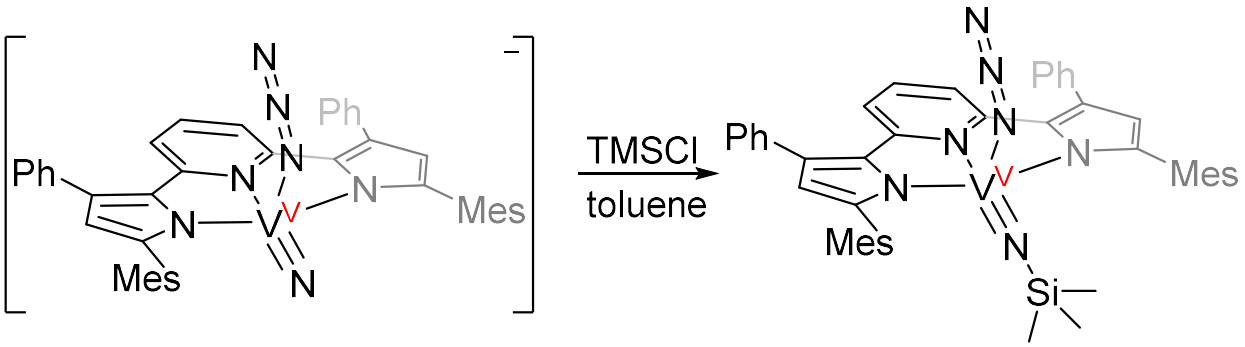

Scheme 3.4: Preparation for (^{Mes}PDP^{Ph})V(NTMS)(N_3).

Proton and ^{13}C NMR data were collected in benzene-d_6, as the purple solids had no issues with solubility in aromatic solvent. The mesityl methyl groups (6H) continued to act as reporters in these data at δ 2.16 (B), 2.20 (C), 2.50 (D) ppm, as well as the new TMS peak (A) at δ -0.08 ppm (s, 9H). These data indicate C_s symmetry, similar to that of the starting material, which we had anticipated with the retention of the azide ligand. The ^{1}H NMR spectrum did not appear to indicate another PDP containing species, such as the potential side-product (^{Mes}PDP^{Ph})V≡N(Cl) from metathesis of the X type ligands with silicon.

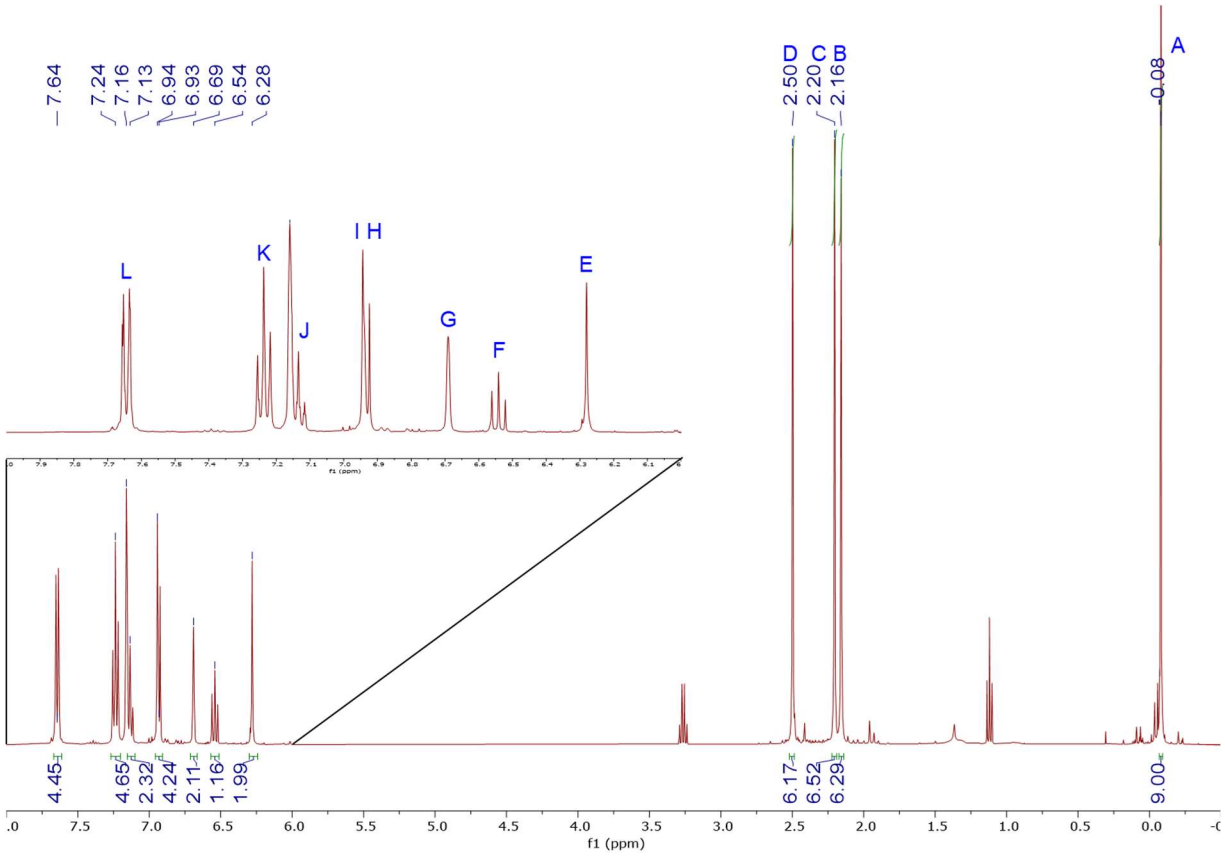

Figure 3.15: ^{1}H NMR spectrum of (^{Mes}PDP^{Ph})V(NTMS)(N_3) in benzene-d_6, where the region between δ 7.0 - 6.0 ppm is expanded for clarity. Peak assignments are notated in blue.

The aromatic region of the spectrum has a few regions of overlap, where the integrations had to be taken together between two signals (H/I, J/C_6D_6). The signals at δ 7.64 (L, dt, 4H), 7.24 (K, tt, 4H), and 7.13 (J, tt, 2H) ppm have obvious coupling (J = ~ 7.5, 1.5 Hz) which, taken with their integrations, lead to their assignment to the back phenyl groups on the PDP ligand. This was reconfirmed with 2D COSY NMR spectroscopy, as well as the relationships of the remaining peaks in the aromatic region (Figure 3.16).

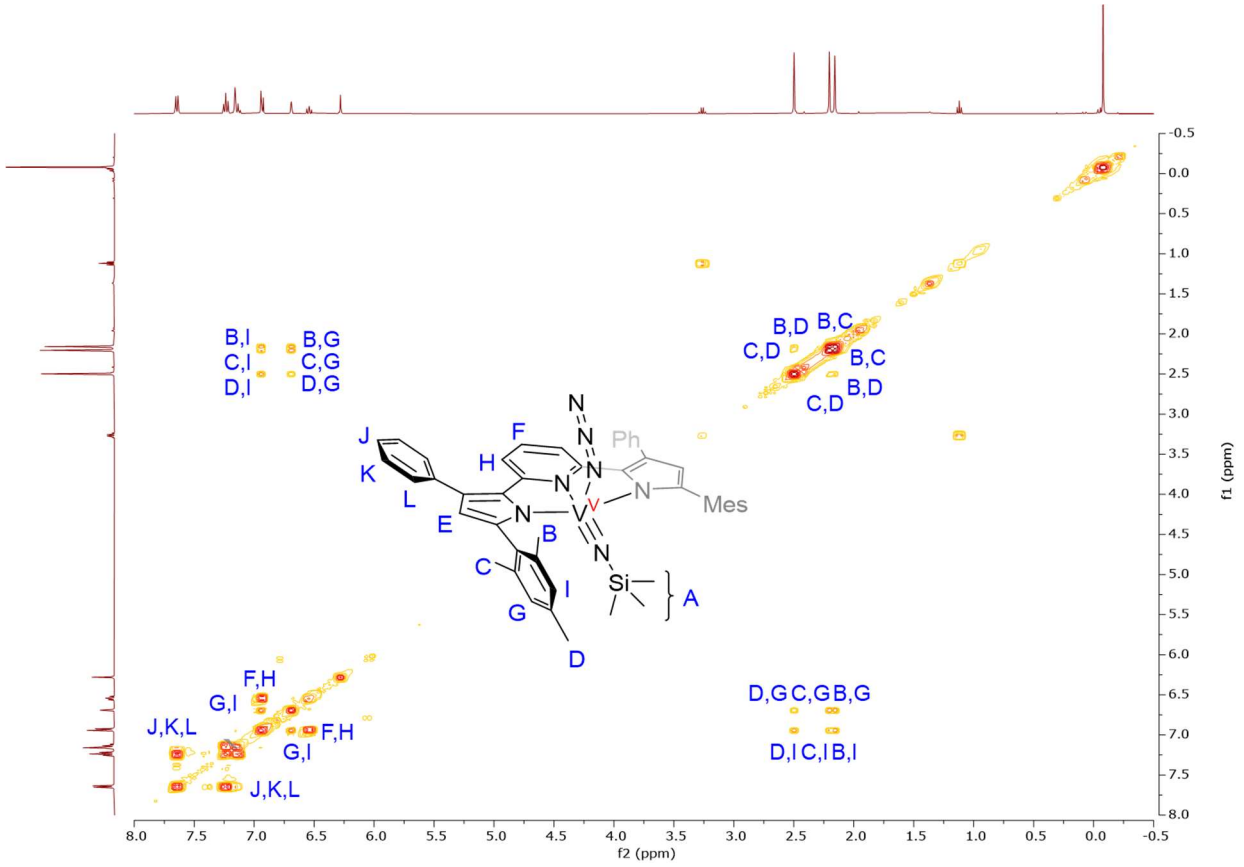

Figure 3.16: (HH) COSY NMR spectrum of [(^{Mes}PDP^{Ph})V(NTMS)(N_3) in benzene-d_6, where coupled signals on the off-diagonal are labelled according to the inset structure, consistent with those in Figure 3.15.

Weak 4J coupling between benzylic signals B/C/D with aromatic signals I and G allowed for the confident assignment of the chemically distinct mesitylene aryl protons, I and G. Further, coupling of F (t, 1H) to H elucidated this signal as a doublet in the absence of reliable integration, where these signals correlate to the backbone of the central pyridine moiety. The lack of coupling to E (s, 2H) leads to the assignment of this as the 3-pyrrolide proton, completing the assignment of the aromatic region.

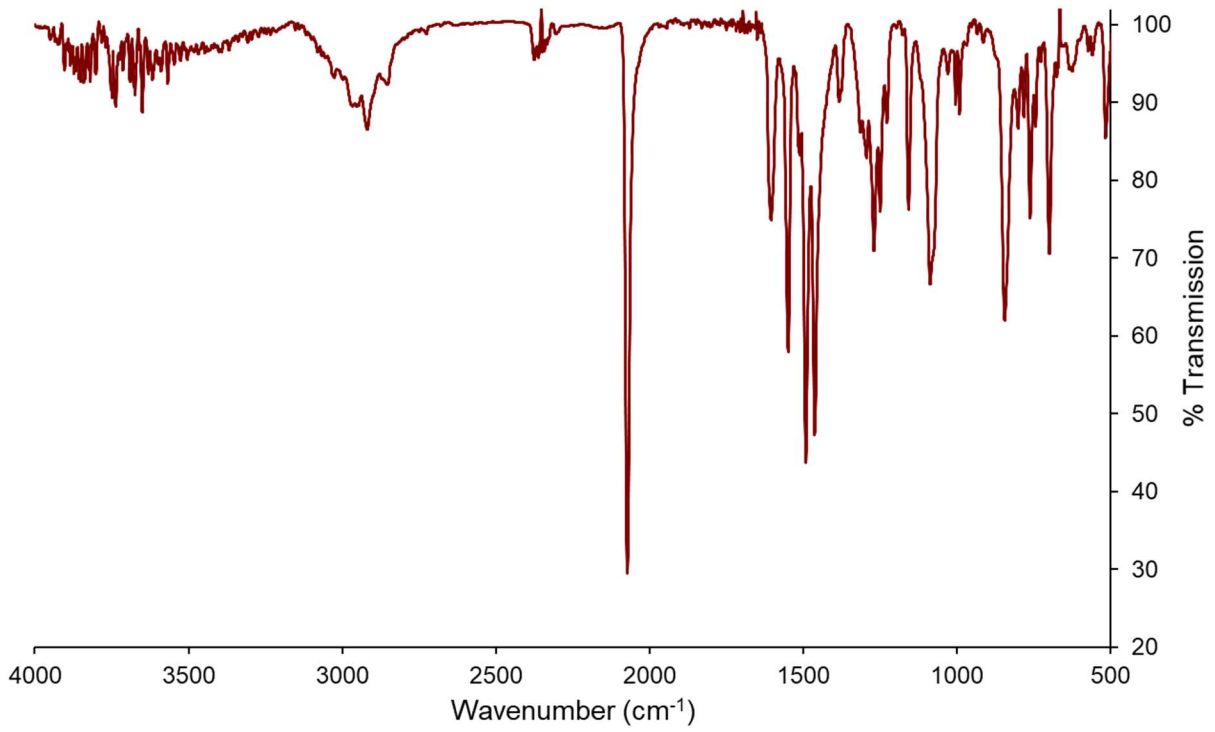

Figure 3.17: Infrared spectrum of (^{Mes}PDP^{Ph})V(NTMS)(N_3) in KBr matrix.

Infrared spectroscopy in pelleted KBr was performed to confirm the presence of the azide moiety, which appeared at 2073 cm^{-1}. From this, we can infer there is basically no change in the asymmetric stretching mode of the azide moiety, as there is no shift in energy from the parent compound. Unfortunately, the stretching frequencies for reported several vanadium imido complexes[21–23] fall around 1500 cm^{-1}, which is obscured by a handful of bands intrinsic to the PDP ligand, and therefore can not be confidently assigned.

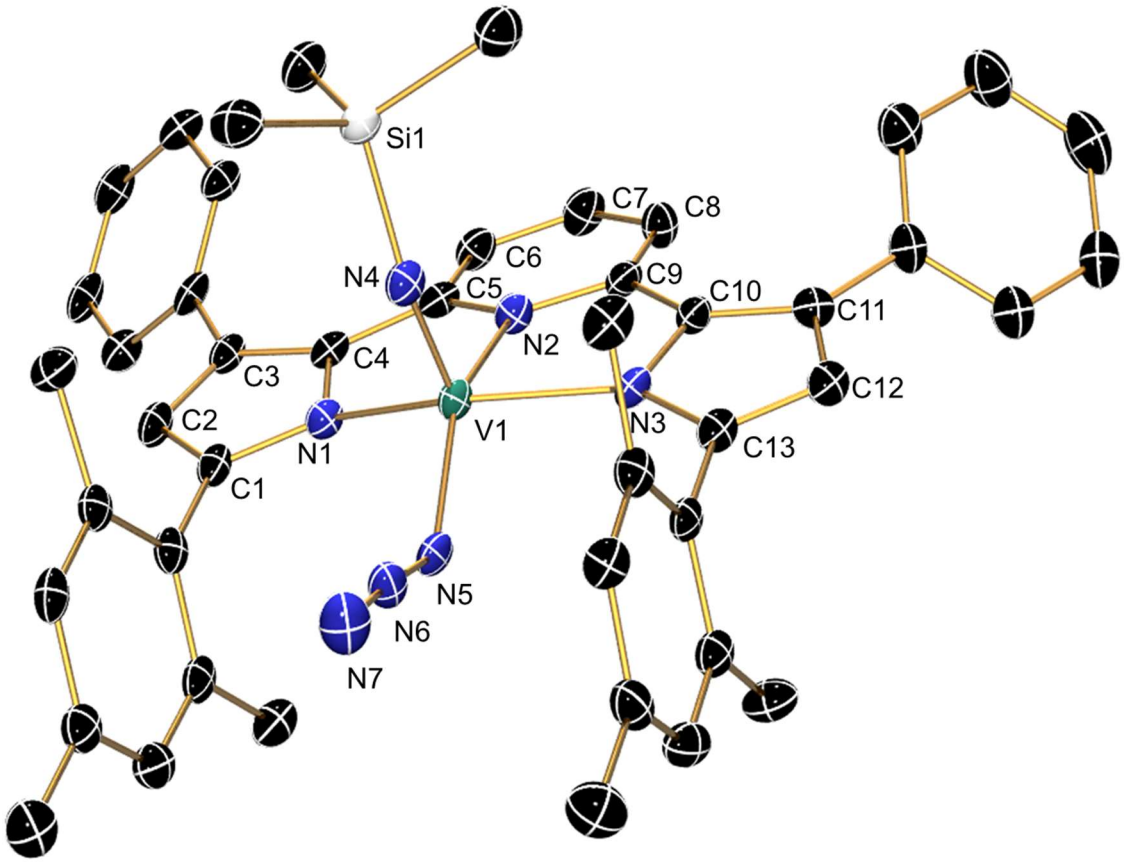

Figure 3.18: ORTEP generated crystal structure of (^{Mes}PDP^{Ph})V(NTMS)(N_3) displayed at 50% probability. Hydrogen atoms and co-crystallized solvent are excluded for clarity.

The structure of this compound was again verified by X-ray crystallography. The neutral V^V complex crystallized from vapor diffusion of pentane into concentrated toluene at -45 ˚C in a triclinic $P\bar{1}$ cell, concurrent with a molecule of toluene in the asymmetric unit. Curiously, the azide is oriented parallel to the equatorial plane, as opposed to pointed down and away from the imido moiety. This orientation was observed in the case of the nitride complex (Figure 3.12), however, the relevance of this observation is yet unclear. The bond lengths of the PDP backbone as well as the vanadium-nitrogen bonds were compared (Table 3.4) between these two species to identify any structural rearrangement outside of the expected conversion from terminal nitride to the TMS-imido moiety.

Table 3.4: Structural comparison of [(^{Mes}PDP^{Ph})VN(N_3)] and (^{Mes}PDP^{Ph})V(NTMS)(N_3). *a*, atom positions symmetry generated via the relationship (+x, 3/2–y, +z).

length (Å)	[(^{Mes}PDP^{Ph})VN(N_3))]$^-$	(^{Mes}PDP^{Ph})V(NTMS)(N_3))
V1≡N	1.615(4)	1.637(5)
N4-Si1	—	1.771(5)
V1-Nα	1.926(10)	1.864(5)
Nα-Nβ	1.245(12)	1.236(6)
Nβ-Nγ	1.137(12)	1.128(6)
V1-N1	2.030(3)	2.023(4)
V1-N2	2.027(6)	2.097(4)
V1-N3	2.030(3)*a*	2.020(5)
N1-C1	1.353(5)	1.373(7)
C1-C2	1.371(6)	1.379(8)
C2-C3	1.393(6)	1.403(8)
C3-C4	1.374(6)	1.386(8)
N1-C4	1.373(6)	1.395(7)
C4-C5	1.426(6)	1.440(8)
N2-C5	1.349(5)	1.366(7)
C5-C6	1.376(6)	1.398(7)
C6-C7	1.376(5)	1.386(8)
C7-C8	1.376(5)*a*	1.392(8)
C8-C9	1.376(6)*a*	1.402(7)
N2-C9	1.349(5)*a*	1.344(7)
C9-C10	1.426(6)*a*	1.450(7)
N3-C10	1.373(6)*a*	1.390(7)
C10-C11	1.374(6)*a*	1.394(8)
C11-C12	1.393(6)*a*	1.410(7)
C12-C13	1.371(6)*a*	1.372(8)
N3-C13	1.353(5)*a*	1.380(7)

The elongation (1.615(4) to 1.637(5)) of the vanadium-nitrogen bond associated with the transition from nitride to imido was anticipated, where silicon is drawing electron density from the V-N triple bond. The V-N-Si angle, 157.2(3)˚, is deviated from a formally sp^2 hybridized imido nitrogen (120˚). However, a linear orientation is more common in early metal imido species[24] such as these due to the electron deficiency proceeding the oxo wall. This deviation from linearity suggests some retention of triple bond character with other substantial electronic contributions to the metal center, lessening the V-N bond order from three. Further characterization, as well as a more detailed discussion of the electronic structure of the imido moiety, will follow in Chapter 4 among related compounds.

The isolation of this species following the nucleophilic addition of a pincer supported vanadium nitride to trimethylsilyl chloride constitutes an interesting deviation from the current literature, where lower coordination numbers are preferred in order to promote these reactions. This exciting result inspired a handful of further experiments with electrophiles such as methyl iodide, methyl triflate, benzyl bromide, and sterically encumbered proton donors such as lutidinium ions. However, these reactions were unclean, with no definable products. We assume this is due to the sensitivity of our deprotonated ligand to acidic and alkylating conditions, leading to decomposition of starting materials as well as intermediates and potential products.

However, because silylation of our nitride proceeded smoothly, we moved on to investigate steps toward the production of silylamines, as discussed earlier in this Chapter. This led to the addition of reducing agents to (^{Mes}PDP^{Ph})V(NTMS)(N_3) as a first foray into this field.

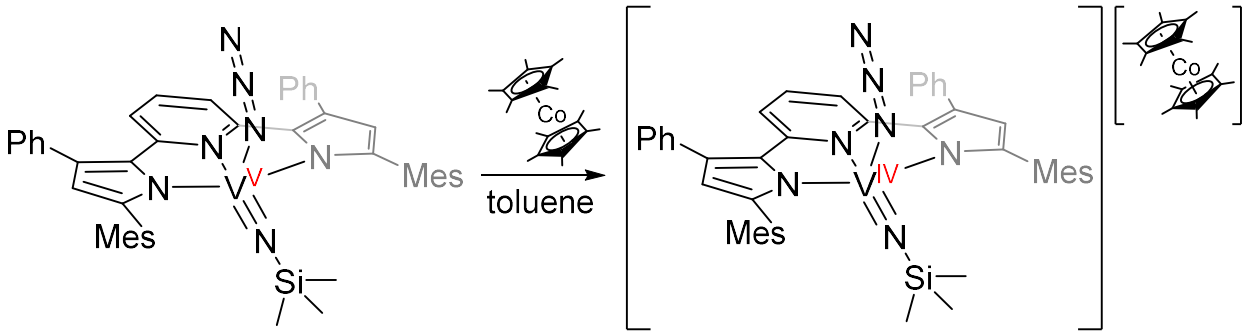

Scheme 3.5: Reduction of (^{Mes}PDP^{Ph})V(NTMS)(N_3) with Co(Cp*)$_2$.

Independently prepared solutions of (^{Mes}PDP^{Ph})V(NTMS)(N_3) and decamethylcobaltocene in toluene were added together at room temperature. Due to the intense coloration of both solutions, no immediate or obvious change was observed. To ensure complete conversion, the reaction was stirred overnight at room temperature. Due to the paramagnetism of the resulting product, NMR spectroscopy could not confirm the structure. However, single crystals were grown from vapor diffusion of pentane into tetrahydrofuran at -45 ˚C.

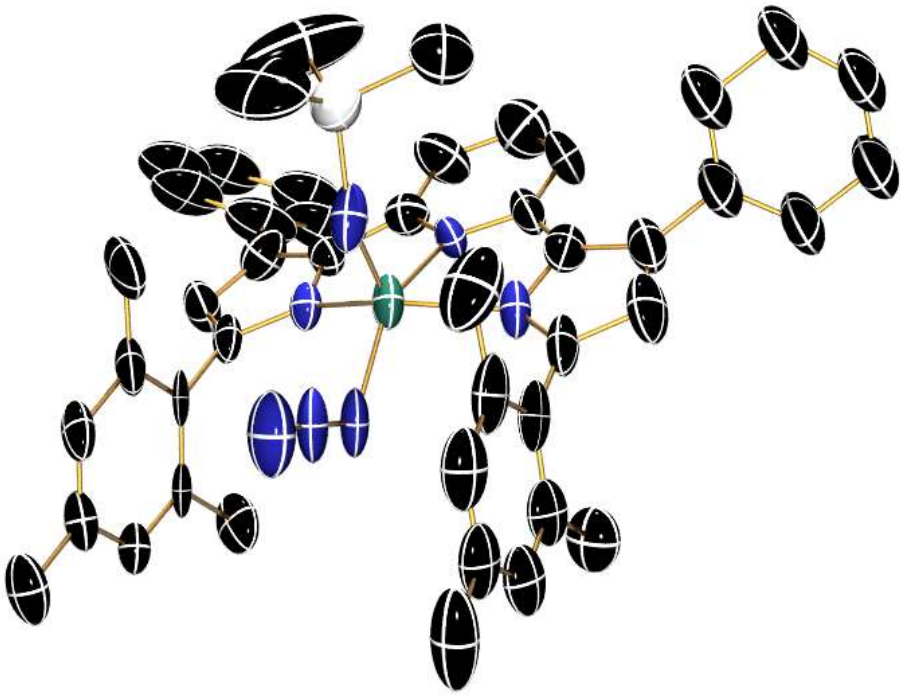

Figure 3.19: ORTEP generated crystal structure of [(^{Mes}PDP^{Ph})V(NTMS)(N_3)][Co(Cp*)$_2$] displayed at 50% probability. Hydrogen atoms, cobaltocenium counterion, disordered azide and phenyl fragments are excluded for clarity.

The resolution of the structure is less than publishable, with a maximum resolution of 2θ = 46.6˚ (0.9 Å). Further, refinement of the model has been insufficient to draw absolute conclusions. The contact ion pair resolved in a monoclinic C2/c cell with an equivalent of decamethylcobaltocenium disordered over a special position, as well as disorder in the azide ligand, back phenyl substituents of the PDP ligand, with large ellipsoids for the silyl bound methyl groups that could not be modelled over multiple positions. While the V-N_{imido} bond does appear to be elongated with respect to the starting material, (^{Mes}PDP^{Ph})V(NTMS)(N_3), these data are not reliable enough to quantify to this expansion. The connectivity of this molecule, however, as well as the evident paramagnetism, gives evidence to the successful reduction of the neutral species, indicating a first step toward the sequential silylation/reduction of a molecular terminal vanadium nitride.

3.5 Conclusions

Salt metathesis of the previously characterized trivalent ($^{Mes}PDP^{Ph}$)VCl(thf)$_2$ complex with sodium azide in the presence of 18-crown-6 yields the bis-azide salt, [Na(18-crown-6)][($^{Mes}PDP^{Ph}$)V(N$_3$)$_2$(thf)]. In the absence of NMR data, this paramagnetic species was characterized thoroughly by X-ray crystallography, infrared spectroscopy, and UV-vis spectroscopy before thermolysis at 120 ˚C, yielding the diamagnetic product [Na(18-crown-6)][($^{Mes}PDP^{Ph}$)VN(N$_3$)]. This mixed nitride/azide was amendable to NMR characterization, as well as X-ray, UV-vis, IR, and computational modelling. This species displayed a rather long terminal nitride bond (1.615 Å) compared to the literature examples (1.565 - 1.591 Å)[21,22,25–30] discussed in Chapter 1, though much shorter than reported imido species (1.614 - 1.688 Å)[20,21,23,31,32] of the formula V≡N-R, where R is a halide or organic alkyl fragment.

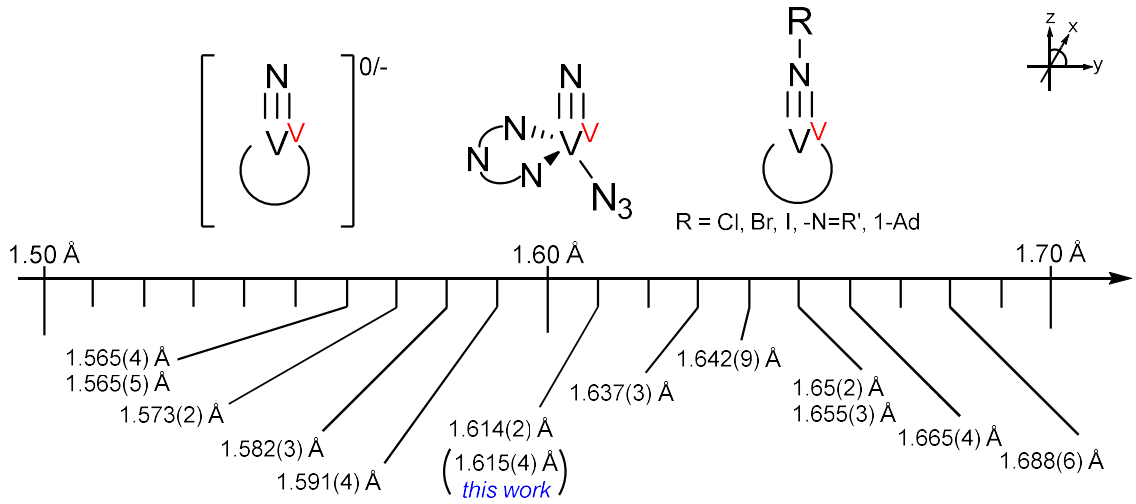

Figure 3.20: Comparison of literature reported V-N multiple bond lengths.

Further, this work demonstrated an example of a pincer supported vanadium nitride, in contrast to the pseudo-tetrahedral orientation put forward the current literature. While our complex is not coordinatively saturated, the meridional coordination of the pincer excludes the four-coordinate environment that has been posited to mitigate the *trans*- stabilization and deactivation of the

nitrido moiety towards electrophiles. Our species would be best described as a trigonal bipyramidal structure turned on its side, where the pyrrolide ligands are in the "apical" positions.

Following this characterization, [(^{Mes}PDP^{Ph})VN(N_3)] was subjected to a host of electrophiles. Only trimethylsilyl chloride was successfully added to the terminal nitride due to the sensitivity of the PDP^{2-} ligand to protonation/alkylation. The success of this electrophile is likely due to its steric bulk, rending it incapable of attack at the inner coordination sphere of the vanadium ion. The product of this reaction, the neutral diamagnetic vanadium imido complex (^{Mes}PDP^{Ph})V(NTMS)(N_3), was characterized by the same methods as the starting material. To probe this species as a step towards the production of silylamines, a target for the synthesis of ammonia and other nitrogen containing materials, (^{Mes}PDP^{Ph})V(NTMS)(N_3) was subjected to an equivalent of decamethylcobaltocene, reducing the imido by one electron. The paramagnetic isolable salt, [Co(Cp*)$_2$][(^{Mes}PDP^{Ph})V(NTMS)(N_3)], constitutes the first step towards this reactivity.

3.6 Experimental Procedures

General Considerations. All air- and moisture-sensitive manipulations were carried out using standard Schlenk line and cannula techniques or in an MBraun inert atmosphere drybox containing an atmosphere of purified nitrogen. Solvents for air- and moisture- sensitive manipulations were dried and deoxygenated using a Glass Contour Solvent Purification System and stored over 4 Å molecular sieves. All solids were dried under high vacuum in oven-dried glassware in order to bring into the glovebox. Deuterated benzene (C_6D_6) for NMR spectroscopy was distilled from sodium. Deuterated methylene chloride (CD_2Cl_2) for NMR spectroscopy was distilled from CaH_2. All solids that were prepared in outside of the box were dried under high vacuum in oven-dried glassware before use in inert atmosphere. Metal halides were purchased and used without further purification.

Physical and Computational Measurements. Nuclear magnetic resonance (NMR) experiments were performed at 400 MHz on a 400-MR DD2 Agilent instrument. All chemical shifts are reported relative to tetramethylsilane with residual solvent proton signal as a secondary standard. Deuterated benzene was distilled from sodium metal and stored over 4 Å molecular sieves. Deuterated methylene chloride was distilled from CaH_2 and stored of 4 Å molecular sieves. Splitting in ^1H NMR studies is notated by: s = singlet, d = doublet, t = triplet, sept = septet, b = broad, m = multiplet or combinations thereof.

Single crystals were prepared for X-ray diffraction in the glovebox by coating with previously degassed polyisobutylene oil (Sigma-Aldrich). These were then picked with a nylon loop (MiTeGen) and mounted to the goniometer head of a Bruker AXS D8 Venture fixed-chi X-ray diffractometer in a cold stream of dry nitrogen. The instrument features a Triumph

monochromator, a Mo Kα radiation source (λ = 0.71073 Å), and a PHOTON 100 CMOS detector. Utilizing the APEX3[33] software package, data was collected, processed with SAINT+, and subjected to absorption correction via SADABS/TWINABS. The space group were determined with XPREP and solved using intrinsic phasing (SHELXL[34]) before refinement with Olex2.[35] Structures are represented at 50% probability thermal ellipsoids via ORTEP-3.

Cyclic voltammetry was recorded under nitrogen atmosphere in anhydrous tetrahydrofuran using NBu_4PF_6 as an electrolyte and referenced to ferrocene/ferrocenium$^+$. Set up included a Gamry Interface 1000 electrochemical workstation in a single compartment cell utilizing a three-electrode system: a glassy carbon working electrode, platinum sheet as the counter electrode, and coiled silver wire as a quasi-reference electrode. All spectra were taken at a rate of 200 mVs^{-1} in 5 mV steps unless otherwise indicated.

UV-visible and emission spectra were acquired via Shimadzu UV-1800 spectrophotometer and RF-5301 PC spectrofluorophotometer, respectively. Samples were prepared in the glove box under nitrogen in either dry benzene or tetrahydrofuran in J-Young adapted quartz cuvettes.

Density functional theory (DFT) and time-dependent density functional theory (TD-DFT) calculations were performed with the ORCA[36,37] program package. Each were carried out at the B3LYP level of theory. Calculated orbitals were plotted using the program Gabedit.[38]

Safety Considerations. Azides are known to be toxic, energetic materials which can decompose violently under pressure, at high temperature, or when irradiated with light. While no incidents occurred during the course of this work, all manipulations involving sodium azide and azide containing products were carried out under nitrogen in the glovebox. Controlled decomposition of

azide moieties (via thermolysis or photolysis) were performed under nitrogen in sealed Schlenk tubes behind a blast shield.

[Na(18-crown-6)][(^{Mes}PDP^{Ph})V(N_3)$_2$(thf)] – In the glovebox, a 20 mL scintillation vial was charged with 36 mg (0.55 mmol) of NaN_3, 33 mg (0.12 mmol) of 18-crown-6, 95 mg (0.11 mmol) of (^{Mes}PDP^{Ph})VCl(thf)$_2$, and a magnetic stirrer. The mixture of solids was taken in THF and stirred overnight at room temperature. The reaction mixture was then filtered through a pipet packed with a microfiber glass wool plug and Celite to remove excess sodium azide and precipitated sodium chloride. The solution was reduced to dryness, triturated successively with toluene and pentane. Preparative recrystallization was carried out by layering pentane on a concentrated solution of THF at -38 °C, giving long, flexible plate crystals. The mother liquor was dried, reconstituted in THF, and layered with pentane to crystallize any remaining product. Combined yield: 107 mg (0.11 mmol, 91%). μ_{eff} = 2.56 μ_B. ^{1}H NMR (400 MHz, C_6D_6): δ 30.43, 17.88, 16.19, 9.04, 8.58, 8.02, 6.20, 5.96, 4.96, 4.66, 3.04, 2.67, 2.29, 1.67, -9.57, -31.20, -36.46. IR (KBr, -N_3): ῡ 2080 cm^{-1}, 2050 cm^{-1}. Crystals suitable for X-ray diffraction were prepared from vapor diffusion of pentane into solutions of either toluene or tetrahydrofuran, resulting in distinct crystalline morphologies.

[Na(18-crown-6)][(^{Mes}PDP^{Ph})VN(N_3)] – In the glovebox, a Schlenk tube was charged with 54 mg (0.05 mmol) of the previously prepared bis-azide salt in a minimum amount of THF. Toluene was added in a quantity at least three times the volume of the THF solution. The solution was sealed under nitrogen, moved to an oil bath at 120 °C, and refluxed overnight. After cooling to room temperature, the tube was returned to the box and opened under an atmosphere of dry nitrogen. The reaction mixture was filtered with Celite and reduced to dryness, then triturated with pentane

to remove residual toluene. The bright red solids were taken in THF and layered with pentane at -30 ˚C to yield 45 mg (0.05 mmol, 85%) pure material. ^{1}H NMR (400 MHz, CD_2Cl_2): δ 7.61 (dt, 4H, *ortho*- phenyl H, J = 7.0 Hz, 1.3 Hz) 7.39 (tt, 4H, *meta*- phenyl H, J = 7.5 Hz, 1.7 Hz), 7.26 (tt, 2H, *para*- phenyl H, J = 7.4 Hz, 1.2 Hz), 7.13 (t, 1H, *para*- pyridine, J = 8.0 Hz), 6.92 (d, 2H, *meta*- pyridine, J = 7.9 Hz), 6.89 (s, 2H, *meta*- mesityl H), 6.86 (s, 2H, *meta*- mesityl H), 6.08 (s, 2H, pyrrole H), 3.54 (s, 24H, 18-crown-6), 2.39 (s, 6H, mesityl -CH_3), 2.28 (s, 6H, mesityl -CH_3), 1.99 (s, 6H, mesityl -CH_3). ^{13}C{^{1}H} NMR (100 MHz, CD_2Cl_2): δ 155.71, 147.50, 139.53, 139.18, 138.95, 138.40, 136.36, 133.63, 129.80, 128.47, 128.34, 127.71, 127.31, 125.91, 114.18, 110.22, 69.04, 21.55, 21.31, 20.70. IR (KBr, -N_3, V≡N): ῡ 2075, 1108 cm^{-1}. Crystals suitable for X-ray diffraction were prepared from vapor diffusion of pentane into solutions of either toluene or tetrahydrofuran, resulting in distinct crystalline morphologies.

(^{Mes}PDP^{Ph})V(NTMS)(N_3) – In the glovebox, a Schlenk tube was charged with 97 mg (0.10 mmol) of [Na(18-crown-6)][(^{Mes}PDP^{Ph})VN(N_3)] and dissolved in toluene. To this was added 25 μL (0.20 mmol) of trimethylsilyl chloride. The reaction mixture was sealed under dinitrogen and refluxed at 120 ˚C overnight. The resulting dark red solution was reduced to dryness and triturated with pentane to remove residual toluene. The solids were taken in diethyl ether, filtered with Celite, and reduced to dryness under vacuum, yielding 70 mg (0.09 mmol, 95%) of dark red powder. ^{1}H NMR (400 MHz, C_6D_6): δ 7.64 (dt, 4H, *ortho*- phenyl H, J = 7.5 Hz, 1.5 Hz), 7.24 (tt, 4H, *meta*- phenyl H, J = 7.5 Hz, 1.5 Hz), 7.13 (tt, 2H, *para*- phenyl H, J = 7.5 Hz, 1.5 Hz), 6.94 (s, 2H, *meta*- mesityl H), 6.93 (d, 2H, *meta*- pyridine H), 6.69 (s, 2H, *meta*- mesityl H), 6.54 (t, 1H, *para*-pyridine H), 6.28 (s, 2H, pyrrole H), 2.50 (s, 6H, mesityl -CH_3), 2.20 (s, 6H, mesityl -CH_3), 2.16 (s, 6H, mesityl -CH_3), -0.08 (s, 9H, TMS -CH_3). ^{13}C{^{1}H} NMR (100 MHz, C_6D_6): δ 154.57, 147.34, 140.85,

138.25, 137.29, 137.18, 136.88, 134.72, 129.31, 128.36, 128.00, 126.60, 115.35, 110.83, 21.55, 20.80, 20.46, 0.18. IR (KBr, $-N_3$): ῡ 2073 cm^{-1} Crystals suitable for X-ray diffraction were grown from vapor diffusion of pentane into toluene.

[(^{Mes}PDP^{Ph})V(NTMS)(N_3)][Co(Cp^*)$_2$] – In the glovebox, a 20 mL scintillation vial was charged with 18 mg (0.02 mmol) of (^{Mes}PDP^{Ph})V(NTMS)(N_3) and 10 mg (0.03 mmol) of decamethylcobaltocene. The mixture was dissolved in toluene and stirred overnight at room temperature. The reaction solution was reduced to dryness under vacuum and washed with pentane to remove residual decamethylcobaltocene. The reside was then reconstituted in tetrahydrofuran and filtered with Celite. The product was isolated (20 mg, 0.02 mmol, 80%) by vapor diffusion of pentane into this solution at -45 ˚C, which gave crystals suitable for X-ray diffraction.

3.7 References

(1) Lerner, H.-W. Supersilyl Ammonia and Supersilyl Hydrazine: Sythesis, Structure, and Properties. *Zeitschrift fur Naturforsch.* **2015**, *46*, 1.

(2) Grant, L. N.; Pinter, B.; Kurogi, T.; Carroll, M. E.; Wu, G.; Manor, B. C.; Carroll, P. J.; Mindiola, D. J. Molecular Titanium Nitrides: Nucleophiles Unleashed. *Chem. Sci.* **2017**, *8* (2), 1209–1224. https://doi.org/10.1039/C6SC03422E.

(3) Yandulov, D. V.; Schrock, R. R. Catalytic Reduction of Dinitrogen to Ammonia at a Single Molybedum Center. *Science* **2003**, *301* (July), 76–79. https://doi.org/10.1126/science.1085326.

(4) Schrock, R. R. Catalytic Reduction of Dinitrogen to Ammonia by Molybdenum: Theory versus Experiment. *Angew. Chemie Int. Ed.* **2008**, *47* (30), 5512–5522. https://doi.org/10.1002/anie.200705246.

(5) Yandulov, D. V.; Schrock, R. R.; Rheingold, A. L.; Ceccarelli, C.; Davis, W. M. Synthesis and Reactions of Molybdenum Triamidoamine Complexes Containing Hexaisopropylterphenyl Substituents. *Inorg. Chem* **2003**, *42*, 796–813. https://doi.org/10.1021/ic0205051.

(6) Wickramasinghe, L. A.; Ogawa, T.; Schrock, R. R.; Müller, P. Reduction of Dinitrogen to Ammonia Catalyzed by Molybdenum Diamido Complexes. *J. Am. Chem. Soc.* **2017**, *139* (27), 9132–9135. https://doi.org/10.1021/jacs.7b04800.

(7) K. Hickey, A.; A. Wickramasinghe, L.; R. Schrock, R.; Tsay, C.; Müller, P. Protonation Studies of Molybdenum(VI) Nitride Complexes That Contain the [2,6-(ArNCH2)2NC5H3]2– Ligand (Ar = 2,6-Diisopropylphenyl). *Inorg. Chem.* **2019**, *58* (6), 3724–3731. https://doi.org/10.1021/acs.inorgchem.8b03346.

(8) Wang, D.; Loose, F.; Chirik, P. J.; Knowles, R. R. N-H Bond Formation in a Manganese(V) Nitride Yields Ammonia by Light-Driven Proton-Coupled Electron Transfer. *J. Am. Chem. Soc.* **2019**, *141* (12), 4795–4799. https://doi.org/10.1021/jacs.8b12957.

(9) Zhang, S.; Zhao, Y.; Shi, R.; Waterhouse, G. I. N.; Zhang, T. Photocatalytic Ammonia Synthesis: Recent Progress and Future. *EnergyChem* **2019**, *1* (2), 100013. https://doi.org/10.1016/j.enchem.2019.100013.

(10) Li, M.; Huang, H.; Low, J.; Gao, C.; Long, R.; Xiong, Y. Recent Progress on Electrocatalyst and Photocatalyst Design for Nitrogen Reduction. *Small Methods* **2019**, *3* (6). https://doi.org/10.1002/smtd.201800388.

(11) Curley, J. J.; Sceats, E. L.; Cummins, C. C. A Cycle for Organic Nitrile Synthesis via Dinitrogen Cleavage. *J. Am. Chem. Soc.* **2006**, *128* (43), 14036–14037. https://doi.org/10.1021/ja066090a.

(12) MacKay, B. A.; Fryzuk, M. D. Dinitrogen Coordination Chemistry: On the Biomimetic Borderlands. *Chem. Rev.* **2004**, *104* (2), 385–401. https://doi.org/10.1021/cr020610c.

(13) Bezdek, M. J.; Chirik, P. J.; Eizawa, A.; Grund, K.; Holland, P. L.; Hou, Z.; Ishida, Y.; Kawaguchi, H.; Kindjajev, A.; Klopsch, I.; Kuriyama, S.; Nishibayashi, Y.; Pappas, I.; Pfeil, M.; Schneider, S.; Shima, T.; Speelman, A. L.; Stucke, N.; Tanaka, H.; Tuczek, F.; Weyrich, T.; Yoshizawa, K.; Yuzick-Klimova, E. Y. *Topics in Organometallic Chemistry - Nitrogen Fixation*; Nishibayashi, Y., Ed.; Springer International Publishing, 2017.

(14) Maclachlan, E. A.; Fryzuk, M. D. Synthesis and Reactivity of Side-On-Bound Dinitrogen Metal Complexes. *Organometallics* **2006**, *25* (7), 1530–1543. https://doi.org/10.1021/om051055i.

(15) Odom, A. L.; McDaniel, T. J. Titanium-Catalyzed Multicomponent Couplings: Efficient

One-Pot Syntheses of Nitrogen Heterocycles. *Acc. Chem. Res.* **2015**, *48* (11), 2822–2833. https://doi.org/10.1021/acs.accounts.5b00280.

(16) Zhang, Y.; Lee, T. S.; Petersen, J. L.; Milsmann, C. A Zirconium Photosensitizer with a Long-Lived Excited State: Mechanistic Insight into Photoinduced Single-Electron Transfer. *J. Am. Chem. Soc.* **2018**, *140* (18), 5934–5947. https://doi.org/10.1021/jacs.8b00742.

(17) Hakey, B. M.; Darmon, J. M.; Zhang, Y.; Petersen, J. L.; Milsmann, C. Synthesis and Electronic Structure of Neutral Square-Planar High-Spin Iron(II) Complexes Supported by a Dianionic Pincer Ligand. *Inorg. Chem.* **2019**, *58* (2), 1252–1266. https://doi.org/10.1021/acs.inorgchem.8b02730.

(18) Evans, D. F. The Determination of the Paramagnetic Susceptibility of Substances in Solution by Nuclear Magnetic Resonance. *J. Chem. Soc.* **1959**, No. 0, 2003–2005. https://doi.org/10.1039/jr9590002003.

(19) Fraser, M. T. R. Sodium Azide as an Internal Standard for Quantitative Infrared Analysis. *Anal. Chem.* **1959**, *31* (9), 1602–1603.

(20) Dehnicke, K.; Strähle, J. The Transition Metal-Nitrogen Multiple Bond. *Angew. Chemie Int. Ed. English* **1981**, *20* (3), 413–486.

(21) Song, J. I.; Gambarotta, S. Preparation, Characterization, and Reactivity of a Diamagnetic Vanadium Nitride. *Angew. Chemie - Int. Ed. English* **1996**, *35* (19), 1258–1263.

(22) Critchlow, S. C.; Lerchen, M. E.; Smith, R. C.; Doherty, N. M. Vanadium Nitride Linear Chain Polymers and Monomers. Synthesis and Structures of [V(μ-N)Cl2(Py)2]∞ and V(N)Cl2(Quin)2. *J. Am. Chem. Soc.* **1988**, *110* (24), 8071–8075. https://doi.org/10.1021/ja00232a019.

(23) Scherfise, K. D.; Dehnicke, K. Nitridokomplexe von Vanadium(V): [VNCl3]- Und

VNCl2(Dipy). *Zeitschrift fur Anorg. und Allg. Chemie* **1986**, *538*, 119–122.

(24) Eikey, R. A.; Abu-Omar, M. M. Nitrido and Imido Transition Metal Complexes of Groups 6-8. *Coord. Chem. Rev.* **2003**, *243* (1–2), 83–124. https://doi.org/10.1016/S0010-8545(03)00048-1.

(25) Tran, B. L.; Krzystek, J.; Ozarowski, A.; Chen, C. H.; Pink, M.; Karty, J. A.; Telser, J.; Meyer, K.; Mindiola, D. J. Formation and Reactivity of the Terminal Vanadium Nitride Functionality. *Eur. J. Inorg. Chem.* **2013**, No. 22–23, 3916–3929. https://doi.org/10.1002/ejic.201300178.

(26) Tran, B. L.; Pink, M.; Gao, X.; Park, H.; Mindiola, D. J. Low-Coordinate and Neutral Nitrido Complexes of Vanadium. *J. Am. Chem. Soc.* **2010**, *132* (5), 1458–1459. https://doi.org/10.1021/ja908303k.

(27) Tran, B. L.; Singhal, M.; Park, H.; Lam, O. P.; Pink, M.; Krzystek, J.; Ozarowski, A.; Telser, J.; Meyer, K.; Mindiola, D. J. Reactivity Studies of a Masked Three-Coordinate Vanadium(II) Complex. *Angew. Chemie Int. Ed.* **2010**, *49* (51), 9871–9875. https://doi.org/10.1002/anie.201005029.

(28) Ishida, Y.; Kawaguchi, H. Nitrogen Atom Transfer from a Dinitrogen-Derived Vanadium Nitride Complex to Carbon Monoxide and Isocyanide. *J. Am. Chem. Soc.* **2014**, *136* (49), 16990–16993. https://doi.org/10.1021/ja510317h.

(29) Henderson, R. A.; Janas, Z.; Jerzykiewicz, L. B.; Richards, R. L.; Sobota, P. Vanadium Phenoxide Complexes with Oxide, Nitride or Hydrazide Co-Ligands: Preparation and Crystal Structures of [V(OC6H3Pri2-2,6) 3NLi(C4H8O)3], [{VO2(OC6H3Pri2-2,6) 2}2{μ-Li(C4H8O)2} 2]. *Inorg. Chim. Acta* **1999**, *285* (2), 178–183. https://doi.org/10.1016/s0020-1693(98)00331-4.

(30) Brask, J. K.; Fickes, M. G.; Sangtrirutnugul, P.; Durà-Vilà, V.; Odom, A. L.; Cummins, C. C. Niobium and Vanadium Iminophosphinimide Complexes. *Chem. Commun.* **2001**, *1* (17), 1676–1677. https://doi.org/10.1039/b105584b.

(31) Lorcher, K. P.; Strähle, J.; Walker, I. Das Komplexchemische Verhalten Des Cl3VN-Cl Gegenuber Lewissauren Und -Basen Die Kristallstruktur Der Komplexe Cl3VNCl(SbCl5)2 Und Cl3(Bipy)VNCl. *Zeitschrift fur Anorg. und Allg. Chemie* **1979**, *452*, 123–140.

(32) Nugent, W. A.; Haymore, B. L. Transition Metal Complexes Containing Organoimido (NR) and Related Ligands. *Coord. Chem. Rev.* **1980**, *31* (2), 123–175.

(33) Bruker. *APEX3 User Manual*; 2016.

(34) Sheldrick, G. M. Crystal Structure Refinement with SHELXL. *Acta Crystallogr. Sect. C Struct. Chem.* **2015**, *71* (Md), 3–8. https://doi.org/10.1107/S2053229614024218.

(35) Dolomanov, O. V.; Bourhis, L. J.; Gildea, R. J.; Howard, J. A. K.; Puschmann, H. OLEX2: A Complete Structure Solution, Refinement and Analysis Program. *J. Appl. Cryst.* **2009**, No. 42, 339–341.

(36) Neese, F. The ORCA Program System. *Wiley Interdiscip. Rev. Comput. Mol. Sci.* **2012**, *2* (1), 73–78.

(37) Neese, F. Software Update: The ORCA Program System, Version 4.0. *Wiley Interdiscip. Rev. Comput. Mol. Sci.* **2017**, *8* (1), e1327.

(38) Allouche, A. R. Gabedit - A Graphical User Interface for Computational Chemistry Softwares. *J. Comput. Chem.* **2011**, No. 32, 174–182.

Chapter 4: High Valent Vanadium Imido Species

4.1 Linear Imidos and Diradical Nitrenes

A more common example of metal-nitrogen multiple bonded species than that of bridged and terminal nitrides contain the imido moiety; an *sp* or sp^2 hybridized nitrogen atom with a pendant organic fragment. The formal hybridization of these atoms is often determined by the linear or bent arrangement of their substituents, which is a result of the electronic structure of the metal-nitrogen bond. These imidos are commonly generated via the coordination of primary amines or addition of amine bases to metal halide precursors.[1] They are also accessible by the coordination and decomposition of organic azides, which are readily available by facile syntheses such as S_n2 substitution for alkyl species and $S_{Ar}1$ substitution for aryl substituents.[2] This route allows for more diversity in starting materials, such as ligated metals of a variety of coordination environments.[3–5] The resulting ligand field allows for the tunability of the electronic structure, leading to interesting activity of metal-nitrogen multiple bonds.

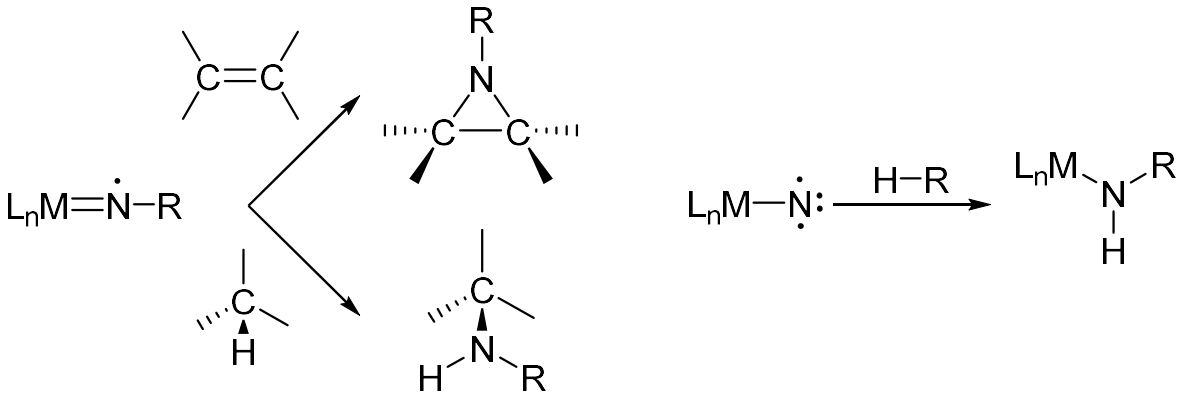

Figure 4.1: Generalized examples of a selection of metal-nitrene reactions.

Azide (N_3^-) and organic azide (RN_3) ligands are of continuing interest for their relatively covalent bonds with metal centers and rich reactivity. Commonly, thermolysis of low valent metal azides and azide adducts yield nitrides and imidos by a concerted two-electron oxidation and

expulsion of N_2. This can also be accomplished via photolysis or the addition of external reductants.[2] The decomposition of the azide moiety can yield a variety of products, and in more rare cases, organic[5] and diradical nitrenes[6,7] (Figure 4.1).

Indeed, the oxidation of low valent metal azides by thermolysis/photolysis goes through a nitrene intermediate. However, in the case of later transition metals, where this oxidation is not always feasible, nitrenes can be directed to do powerful chemical transformations.[3,5–10] This is due primarily to the occupation of lower energy bonding and non-bonding orbitals by d-electrons, weakening the metal-nitrogen π bonds by populating π* orbitals. The asymmetric electronic structure of these systems displays higher levels of nitrogen centered electron density, resulting in electrophilic behaviors. Due to the reactivity of these species, much work has been put into performing limited deactivation of later metal complexes by several methods: Redox active ligands, ligand field manipulation, and steric control of the coordination sphere have been utilized with much success with models of iron[11–16] and cobalt.[17,18]

For example, work in the labs of Chirik[11,12] and Betley[13,14] have demonstrated isolable iron nitrenes utilizing pyridine di-imine (PDI) and dipyrrin ligands, respectively, which are capable of doing desirable transformations such as nitrene transfer and hydrogenation to amine products. While these are valuable studies, a model closer to this work was reported by Caulton and Mindiola[16], where a PDP supported iron-nitrogen multiple bond was characterized.

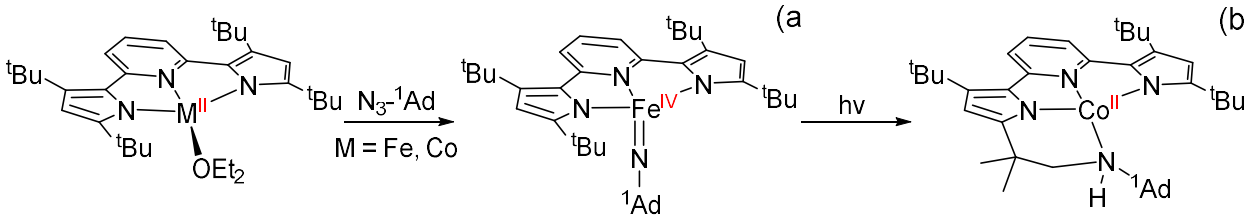

Figure 4.2: a) Isolable PDP-Fe(IV) nitrene, proposed intermediate for analogous cobalt reaction b) Product isolated from these conditions utilizing cobalt starting materials.

Their tertiary butyl substituted ligand arrested ligation in the equatorial plane, leading to a cis-divacant octahedral coordination geometry with a diamagnetic ground state (S = 0) and a formal iron(IV) center (Figure 4.2, a). After an exhaustive characterization of the electronic structure of this species by experimentation and computation, no nitrene chemistry chemistry was reported for this markedly stable species. This was quickly followed by the synthesis of a cobalt analogue of their starting material (Figure 4.2, b), and characterization of the resulting intramolecular nitrene insertion.

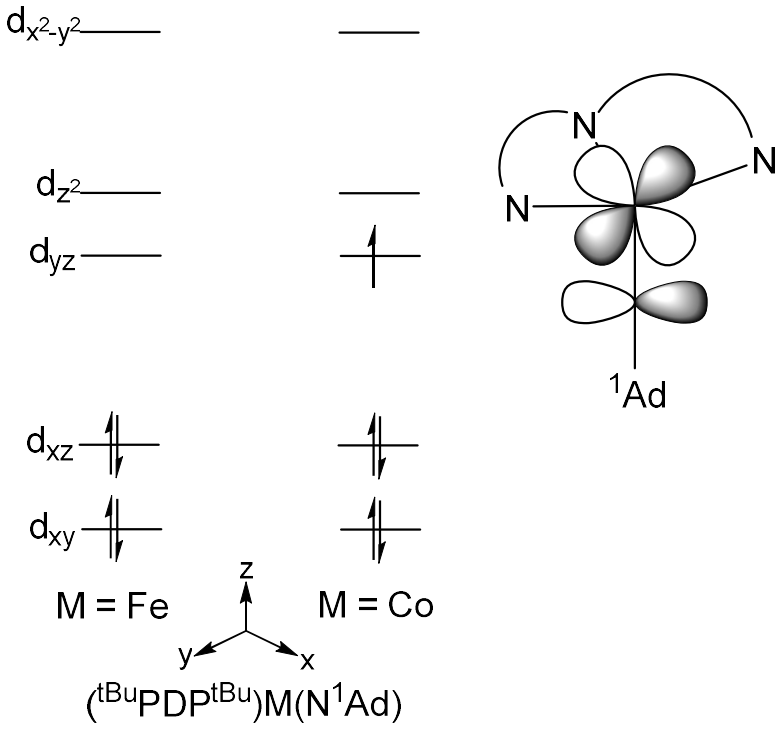

Figure 4.3: Qualitative ligand field splitting diagram to rationalize the difference in activity between iron and cobalt ^{tBu}PDP^{tBu} nitrenes.

The ease of insertion and lack of isolable intermediate is attributed to the electronic configuration of Co^{2+} ([Ar]$4s^0 3d^7$) compared to iron, where cobalt has one more electronic in its valence shell. This allowed for the population of the Co-N π* orbital and access to an electronic structure suitable for C-H insertion. While moving to cobalt was an effective method for the cis-

divalent octahedral ligand field, work in this lab by Dr. Brett Hakey went on to explore other geometries of the Fe(PDP) moiety.

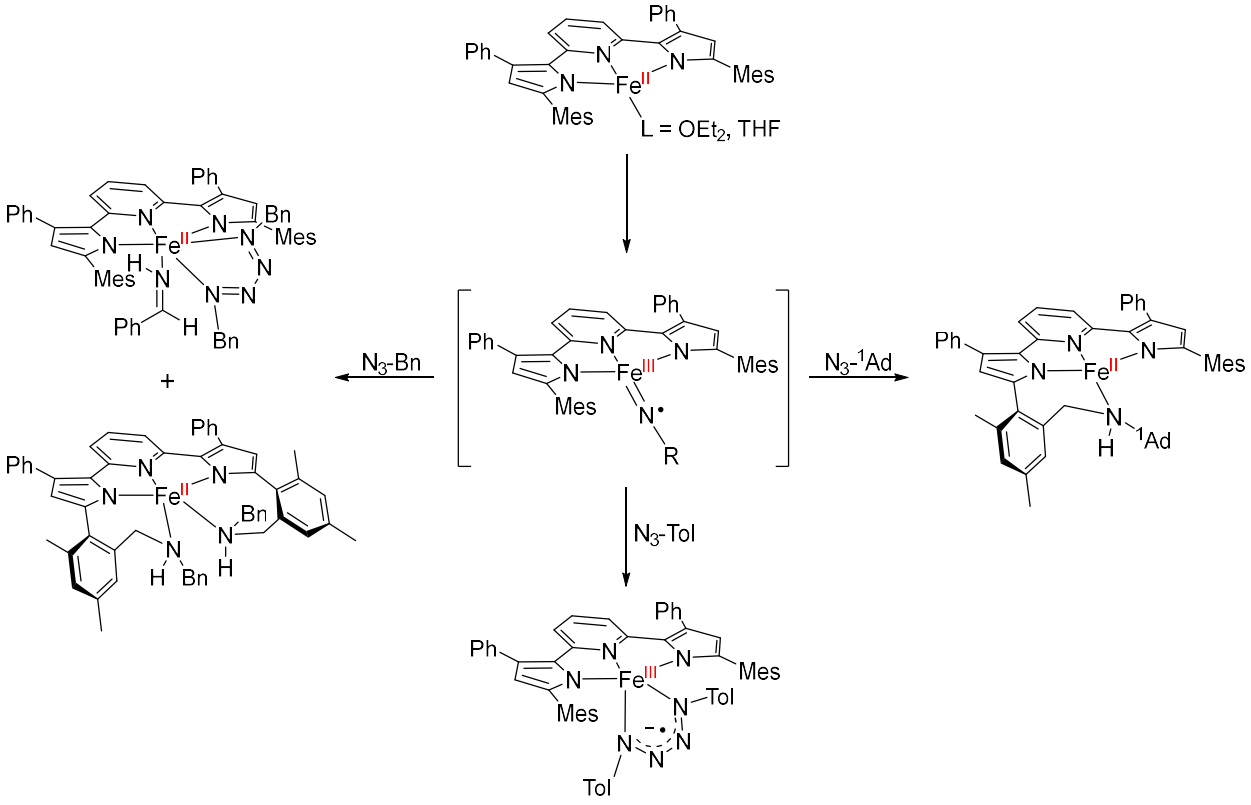

Figure 4.4: Reactions of (^{Mes}PDP^{Ph})Fe(L) with organic azides and their unique products.

By utilizing the 2,4,6-trimethylphenyl substituted PDP ligand, which is utilized in this work, a square planar iron(II) starting material was isolated and characterized. This starting material was amenable to a variety of inter/intra-molecular interactions following the generation of a transient iron nitrene, including nitrene insertion into C-H bonds and [2+3] cycloaddition of the transient nitrene to another equivalent of organic azide. Further, from this active electronic structure, the extent of this reactivity was found to be sterically controlled by the substrate. For example, with 1-adamantyl azide, a single nitrene insertion was the exclusive product, where in the case of aryl substituents such as 4-tolyl azide, tetrazene formation was the sole product. From

this, we infer that the coordination sphere is gated by the mesityl substituents, allowing selective reaction mechanisms.

From these later first row transition metal examples, which utilize steric encumbrance and ligand field effects to tune the activity of metal-nitrogen multiple bonds, we can draw inspiration for nitrene chemistry at early metal sites. As discussed in Chapter 3, where the activation of vanadium nitrogen multiple bonds was the target of that work, it was noted that these bonds are markedly inert under most conditions. This Chapter will focus on the utilization of that stability as a stage for radical nitrene chemistry that is akin to that of late metal species by appending an azide (N_3^-) ligand to the d^0 V≡N-R center. Using organic ligands as a light scavenger to promote the decomposition of the azide, the transient nitrene fragment can be directed in a similar fashion to the of the discussed late metal examples.

From Chapter 3, there are two species that are pursuant to the generation of nitrenes, [(^{Mes}PDP^{Ph})VN(N_3)] and (^{Mes}PDP^{Ph})V(NTMS)(N_3). To further this work, the synthesis and characterization of the 1-adamantyl derivative, (^{Mes}PDP^{Ph})V(N-^{1}Ad)(N_3), will be presented here. This work constitutes the beginnings of this chemistry, relegated to intramolecular activation of the ligand, as well as represents a novel concept where the stability of inorganic fragments can be utilized to do powerful organic transformations in homogeneous solution.

4.2 Synthesis and Characterization of (^{Mes}PDP^{Ph})V≡N-^{1}Ad(N_3)

The 1-adamantyl imido chloride was generated from a trivalent starting material, (^{Mes}PDP^{Ph})VCl(thf)$_2$, via thermolysis with an equivalent of 1-adamantyl azide under dinitrogen atmosphere. Due to the solid phase of ^{1}AdN_3 at room temperature, this was a facile reaction to prepare, where the solid reagents were added to a Schlenk tube and washed in with toluene.

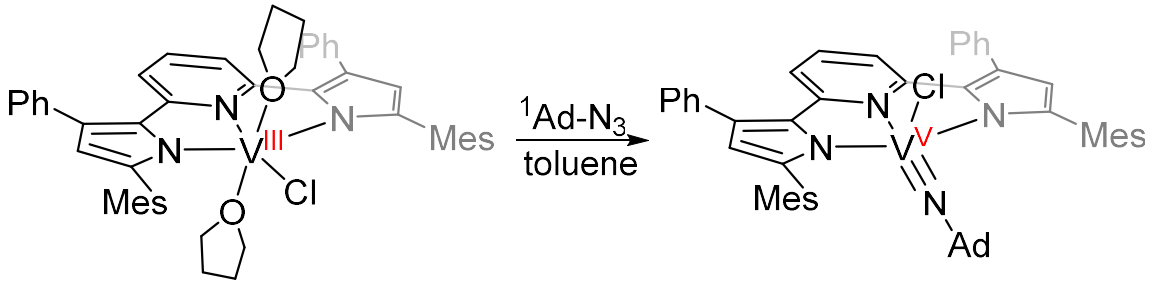

Scheme 4.1: Synthesis of (^{Mes}PDP^{Ph})V(N-^{1}Ad)(Cl).

Upon addition of the solvent, there is no immediate color change that would indicate an adduct of the azide ligand, or expulsion of N_2. After heating overnight at 120 ˚C, however, the reaction mixture deepens in color to a dark purple. The reaction mixture was reduced to dryness under vacuum, reconstituted in a minimal amount of toluene, and filtered with Celite to remove any solids. The solution was again reduced to dryness, and the solids triturated with pentane to remove toluene and tetrahydrofuran from the lattice of the dark purple powder, isolated in 99% yield.

Recrystallization of the product has proved incredibly difficult, as the neutral species is readily soluble in most solvents, as well as sparingly soluble in pentane. As these efforts are ongoing, a structural comparison of vanadium-imido bond lengths will not be discussed here. However, due to the diamagnetism observed in the V(V) product by NMR spectroscopy, connectivity and reactivity can be probed by this method.

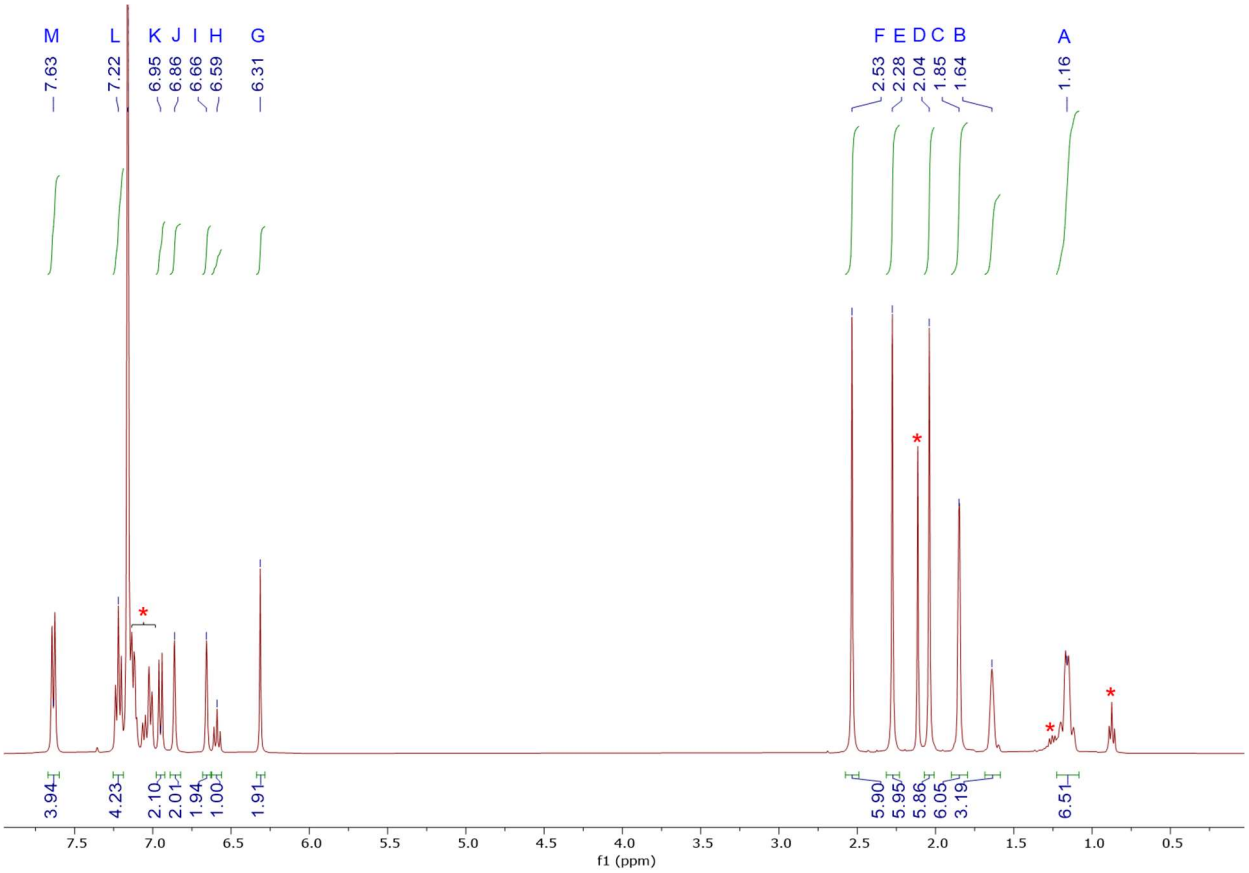

Figure 4.5: ^{1}H NMR spectrum of (^{Mes}PDP^{Ph})V(N-^{1}Ad)(Cl) in benzene-d_6. Toluene and pentane impurities are marked with *. Peak assignments referenced in the text are labelled in blue.

From this ^{1}H NMR spectrum, the three equivalent (6H) mesityl -CH_3 resonances in the aliphatic region (δ 2.53 (F), 2.28 (E), 2.04 (D) ppm) indicate a C_s symmetric structure, where a vertical mirror plane bisects the ligand pincer. This is consistent with the previously characterized (^{Mes}PDP^{Ph})V(NTMS)(N_3), as well as [(^{Mes}PDP^{Ph})VN(N_3)], where the five-coordinate vanadium center has two unique ligands outside of the tridentate pincer. The PDP ligand backbone appears to be consistent with this assessment, where the *para*- pyridine proton at δ 6.59 ppm (H, t, 1H) is coupled to the *meta*- pyridine protons indicated by the doublet at δ 6.95 ppm (K, d, 2H). The sharp signal for the pyrrolic protons at δ 6.31 ppm (G, s, 2H) also is an indication of left/right mirror symmetry. However, it is noted here that a triplet of triplets (2H) belonging to the back phenyl

ligands is missing from this spectrum. In order to elucidate its location, and reaffirm these coupling patterns, correlated spectroscopy was performed.

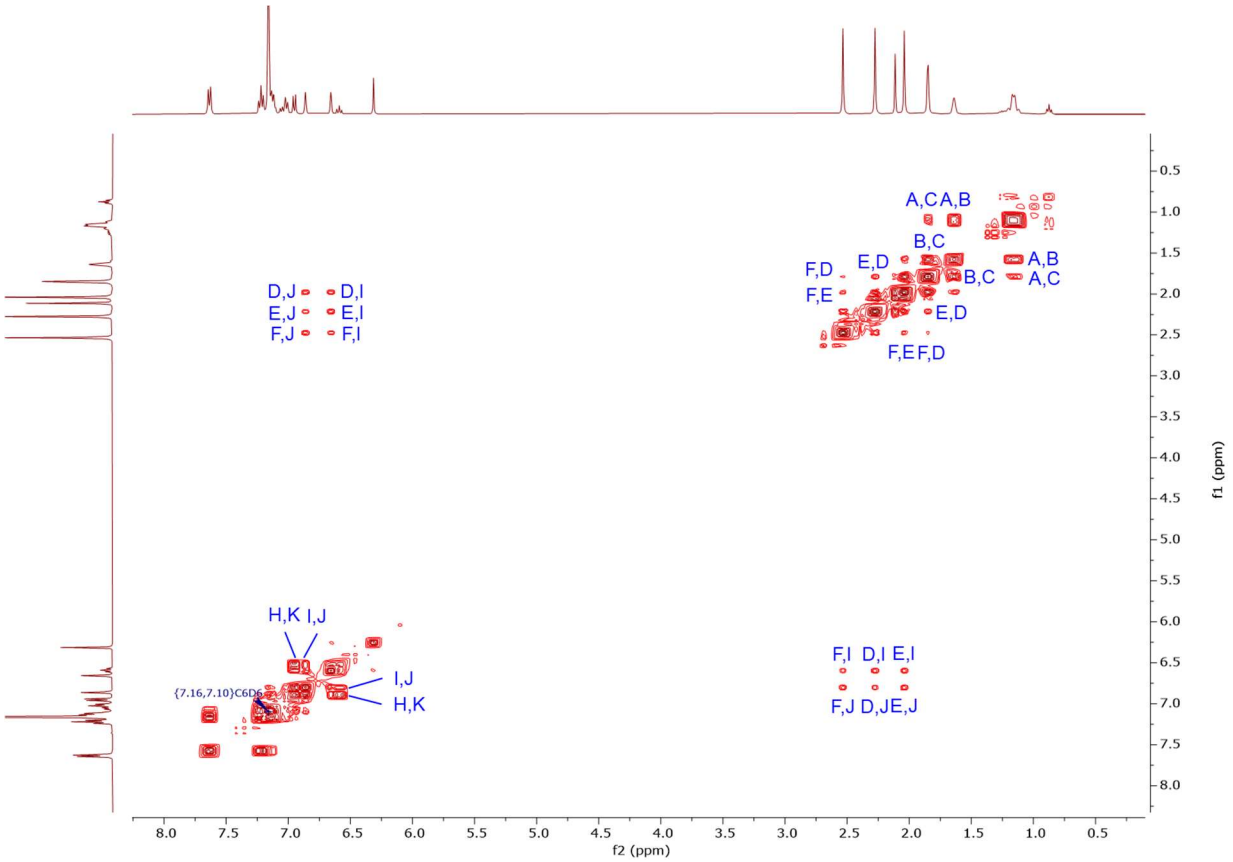

Figure 4.6: (HH) COSY NMR spectrum of (^{Mes}PDP^{Ph})V(N-^{1}Ad)(Cl) in benzene-d_6. Coupling relationships are given in blue by the same assignment as Figure 4.5.

The coupling between signals H and K were confirmed as the protons on the pyridine backbone with J = 8.0 Hz, as indicated by the off-diagonal in Figure 4.6. Weak 4J coupling between the mesityl -CH_3 and the mesityl *meta*- proton allows for the confident assignment of the later signals I (δ 6.66 ppm, s, 2H) and J (δ 6.86 ppm, s, 2H), which are also show coupling to each other. The lack of splitting for these signals can be rationalized by a small J value from the extended aromatic ring, where line broadening is observed but continues to be coalesce.

The 1-adamantyl group is represented by peaks A (δ 1.16 ppm, bs, 6H), B (δ 1.64 ppm, bs, 3H), and C (δ 1.85 ppm, m, 6H), where A is concomitant with a small amount of pentane. The

splitting pattern of these signals is typical of this substituent, where the coupling between chemically inequivalent positions of the rigid tetrahedron is small and not well resolved. Further, the 2D spectrum shows indication of a third phenyl resonance beneath the benzene peak. While the integration of this signal can not be attained, the previously described data supports our hypothesis of its assignment: the *para*- phenyl H in the back of the PDP ligand.

The cumulative NMR data allowed for the confident assignment of connectivity resulting from the reaction of paramagnetic (^{Mes}PDP^{Ph})VCl(thf)$_2$ with 1-adamantyl azide. However, while the organic fragments of the resulting species have been established, the imido and chlorido ligands can not be verified by these methods. In the absence of a structure from crystal data, further reactivity and chemical intuition lead us forward to the preparation of the mixed vanadium-imido/azides. In order to first establish a baseline spectrum before the addition of azide to this species, infrared spectroscopy was performed in a KBr matrix.

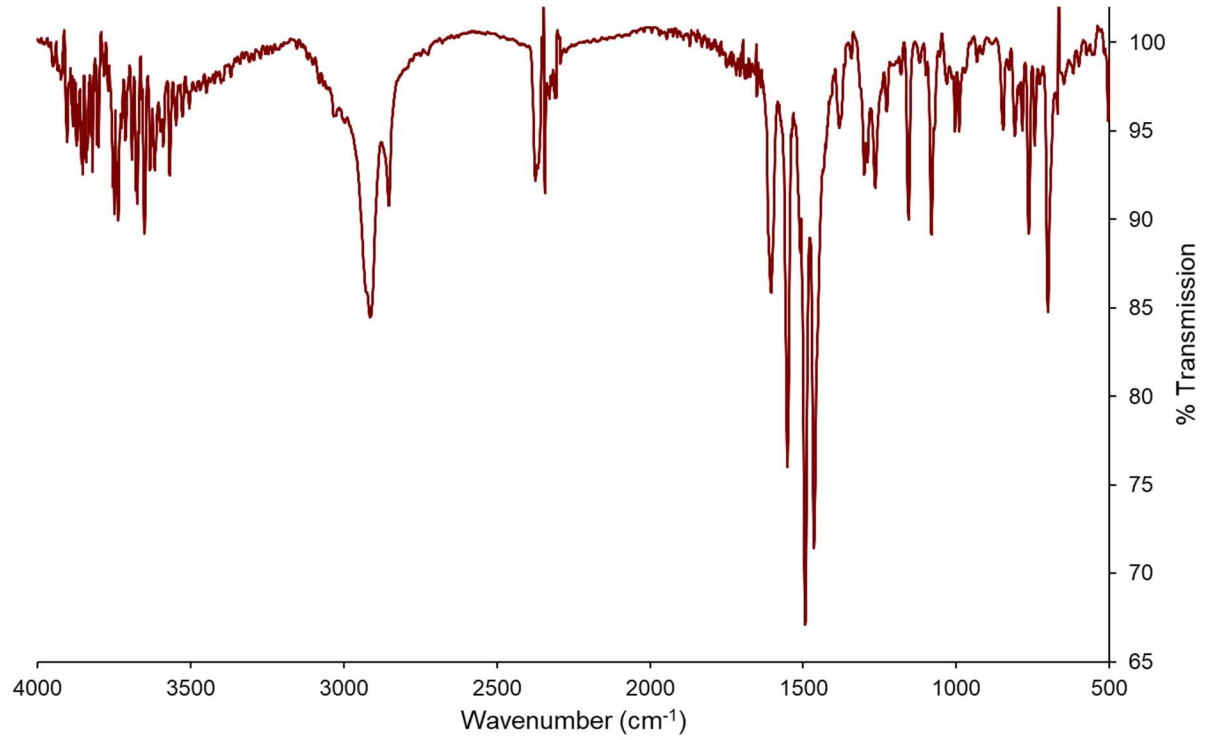

Figure 4.7: IR spectrum of (^{Mes}PDP^{Ph})V(N-^{1}Ad)(Cl) in KBr matrix.

The absence of signal from 2300 – 1800 cm^{-1} will be useful in identifying the addition of the azide ligand in subsequent reactions. Unfortunately, as noted in the case of (^{Mes}PDP^{Ph})V(NTMS)(N_3), it is not possible to identify the V-N_{imido} stretching frequency (commonly around 1500 cm^{-1}), due to several transitions belonging to the PDP ligand scaffold.

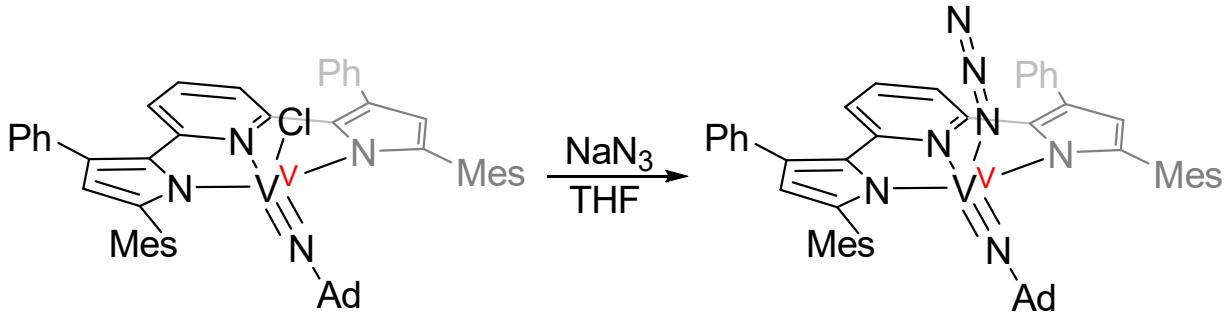

Scheme 4.2: Synthesis of (^{Mes}PDP^{Ph})V(N-^{1}Ad)(N_3).

With this starting material in hand, metathesis of the appended chloride with sodium azide in tetrahydrofuran was performed. After stirring overnight at room temperature, the reaction

mixture was reduced to dryness under vacuum and reconstituted with a minimal amount of toluene to precipitate any dissolved salts. This solution was then filtered with Celite and again reduced to dryness under vacuum. The resulting solid residue was triturated with pentane to removed toluene and THF from the solid. The nearly black solids were isolated in 98% yield.

NMR spectroscopy was performed to detect any change in the organic framework of the product with respect to the starting material. While these compounds are very similar, we would expect small changes in the chemical shift of these resonances.

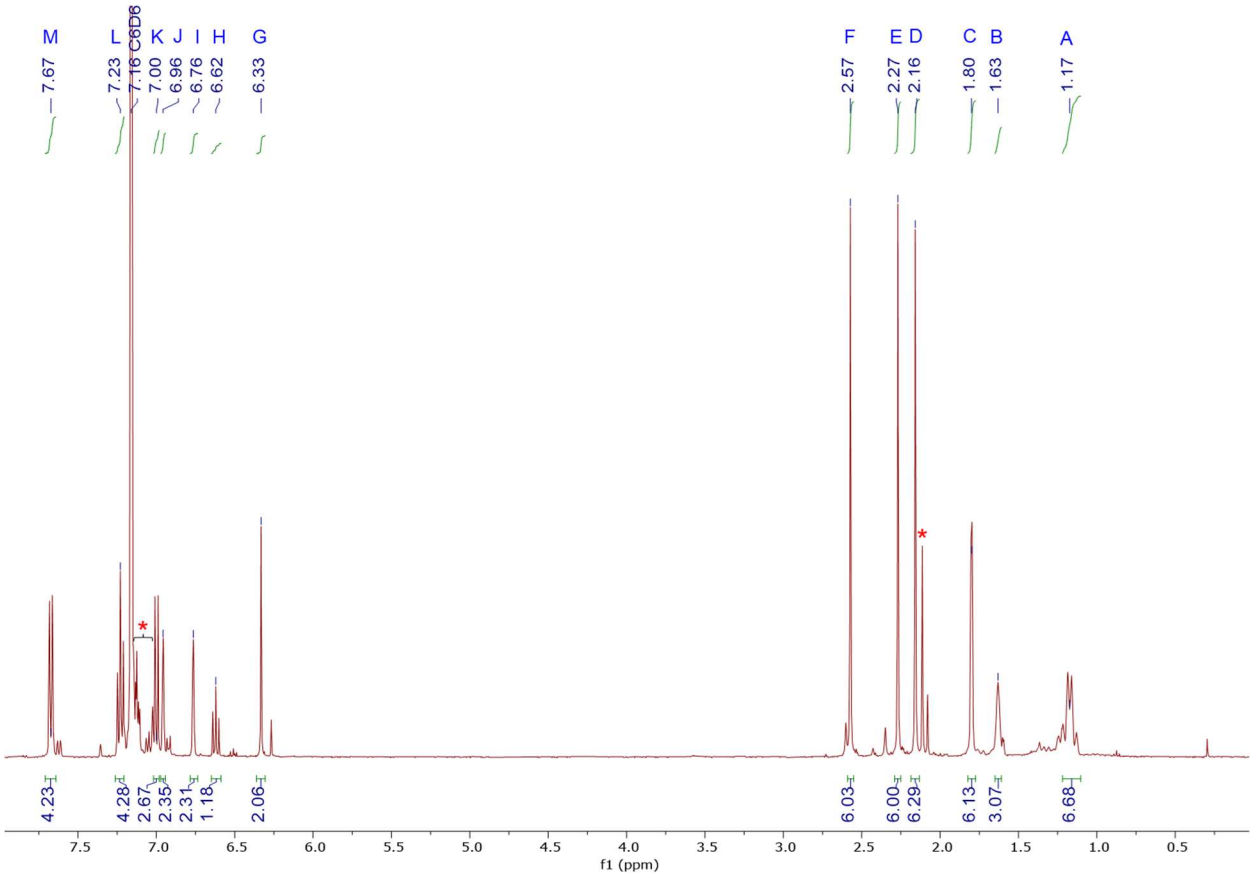

Figure 4.8: ^{1}H NMR spectrum of (^{Mes}PDP^{Ph})V(N-^{1}Ad)(N_3) in benzene-d_6. Toluene impurity marked with *. Peak assignments referenced in the text are labelled in blue.

From the ^{1}H NMR spectrum, it appears that the symmetry and connectivity of the molecule is unchanged from the starting material. However, the chemical shifts of these peaks are shifted as we anticipated. As a result, an exhaustive study of the connectivity of this species would be

redundant with respect to the starting material. Rather than discuss the symmetry and splitting of this spectrum (Figure 4.8) independently, these resonances are summarized in Table 4.1 alongside the chloride. Correlated ^{1}H NMR spectroscopy was also performed and the results are provided in the Appendix A4. No new or unexpected coupling was observed. The resonance associated with the *para*- position of the back phenyl group of the PDP ligand is covered by the solvent (C_6D_6) in both species.

Table 4.1: Comparison of ^{1}H NMR resonances between (^{Mes}PDP^{Ph})V(N-^{1}Ad)(X), where X is an X-type ligand Cl^- or N_3^-. Signal assignments (in blue) are consistent with the structure of both species.

Signal Assignment (ppm)	(^{Mes}PDP^{Ph})V≡N-^{1}Ad(Cl)	(^{Mes}PDP^{Ph})V≡N-^{1}Ad(N_3)	Δδ (ppm)
A	1.16 (m, 6H)	1.17	0.01
B	1.64 (bs, 3H)	1.63	0.01
C	1.85 (bs, 6H)	1.80	0.05
D	2.04 (s, 6H)	2.16	0.12
E	2.28 (s, 6H)	2.27	0.01
F	2.53 (s, 6H)	2.57	0.04
G	6.31 (s, 2H)	6.33	0.02
H	6.59 (t, 1H)	6.62	0.03
I	6.66 (s, 2H)	6.76	0.10
J	6.86 (s, 2H)	6.96	0.10
K	6.95 (d, 2H)	7.00	0.05
L	7.22 (tt, 4H)	7.23	0.01
M	7.63 (dt, 4H)	7.67	0.04

From Table 4.1, it is clear that the change in chemical shift between these species is minute, with a maximum Δδ of 0.12 ppm (48 Hz). This indicates a similar electronic structure, where the exchange of X-type ligands on the vanadium center has little effect on the organic fragments or

overall frontier molecular orbitals. This has been consistent over the course of this work, where the ground state highest occupied molecular orbital (HOMO) has been centered on the π system of the pyrrolic portions of the PDP ligand.

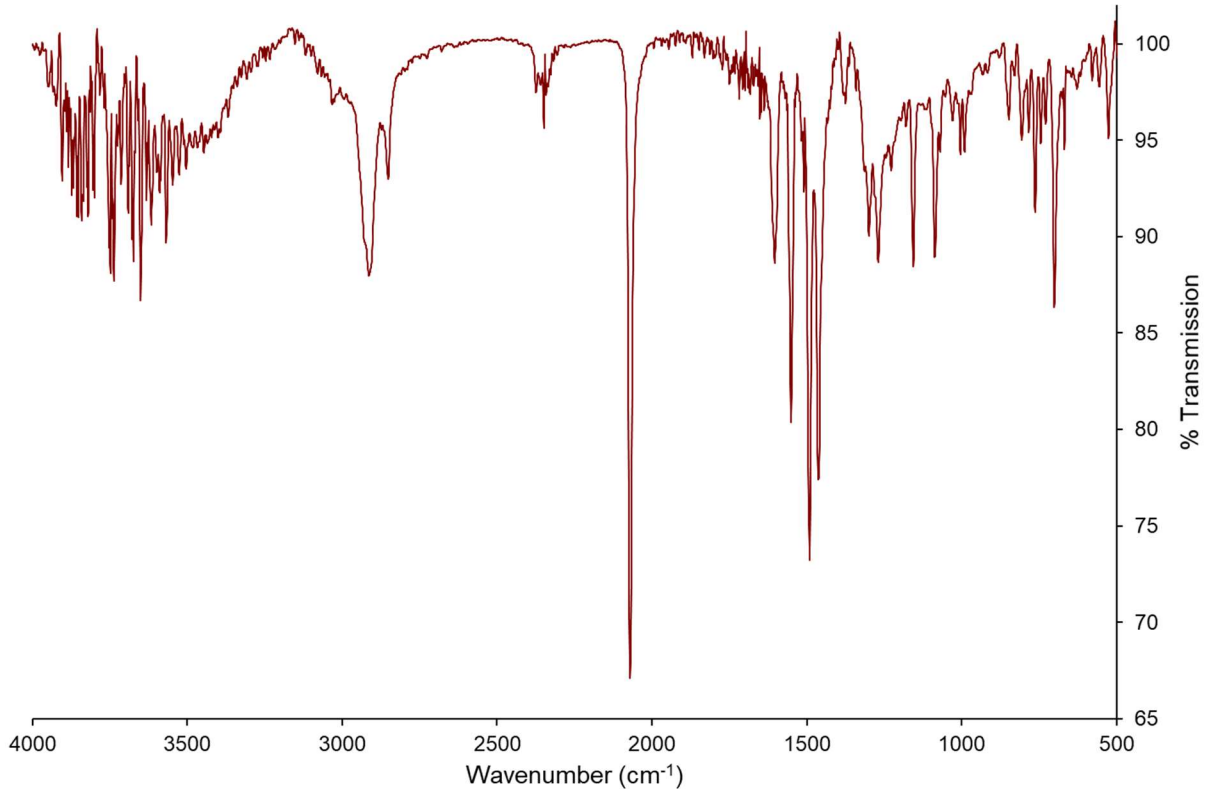

Figure 4.9: IR spectrum of (^{Mes}PDP^{Ph})V(N-^{1}Ad)(N_3) in KBr matrix.

This complex was further characterized by infrared spectroscopy in order to give evidence to the ligation of the azide moiety. From Figure 4.8 to Figure 4.9, there is an immediate and obvious addition of a strong, sharp band at 2070 cm^{-1}. This is consistent with the azide stretching mode observed in (^{Mes}PDP^{Ph})V(NTMS)(N_3) as well as the [(^{Mes}PDP^{Ph})VN(N_3)]$^{-}$ anion, which were 2073 cm^{-1} and 2075 cm^{-1}, respectively.

4.3 Reactivity of (^{Mes}PDP^{Ph})V≡N-R(N_3) with Light

Following the synthesis and characterization of another high valent vanadium imido species, (^{Mes}PDP^{Ph})V(N-^{1}Ad)(N_3), both (^{Mes}PDP^{Ph})V(N-^{1}Ad)(N_3) and (^{Mes}PDP^{Ph})V(N-TMS)(N_3), as well as the [(^{Mes}PDP^{Ph})VN(N_3)]$^{-}$ anion, were subjected to photolytic conditions to probe their reactivity with light. The proposed products (Scheme 4.3) of these reactions are attributed to the C-H activation of the adjacent benzylic protons on the mesityl substituent of the ligand as show in the (^{Mes}PDP^{Ph})Fe(L) example,[15] where the intermediate nitrene inserts rapidly into the relatively weak C-H bond. In order to monitor these reactions, samples were prepared in J-Young adapted NMR tubes and sealed under nitrogen. These were then irradiated in a water-cooled jacket wrapped in green LEDs (λ_{max} = 520 nm). Later reactions on larger scales were performed Schlenk tubes under similar conditions.

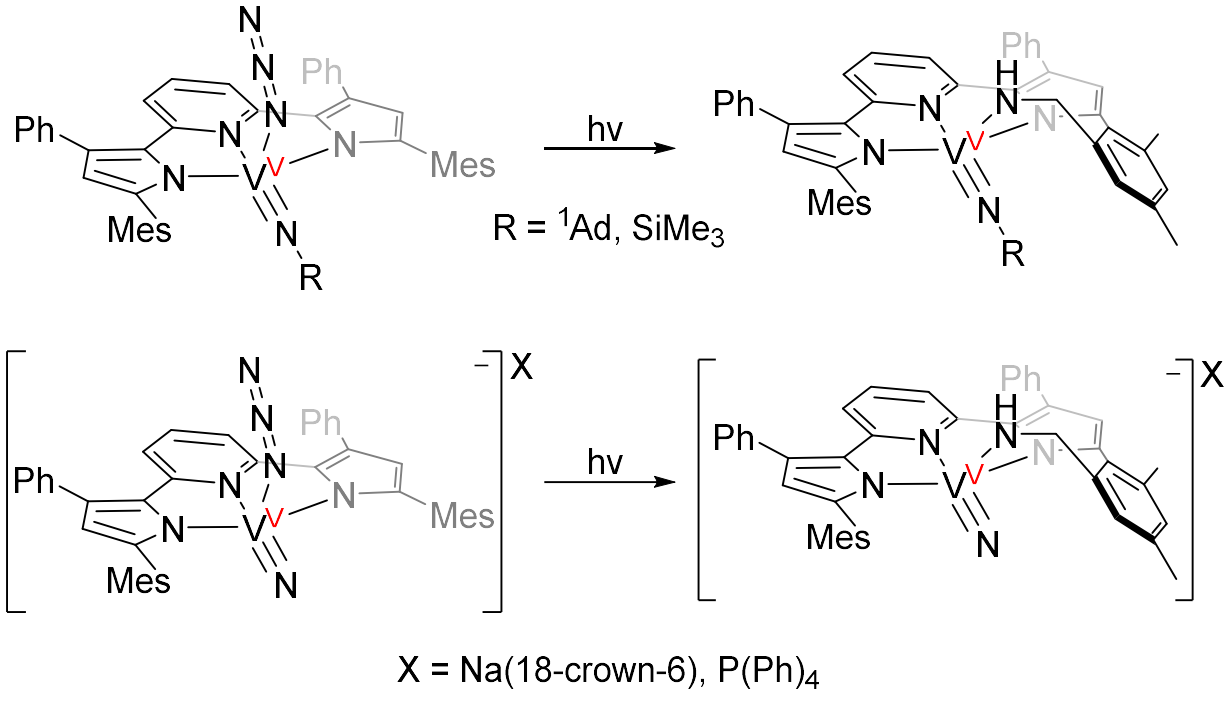

Scheme 4.3: Potential photolysis products from azide ligated [(^{Mes}PDP^{Ph})V≡N]. No reaction was observed where R = ^{1}Ad.

Irradiation of the 1-adamantyl derivative with green or black light for up to two weeks gave no indication of conversion to the C-H activated product. However, from [(^{Mes}PDP^{Ph})VN(N_3)] or (^{Mes}PDP^{Ph})V(NTMS)(N_3), reactivity was observed. With respect to [(^{Mes}PDP^{Ph})VN(N_3)], conversion to the product required at least 48 hours of light exposure.

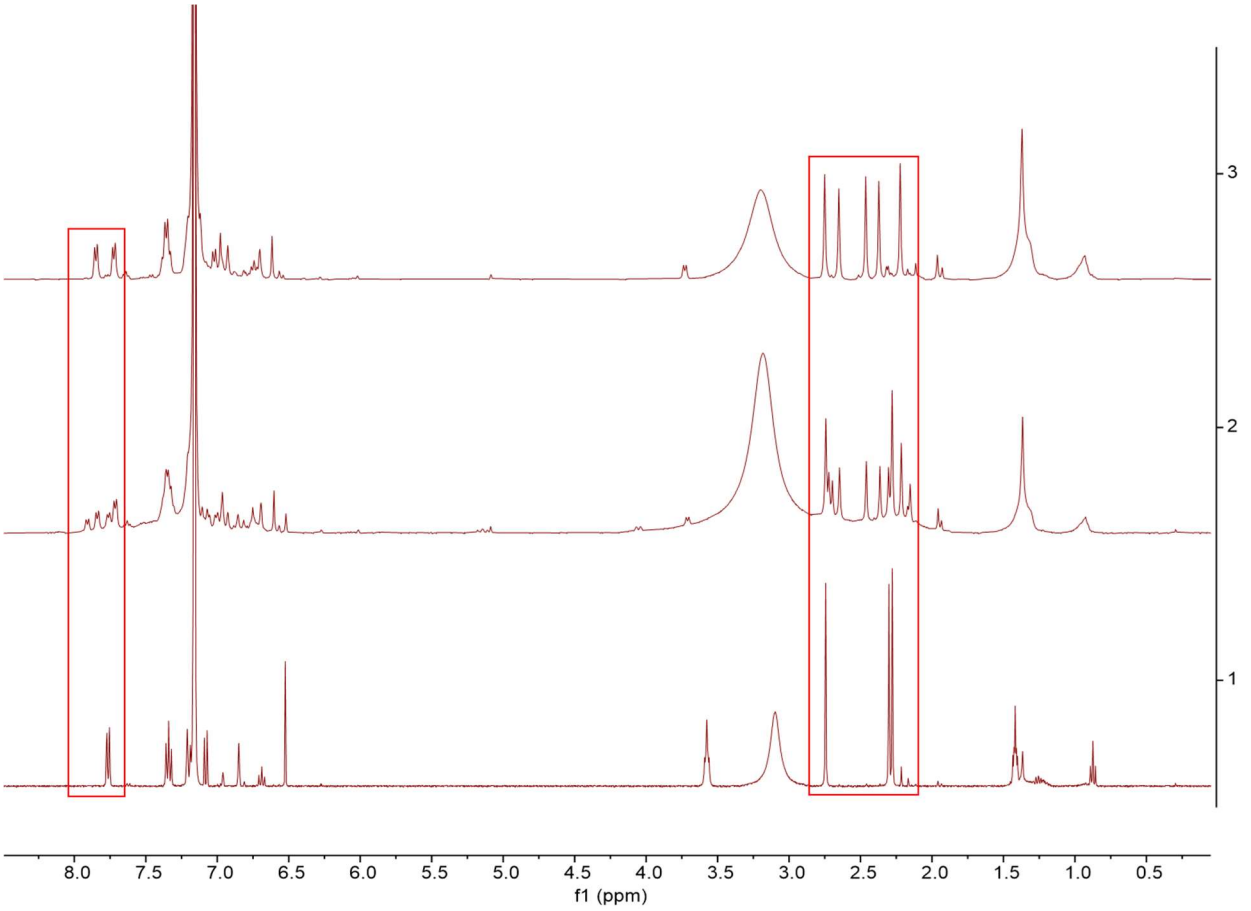

Figure 4.10: ^{1}H NMR spectra of the photolysis of [Na(18-crown-6)][(^{Mes}PDP^{Ph})VN(N_3)] in benzene-d_6 at 0 hours (bottom), 24 hours (middle), and 48 hours (top). Red boxes indicate reporter peaks which represent most identifiable change.

Over the course of the photolysis experiment, [Na(18-crown-6)][(^{Mes}PDP^{Ph})VN(N_3)] slowly converted to the product depicted in Figure 4.10 (top). From the starting material (bottom), there are some more obvious changes in reporter signals which are reasonably uncomplicated to follow. From the ^{1}H NMR spectra of the product, there are five peaks (3H) in the aliphatic region which allude to an asymmetric PDP ligand environment, where the mesityl methyl substituents are

chemically inequivalent with respect to each other. At 24 hours, these peaks are concomitant with the starting material. This spectral feature also indicates a direct conversion of starting materials to products without an isolable intermediate, which we would not anticipate in a radical mechanism.

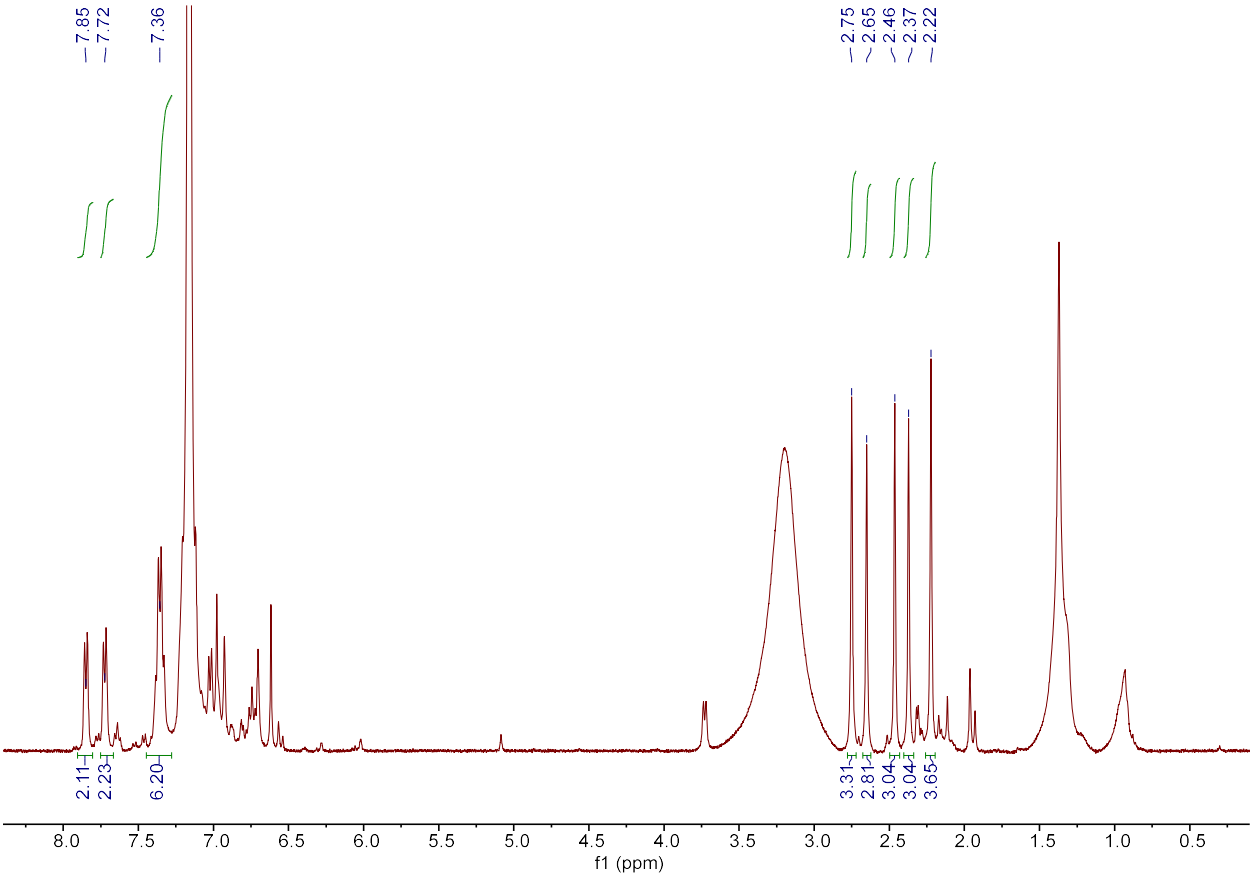

Figure 4.11: ^{1}H NMR spectrum of the photolysis product of [Na(18-crown-6)][(^{Mes}PDP^{Ph})VN(N$_3$)] in benzene-d_6.

A sixth mesityl resonance would be expected, integrating to 2H, where the nitrene has inserted. However, the chemical shift of this signal would be shifted downfield from the shielding effects associated with the presence of an adjacent heteroatom. The absence of this peak may be due to coverage by the 18-crown-6 signal, which dominates the region from δ 3.5 – 2.75 ppm.

The aromatic region (δ 8.0 – 6.5 ppm) shows a complex pattern of resonances, with several overlapping multiplets. However, the peak furthest downfield in the starting material (identified

as the *ortho*- phenyl protons in back of the ligand framework) is cleanly split into two signals (δ 7.85, 7.72 ppm), each integrating to 2H. The similar chemical shift, as well as the integration, indicate the same speciation as that of [Na(18-crown-6)][(^{Mes}PDP^{Ph})VN(N_3)]. This is also evident in the multiplet at δ 7.36 ppm, where two triplets belonging to the now inequivalent *meta*- phenyl protons are closely related. Unfortunately, due to the low solubility of this product in benzene, and apparent sensitivity to methylene chloride, reliable $^{13}C\{^1H\}$ data could not be obtained. Further, the convolution of the remaining peaks in the ^1H spectra make the identification of connectivity non-trivial, however, single crystals were isolated from vapor diffusion of pentane into a concentrated solution of toluene at -45 ˚C.

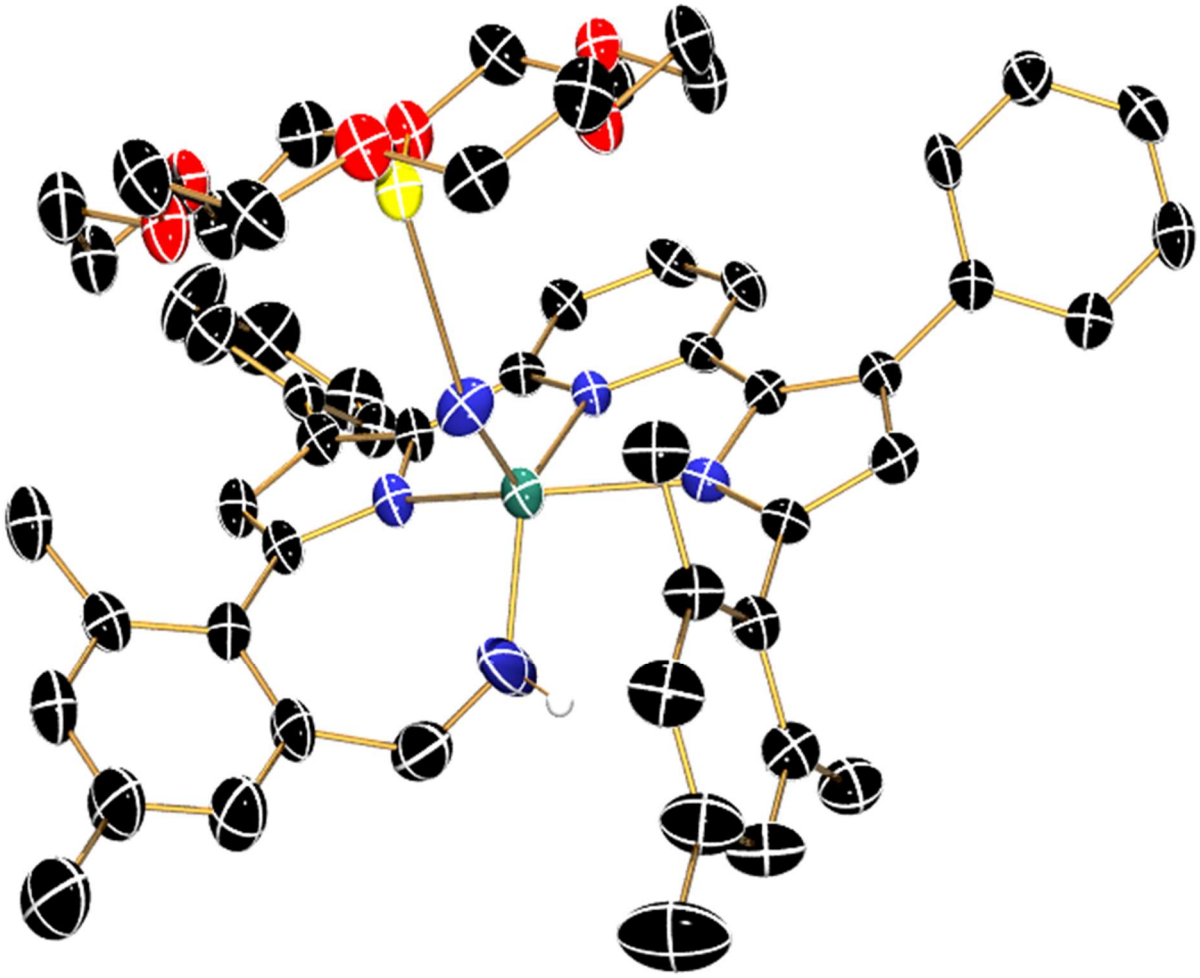

Figure 4.12: ORTEP generated crystal structure of [Na(18-crown-6)][(^{Mes}PDP^{Ph}-NH)VN)] displayed at 50% probability. Hydrogen atoms and co-crystallized solvent are excluded for clarity.

The structure solved in a monoclinic $P2_1/n$ cell, with three equivalents of toluene in the asymmetric unit, two of which were disordered. Unfortunately, the sample was weakly diffracting ($2\theta = 36^{\circ}$), resulting in low resolution data (1.14 Å). Despite this, the model refined very nicely ($R_1 = 4.27\%$, $wR_2 = 11.24\%$) with a few caveats. The nitride and sodium fragments are refined with free occupancy, resulting in occupancies of 1.2 and 1.6, respectively. The cation would resolve as a potassium ion; however, the nitride in that case is non-positive definite. With these caveats in mind, the results from this preliminary X-ray structural analysis primarily establish the

connectivity of the molecule (Figure 4.12), and aid in the interpretation of the NMR data. This model also assists in the characterization of related species.

Returning to the photolysis of other vanadium (V) azides, (^{Mes}PDP^{Ph})V(NTMS)(N_3) was similarly prepared in benzene-d_6 in a J-Young adapted NMR tube and irradiated in a water-cooled jacked wrapped in green LEDs. The reaction proceeded over the course of seven days before complete conversion.

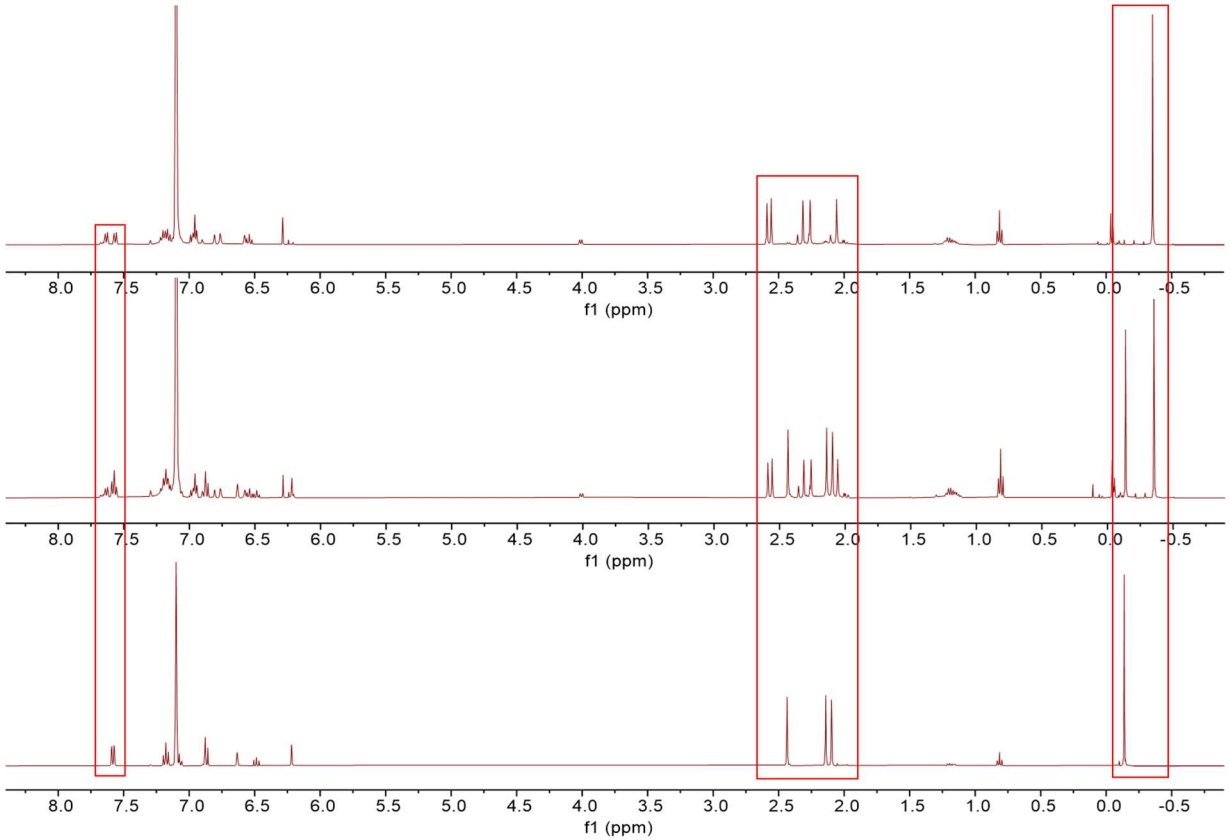

Figure 4.13: ^{1}H NMR spectra of the photolysis of (^{Mes}PDP^{Ph})V(NTMS)(N_3) in benzene-d_6 at before irradiation (bottom), 2 days (middle), and 7 days (top). Red boxes indicate reporter peaks which represent most identifiable change. Special thanks to Andrew E. Martinez, who assisted in the collection of the final spectrum.

The ^{1}H NMR spectrum of this neutral starting material is easier to analyze due to the absence of 18-crown-6, unlike the previous species. Again, there appears a mixture of starting material and product, without an intermediate species. Reporters in the aliphatic and aromatic regions are analogous to the nitride, where the C_s symmetric spectrum loses mirror symmetry. The

trimethylsilyl resonance cleanly shifts to δ -0.35 ppm, evidenced by the mixture after two days (Figure 4.13, middle). Interestingly, the methylene protons resulting from nitrene insertion were identified at δ 2.31 and 2.10 ppm, seemingly uncoupled with integrations of 1H, respectively (Figure 4.14).

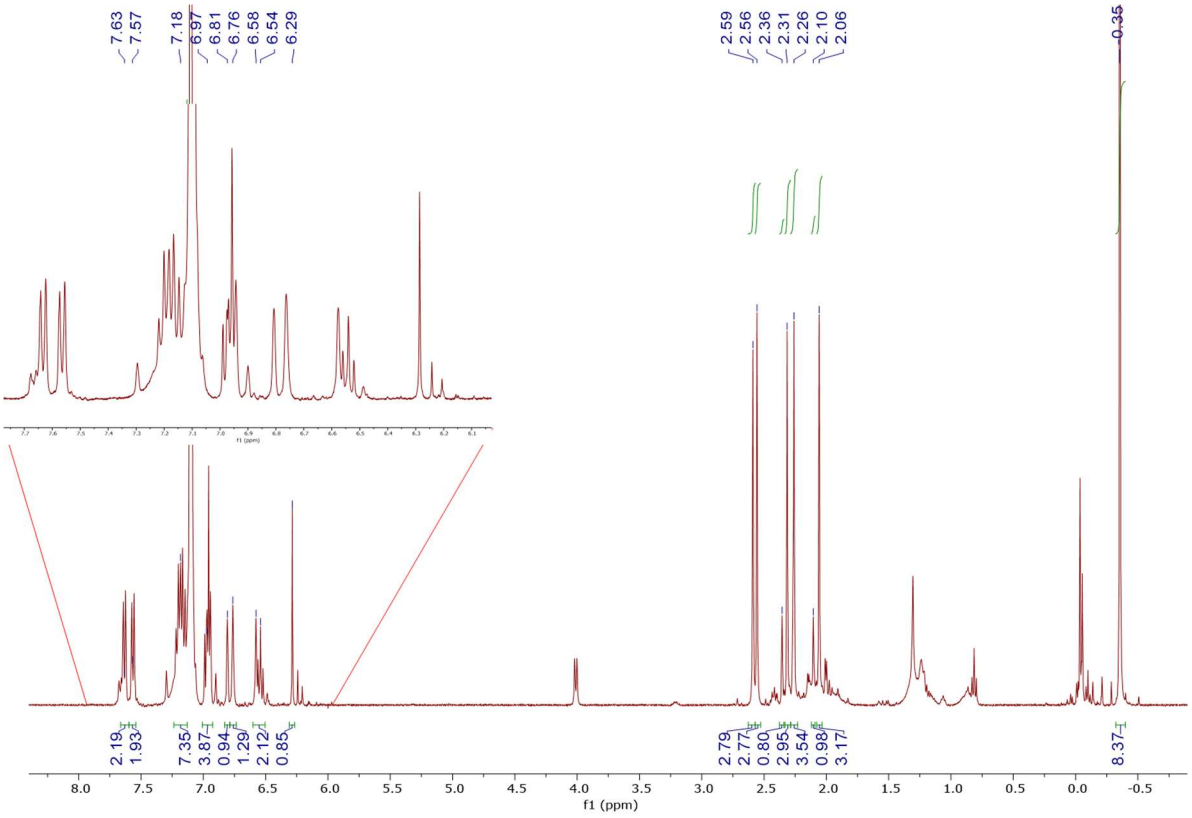

Figure 4.14: ^{1}H NMR spectrum of (^{Mes}PDP^{Ph}-NH)V(NTMS) in benzene-*d*$_6$. Inset: expanded aromatic region from δ 8.0 – 6.0 ppm.

Indeed, relative integrations of the aliphatic region give 5 equivalent methyl groups (s, 3H) and the methylene protons (s, 1H) separated by δ 0.21 ppm. The aromatic region also has more isolated resonances, with a few instances of overlap. The singlets (1H) at δ 6.29, 6.58, 6.76, and 6.81 ppm are most likely attributed to the mesityl and pyrrole protons. A correlated ^{1}H{^{1}H} COSY experiment was performed in effort to deconvolute the overlapped multiplets (Figure 4.15).

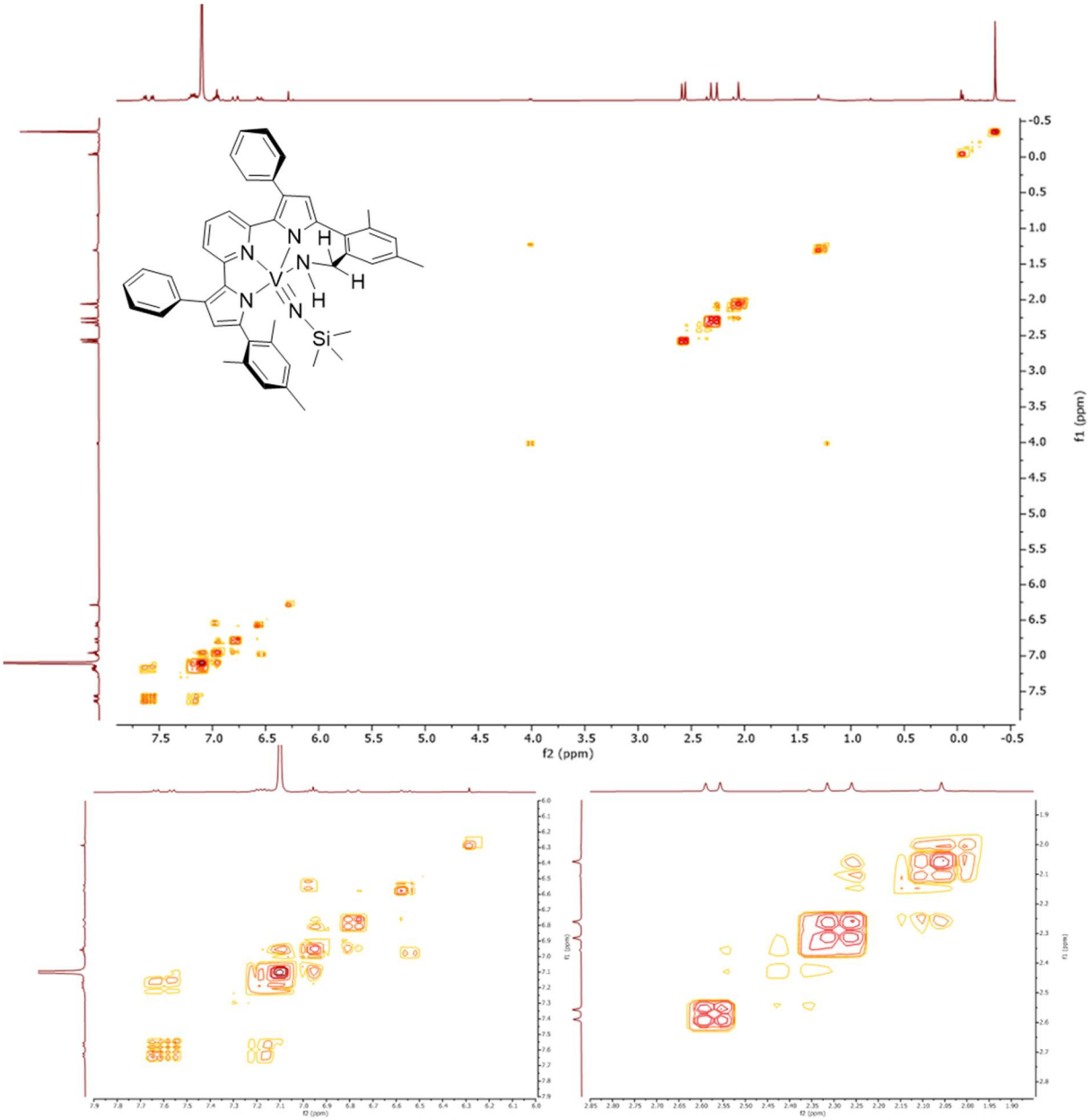

Figure 4.15: (HH) COSY of (^{Mes}PDP^{Ph}-NH)V(NTMS) in benzene-d_6 (top). Below: expanded aromatic (left) and aliphatic regions (right).

This spectrum confirmed that the back phenyl signals coupled to the reporter peaks at δ 2.31 and 2.10 ppm are clustered under and adjacent to the residual solvent signal. While the crystal structure of this species was not collected due to the near-universal solubility of (^{Mes}PDP^{Ph}-NH)V(NTMS), the similarity of the spectra between these products and the structure of [Na(18-crown-6)][(^{Mes}PDP^{Ph}-NH)VN)] give us confidence in these assignments.

In order to understand the mechanism of the photolytic generation of the nitrene moiety, the isolable species over the course of this work, the $[(^{Mes}PDP^{Ph})VN(N_3)]^-$ anion, $(^{Mes}PDP^{Ph})V(NTMS)(N_3)$, and $(^{Mes}PDP^{Ph})V(N\text{-}^1Ad)(N_3)$, were subjected to UV-vis spectroscopy to study their interactions with light. Although the accumulated spectra were measured in different solvents, no apparent solvatochromism was observed during the manipulation of these compounds. The features of these spectra are unique to each species.

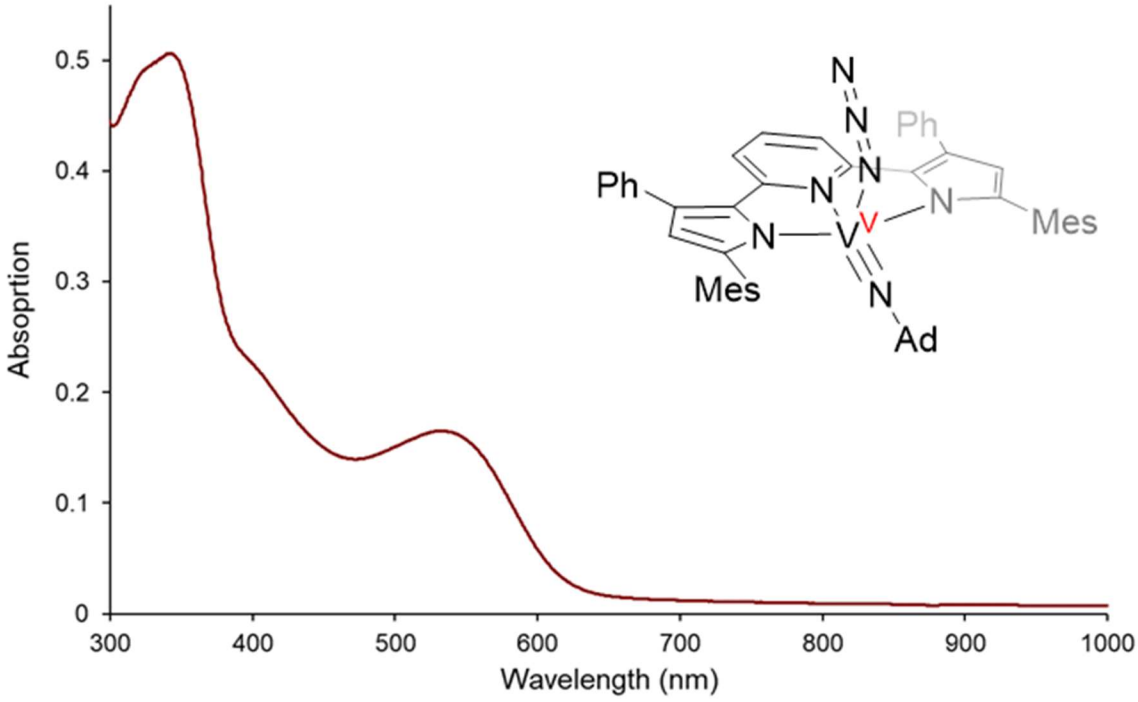

Figure 4.16: UV-vis spectrum of $(^{Mes}PDP^{Ph})V(N\text{-}^1Ad)(N_3)$ in benzene.

Continuing our characterization from the previous section of this Chapter, the UV-vis spectrum of 1-adamantyl imido vanadium azide was measured at room temperature in benzene (Figure 4.16). The spectrum shows a large peak with a maximum in the visible region around 540 nm. This, in combination with the shoulder emerging from the UV absorption at ~410 nm, likely accounts for the deep purple coloration of the material, as absorption ends smoothly around 630 nm.

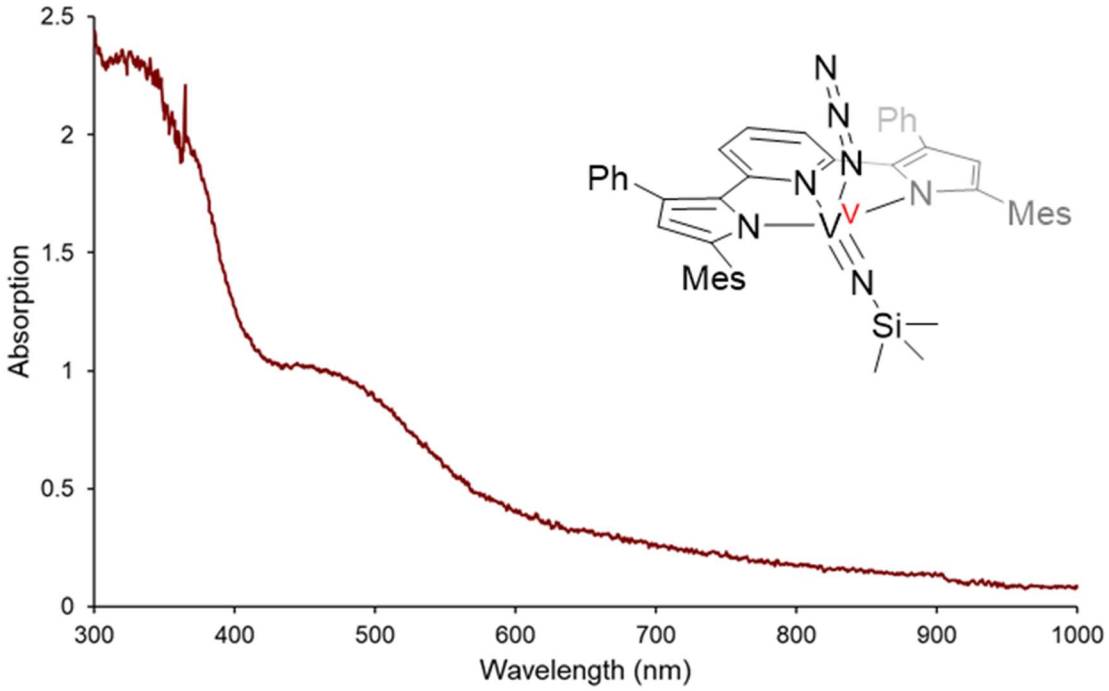

Figure 4.17: UV-vis spectrum of (^{Mes}PDP^{Ph})V(NTMS)(N_3) in tetrahydrofuran.

The UV-vis spectrum of the trimethylsilyl imido species displayed features similar in shape to the 1-adamantyl derivative with a marked blue shifting of the farthest right peak to a maximum at 470 nm. This shifting appears to result in overlap which eliminated the minimum (475 nm) that was displayed previously between two features noted before (410, 540 nm). Further, this absorption event appears less resolved than that of the former species, trailing well into the visible region out to 700 – 800 nm.

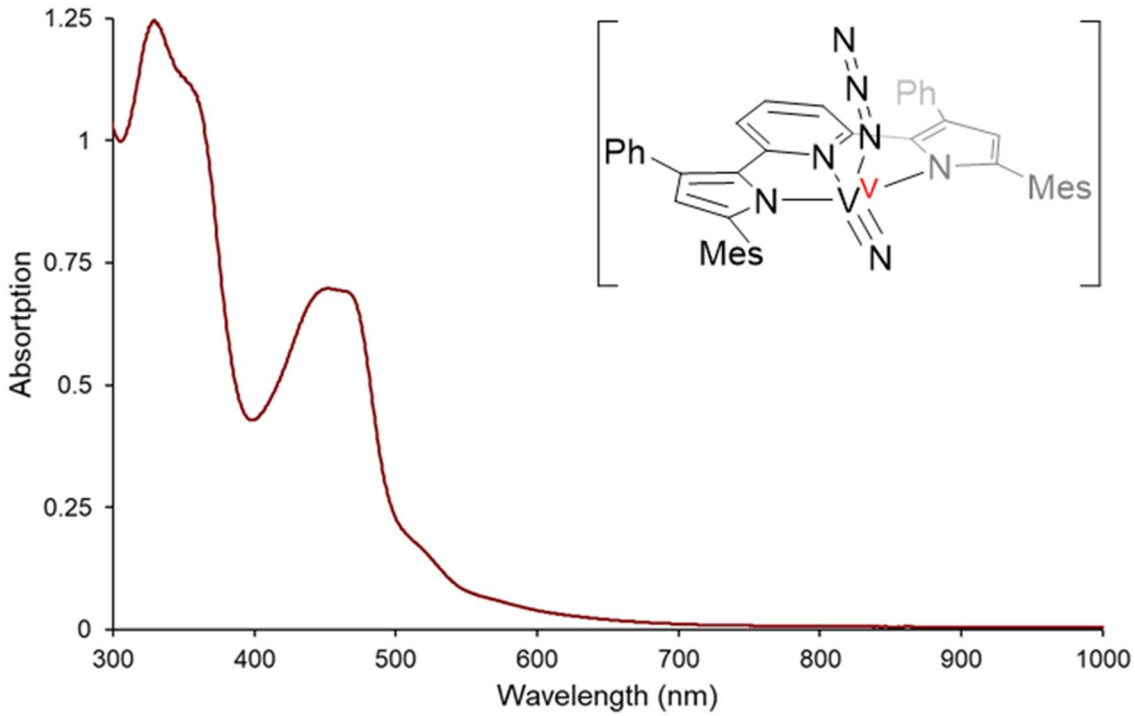

Figure 4.18: UV-vis spectrum of [Na(18-crown-6)][(^{Mes}PDP^{Ph})VN(N_3)] in fluorobenzene.

The UV-vis of the nitrido azide salt had a distinct absorption profile from the two imido species, with more well resolved features. The largest peak in the visible region has some obvious plateauing, from 445 – 470 nm, most likely comprising at least two peak maxima. Further, a shoulder emerges at 515 nm from this peak, trailing past 600 nm. This is consistent with the red appearance of this compound in contrast to the more purple imido complexes.

Following the collection of these data, fluorometry was performed in an attempt to detect an observable excited state. However, none of these species were luminescent at room temperature. This result was not unexpected, as the pseudo trigonal bipyramidal structure could freely interchange with a square pyramidal geometry, where the V-N multiple bond swings into the apical position with the azide ligand *trans*- to the PDP pyridine. This rearrangement would allow access to non-radiative decay pathways associated with these molecular vibrations.

In order to visualize the orbitals responsible for these transitions, the electronic spectra were calculated utilizing the ORCA[19,20] computational package. Following the geometry optimization of each of these species, time-dependent density function theory (TD-DFT) calculations were performed at the B3LYP level of theory utilizing the def2-TZVP(-f) basis set for all atoms. For the selected transitions (~ 500 nm), natural transition orbitals (NTOs) were modelled for the purpose of this analysis. Solvent corrections were not applied to TD-DFT solutions.

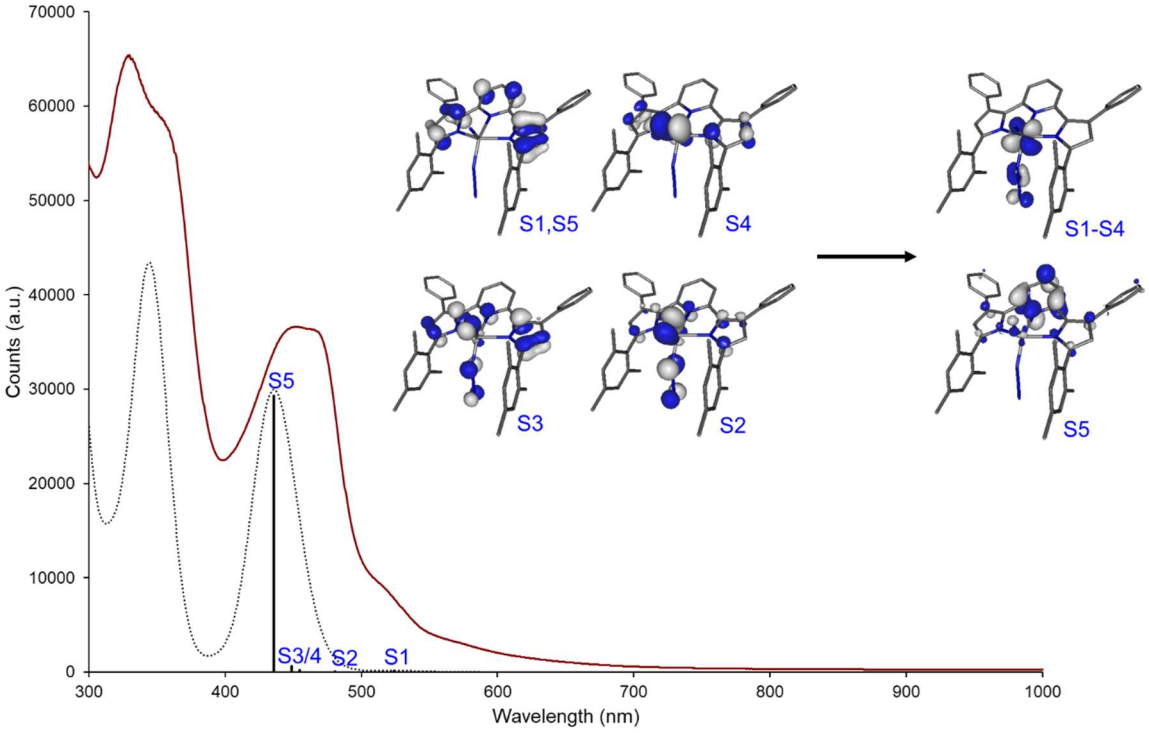

Figure 4.19: UV-vis spectrum of [Na(18-crown-6)][(^{Mes}PDP^{Ph})VN(N$_3$)] (red trace) with calculated spectrum (dotted black trace) as well as transitions S1-S5 (black traces). Natural transition orbitals for these states are inset and labelled in blue.

Beginning our analysis with [Na(18-crown-6)][(^{Mes}PDP^{Ph})VN(N$_3$)], the geometry of this molecular anion was optimized using the crystal structure as a starting point, where the sodium crown was truncated to increase efficiency. The shape of the calculated spectrum (Figure 4.19) is in reasonable agreement with the empirical data, where the major features are generally aligned. The previously noted plateauing (445 – 470 nm) contrasted with the sharp calculated transition,

however, this may be attributed to an equilibrium of the association and dissociation of the ionic pair in solution, yielding similar electronic spectra simultaneously.

Modeling the orbitals responsible for the lowest energy transition (523 nm) revealed the HOMO of this species to be PDP centered, as we would anticipate with an early metal species from our work with photosensitizers of the d^0 Zr(IV) moiety.[21–23] Also considering the donor orbitals from states 2 (478 nm), 3 (453 nm), and 4 (446 nm) transition into this acceptor at near unity (> 90%) it would be reasonable to infer that visible light populates this orbital nearly exclusively. The secondary acceptor orbital in this region, belonging to state 5 (425 nm), is primarily an ligand centered orbital which would result from an intra-ligand charge transfer, or ligand-to-ligand charge transfer (LLCT) mechanism. However, we would not expect this excited state transition to be impactful on this chemistry.

The LUMO acceptor orbital (states 1, 2, 3, and 4) appears to consist primarily of metal character appreciably mixed between the vanadium d_{xy} orbital (68%) and the azide ligand in an antibonding relationship with the Nα and Nβ π bond. Curiously, this acceptor orbital also appears to be antibonding with the terminal Nγ atom. Overall, this is not an intuitive LUMO where one would expect bond scission between Nα and Nβ, concomitant with the expulsion of dinitrogen (Nβ-Nγ) in a unimolecular system.

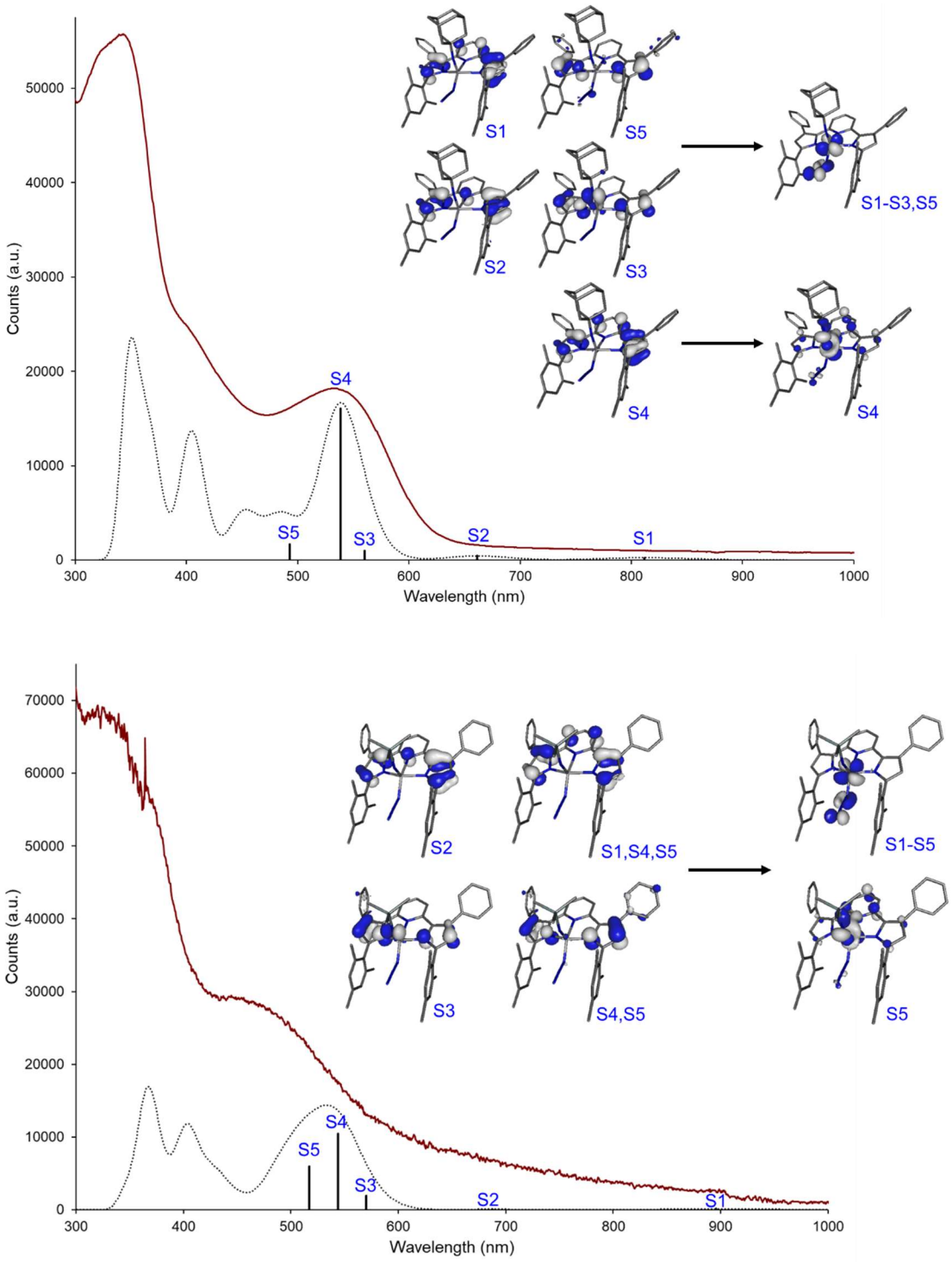

Figure 4.20: Top – UV-vis spectrum of (^{Mes}PDP^{Ph})V(NTMS)(N_3) (red trace) with calculated spectrum (dotted black trace) as well as transitions S1-S5 (black traces). Natural transition orbitals for these states are inset and labelled in blue. Bottom – UV-vis spectrum of (^{Mes}PDP^{Ph})V(N-^{1}Ad)(N_3) (red trace) with calculated spectrum (dotted black trace) as well as transitions S1-S5 (black traces). Natural transition orbitals for these states are inset and labelled in blue.

Moving to the imido azide species, the molecular structures of (^{Mes}PDP^{Ph})V(NTMS)(N_3) and (^{Mes}PDP^{Ph})V(N-^{1}Ad)(N_3) were fabricated in Avogadro[24] before geometry optimization, using the crystal structure of [Na(18-crown-6)][(^{Mes}PDP^{Ph})VN(N_3)] as a starting structure. The computational results (Figure 4.20) have excited state transition characteristics similar to that of the nitrido azide, though far more into the red regions (> 600 nm) of the visible spectrum. This shift is likely due to the stabilization of the vanadium-nitrogen triple bond, which was a major donor orbital in states 2, 3, and 4 for the [(^{Mes}PDP^{Ph})VN(N_3)]$^-$ anion (Figure 4.19), and markedly absent as a donor in (^{Mes}PDP^{Ph})V(NTMS)(N_3) and (^{Mes}PDP^{Ph})V(N-^{1}Ad)(N_3). Indeed, in both imido species, the secondary acceptor to the HOMO is shared between the vanadium d_{z^2} orbital and imido fragment of the molecule. While this paradigm inversion is interesting, these transitions are still dominated by the previously noted orbitals comprised of the d_{xy} orbital and azide ligand.

The density on the terminal nitrogen of the azide ligand is curious and adds ambiguity to the mechanism of the observed nitrene generation/insertion. However, this may be attributed to a divergent pathway, such as bimolecular activation or deazotation from a cyclic metallotriazete intermediate.[25]

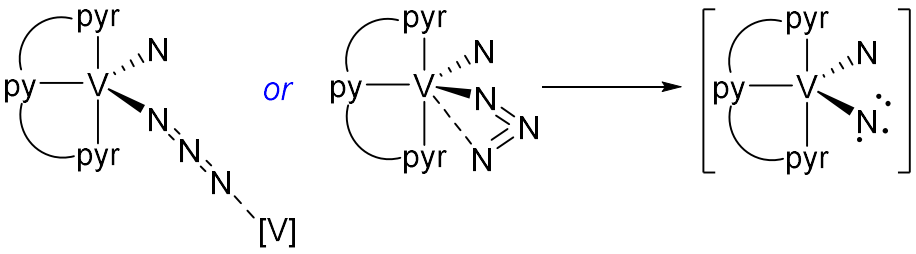

Figure 4.21: Potential pathways for divergent deazotation mechanisms.

The deazotation pathway is unlikely, as the V-Nα bond should not be capable of taking on any multiple bond character. However, the alternative bimolecular pathway may explain the lack of reactivity of (^{Mes}PDP^{Ph})V(N-^{1}Ad)(N_3), where the 1-adamantyl substituent is too sterically demanding to participate in bimolecular activation.

4.4 Conclusions

The reactivity of the $[(^{Mes}PDP^{Ph})VN(N_3)]^-$ anion and $(^{Mes}PDP^{Ph})V(NTMS)(N_3)$ constitutes a novel transformation where dative azide ligands may participate in N-atom insertion chemistry. This example of d^0 early metal coordination complexes participating in nitrene transfer reactions stands in stark contrast to the current literature, where late metals with populated d orbitals force electron density on substituent imido/imidyl fragments. While these methods are not directly comparable, we propose they rely on a similar diradical intermediate which has been rarely characterized.[26]

Further, the pyridine di-pyrrolide ligand appended to vanadium in this case behaves as a light scavenger, allowing access to radical chemistry through the use of relatively low energy light sources. This is a distinct advantage over organic nitrene chemistry,[2] which often requires hard UV radiation to cleave the bonds necessary to produce these intermediates. Though the electronic structure of each of these compounds should allow access to this intramolecular reaction, it seems that the 1-adamantyl derivative ($(^{Mes}PDP^{Ph})V(N\text{-}^1Ad)(N_3)$) does not participate in this transformation. Calculation of the natural transition orbitals for these species suggests the possibility of an unusual deazotation mechanism such as bimolecular activation of azide or cylic intermediates, however, it is unclear what property of this species does not allow for the activation of the azide ligand.

4.5 Experimental Procedures

General Considerations. All air- and moisture-sensitive manipulations were carried out using standard Schlenk line and cannula techniques or in an MBraun inert atmosphere drybox containing an atmosphere of purified nitrogen. Solvents for air- and moisture- sensitive manipulations were dried and deoxygenated using a Glass Contour Solvent Purification System and stored over 4 Å molecular sieves. All solids were dried under high vacuum in oven-dried glassware in order to bring into the glovebox. Deuterated benzene (C_6D_6) for NMR spectroscopy was distilled from sodium. Deuterated methylene chloride (CD_2Cl_2) for NMR spectroscopy was distilled from CaH_2. All solids that were prepared in outside of the box were dried under high vacuum in oven-dried glassware before use in inert atmosphere. Metal halides were purchased and used without further purification.

Physical and Computational Measurements. Nuclear magnetic resonance (NMR) experiments were performed at 400 MHz on a 400-MR DD2 Agilent instrument. All chemical shifts are reported relative to tetramethylsilane with residual solvent proton signal as a secondary standard. Deuterated benzene was distilled from sodium metal and stored over 4 Å molecular sieves. Deuterated methylene chloride was distilled from CaH_2 and stored of 4 Å molecular sieves. Splitting in ^1H NMR studies is notated by: s = singlet, d = doublet, t = triplet, sept = septet, b = broad, m = multiplet or combinations thereof.

Single crystals were prepared for X-ray diffraction in the glovebox by coating with previously degassed polyisobutylene oil (Sigma-Aldrich). These were then picked with a nylon loop (MiTeGen) and mounted to the goniometer head of a Bruker AXS D8 Venture fixed-chi X-ray diffractometer in a cold stream of dry nitrogen. The instrument features a Triumph

monochromator, a Mo Kα radiation source (λ = 0.71073 Å), and a PHOTON 100 CMOS detector. Utilizing the APEX3[27] software package, data was collected, processed with SAINT+, and subjected to absorption correction via SADABS/TWINABS. The space group were determined with XPREP and solved using intrinsic phasing (SHELXL[28]) before refinement with Olex2.[29] Structures are represented at 50% probability thermal ellipsoids via ORTEP-3.

UV-visible and emission spectra were acquired via Shimadzu UV-1800 spectrophotometer and RF-5301 PC spectrofluorophotometer, respectively. Samples were prepared in the glove box under nitrogen in either dry benzene or tetrahydrofuran in J-Young adapted quartz cuvettes.

Density functional theory (DFT) and time-dependent density functional theory (TD-DFT) calculations were performed with the ORCA[19,20] program package. Each were carried out at the B3LYP level of theory. Calculated orbitals were plotted using the program Gabedit.[30]

Safety Considerations. Azides are known to be toxic, energetic materials which can decompose violently under pressure, at high temperature, or when irradiated with light. While no incidents occurred during the course of this work, all manipulations involving sodium azide and azide containing products were carried out under nitrogen in the glovebox. Controlled decomposition of azide moieties (via thermolysis or photolysis) were performed under nitrogen in sealed Schlenk tubes behind a blast shield.

(^{Mes}PDP^{Ph})V(N-^{1}Ad)(Cl) – In the glovebox, a Schlenk tube was charged with 103 mg (0.125 mmol) of (^{Mes}PDP^{Ph})VCl(thf)$_2$ and 44 mg (0.248 mmol) of solid 1-adamantyl azide and taken in toluene. The reaction vessel was sealed under dinitrogen and heated at 120 ˚C overnight with good stirring. The mixture was then reduced to dryness under vacuum, triturated with pentane, and

reconstituted in a minimal amount of toluene. The solution was filtered with Celite, reduced to dryness, and triturated with pentane to remove residual solvent. The dark purple powder (102 mg, 0.123 mmol) was isolated in 99% yield. ^{1}H NMR (400 MHz, C_6D_6) δ 7.63 (d, 4H, *ortho*- phenyl H), 7.22 (t, 4H, *meta*- phenyl H), 6.95 (d, 2H, *meta*- pyridine H, J = 8 Hz), 6.86 (s, 2H, *meta*- mesityl H), 6.66 (s, 2H, *meta*- mesityl H), 6.59 (t, 1H, *para*- pyridine H, J = 8 Hz), 6.31 (s, 2H, pyrrole H), 2.53 (s, 6H, mesityl -CH_3), 2.28 (s, 6H, mesityl -CH_3), 2.04 (s, 6H, mesityl -CH_3), 1.85 (bs, 6H, adamantyl -CH_2), 1.64 (bs, 3H, adamantyl -CH), 1.16 (m, 6H, adamantyl -CH_2). ^{13}C{^{1}H} NMR (100 MHz, C_6D_6) δ 154.48, 149.32, 138.70, 137.90, 137.47, 137.05, 136.38, 135.53, 129.71, 129.34, 128.80, 128.61, 128.57, 127.11, 125.70, 117.26, 111.19, 43.13, 35.57, 29.59, 22.33, 21.20, 21.07.

(^{Mes}PDP^{Ph})V(N-^{1}Ad)(N_3) – In the glovebox, a 20 mL scintillation vial was charged with 16 mg of NaN_3 (0.246 mmol) and 51 mg (0.061 mmol) previously prepared (^{Mes}PDP^{Ph})V(N-^{1}Ad)(Cl) in tetrahydrofuran. The reaction mixture was left to stir overnight at room temperature. This was then reduced to dryness under vacuum, triturated with pentane, and taken in a minimal amount of toluene. The resulting solution was filtered with Celite, reduced to dryness, and triturated with pentane to remove residual solvent. The dark purple powder (50 mg, 0.060 mmol) was isolated in 98% yield. ^{1}H NMR (400 MHz, C_6D_6) δ 7.67 (d, 4H, *ortho*- phenyl H), 7.23 (t, 4H, *meta*- phenyl H), 7.00 (d, 2H, *meta*- pyridine H, J = 8 Hz), 6.96 (s, 2H, *meta*- mesityl H), 6.76 (s, 2H, *meta*- mesityl H), 6.62 (t, 1H, *para*- pyridine H, J = 8 Hz), 6.33 (s, 2H, pyrrole H), 2.57 (s, 6H, mesityl -CH_3), 2.27 (s, 6H, mesityl -CH_3), 2.16 (s, 6H, mesityl -CH_3), 1.80 (bs, 6H, adamantyl -CH_2), 1.63 (bs, 3H, adamantyl -CH), 1.17 (m, 6H, adamantyl -CH_2). ^{13}C{^{1}H} NMR (100 MHz, C_6D_6) δ

154.67, 147.74, 140.99, 138.73, 137.73, 137.48, 136.81, 135.06, 129.87, 129.76, 129.33, 128.77, 128.57, 128.53, 126.97, 116.32, 111.19, 43.35, 35.61, 29.55, 22.21. IR (KBr, -N_3): ῡ 2070 cm^{-1}.

(^{Mes}PDP^{Ph})V(NTMS)(N_3) – In the glovebox, a Schlenk tube was charged with 73 mg (0.088 mmol) of (^{Mes}PDP^{Ph})VCl$(thf)_2$ in toluene. Excess N_3TMS was added (48 μL, 0.365 mmol) and the reaction vessel sealed under dinitrogen and heated at 120 ˚C overnight with good stirring. The mixture was then reduced to dryness under vacuum, triturated with pentane, and reconstituted in a minimal amount of toluene. The resulting solution was filtered with Celite, reduced to dryness, and triturated with pentane to remove residual solvent. The dark purple powder (51 mg, 0.067 mmol) was collected in 76% yield. ^{1}H NMR (400 MHz, C_6D_6): δ 7.64 (dt, 4H, *ortho*- phenyl H, J = 7.5 Hz, 1.5 Hz), 7.24 (tt, 4H, *meta*- phenyl H, J = 7.5 Hz, 1.5 Hz), 7.13 (tt, 2H, *para*- phenyl H, J = 7.5 Hz, 1.5 Hz), 6.94 (s, 2H, *meta*- mesityl H), 6.93 (d, 2H, *meta*- pyridine H), 6.69 (s, 2H, *meta*- mesityl H), 6.54 (t, 1H, *para*-pyridine H), 6.28 (s, 2H, pyrrole H), 2.50 (s, 6H, mesityl -CH_3), 2.20 (s, 6H, mesityl -CH_3), 2.16 (s, 6H, mesityl -CH_3), -0.08 (s, 9H, TMS -CH_3). ^{13}C{^{1}H} NMR (100 MHz, C_6D_6): δ 154.57, 147.34, 140.85, 138.25, 137.29, 137.18, 136.88, 134.72, 129.31, 128.36, 128.00, 126.60, 115.35, 110.83, 21.55, 20.80, 20.46, 0.18. IR (KBr, -N_3): ῡ 2073 cm^{-1} Crystals suitable for X-ray diffraction were grown from vapor diffusion of pentane into toluene.

[Na(18-crown-6)][(^{Mes}PDP^{Ph}-NH)VN] – In the glovebox, a Schlenk tube was charged with 65 mg (0.066 mmol) of [Na(18-crown-6)][(^{Mes}PDP^{Ph})VN(N_3)] and taken in tetrahydrofuran. The vessel was sealed under dinitrogen and irradiated in a water-cooled jacket wrapped in green LEDs (520 nm) for 48 hours. The reaction mixture was then filtered with Celite, reduced to dryness, and triturated with pentane. The bright red solids (61 mg, 0.063 mmol) were isolated in 95% yield. ^{1}H

NMR (400 MHz, C_6D_6) δ 7.85 (d, 2H), 7.72 (d, 2H), 7.36 (m, 4H), 3.20 (bs, 24H, 18-crown-6), 2.75 (s, 3H, mesityl -CH_3), 2.65 (s, 3H, mesityl -CH_3), 2.46 (s, 3H, mesityl -CH_3), 2.37 (s, 3H, mesityl -CH_3), 2.22 (s, 3H, mesityl -CH_3). Crystals suitable for X-ray diffraction were grown from vapor diffusion of pentane into toluene.

(^{Mes}PDP^{Ph}-NH)V(NTMS) – In the glovebox, a Schlenk tube was charged with 70 mg (0.093 mmol) of (^{Mes}PDP^{Ph})V(NTMS)(N_3) and taken in tetrahydrofuran. The vessel was sealed under dinitrogen and irradiated in a water-cooled jacket wrapped in green LEDs (520 nm) for 7 days. The reaction mixture was then filtered with Celite, reduced to dryness, and triturated with pentane. The dark purple solids (57 mg, 0.078 mmol) were isolated in 84% yield. ^{1}H NMR (400 MHz, C_6D_6) δ 7.63 (d, 2H), 7.57 (d, 2H), 7.18 (m, 7H), 6.97 (m, 4H), 6.81 (s, 1H), 6.76 (s, 1H), 6.58 (s, 1H), 6.54 (t, 1H), 6.29 (s, 1H), 2.59 (s, 3H, mesityl -CH_3), 2.56 (s, 3H, mesityl -CH_3), 2.36 (s, 1H, methylene -CH_2), 2.31 (s, 3H, mesityl -CH_3), 2.26 (s, 3H, mesityl -CH_3), 2.10(s, 1H, methylene -CH_2), 2.08 (s, 3H, mesityl -CH_3), -0.35 (s, 9H, TMS -CH_3). ^{13}C{^{1}H} NMR (100 MHz, C_6D_6) δ 154.62, 154.36, 152.43, 146.73, 141.20, 138.87, 138.76, 137.74, 137.52, 135.12, 134.83, 133.92, 129.95, 129.88, 129.84, 129.03, 128.88, 128.77, 127.12, 127.07, 126.99, 116.06, 114.20, 111.97, 111.67, 30.24, 23.88, 22.24, 21.27, 21.21, 20.37, 3.04, 0.23.

4.6 References

(1) Eikey, R. A.; Abu-Omar, M. M. Nitrido and Imido Transition Metal Complexes of Groups 6-8. *Coord. Chem. Rev.* **2003**, *243* (1–2), 83–124.

(2) Scriven, F. V. E.; Turnbull, K. Azides: Their Preparation and Synthetic Uses. *Chem. Rev.* **1988**, *88* (2), 297–368.

(3) Berry, J. F. Terminal Nitrido and Imido Complexes of the Late Transition Metals. *Comments Inorg. Chem.* **2009**, *30* (1–2), 28–66.

(4) Seok, W. K.; Klapötke, T. M. Inorganic and Transition Metal Azides. *Bull. Korean Chem. Soc.* **2010**, *31* (4), 781–788.

(5) Kuijpers, P. F.; van der Vlugt, J. I.; Schneider, S.; de Bruin, B. Nitrene Radical Intermediates in Catalytic Synthesis. *Chem. Eur. J.* **2017**, *23* (56), 13819–13829.

(6) SIMA, J. Photochemistry of Azide-Moiety Containing Inorganic Compounds. *Coord. Chem. Rev.* **2006**, *250* (17–18), 2325–2334.

(7) Dequirez, G.; Pons, V.; Dauban, P. Nitrene Chemistry in Organic Synthesis: Still in Its Infancy? *Angew. Chemie Int. Ed.* **2012**, *51* (30), 7384–7395.

(8) Halfen, J. A. Recent Advances in Metal-Mediated Carbon-Nitrogen Bond Formation Reactions: Aziridination and Amidation. *Curr. Org. Chem.* **2005**, *9*, 657–669.

(9) Park, Y.; Kim, Y.; Chang, S. Transition Metal-Catalyzed C-H Amination: Scope, Mechanism, and Applications. *Chem. Rev.* **2017**, *117* (13), 9247–9301.

(10) Suarez, A. I. O.; Lyaskovskyy, V.; Reek, J. N. H.; Van Der Vlugt, J. I.; De Bruin, B. Complexes with Nitrogen-Centered Radical Ligands: Classification, Spectroscopic Features, Reactivity, and Catalytic Applications. *Angew. Chemie Int. Ed.* **2013**, *52* (48), 12510–12529.

(11) Bowman, A. C.; Milsmann, C.; Bill, E.; Turner, Z. R.; Lobkovsky, E.; Debeer, S.; Wieghardt, K.; Chirik, P. J. Synthesis and Electronic Structure Determination of N-Alkyl-Substituted Bis(Imino)Pyridine Iron Imides Exhibiting Spin Crossover Behavior. *J. Am. Chem. Soc.* **2011**, *133* (43), 17353–17369.

(12) Bart, S. C.; Lobkovsky, E.; Bill, E.; Chirik, P. J. Synthesis and Hydrogenation of Bis(Imino)Pyridine Iron Imides. *J. Am. Chem. Soc.* **2006**, *128* (16), 5302–5303.

(13) King, E. R.; Hennessy, E. T.; Betley, T. A. Catalytic C-H Bond Amination from High-Spin Iron Imido Complexes. *J. Am. Chem. Soc.* **2011**, *133* (13), 4917–4923.

(14) Iovan, D. A.; Betley, T. A. Characterization of Iron-Imido Species Relevant for N-Group Transfer Chemistry. *J. Am. Chem. Soc.* **2016**, *138* (6), 1983–1993.

(15) Hakey, B. M.; Darmon, J. M.; Akhmedov, N. G.; Petersen, J. L.; Milsmann, C. Reactivity of Pyridine Dipyrrolide Iron(II) Complexes with Organic Azides: C-H Amination and Iron Tetrazene Formation. *Inorg. Chem.* **2019**, *58* (16), 11028–11042.

(16) Searles, K.; Fortier, S.; Khusniyarov, M. M.; Carroll, P. J.; Sutter, J.; Meyer, K.; Mindiola, D. J.; Caulton, K. G. A Cis -Divacant Octahedral and Mononuclear Iron(IV) Imide. *Angew. Chemie Int. Ed.* **2014**, *53* (51), 14139–14143.

(17) Ragaini, F.; Penoni, A.; Gallo, E.; Tollari, S.; Li Gotti, C.; Lapadula, M.; Mangioni, E.; Cenini, S. Amination of Benzylic C-H Bonds by Arylazides Catalyzed by CoII–Porphyrin Complexes: A Synthetic and Mechanistic Study. *Chem. – A Eur. J.* **2003**, *9* (1), 249–259.

(18) Grant, L. N.; Carroll, M. E.; Carroll, P. J.; Mindiola, D. J. An Unusual Cobalt Azide Adduct That Produces a Nitrene Species for Carbon-Hydrogen Insertion Chemistry. *Inorg. Chem.* **2016**, *55* (16), 7997–8002.

(19) Neese, F. The ORCA Program System. *Wiley Interdiscip. Rev. Comput. Mol. Sci.* **2012**, *2*

(1), 73–78.

(20) Neese, F. Software Update: The ORCA Program System, Version 4.0. *Wiley Interdiscip. Rev. Comput. Mol. Sci.* **2017**, *8* (1), e1327.

(21) Zhang, Y.; Petersen, J. L.; Milsmann, C. A Luminescent Zirconium(IV) Complex as a Molecular Photosensitizer for Visible Light Photoredox Catalysis. *J. Am. Chem. Soc.* **2016**, *138* (40), 13115–13118.

(22) Zhang, Y.; Lee, T. S.; Petersen, J. L.; Milsmann, C. A Zirconium Photosensitizer with a Long-Lived Excited State: Mechanistic Insight into Photoinduced Single-Electron Transfer. *J. Am. Chem. Soc.* **2018**, *140* (18), 5934–5947.

(23) Zhang, Y.; Lee, T. S.; Favale, J. M.; Leary, D. C.; Petersen, J. L.; Scholes, G. D.; Castellano, F. N.; Milsmann, C. Delayed Fluorescence from a Zirconium(Iv) Photosensitizer with Ligand-to-Metal Charge-Transfer Excited States. *Nat. Chem.* **2020**, *12* (4), 345–352.

(24) Hanwell, M. D.; Curtis, D. E.; Lonie, D. C.; Vandermeersch, T.; Zurek, E.; Hutchison, G. R. Avogadro: An Advanced Semantic Chemical Editor, Visualization, and Anaylsis Platform. *J. Cheminform.* **2012**, No. 4, 1–17.

(25) Reinholdt, A.; Kwon, S.; Jafari, M. G.; Gau, M. R.; Caroll, P. J.; Lawrence, C.; Gu, J.; Baik, M. H.; Mindiola, D. J. An Isolable Azide Adduct of Titanium(II) Follows Bifurcated Deazotation Pathways to an Imide. *J. Am. Chem. Soc.* **2022**, *144* (1), 527–537.

(26) De Bruin, B.; Hunger, D.; Würtele, C.; Slageren, J. Van. A Platinum(Ii) Metallonitrene with a Triplet Ground State. *Nat. Chem.* **2020**, *12*, 1054–1059.

(27) Bruker. *APEX3 User Manual*; 2016.

(28) Sheldrick, G. M. Crystal Structure Refinement with SHELXL. *Acta Crystallogr. Sect. C*

Struct. Chem. **2015**, *71* (Md), 3–8.

(29) Dolomanov, O. V.; Bourhis, L. J.; Gildea, R. J.; Howard, J. A. K.; Puschmann, H. OLEX2: A Complete Structure Solution, Refinement and Analysis Program. *J. Appl. Cryst.* **2009**, No. 42, 339–341.

(30) Allouche, A. R. Gabedit - A Graphical User Interface for Computational Chemistry Softwares. *J. Comput. Chem.* **2011**, No. 32, 174–182.

Chapter 5: Synthesis and Characterization of Complexes of Ti, Zr, V, and Nb Bearing 2,6-(methylanilido)Pyridine Ligands

5.1 Towards Early Metal Photosensitizers

With the steady decline in the supply of fossil fuels, the development of efficient methods for harvesting light energy has become an important goal.[1–8] The World Energy Assessment Update of 2004[9] reported that of 418 exajoules (418×10^{18} J) of energy used in 2001, 0.6 percent was contributed from combined renewable sources including solar and geothermal, excluding hydroelectric. Sixty-five percent were derived from non-renewable sources. Meanwhile, the sun provides the earth with more light energy in an hour than could be used in a year.[1] The efficient collection of solar energy remains problematic. High purity silicon, which is the basis of the most common (and most efficient) solar cells[7] is simply too expensive to produce on any large scale. An alternative approach for photon harvesting involves the use of molecular photosensitizers as dopants in semiconductors towards dye-sensitized solar cells (DSSCs).[3,4,6,10,11] The fundamental properties of these photosensitizers also contribute to promoting specific chemical processes in homogenous systems, such as photoredox catalysts. The design principles of single molecule photosensitizers towards practical applications branches widely but comes together in a common root: an accessible excited state as a result of photon absorption.[12–17]

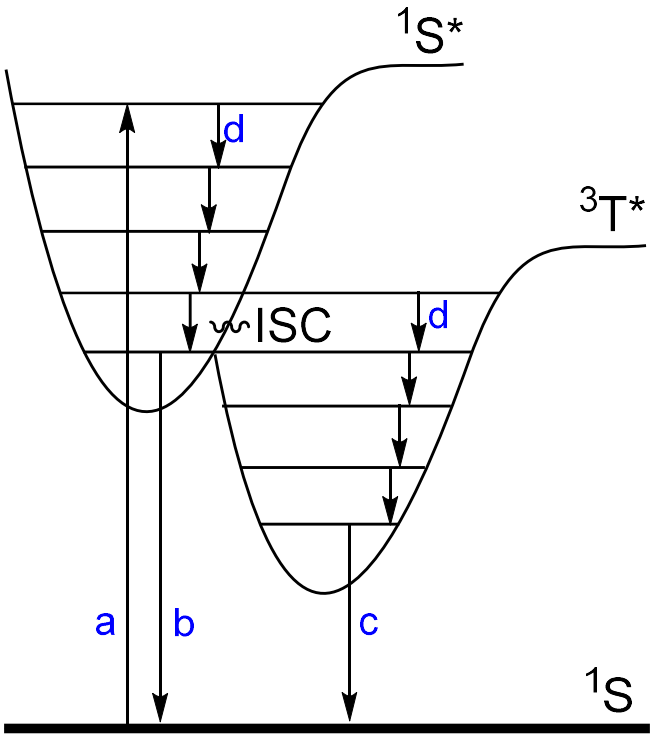

Figure 5.1: Simplified Jablonski diagram depicting intramolecular relaxation mechanisms following photon absorption from the ground state.

The absorption of a photon from a ground state (Figure 5.1, a) to an excited state proceeds a cascade of potential electronic and structural rearrangements.[18–22] For the purpose of this discussion, we restrict ourselves to a model with a singlet excited state. As an electron is promoted from the highest occupied molecular orbital (HOMO), the electronic transition to an isostructural excited state is incredibly fast. This state can then decay in energy by intramolecular vibrational modes (d) back to the ground state, or to the lowest energy singlet excited state geometry and fluoresce (b). In the case of transition metal photosensitizers and some extended π systems, intersystem crossing can occur (ISC) at a point of Franck-Condon overlap of identical geometry.[19,23,24] Assisted by spin-orbit coupling, the orientation of the model system undergoes a Laporte forbidden transition to a higher multiplicity. As a result, the lifetime of these higher multiplicity excited states is considerably longer, and decay through vibrational cooling (d) or

phosphorescence (c).[23] A firm grasp of these mechanism allows for the rational design of photosensitizers.

When considering the capture of light, whether by nature or engineering, there are three desirable properties of a functional photosensitizer: First, the efficient absorption of visible light is essential. [4,15,25] Radiation from the sun is primarily in the visible region of the spectrum, but also consists of infrared and ultraviolet wavelengths, which are more difficult to capture. The former is low energy light and easily lost as heat while the latter is high energy, relatively low in abundance, and destructive.

Second, a photosensitizer must possess reversible reduction/oxidation processes. Electron donation/acceptance from the excited state constitutes a major reorganization of the electronic structure of the photosensitizer. The molecule must be stable in these intermediate species. A straightforward design principle for reversible redox events is extended conjugation; utilizing π clouds to delocalize radical character has been shown to be an efficient route for redox stability.[26–28] Another is steric protection of electronically vulnerable positions,[29] where redox mediated chemical reactions may occur. Bulky hydrocarbon substituents like alkyl and aryl groups are not very polarizable and can shield heteroatoms, as well as electrophilic and nucleophilic resonance contributors.

Finally, the photosensitizer should have a reasonably long-lived excited state, dependent upon the application. For the excited state of a photoredox catalyst to act upon a substrate or transfer an electron, it must endure for some time, on the scale of nanoseconds or longer.[14,16,17] As molecular LEDs, the excited state decay should not be instantaneous, but not persist into milliseconds.[30,31] These examples are far from the breadth of potential applications and target

properties. In general, a triplet state is often a design principle to achieve longer lifetimes, as previously discussed.

Designing molecules that are luminescent, either by fluorescence or phosphorescence, is a common method of convenience in quantifying the energy of these excited states. By coupling wavelength of the emission with the potential of the associated redox event, the energy of can be derived from the Rehm-Weller formalism[32] for excited state potentials.

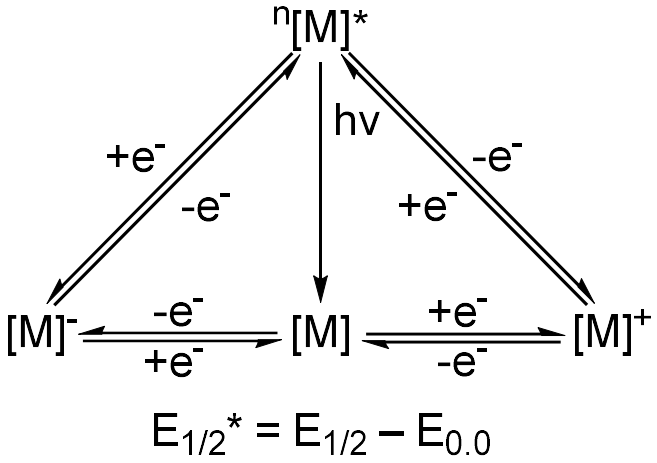

Figure 5.2: Latimer diagram depicting the approximation of excited state potentials from coupling redox events and photon absorption.

Here is where the introduction of metal centers becomes of beneficial design principle. Spin-orbit coupling contributions allow for easier ISC transitions, and as a result, much effort in the last few decades has been put into understanding the photo-physics of hallmark photosensitizers, $[Ru(bipy)_3]^{2+}$ [16,19,21,33] and $[Ir(ppy)_3]^{2+}$.[14,17,34] These electron rich metal centers are coordinated to redox non-innocent ligands and have been shown to operate by a metal-to-ligand charge transfer mechanism in the excited state.

Conversely, complexes with d^0 metals like zirconium (IV), titanium (IV), and niobium (V) have no accessible metal-centered electrons to excite. By using electron rich ligands with these

metals, one can access the "reverse" ligand-to-metal charge transfer (LMCT) pathway, which is considerably less common.[29,35–40] Work in this lab has recently reported a few generations of zirconium (IV) bis-PDP complexes[41,42] that are amendable to this charge transfer mechanism, and demonstrably potent photoredox catalysts. Further, studies in collaborations with the Castellano group have shown these complexes relax via a thermally activated delayed fluorescence (TADF),[29] where the triplet and singlet states are relatively close in energy. In this mechanism, after the absorption of a photon, ISC and reverse ISC (rISC) establish an equilibrium. When the rate of ISC and rISC are roughly equivalent, this leads to a markedly long lifetime with limited Stokes shifting compared to phosphorescent lumiphores.

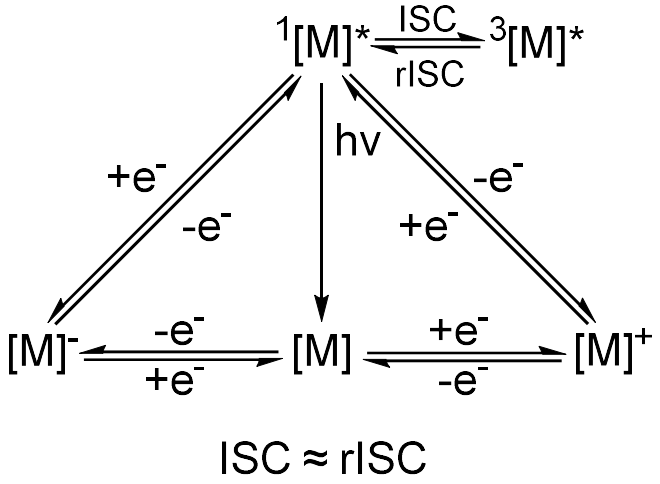

Figure 5.3: Latimer diagram depicting the Rehm-Weller formalism for estimating excited state potentials including the equilibrium between the singlet excited state and the triplet excited state where the energy of ^{1}M* is comparable to ^{3}M*, and ISC is roughly equivalent to rISC.

The culmination of this work has led to more questions about the fundamental nature of these specific Zr-based photosensitizers. In effort to address these hypotheses, which will be discussed in the next section of this chapter, a series of structurally similar species bearing LX_2 pincer ligands were prepared and characterized.

5.2 Structure-Property Relationships in LX_2 Pincers

One hypothesis for the performance of the zirconium pyridine dipyrrolide system is that the PDP ligand is responsible for the base luminescence of the molecule, as the ligands themselves are luminescent. By studying the photophysical properties of the ligand we can attempt to separate new features from the molecular photosensitizer and its component parts. In this line of thinking, it is the addition of a coordinating heavy atom that ISC becomes a feasible mechanism. It is also hypothesized that the orthogonal orientation of the two PDP ligands relative to each other has some bearing on the photoluminescent properties. As a result, efforts to study monomeric and dimeric species of the PDP ligand were made and are discussed here. This study will focus on the $^{Mes}PDP^{Ph}$ derivative of the PDP scaffold, as it is most heavily applied to the rest of this body of work.

Initial observations of $^{Mes}PDP^{Ph}$ dynamics occurred in solution while taking NMR spectra. It was found that the speciation of pure material was solvent dependent with respect to polarity, with a heavy influence from hydrogen bonding contributions (Scheme 5.1).

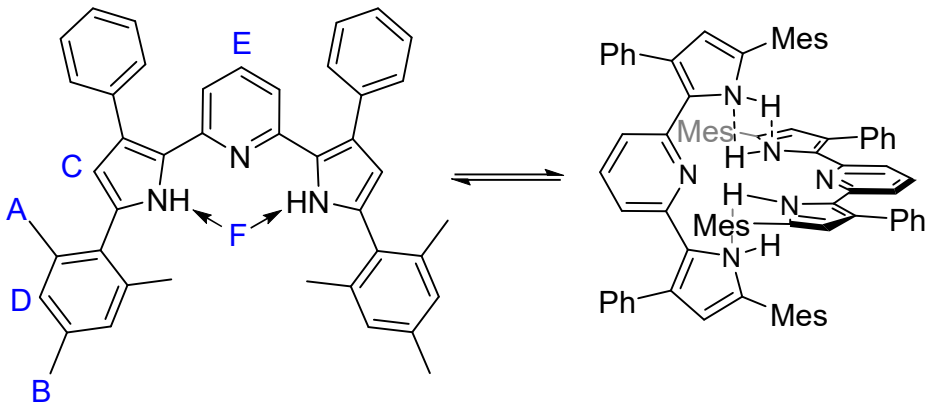

Scheme 5.1: Depiction of the monomeric and dimeric isomers of $^{Mes}PDP^{Ph}$ with assignments of spectroscopically distinct protons A-F. The selected proton assignments represented on the monomeric form will also be represented on the dimer in the same positions.

With this in mind, ^{1}H NMR spectra of ^{Mes}PDP^{Ph} were measured both in deuterated tetrahydrofuran as well as deuterated benzene. As expected, these solvents were sufficient to drive the molecule to its respective monomeric and dimeric state, depicted in Figure 5.4.

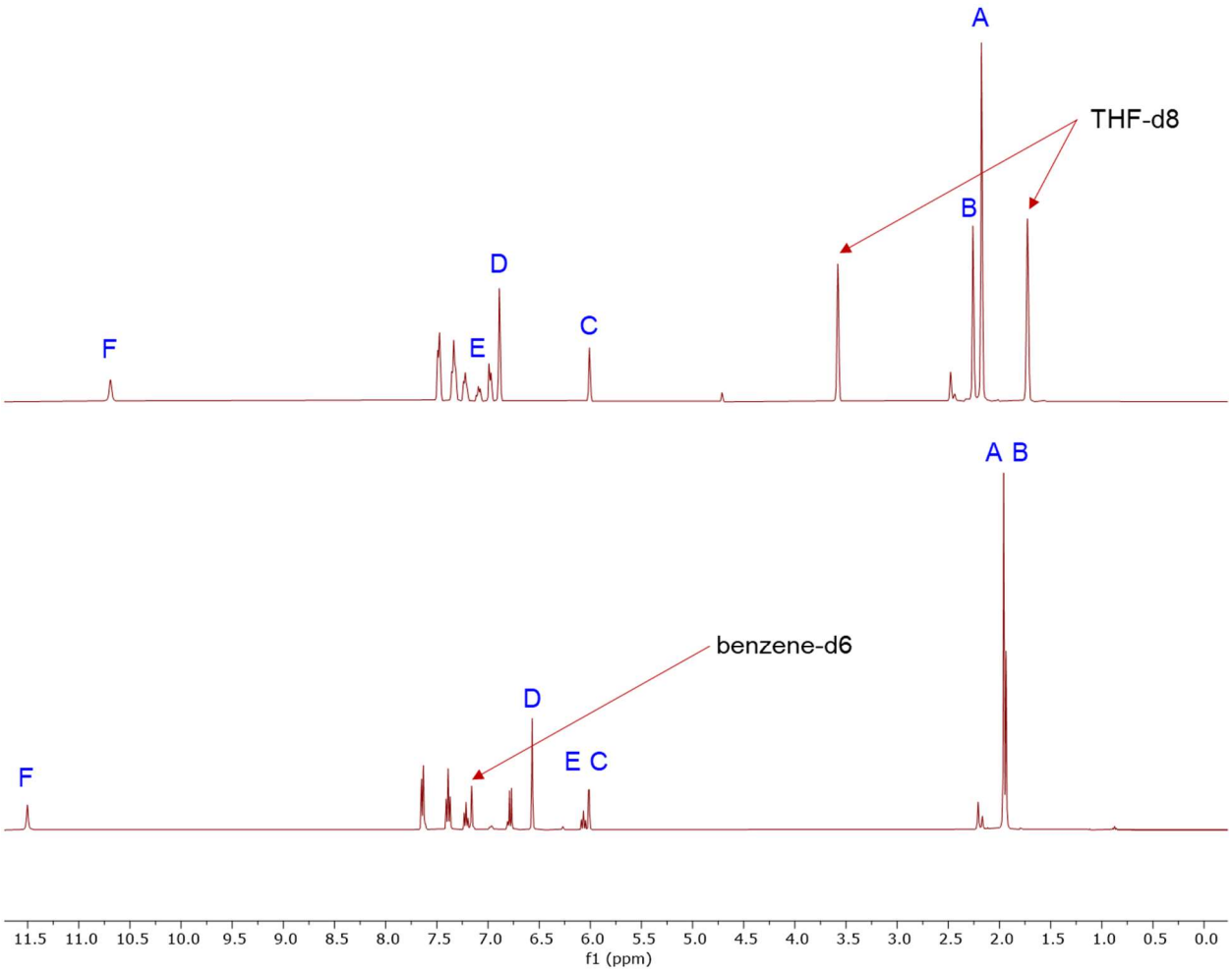

Figure 5.4: ^{1}H NMR spectra of ^{Mes}PDP^{Ph} in THF-d_8 and benzene-d_6, illustrating the solvent dependency of speciation between isomers.

With the two isomeric extremes identified, variable temperature ^{1}H NMR spectroscopy in chloroform was performed to illustrate the presence of a dynamic equilibrium. In the chosen solvent, both forms are present in an approximately 1:1 ratio at room temperature, slightly leaning toward the dimer. We would expect there to be a change in concentration of each species with

variable temperature if the process an equilibrium, where the monomer freely dimerizes and vice versa.

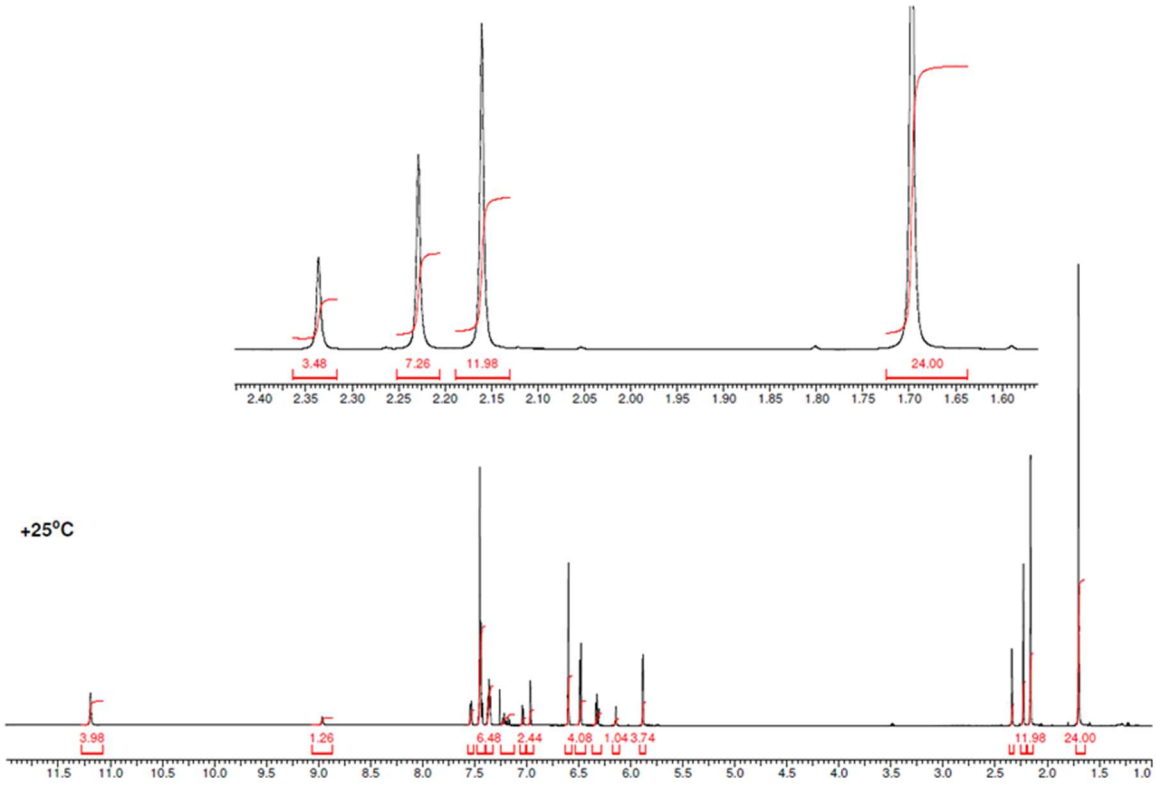

Figure 5.5: ^{1}H NMR spectra of ^{Mes}PDP^{Ph} in $CDCl_3$ collected by Dr. Novruz Akhmedov, depicting the relative integration of mesityl -CH_3 resonances of both isomers at room temperature.

By probing the region of the spectrum associated with the pyrrolic nitrogen bound protons, we were able to observe an increase in the relative concentration of the monomer compared to the dimer as the temperature increased to 60 ˚C (Figure 5.6). These data provide evidence that the observed speciation is a dynamic equilibrium, rather than an A to B irreversible process. A more rigorous kinetic study of this equilibrium was not performed, as isolation of each exclusive isomer had already been demonstrated, and there was no useful data to be garnered from such an experiment. This VT study was largely qualitative in order to confirm our hypothesis that the dimerization was a dynamic process.

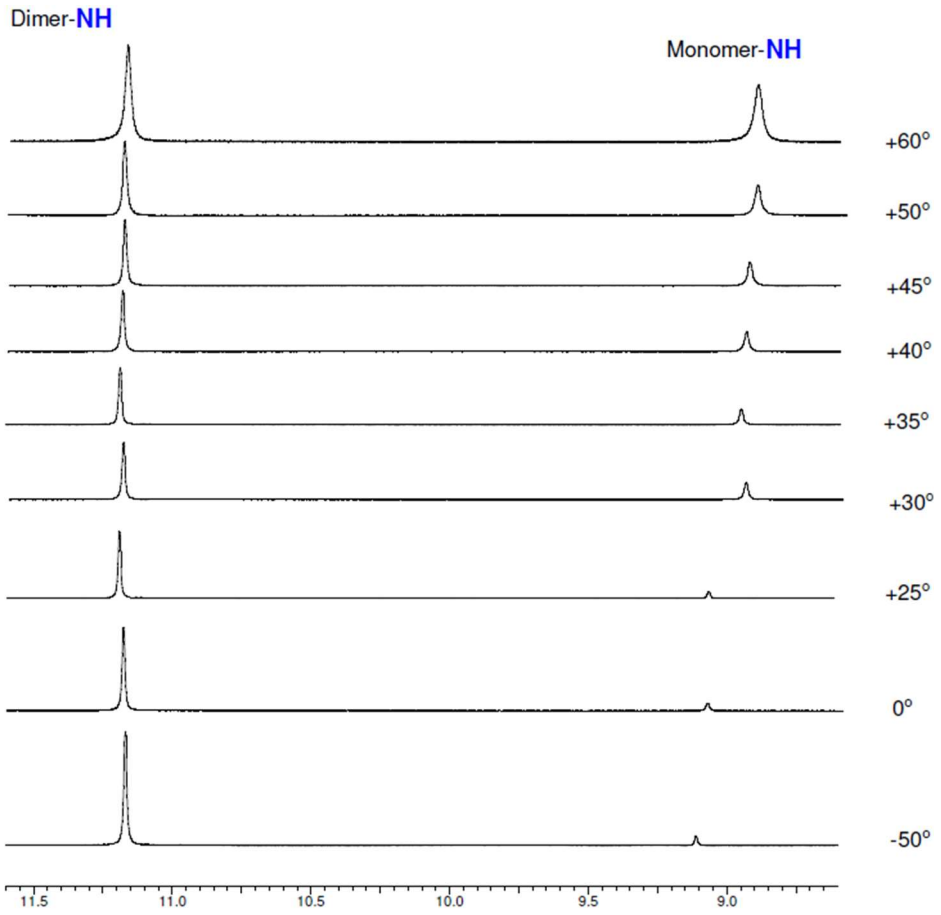

Figure 5.6: ^{1}H NMR spectra of ^{Mes}PDP^{Ph} in $CDCl_3$ collected by Dr. Novruz Akhmedov, depicting the relative intensity of the pyrrolic proton of each isomer as a function of temperature.

Solid state isolation by careful recrystallization of pure material in polar and nonpolar media allowed access to the static structures of each end of the equilibrium. Single crystals of the monomer and dimer were grown from slow evaporation of tetrahydrofuran and vapor diffusion of pentane into toluene, respectively.

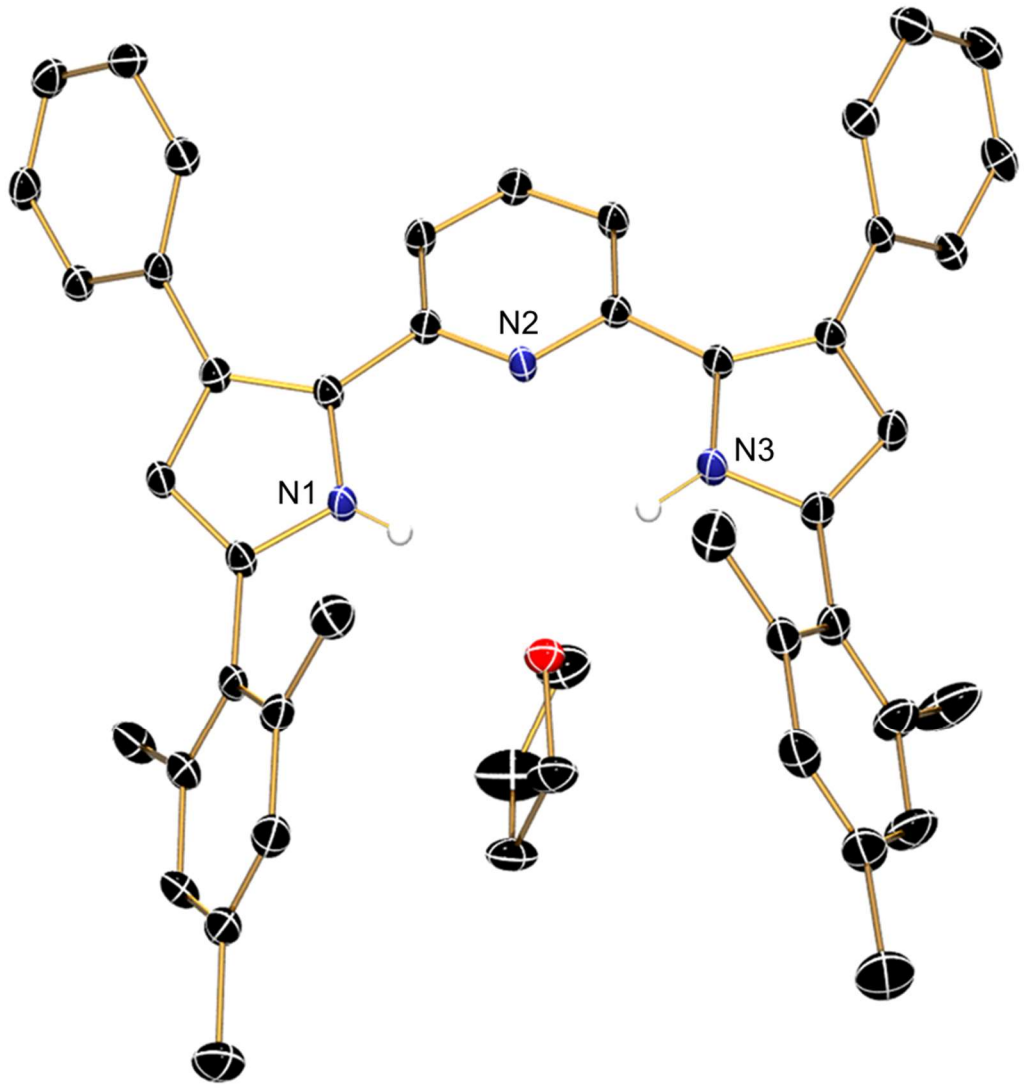

Figure 5.7: ORTEP depiction of $H_2^{Mes}PDP^{Ph}$ at 50% ellipsoid probability. Solvent of crystallization and hydrogen atoms (with the exception of N bound hydrogen atoms) were omitted for clarity.

The monomer of $H_2^{Mes}PDP^{Ph}$ crystallized in the triclinic space group $P\bar{1}$ with a unit cell volume of 2241.2(2) $Å^3$ and two molecules per cell. The refined structure gave the asymmetric unit depicted in Figure 5.7. The monomer co-crystallized with a molecule of tetrahydrofuran in the pocket between the mesityl substituents, as anticipated, which is disordered over two positions. There is also another molecule of THF that was amendable to refinement (not depicted), however, a non-integer value of

residual THF was squeezed from the unit cell. A void with a volume of 275 Å^3 was calculated to contain 63 unmodeled electrons, assigned to 0.75 equivalents of the disordered solvent.

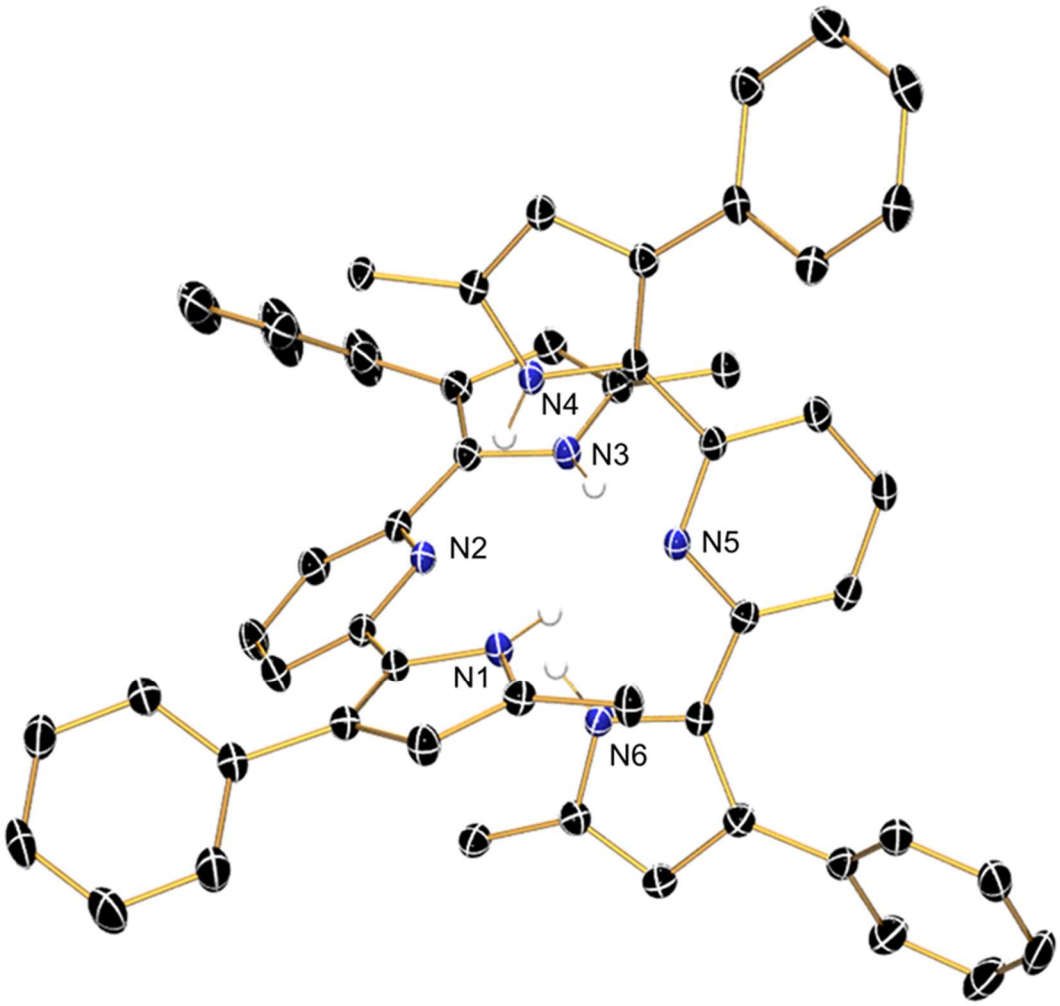

Figure 5.8: ORTEP depiction of $H_4(^{Mes}PDP^{Ph})_2$ at 50% ellipsoid probability. The mesityl substituents on each pyrrole were truncated from the *ipso* carbon to improve the depiction of the hydrogen bonding interactions at the center of the dimer. Solvent of crystallization and hydrogen atoms (with the exception of N bound hydrogen atoms) were omitted for clarity.

The dimeric isomer of $H_2{}^{Mes}PDP^{Ph}$ crystallized the triclinic space group $P\bar{1}$, with two molecules per unit cell (V = 3601.5(3) Å^3). The dimer resolved as four fragments which were in two pairs, rotated 90˚ with respect to each other on the same face of the cell, and 180˚ with respect to the opposing pair. These were related by symmetry to give the asymmetric unit depicted in

Figure 5.8, with a disordered pentane that was omitted for clarity. These crystal structures readily fit our expectations for the NMR data previously discussed and allowed us to move forward with some confidence in our assertions regarding the structure of the active chromophore in solutions of tetrahydrofuran and benzene, respectively.

With these data in hand, we were able to utilize the observed solvent polarity/isomer relationship to study the ligand both as a model for a monomeric fluorophore and orthogonal emissive dimer. This photophysical characterization was carried out primarily by Dylan Leary, a PhD candidate in our group. The data generated by his efforts will be clearly indicated in the figure captions, as his time and expertise are invaluable to this work. His thesis will deepen this discussion on the dynamic processes that occur during excitation/relaxation of photoactive species. The preliminary data are presented here for the purpose of our comparison between PDP and PDA moieties.

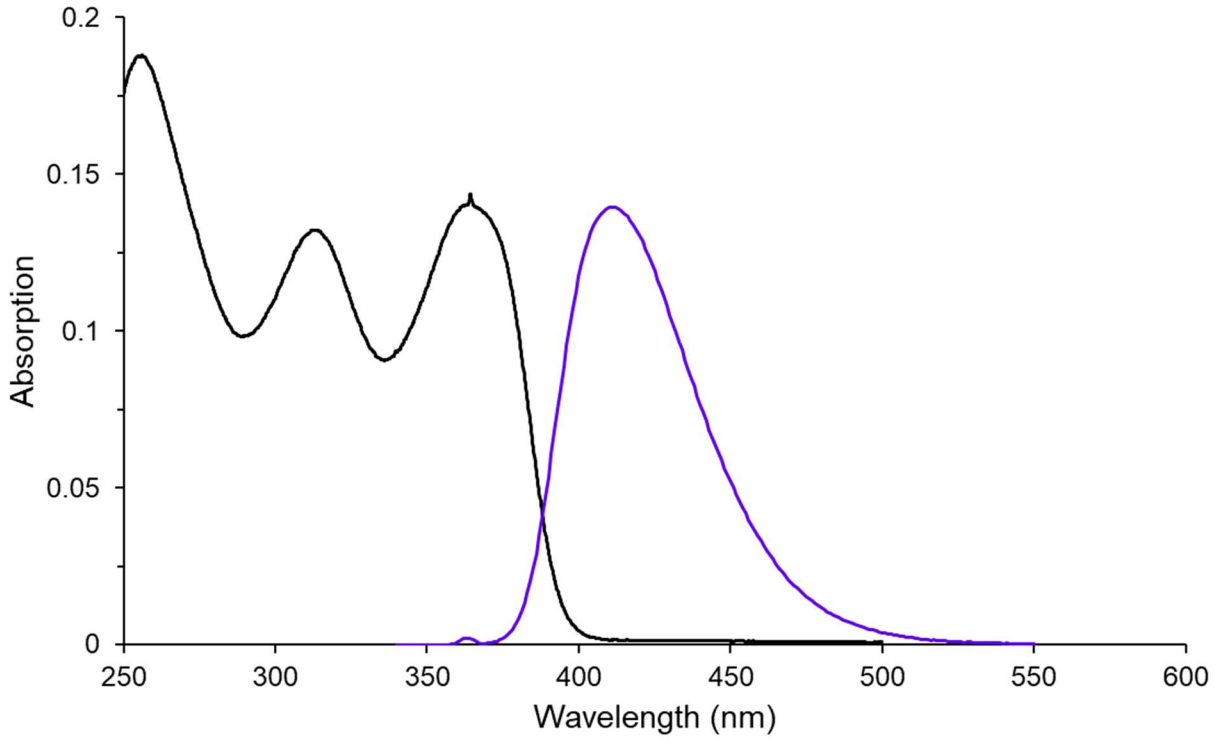

Figure 5.9: UV-vis spectrum of $^{Mes}PDP^{Ph}$ taken in THF under nitrogen utilizing J-Young adapted quartz cuvettes. The emission signal depicted has been normalized to the absorption spectrum. These data were provided by Dylan Leary.

The lowest energy electronic transition of the H_2 $^{Mes}PDP^{Ph}$ monomer was promoted by light with a peak maximum 365 nm which trailed into the violet region of the spectrum. This is consistent with the off-white coloration of the pure ligand that indicates only weak absorption of visible light. In tetrahydrofuran solution, no emission is observed with the naked eye in ambient light. When subjected to fluorometry, a strong emission band was observed at 415 nm, giving a Stokes shift of 50 nm (3,300.87 cm^{-1}) from the absorption. The small magnitude of this shift suggests a fluorescent relaxation mechanism, where thermal relaxation to a lower energy emission event is relatively minimal. This conclusion is supported also by lifetime measurements, which provided a value of $\tau = 2.18$ ns.

The electronic structures of these transitions were also investigated computationally to gain insight into our empirical observations. This was done using ORCA[43,44] semiempirical

computational methods. Following geometry optimization, TD-DFT was performed at the B3LYP level of theory utilizing the def2-TZVP(-f) basis set. It is noted that calculated transition states rely on a static structure, which are not representative of the solution state dynamics. We should consider these insights as only a slice of a statistical distribution of transitions that are similar in energy from slightly different geometries, but reasonably representative of the empirical observation.

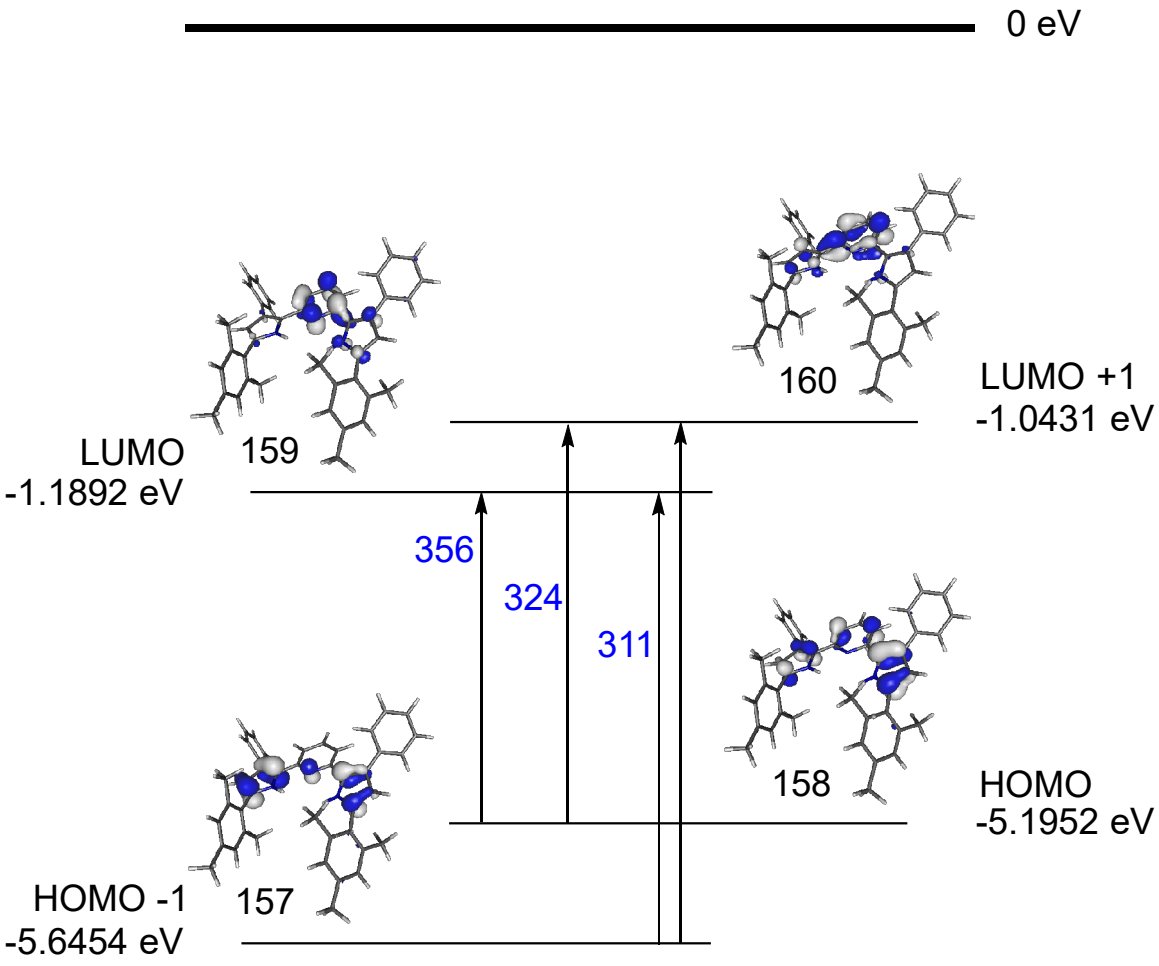

Figure 5.10: Calculated transitions of the $^{Mes}PDP^{Ph}$ monomer with depictions of major molecular orbital contributions of each transition.

The wavelength of each transition, depicted in blue in Figure 5.10, are representative of three lowest energy transitions that were calculated. The predicted transitions are slightly blue

shifted compared to the empirical data, though this is likely an artifact of the preceding geometry optimization. The molecular orbitals are depicted along with the transitions between these states, so that a qualitative visual representation of the reorganization of the electronic structure of each transition can be readily identified. This analysis shows what appears to be an intramolecular charge transfer between the pyrrolic "donor" and pyridinyl "acceptor" portions of the molecule.

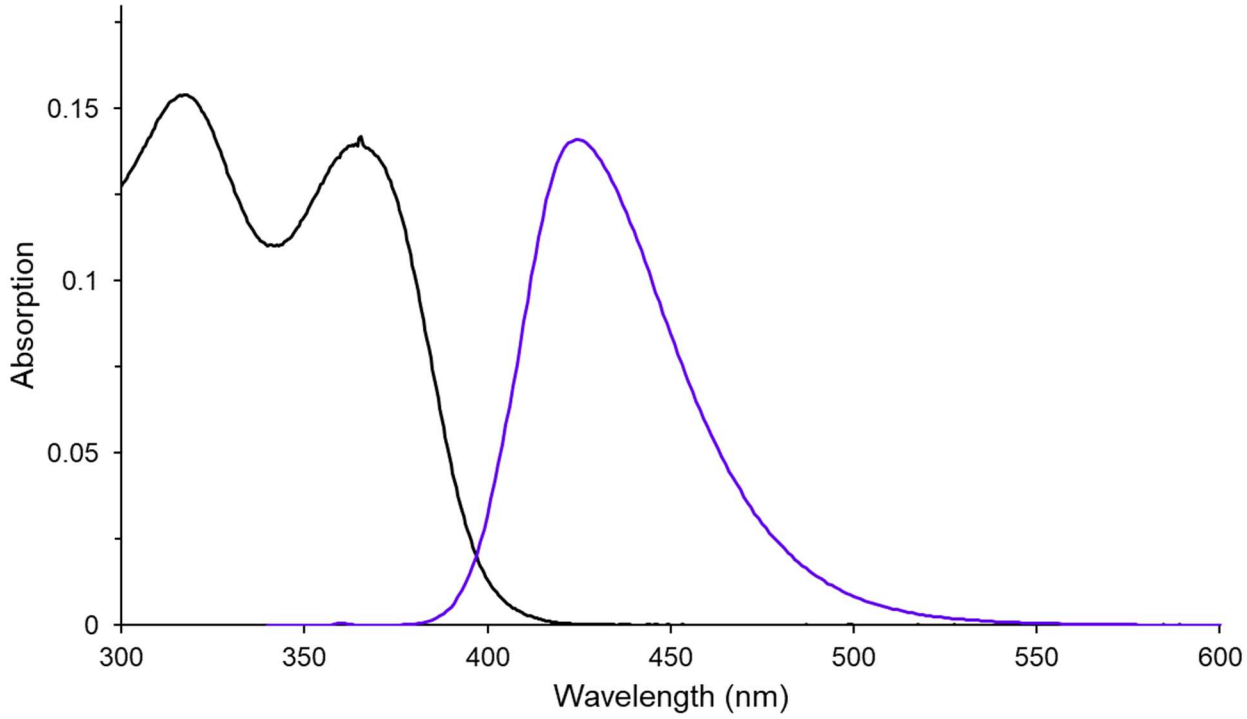

Figure 5.11: UV-vis spectrum of $^{Mes}PDP^{Ph}$ taken in benzene under nitrogen utilizing J-Young adapted quartz cuvettes. The emission signal depicted has been normalized to the absorption spectrum. These data were provided by Dylan Leary.

These data were then compared to a solution of the pure material in benzene. However, as benzene absorbs UV radiation at a lower wavelength than 275 nm, this UV-vis spectrum depicted in Figure 5.11 is given only from 300 nm to 600 nm. Interestingly, the lowest energy absorption is unchanged from 365 nm, where the emission maximum is 425 nm. These electronic absorptions were modelled by calculation in the same fashion as the proceeding study.

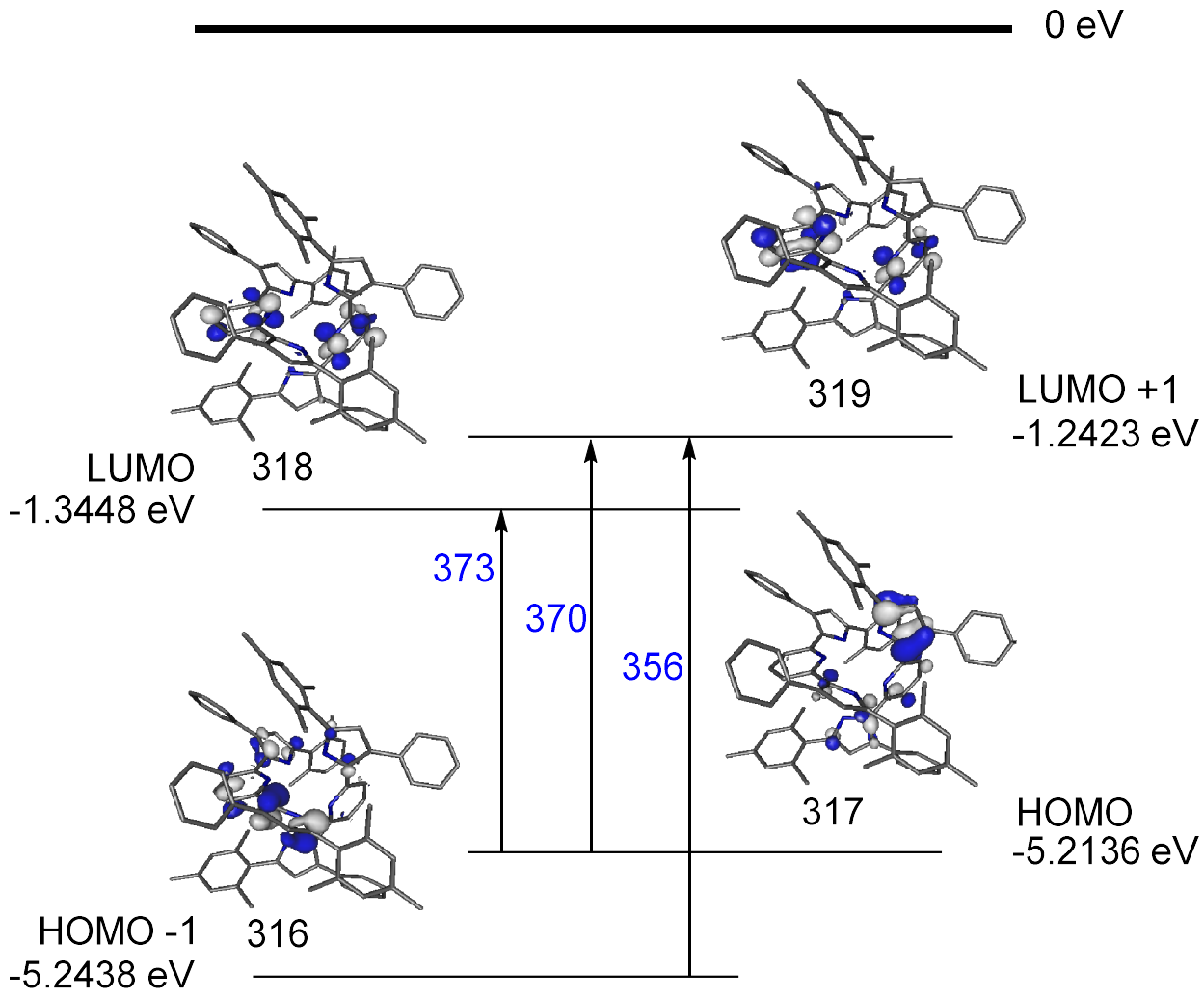

Figure 5.12: Calculated transitions of the ^{Mes}PDP^{Ph} dimer with depictions of major molecular orbital contributions of each transition.

The observed transitions are significantly red shifted with respect to the monomeric species, where the HOMO and HOMO-1 appear to be a nearly degenerate set of pyrrolic donors on either molecule, and the LUMO and LUMO+1 appear as a set of pyridinyl acceptors. The shape of these four orbitals are comparable to those of the corresponding HOMOs and LUMOs calculated for the PDP monomer. It is likely due to the stabilization of these molecules with respect to each other that allows for the lowered barrier for intramolecular electronic transitions, where

structural reorganization is mitigated by hydrogen bonding. This is further supported by our calculations of each respective LUMO, where the monomer is 0.1556 eV higher in energy.

The culmination of these data suggests a donor/acceptor relationship between the pyrrole and pyridine fragments of the ligand, respectively, which is stabilized by resonance contributions from an extended planar π system. The π* excited state of each isomer is responsible for the observed luminescence, however, the Stokes shift of the emission is markedly different between these structures. This is likely due to the restricted vibrational modes in dimeric species, as opposed to the free monomer.

Considering our model, we anticipate that the neutral ligand may not be representative of the electronic structure of the metal-bound ligand. We specifically performed the following study due to the observations repeatedly made when using this molecule for synthesis: the deprotonated ligand is strongly luminescent in ambient light and temperature. The PDP nitrogen donors, be they either pyrrolic or pyridinyl, would be much more strongly polarized with zirconium than with protons, with a Zr-N electronegativity difference of roughly two.[45] In order to investigate these potential differences, the deprotonated compound was similarly characterized.

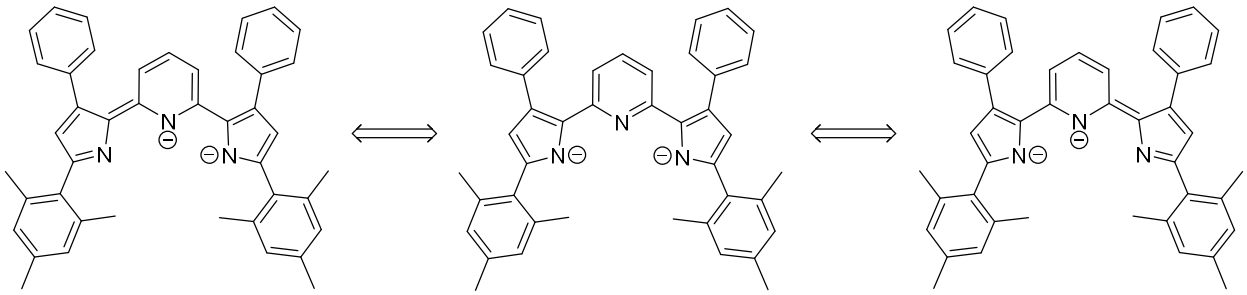

Scheme 5.2: Resonance structures of the deprotonated $[^{Mes}PDP^{Ph}]^{2-}$ ligand.

When considering the dianionic structure of the $[^{Mes}PDP^{Ph}]^{2-}$ ligand, it was noted that there is a statistically significant set of resonance contributions where the pyridine moiety is more electron rich. Recalling the calculations modelling the neutral ligand HOMO/LUMO, we would

expect the electronic structure of these fragments to be more appreciably mixed. This would likely lead to an energetic overlap in the observed transitions, resulting in a stabilization of the LUMO. Further, due to the deprotonation of the electron-rich pyrrole moiety, there would be a significant destabilization of the HOMO, shrinking the energy gap between these electronic states. With these hypotheses, characterization proceeded in a similar fashion to the neutral molecule.

These measurements were much more sensitive to air, especially its water content, as the lithio-pyrrolide moiety is highly basic. For this reason, ^{1}H NMR measurements were collected immediately after sample preparation in a J-Young adapted NMR tube in benzene-d_6. The spectrum of ^{Mes}PDP^{Ph} is expected to lack an N-H signal (>δ 8.0 ppm), but otherwise are uninformative to the absolute structure.

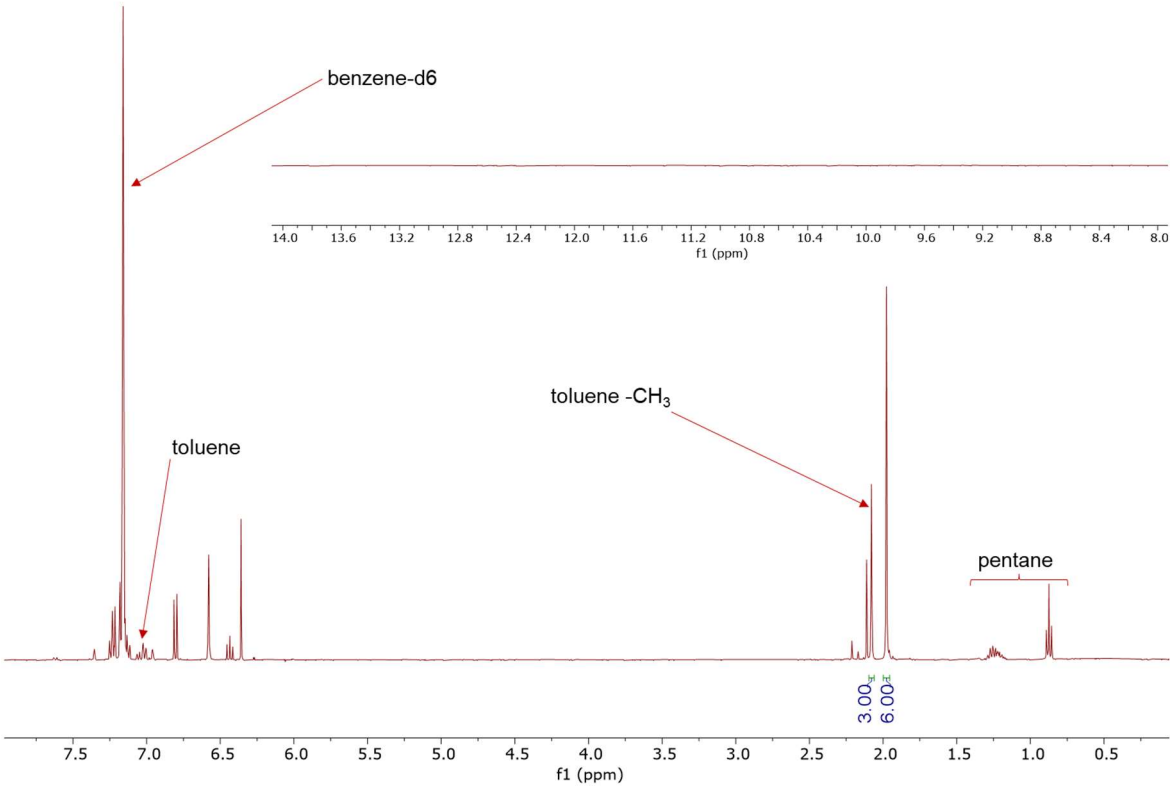

Figure 5.13: ^{1}H NMR spectrum of $Li_2{}^{Mes}$PDP^{Ph} in benzene-d_6 with relative integrations of the mesityl -CH_3 moieties as reporters. Inset: region from 14 – 8 ppm, where the N-H resonances would be expected. These data were provided by Dylan Leary.

Some solvent of crystallization is evident in the spectrum, but the lack of N-H resonances is clear. Importantly, there appears to be only one unique species that arises as a product in benzene, which is consistent with our expectations for aromatic solvent. Unfortunately, due to the sensitivity of the complex, extended manipulations of the sample, such as freeze-pump-thaw degassing on a high vacuum line, collection of NMR data in THF-d_8 was not performed. However, if this behavior is entirely consistent with the neutral regime as the benzene-d_6 NMR spectrum would suggest, we would expect a monomeric form to dominate in ethereal solution, and these extremes to be isolable in the solid state. This hypothesis was probed by X-ray crystallography.

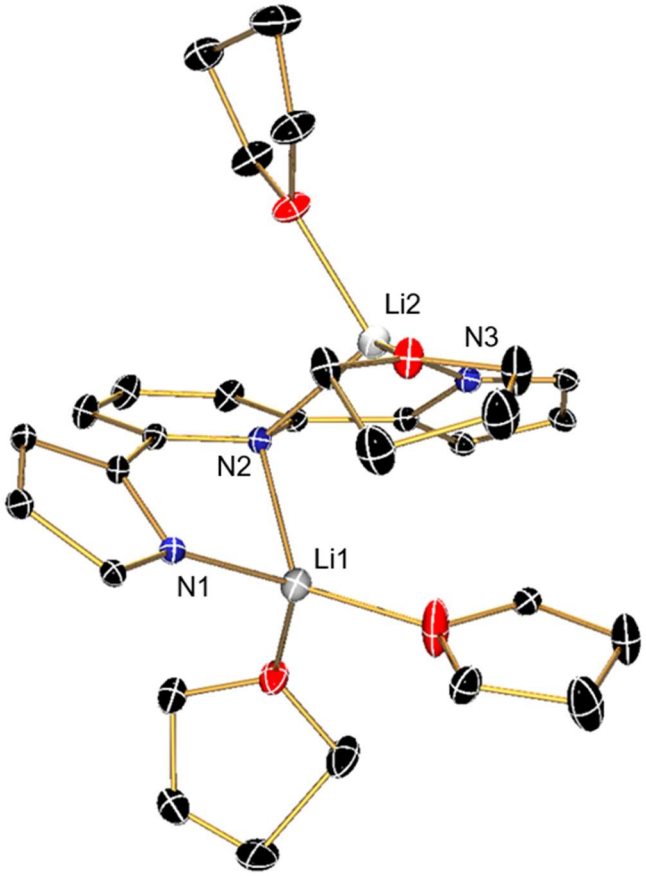

Figure 5.14: ORTEP depiction of $Li_2^{Mes}PDP^{Ph}$ at 50% ellipsoid probability. Solvent of crystallization, pyrrolide substituents, and hydrogen atoms were omitted for clarity.

The monomeric structure was isolated by slow evaporation of tetrahydrofuran at room temperature. The intensely orange crystals solved in a monoclinic $P2_1/n$ cell, with 1.5 molecules per cell. Each four-coordinate lithium ion is bound to a different pyrrolide donor and the same neutral pyridine donor of the $[^{Mes}PDP^{Ph}]^{2-}$ dianion and two tetrahydrofuran solvent molecules. The THF ligands on Li1 were disordered over two positions, but otherwise refined nicely. This tetrahedral moiety is favored for lithium ions, as represented in a wide variety of examples. The N-Li bonds are responsible for the torsion between either pyrrole and the central pyridine, 35.62˚ (avg) above and below the plane of the pincer. This results in a Li1-Li2 distance of is 3.214(4) Å, completely unassociated with each other, as expected for these cations.

The dimeric structure was isolated by the slow diffusion of pentane into a solution of freshly deprotonated ligand in toluene at low temperature. The bright yellow solid was resolved in a triclinic $P\bar{1}$ cell with two independent molecules per cell, with an equivalent of toluene co-crystallized in the asymmetric unit.

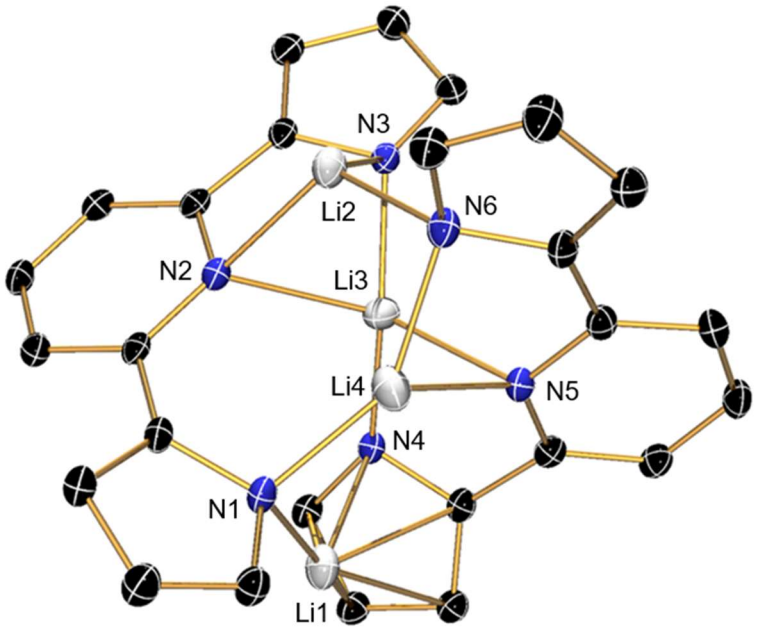

Figure 5.15: ORTEP depiction of $Li_4(^{Mes}PDP^{Ph})_2$ at 50% ellipsoid probability. Solvent of crystallization, pyrrolide substituents, and hydrogen atoms were omitted for clarity.

The relatively small ionic radius of the lithium counter cations allowed for all four to fit between the ligands, though entirely asymmetrically. This structure is not representative of the solution structure, as shown by the ^{1}H NMR spectrum to be D_{2d} symmetric (Figure 5.13) and indicates a fast equilibrium of different conformations on the NMR timescale.

The optical properties of these pyrrolide salts were obtained in a similar method to the neutral ligand, sealed under nitrogen in J-Young adapted cuvettes and rigorously anhydrous solvent. The concentrations of these samples are not put forward with confidence, due to potential degradation over the course of these experiments. To provide context, the standard concentration of analyte under optically dilute conditions for this work is 1×10^{-5} M. A single equivalent of water would halve the concentration of analyte to 5×10^{-6} M, and an equimolar concentration of the neutral species. As such, the resulting spectra are qualitative, so that wavelength of absorption and emission can be identified. These spectra are reported from 350 nm – 700 nm, in accordance with the limitation of benzene as a UV absorbing solvent.

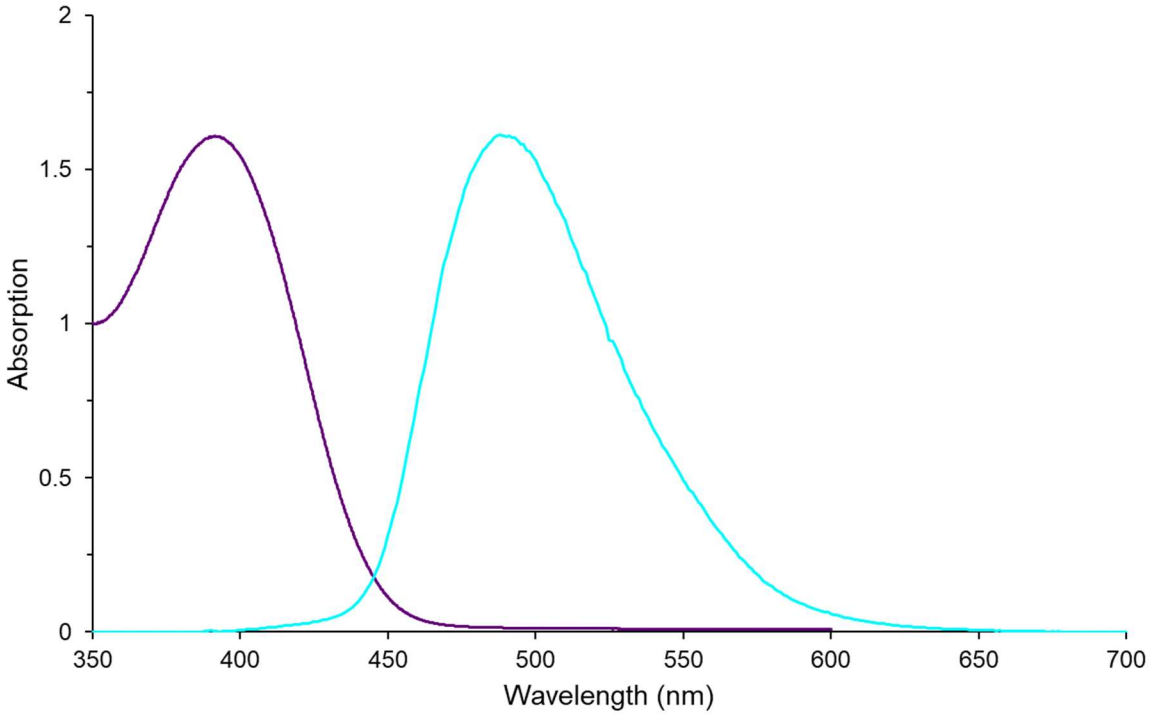

Figure 5.16: UV-vis spectrum of deprotonated $^{Mes}PDP^{Ph}$ taken in benzene under nitrogen utilizing J-Young adapted quartz cuvettes. The emission signal depicted has been normalized to the absorption spectrum.

The absorption profile of the deprotonated ligand in benzene solution is expected to be composed primarily of the dimeric species due to previous observations. The absorption maximum is slightly shifted towards 400 nm from the neutral species; however, the emission band is markedly shifted (from 425 nm to 490 nm). When these data were compared to deprotonated $^{Mes}PDP^{Ph}$ in tetrahydrofuran, significant overlap was observed.

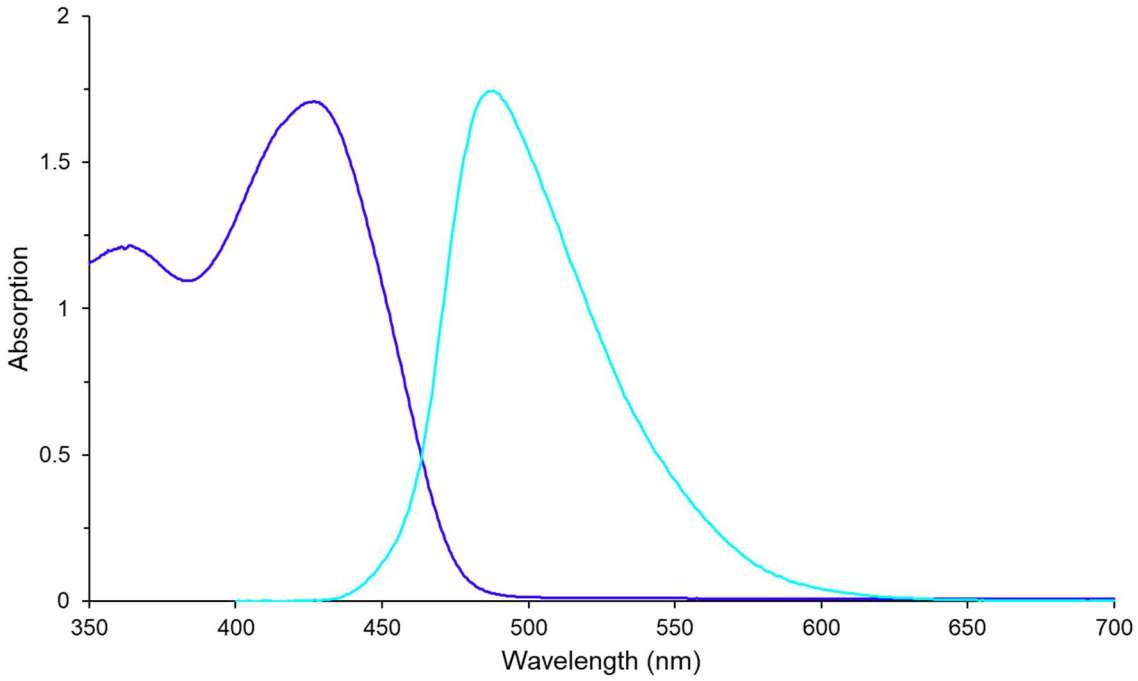

Figure 5.17: UV-vis spectrum of deprotonated $^{Mes}PDP^{Ph}$ taken in THF under nitrogen utilizing J-Young adapted quartz cuvettes. The emission signal depicted has been normalized to the absorption spectrum.

In tetrahydrofuran, the monomeric form is expected to be the primary species in solution. The absorption event is markedly unique from that of the deprotonated dimer (430 nm vs 390 nm); however, the emission event is nearly exactly that as was recorded in benzene. Due to THF's propensity to behave as a ligand for lithium cations, it is unlikely that the emissive species in THF solution is an isostructural dimeric species as anticipated in benzene. However, speciation of these solvates would be incredibly difficult to probe by empirical means, and is not being pursued at this time.

5.3 Synthesis and Characterization of Group 4 PDA Complexes

We intend to further investigate the zirconium bis-PDP system by probing the electronic structure of related compounds. By substituting the anionic nitrogen donor on the ligand from pyrrolide to amide, the effect is twofold. There should be a marked increase in electronic donation from the anionic X-type moiety *and* a break the aromaticity of the ligand backbone. Our investigation of this change will provide insight into the electronic structure required to do effective ligand-to-metal charge transfer.

While simple and straightforward to prepare, the pyridine diamide (PDA) LX_2 moiety has been largely overlooked in coordination chemistry. It was briefly considered as a supporting ligand for early metal catalysis, though it was often written off as a structural novelty, providing no remarkable activity. Its reported susceptibility to chemical oxidation also may contribute to the lack of reference in the literature. The electrochemical innocence of the ligand would likely inhibit activity in a system where varying oxidation states must continuously turn over.

Though the pharmaceutical and catalytic activity of PDA compounds and metal PDA complexes are documented in the literature, little is known about their photochemical or electrochemical properties. When comparing the PDA to the PDP ligand, the PDA ligand is a similar LX_2 type pincer ligand (Scheme 5.3). They each possess a central pyridine flanked by two chemically equivalent anionic nitrogen donors. It was proposed that utilizing the PDA ligand as a framework for a zirconium-based photosensitizer could further probe the nature of the ligand-to-metal charge transfer event.

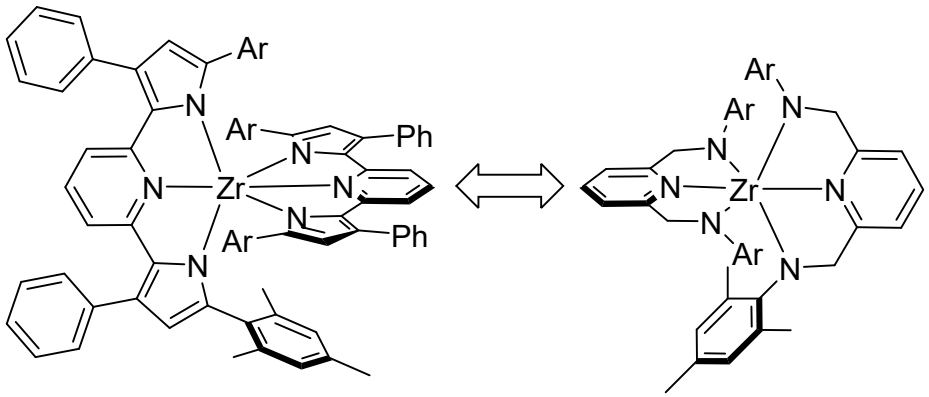

Scheme 5.3: Structural comparison of Zr(^{Mes}PDP^{Ph})$_2$ and Zr(^{Mes}PDA)$_2$.

The extended conjugation of the PDP ligand would be broken by isolating the ligand donor/acceptor pair in the PDA. The π donation of the amide nitrogen donor on the PDA would also be greater than that of the pyrrolide function, whose second lone pair participates in the aromaticity of the pyrrole heterocycle. This work will directly contrast the Zr(^{Mes}PDP^{Ph})$_2$ complex, reported by our group in 2020, which has shown remarkable stability even in the presence of air, water, and acid. This gave inspiration to the anilido moiety of the PDA ligand in an effort to make a bulky bis-PDA zirconium photosensitizer (Scheme 5.3). This modification would presumably provide steric protection of the inner coordination sphere and thereby inhibit degradation in solution.

From 2,6-pyridinecarboxaldhyde, most pyridine diimines can be generated via a Schiff-base condensation with anilines in alcoholic solvent with an organic acid catalyst. This work relied on two derivatives of this scheme: the para-tolyl[46] and mesityl[47] aryl moieties. Reduction of the intermediate pyridine diimine (PDI) occurs in a second step, same pot reaction with a mild reducing agent. These products are easily purified by recrystallization or filtration through a silica plug.

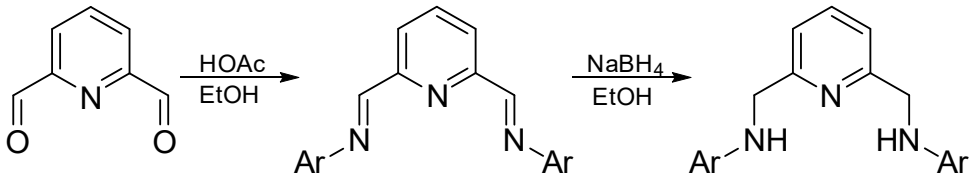

Scheme 5.4: General synthesis of PDA ligands via Schiff base condensation and subsequent hydride reduction.

These two PDA ligands were characterized by ^{1}H and ^{13}C NMR spectroscopy, available in Appendix 5.2. In the literature, the mesityl derivative was prepared by a different procedure, and was characterized by the same methods. It is noted that these compounds show no evidence of dynamic behavior on the NMR timescale, such as the case with the dimerization of the PDP species. However, neither PDA species have reported optical properties. As a result, UV-visible spectroscopy was performed on the ^{Tol}PDA derivative in anhydrous tetrahydrofuran.

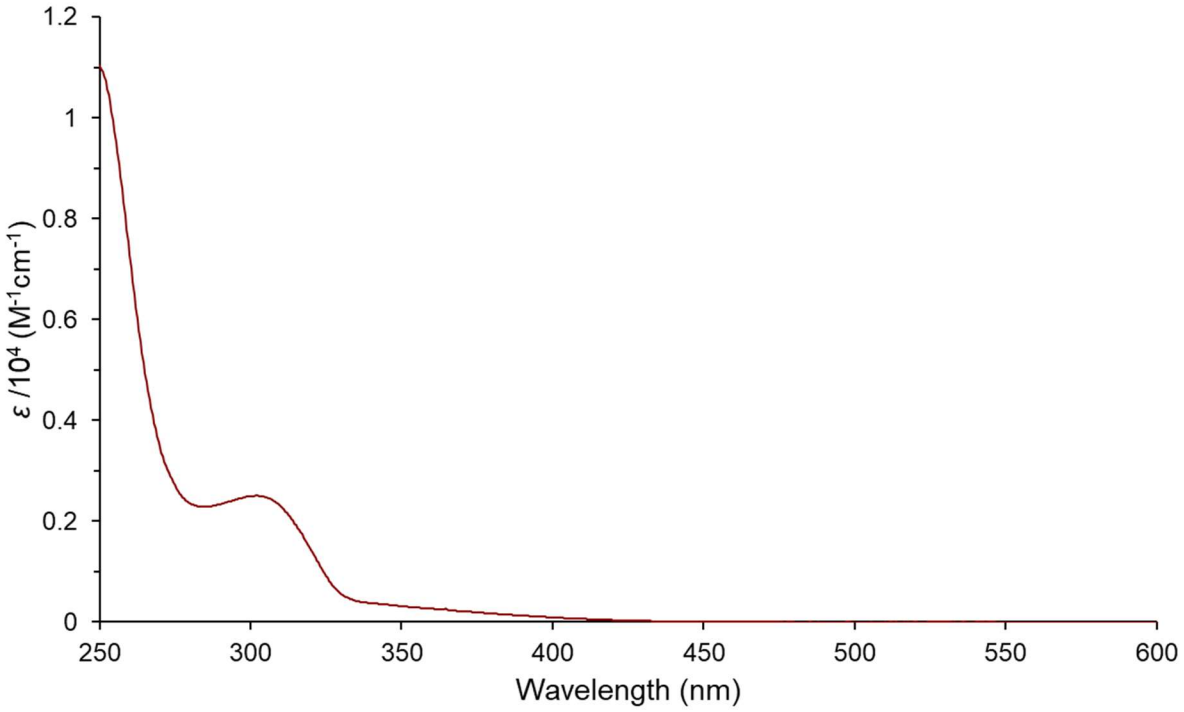

Figure 5.18: UV-visible spectrum of ^{Tol}PDA in anhydrous THF under nitrogen.

The absorption tailing into the purple region of the visible spectrum is weak and would account for the off-white coloring of the pure solid. No emission was observed at room temperature. The optical properties of ^{Mes}PDA derivative were not recorded due to a persistent bright orange impurity but would not be expected to be appreciably dissimilar. These data will act as a baseline for the following discussion of metal ligated species.

Attempts to synthesize the bis-^{Mes}PDA zirconium complex led to the isolation of (^{Mes}PDA)Zr(Bn)$_2$. Regardless of ligand excess, it quickly became apparent that the mesityl moiety was sufficiently sterically demanding to block the addition of the second PDA ligand to the metal center. In a vial blacked out with tape, tetrabenzylzirconium was dissolved in benzene with good stirring. A separately prepared solution of ^{Mes}PDA was added dropwise before the reaction was sealed and excluded from light for a few hours. The product was precipitated with excess pentane at low temperature (38% yield). It was not possible to get a reliable elemental analysis as both the zirconium starting material and product are markedly light sensitive, and prone to rapid decomposition in ambient light and temperature.

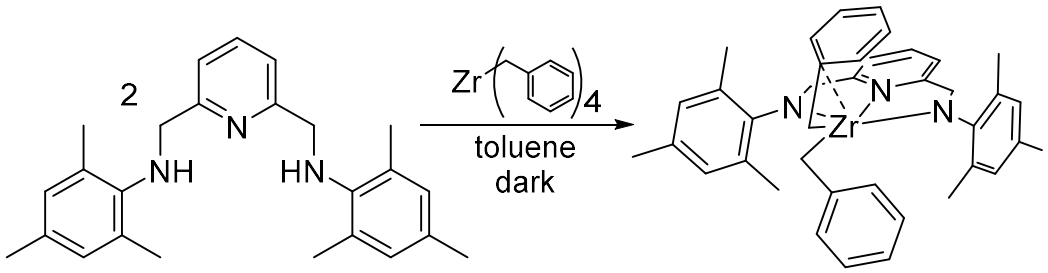

Scheme 5.5: Synthesis of (^{Mes}PDA)Zr(Bn)$_2$.

The chemically equivalent benzylic protons of the PDA ligand show a sharp singlet (4H) at δ 4.54 ppm. The mesityl methyl protons appear at δ 2.48 ppm (12H) and δ 2.14 ppm (6H), respectively, in 2:1 ratio. None of the protons on the benzyl substituents were identifiable in the collected spectra, indicating a rapid thermal reorganization on the NMR timescale. This would be

consistent with a C_{2v} symmetric structure in solution, as indicated by the equivalent mesityl methyl groups in the 2 and 6 positions.

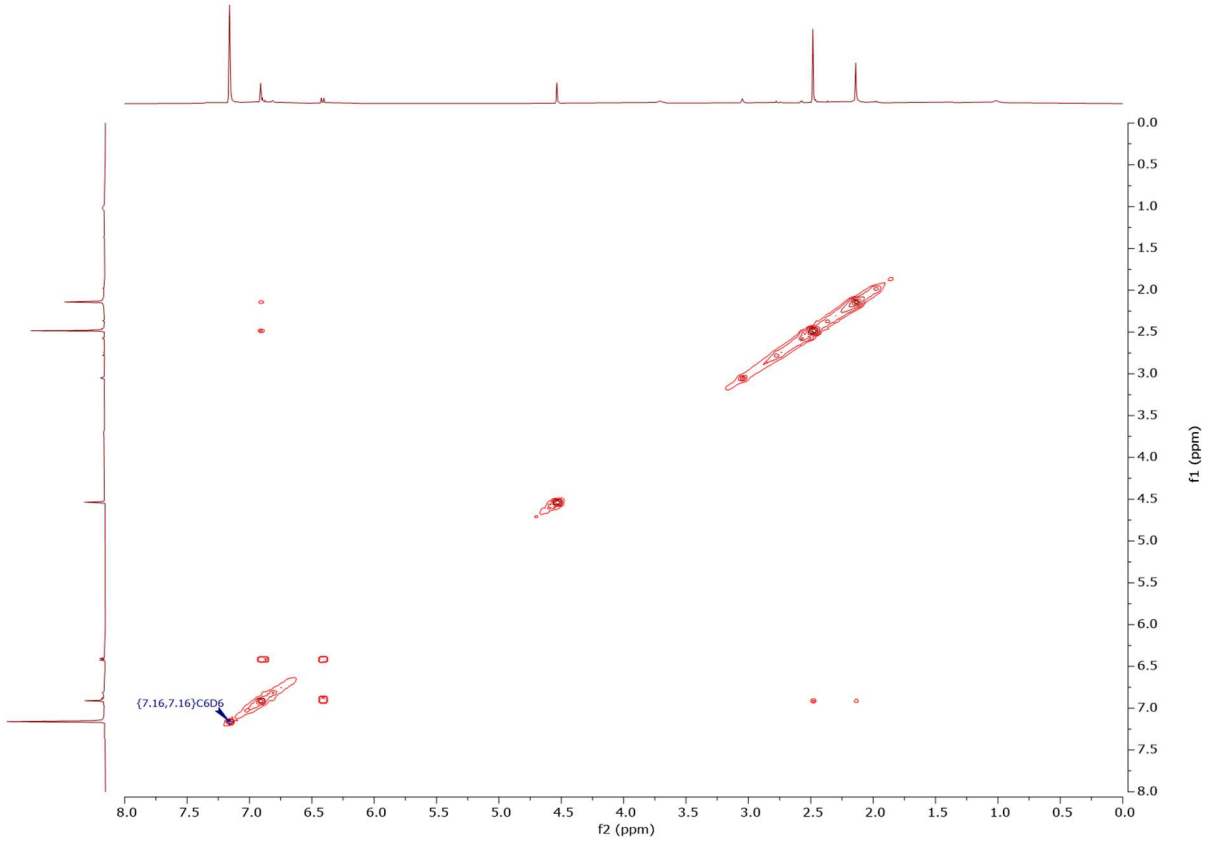

Figure 5.19: (HH) COSY NMR spectrum of (^{Mes}PDA)Zr(Bn)$_2$ in benzene-d_6.

The aryl protons of the molecule were identified at δ 6.91 ppm (s, 4H), δ 6.90 ppm (t, 1H), and δ 6.41 ppm (d, 2H). The singlet, assigned to the mesityl substituents, and the 4-pyridine triplet were significantly overlapped, and their integrations taken together (~ 5H). In order to ensure the accuracy of this assessment, a proton correlated COSY NMR spectroscopy was performed (Figure 5.19). The result of this analysis shows the triplet at δ 6.90 ppm and doublet at δ 6.41 ppm are coupled together (J = 8 Hz), while the singlet at δ 6.91 ppm exhibits ^{3}J coupling to the singlets at δ 2.48 ppm and δ 2.14 ppm. The lack of singlet splitting in this weak spin system can be rationalized by the local aromatic system of the mesityl substituent, where the coupling constant

is incredibly small. Further, the doublet at δ 6.41 ppm, assigned as the two equivalent protons in the 3-pyridine position, shows a weak Nuclear Overhauser spin-crossover with the triplet at δ 6.90 ppm, but not the singlet at δ 6.91 ppm, indicating its proximity to the 4-pyridine proton.

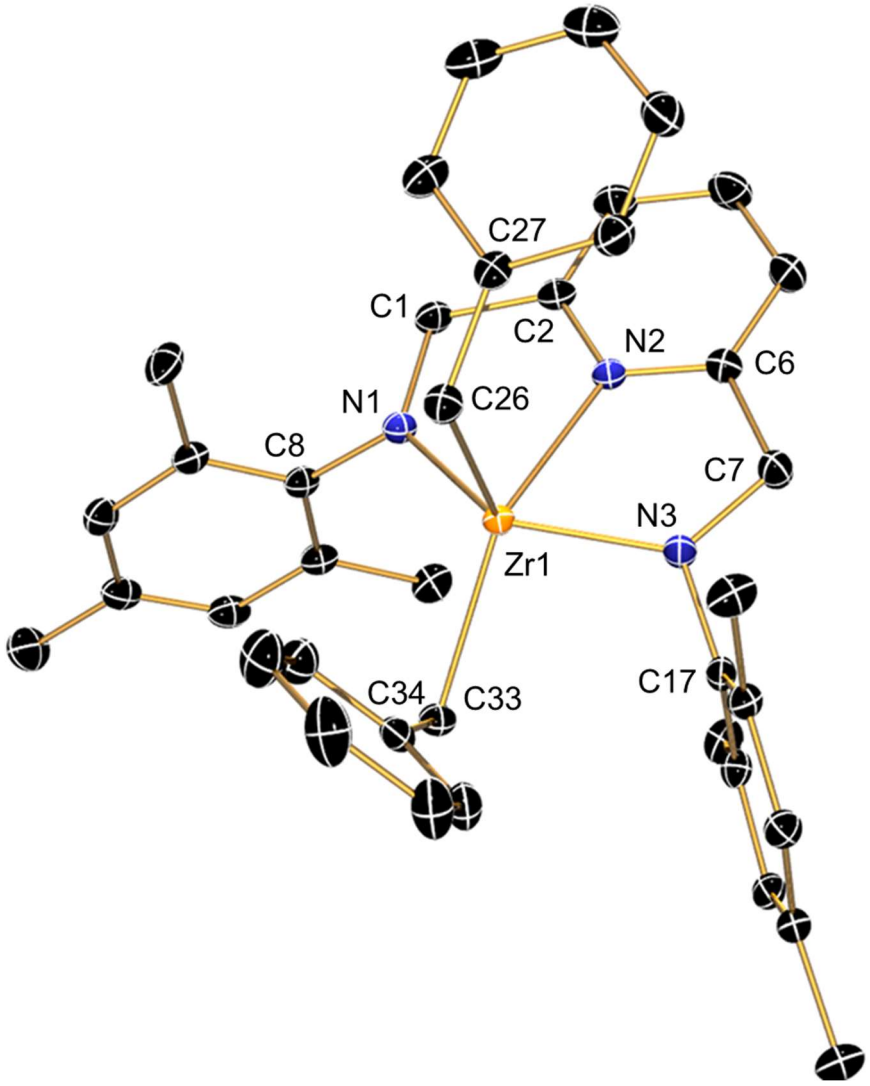

Figure 5.20: ORTEP depiction of (^{Mes}PDA)Zr(Bn)$_2$ at 50% ellipsoid probability. Solvent of crystallization and hydrogen atoms were omitted for clarity.

Solid state structure analysis gathered from single crystal X-ray diffraction (Figure 5.20) was also performed (Table 5.1). The transparent orange crystals solved in an orthorhombic cell of the space group $P2_12_12_1$. There were four molecules per unit cell (V = 3848.3(3) Å^3) with one in

the asymmetric unit along with a molecule of toluene. The structure showed the mesityl substituents sat perpendicular to the plane of the pyridine backbone (~ 87˚), oriented 121.55(avg)˚ from Zr-N-aryl, where the *ipso* carbons (C8, C17) of the two mesityl substituents are separated by 5.943(2) Å. This distance would allow for a certain degree of freedom for rotation about the C-N bond. Coupled with the rapid wagging of the benzyl substituents, these data support the hypothesis of steric protection at zirconium to substitution by a second equivalent of ^{Mes}PDA ligand.

Table 5.1: Relevant bond lengths and angles of (^{Mes}PDA)Zr(Bn)$_2$.

length (Å)		angle (˚)		torsion (˚)	
Zr1-N1	2.0977(16)	N1-Zr1-N2	70.03(6)	N1-N2-N3-C27	3.53(8)
N1-C1	1.456(3)	N3-Zr1-N2	69.52(6)	C1-C8-N1-Zr1	5.62(18)
N1-C8	1.434(2)	C8-N1-Zr1	121.42(12)	C8-C17-N3-Zr1	5.85(14)
C1-C2	1.495(3)	C17-N3-Zr1	119.68(11)	C1-N1-C8-C9	87.6(2)
Zr1-N2	2.3082(16)	C26-Zr1-C33	125.04(7)	C7-N3-C17-C18	87.0(2)
N2-C2	1.347(2)	N2-Zr1-C26	100.92		
N2-C6	1.345(2)	N2-Zr1-C33	100.65		
Zr1-N3	2.0984(16)	Zr1-C26-C27	107.42(12)		
N3-C7	1.454(3)	Zr1-C33-C34	86.50(11)		
N3-C17	1.434(2)				
C7-C6	1.498(3)				
Zr1-C26	2.320(2)				
C26-C27	1.486(3)				
Zr1-C33	2.3223(19)				
C33-C34	1.461(3)				
Zr1-C27	3.1069(19)				
Zr1-C34	2.6669(19)				

Interestingly, though the amide donor as a part of the neutral ligand would be a tetrahedral sp^3 hybridized nitrogen atom, we observe that the torsion angle between its three substituents in this molecule is 3.53(8)˚/5.62(18)˚, roughly planar. The N_{amide}-Zr bond lengths are also significantly contracted with respect to the analogous pyrrolide moiety, from ~2.4 Å (pyrr) to ~2.1 Å (amide). These parameters, along with the bond contraction, can be attributed to the increased π donation of the amide moiety, which donates strongly into the zirconium d_{yz} orbital. This is further supported by the C-N_{amide} bond lengths, 1.456(3) Å/1.454(3) Å, which are not indicative of a contraction associated with a change in the hybridization of either atom.

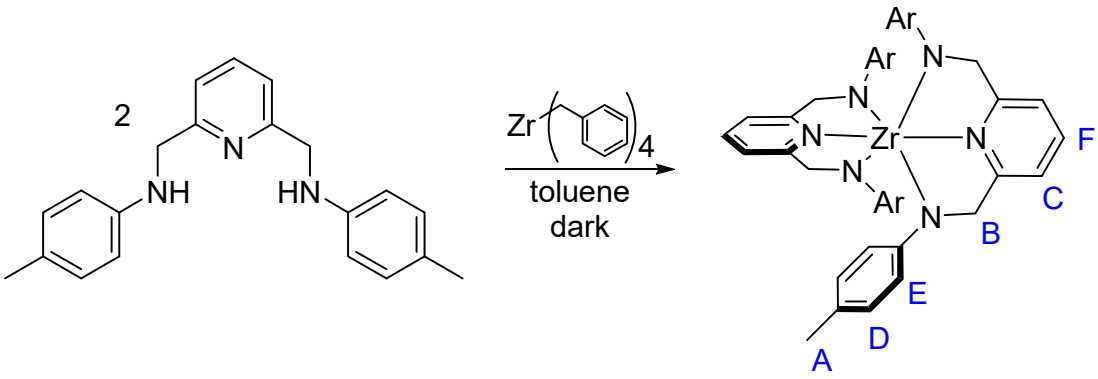

Scheme 5.6: Synthesis of Zr(^{Tol}PDA)$_2$ with proton assignments.

The first bis-PDA zirconium complex, Zr(^{Tol}PDA)$_2$, was successfully prepared by the same reaction conditions as the previous species. In a vial blacked out with tape, a solution of ^{Tol}PDA in toluene was prepared with good stirring. Tetrabenzylzirconium was dissolved in a separate vial and added dropwise at room temperature. Upon completion, the vial was capped to ensure the exclusion of light, and stirred overnight.

The complex was readily precipitated from a solution of concentrated toluene by layering with excess pentane at low temperature. The resulting bright yellow powder (96% yield) was reasonably soluble in benzene and subjected to NMR characterization. The ^{1}H spectrum (Figure

5.21) showed only 6 peaks. Compared to the ^{1}H NMR spectrum of the free ligand, many were markedly shifted by comparison, especially those assigned to the 2- and 3- positions of the anilido substituents, as well as the 4- pyridine proton and benzylic methylene units.

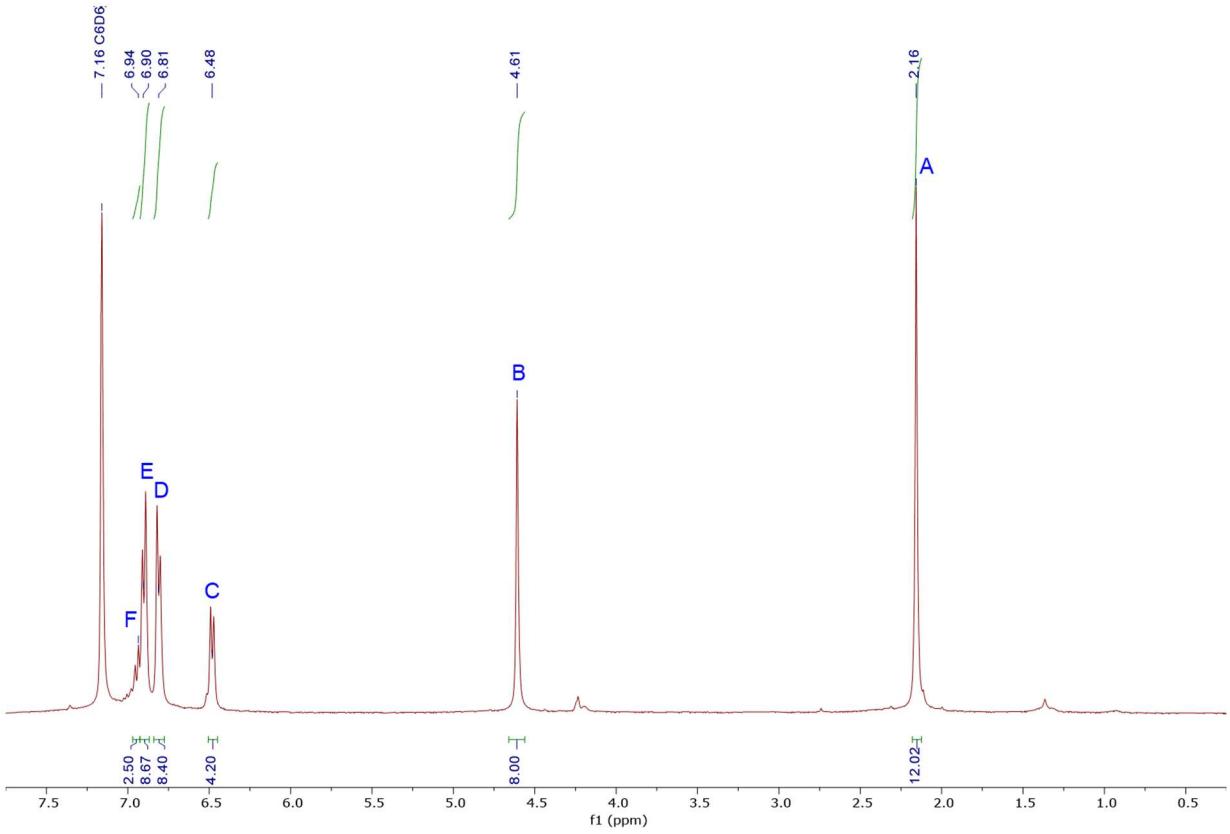

Figure 5.21: ^{1}H NMR spectrum of Zr(^{Tol}PDA)$_2$ in benzene-d_6 with integrations and peak assignments.

Two-dimensional proton correlated COSY NMR spectroscopy was performed to elucidate the relationships of these resonances to each other (Figure 5.22). The off-diagonal association between peaks D and E were anticipated from the proposed structure and visible roofing in the ^{1}H spectrum. The 4- pyridinyl triplet (F) and 3- doublet (C) are also nicely coupled together. Weaker ^{3}J coupling between signals B and C can be rationalized from resonance effects from the isolated aromatic pyridine ring, while A and D couple in the separate anilido tolyl system.

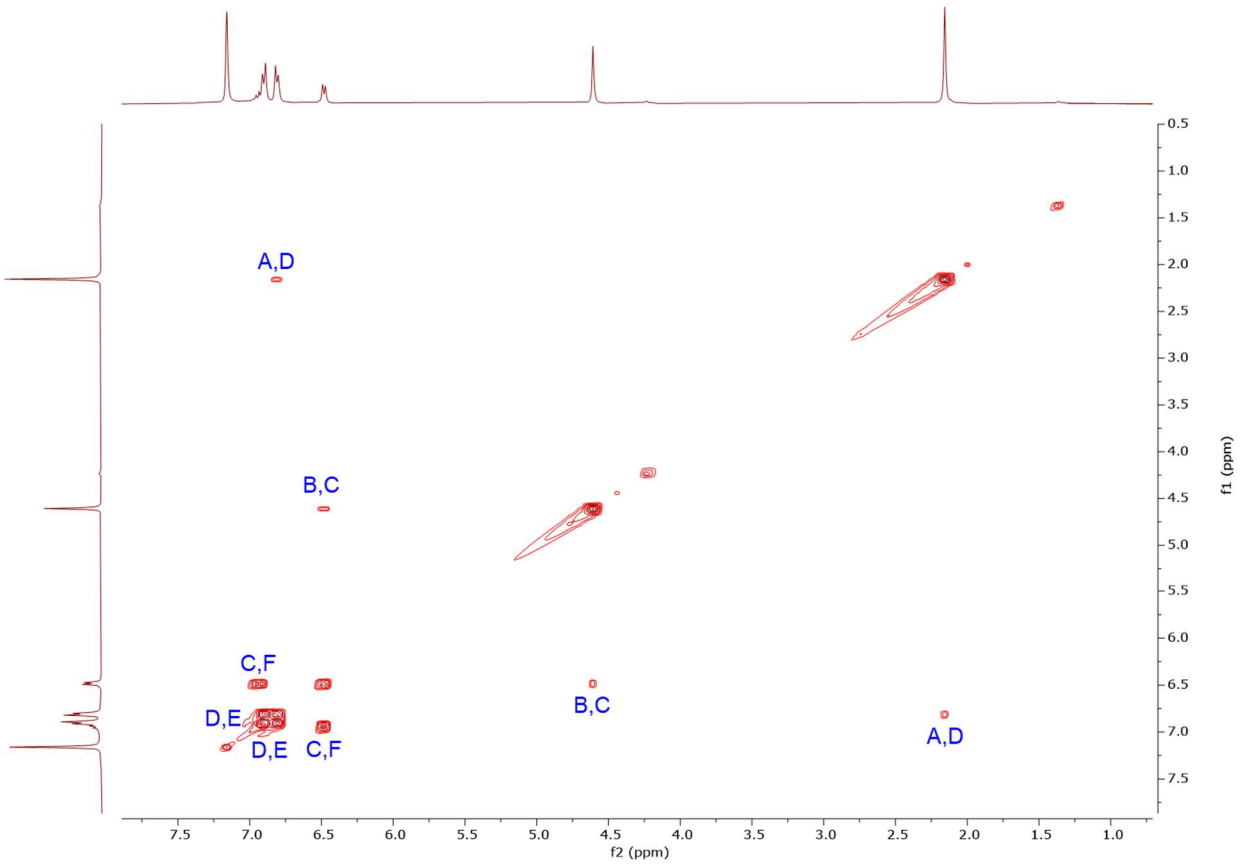

Figure 5.22: (HH) COSY NMR spectrum of Zr(^{Tol}PDA)$_2$ in benzene-d_6, where coupled signals on the off-diagonal are labelled with the previously established assignment scheme.

The NMR data are consistent with the structure of the ligand, and are indicative of a D_{2d} symmetric molecule on the NMR timescale. However, highly symmetric spectra may be misassigned in the case of single ligand addition. In these spectra (Figure 5.21 and Figure 5.22), there does not appear to be a second benzylic resonance or unsubstituted phenyl peaks, which would indicate a single ligand on zirconium with two remaining benzyls groups, though this absence was also observed in the case of (^{Mes}PDA)Zr(Bn)$_2$. Carbon NMR experiments would be equally uninformative to the absolute structure of this product. To combat this, an X-ray structural analysis was performed.

Single crystals were grown from slow diffusion of pentane into toluene at -35 ℃. The crystal structure shows a six-coordinate zirconium center in a distorted octahedral geometry, where the idealized coordination positions are restricted by the chelation angle of the ligand.

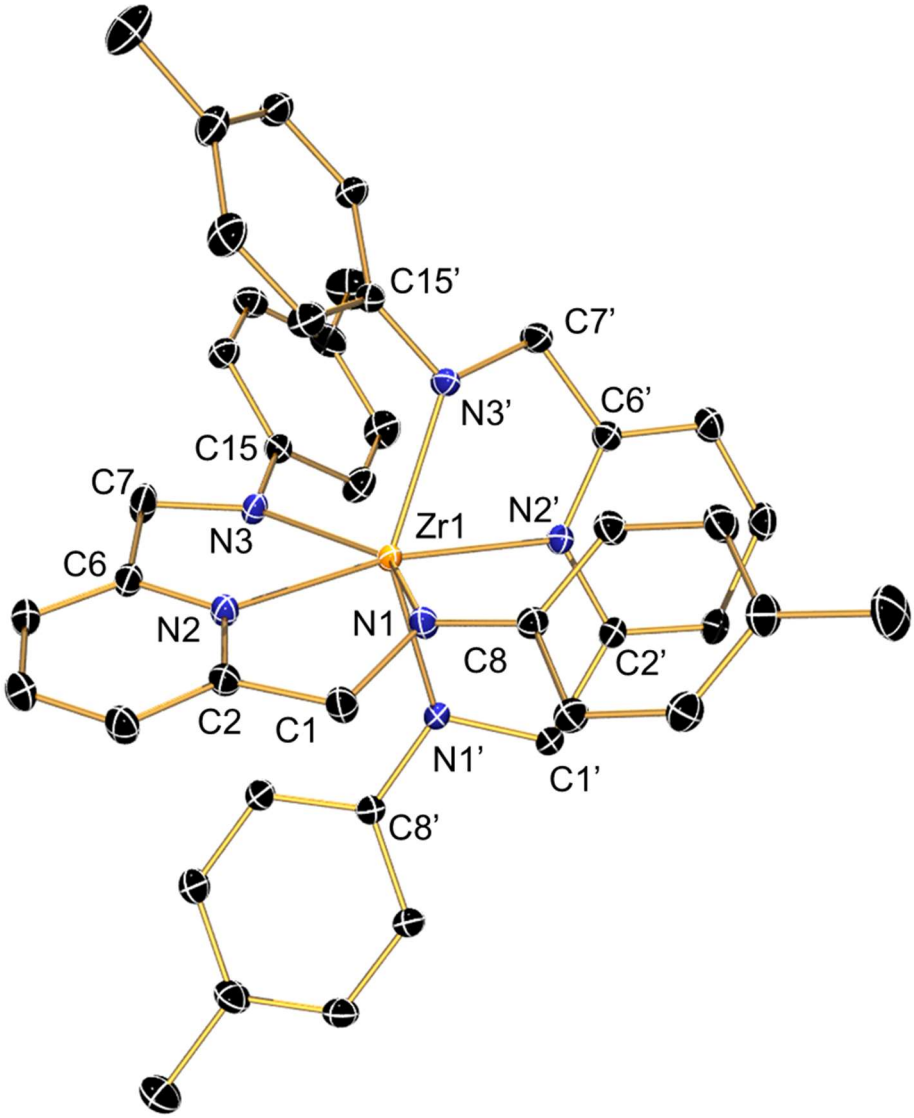

Figure 5.23: ORTEP depiction of Zr(^{Tol}PDA)$_2$ at 50% ellipsoid probability. Hydrogen atoms were omitted for clarity.

The monoclinic cell resolved in the space group C2/c with one half a molecule in the asymmetric unit and four molecules in the unit cell (V = 3635.9(3) Å^3). The second ligand was generated by the symmetry relationship (-X, +Y, ½ - Z). The unique angle, β, was 103.0313(11)˚,

and there were no accessible voids for solvent of crystallization. The relevant bond lengths and angles are summarized in Table 5.2.

Table 5.2: Relevant bond lengths and angles of $Zr(^{Tol}PDA)_2$.

length (Å)		angle (˚)		torsion (˚)	
Zr1-N1	2.1837(9)	N1-Zr1-N2	69.66(3)	N1-C2-N2-Zr1	13.38(6)
N1-C1	1.4567(14)	N3-Zr1-N2	52.04(3)	N3-C6-N2-Zr1	2.98(6)
N1-C8	1.3994(12)	N2'-Zr1-N1	102.90(3)		
C1-C2	1.4973(14)	N2'-Zr1-N3	119.13(3)		
Zr1-N2	2.3154(9)	N2-Zr1-N2'	169.37(4)		
N2-C2	1.3432(14)				
N2-C6	1.3467(13)				
Zr1-N3	2.1314(8)				
N3-C7	1.4479(15)				
N3-C15	1.4035(14)				
C7-C6	1.4948(16)				

From these data, it is clear that the aryl substituents on the anilido nitrogen atoms are no longer restricted to being perpendicular to the plane of the pyridine fragment. This is consistent with our expectations for the ^{Tol}PDA ligand over the ^{Mes}PDA derivative. These substituents are in fact slightly turned together in order to accommodate the second ligand, which is also not perfectly perpendicular to the first. This distortion of the octahedral ligand field is likely due to the flexibility of the sp^3 hybridized methylene linkers, where the chelation of the zirconium atom is not rigidly enforced to be planar.

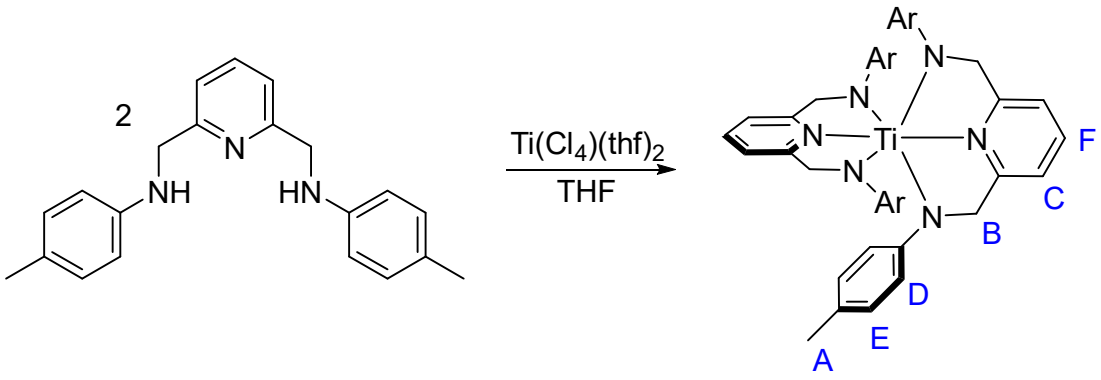

Scheme 5.7: Synthesis of Ti(^{Tol}PDA)$_2$ with proton assignments (in blue).

The titanium analogue was prepared by the addition of deprotonated ligand to the metal halides in THF. Interestingly, proceeding from either $TiCl_3(thf)_3$ or $TiCl_4(thf)_2$, the Ti^{IV} bis-ligand species was observed. The mechanism of this oxidation is unclear, though evidence for ligand innocence shall be presented later in this Chapter via isolable intermediates. The ligand was deprotonated with n-butyllithium in a solution of tetrahydrofuran before dropwise addition into a stirring slurry of $TiCl_4(thf)_2$. After the addition was complete, the reaction was allowed to stir overnight at room temperature. The reaction mixture was reduced to dryness and reconstituted in toluene to precipitate dissolved salts. After filtering with Celite, reducing to dryness under vacuum, and trituration with pentane (77% yield), characterization of Ti(^{Tol}PDA)$_2$ proceeded exactly as the zirconium species.

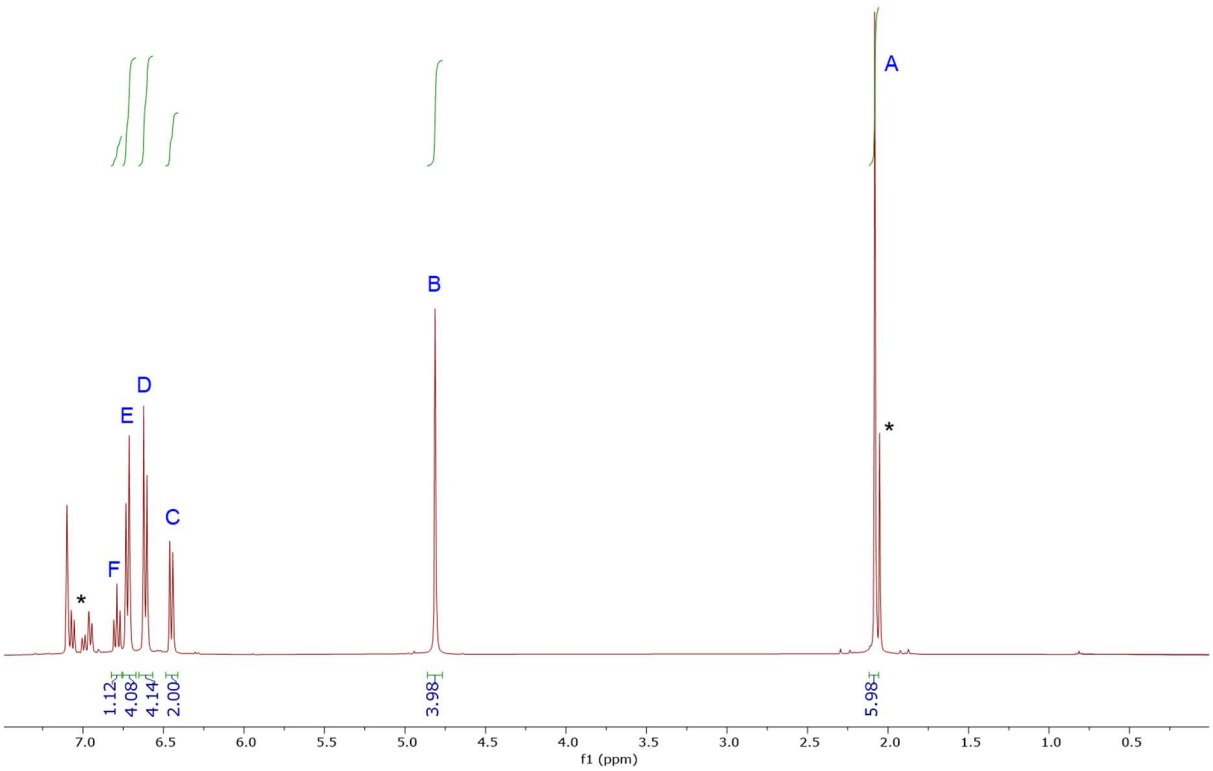

Figure 5.24: ^{1}H NMR spectrum of Ti(^{Tol}PDA)$_2$ in benzene-d_6 with integrations and peak assignments. Solvent of crystallization (toluene, *) is present, but not accounted for in these integrations.

Proton NMR spectroscopy of crystalline material afforded the spectrum above (Figure 5.24), where the pure material was concomitant with residual toluene. Notably, there are no resonances in the aliphatic region, which would otherwise indicate the presence dimethylamido groups from starting material or partially substituted intermediates. Correlated spectroscopy was performed to ensure that these signals belong to the same species.

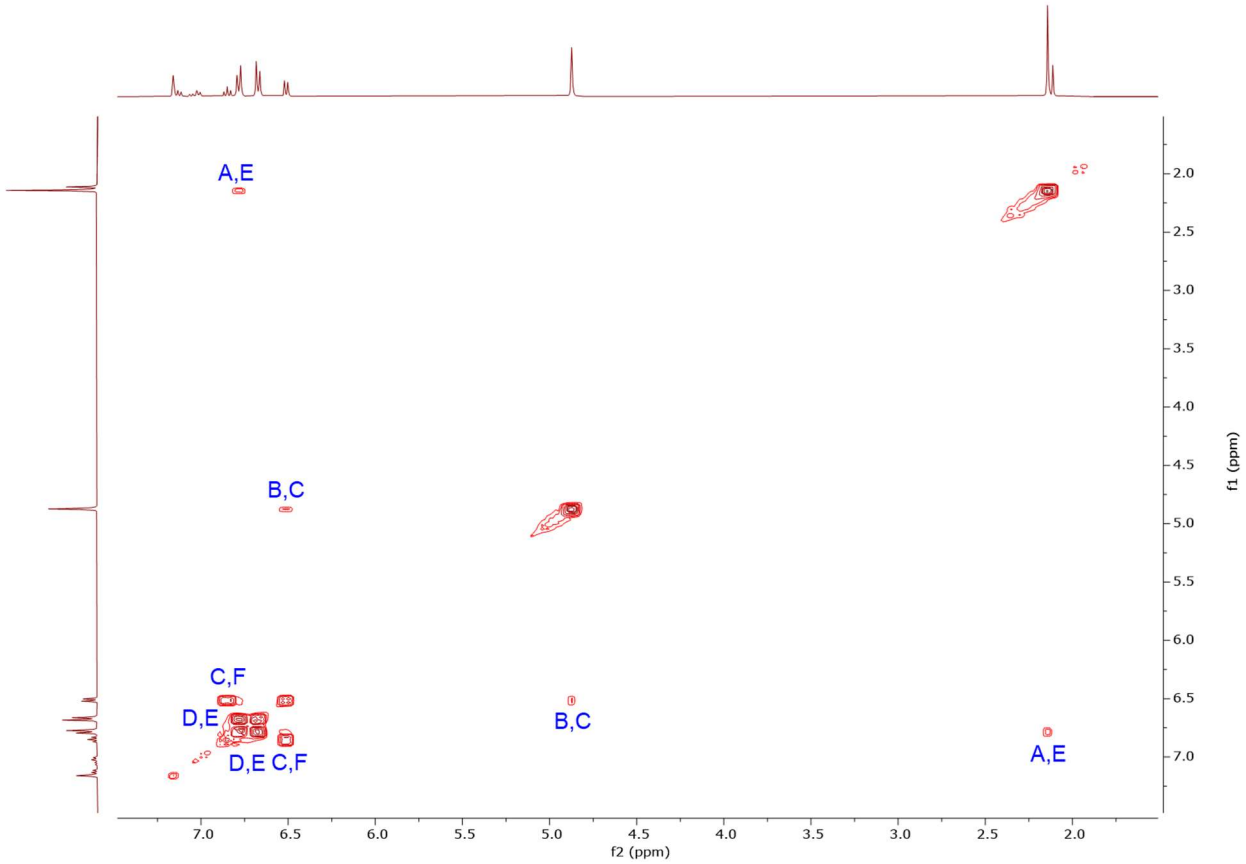

Figure 5.25: (HH) COSY NMR spectrum of Ti(^{Tol}PDA)$_2$ in benzene-d_6, where coupled signals on the off-diagonal are labelled with the previously established assignment scheme.

These data showed weak ^{3}J coupling between the benzylic methylene protons (B) and the 3- pyridinyl protons (C), likely due to aromatic resonance effects, as there is also a strong coupling of C to the para pyridinyl resonance (F). The tolyl methyl (A) is shown to couple weakly with the proximate anilido aryl (E). The 2- and 3- protons on these rings are strongly coupled (D, E). The culmination of these data does not lend evidence to the bis-ligated titanium center, as was an issue with the zirconium derivative. Again, the absolute structure was determined by X-ray diffraction.

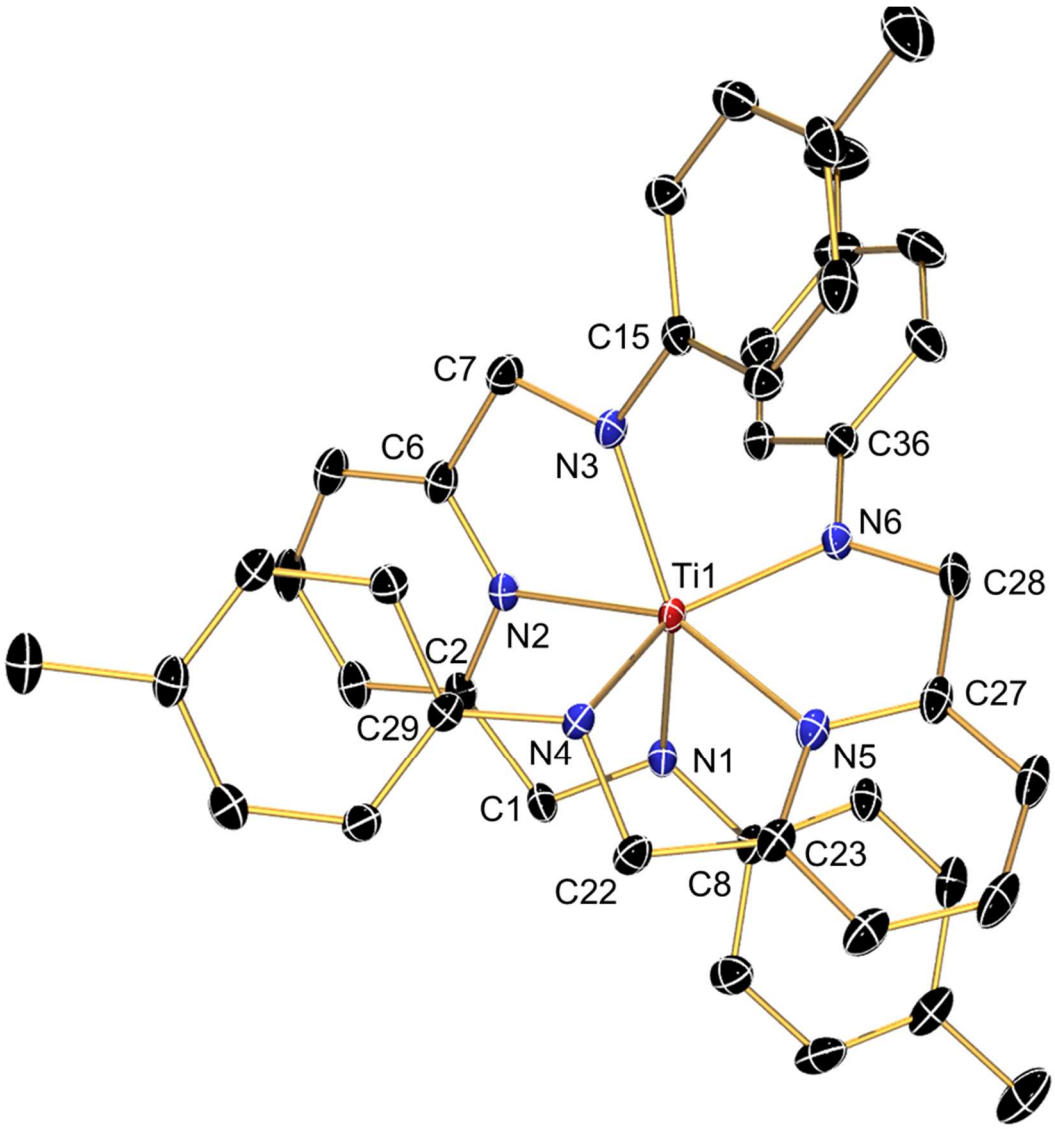

Figure 5.26: ORTEP depiction of Ti(^{Tol}PDA)$_2$ at 50% ellipsoid probability. Solvent of crystallization and hydrogen atoms were omitted for clarity.

The structure solved in a triclinic cell of the space group $P\bar{1}$, with two independent molecules in each cell (V = 2311.8(2) Å^3). The unit cell and its contents of the titanium species were not analogous to the zirconium complex and had two molecules of toluene per asymmetric unit. Generally, the structure of this molecule is significantly distorted with respect to the zirconium analogue, where the buckling of the methylene bridge between the pyridinyl fragment

and anilido nitrogen is more heavily pronounced on one side. This distortion is likely the reason for the co-crystallization of solvent. The relevant bond lengths and angles are listed in Table 5.3.

Table 5.3: Relevant bond lengths and angles of Ti(^{Tol}PDA)$_2$.

length (Å)		angle (˚)		torsion (˚)	
Ti1-N1	2.0487(11)	N1-Ti1-N2	72.69(5)	N1-C2-N2-Ti1	16.89(11)
N1-C1	1.4623(18)	N3-Ti1-N2	73.24(5)	N3-C6-N2-Ti1	1.19(11)
N1-C8	1.398(2)	N2-Ti1-N5	154.26(6)	N5-C23-N4-Ti1	16.81(7)
C1-C2	1.487(2)	N4-Ti1-N5	72.60(6)	N5-C27-N6-Ti1	0.30(7)
Ti1-N2	2.1527(13)	N6-Ti1-N5	72.59(6)		
N2-C2	1.3451(16)	N1-Ti1-N5	89.80(5)		
N2-C6	1.335(2)	N3-Ti1-N5	127.49(5)		
Ti1-N3	2.0253(14)	N4-Ti1-N2	89.95(6)		
N3-C7	1.450(2)	N6-Ti1-N2	127.94(7)		
N3-C15	1.3953(16)				
C7-C6	1.4859(19)				
Ti1-N4	2.0423(17)				
N4-C22	1.460(2)				
N4-C29	1.4040(19)				
C22-C23	1.492(2)				
Ti1-N5	2.1633(15)				
N5-C23	1.341(3)				
N5-C27	1.341(2)				
Ti-N6	2.0095(14)				
N6-C28	1.449(2)				
N6-C36	1.396(3)				
C27-C28	1.491(3)				

The electronic structure of this family of compounds was elucidated by UV-visible absorption. Our first observation is that when the zirconium derivative was taken in anhydrous THF, the shape of the ultraviolet region (< 350 nm) of the zirconium bis-PDA compound is nearly unchanged from the pure ligand, though shifted by a few hundred nanometers toward the visible spectrum.

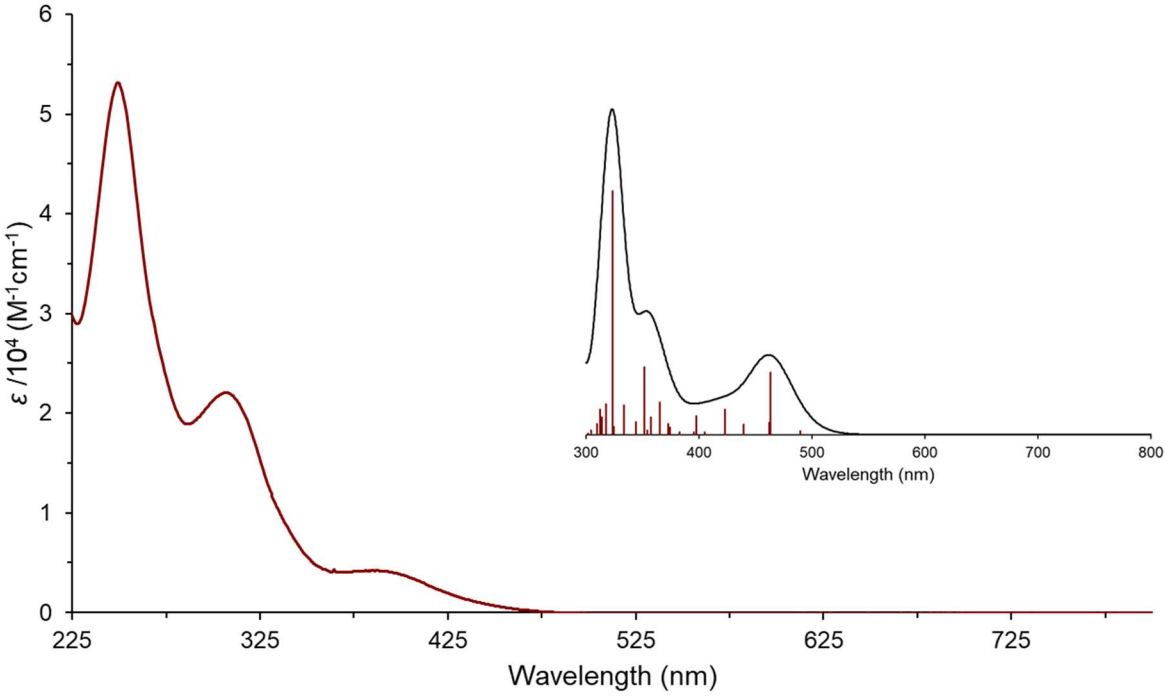

Figure 5.27: UV-visible spectrum of Zr(^{Tol}PDA)$_2$ in THF under nitrogen. Inset: Calculated spectrum.

At room temperature in THF solution, the complex was not found to be emissive. However, later experiments allowed access to fluorometry at 77 K in a glass of 2-methyltetrahydrofuran. We would expect this setup to effectively dampen or arrest vibrational relaxation mechanism which lead to quenching of a potential luminescent excited state. Following a room temperature collection (gray trace), the solution was frozen in liquid nitrogen and irradiated with a black light source (red trace).

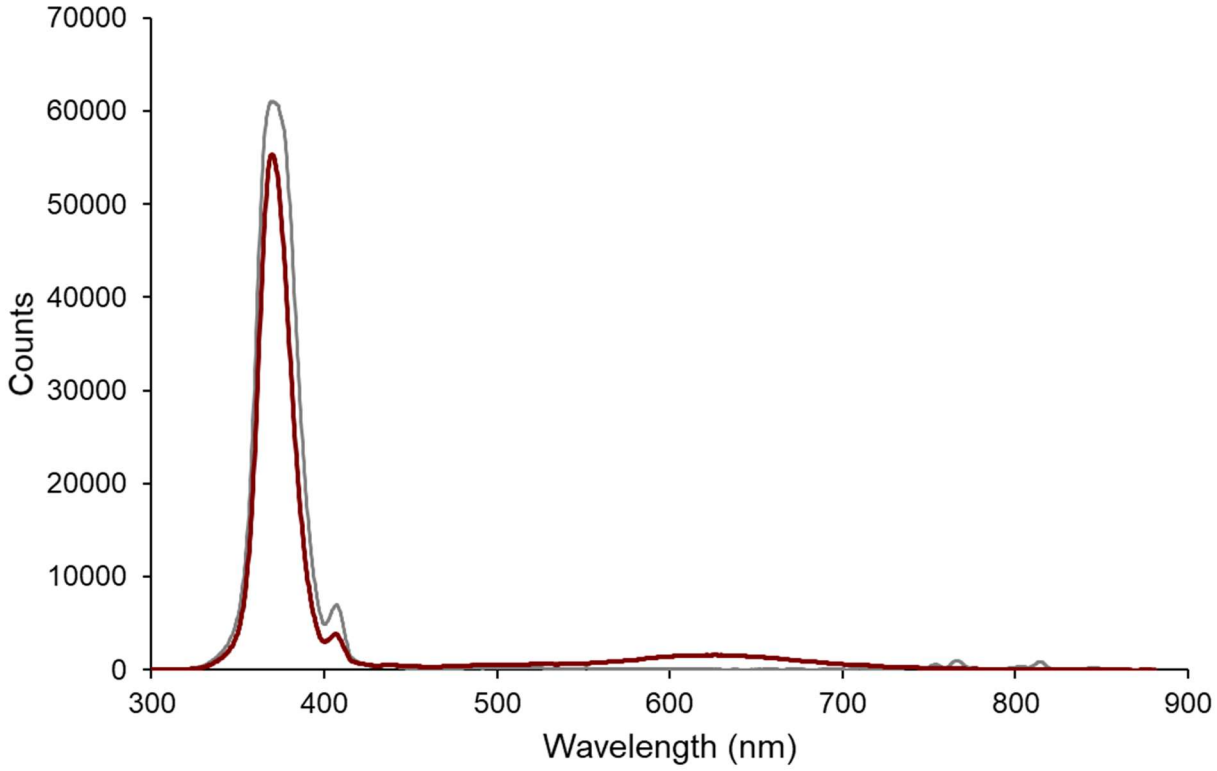

Figure 5.28: Emission spectrum of Zr(^{Tol}PDA)$_2$ in a glass of 2-MeTHF under nitrogen at 77K. The signals proceeding 450 nm are attributed to the black light source.

The observed phenomenon centered around 620 nm is extremely weak but stands out from what may be considered noise. While this is a promising result with regard to our hypothesis concerning thermal relaxation, these data are treated with the utmost caution. This work does not include empirical characterization of this presumed excited state, as further experiments are required before the observed luminescence can be attributed to this molecule rather than a potential impurity.

The absorption profile of the Ti(^{Tol}PDA)$_2$ species is also markedly different from both the free ligand and zirconium congener. As shown below in Figure 5.29, there is a sharp decrease in the absorption feature at 300 nm, while the band at 400 nm increases as it broadens out well into the visible spectrum. These changes are indicative of an entirely separate electronic structure as indicated by computational data, which will be discussed later in this Chapter.

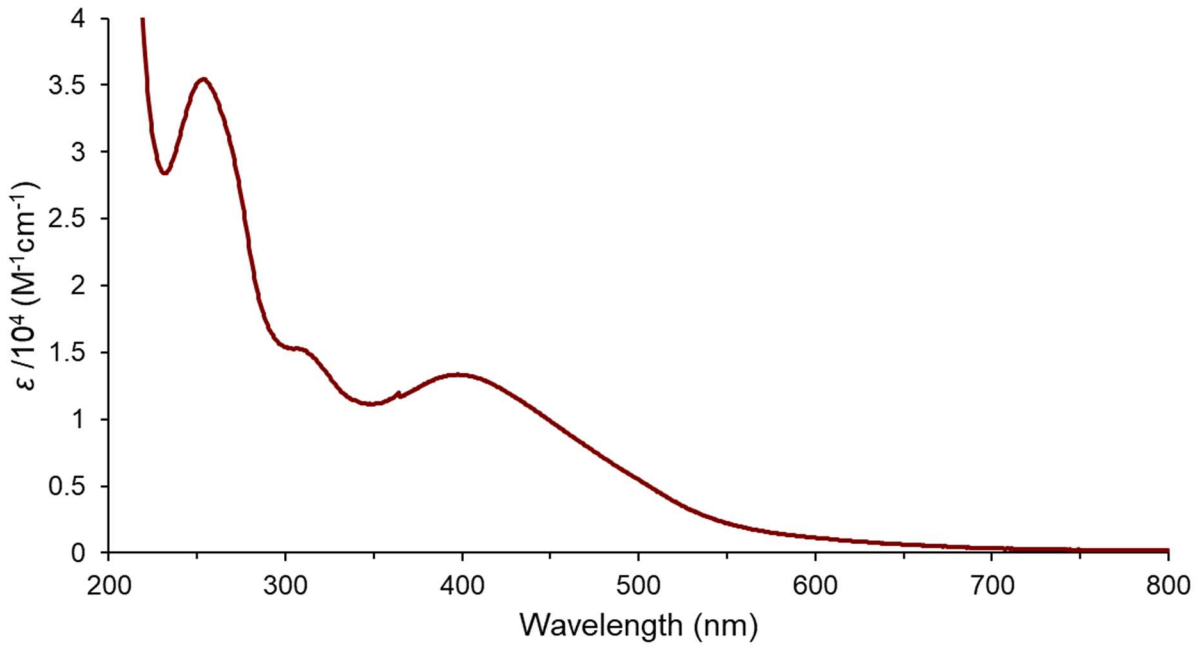

Figure 5.29: UV-visible spectrum of Ti(^{Tol}PDA)$_2$ in THF under nitrogen.

The titanium analogue, however, showed no luminescence at 77 K. The electronic transitions of this family of compounds were calculated by time-dependent density functional theory (TD-DFT) and compared to their experimental absorption profiles. The calculated spectra are slightly red shifted but contain nearly identical features. Of these features, individual transitions were considered and the molecular orbitals which contributed were plotted. Conclusions about the mechanism of these transitions were made based on the percentages of contribution of atoms between the donor (HOMO) and acceptor (LUMO) orbitals.

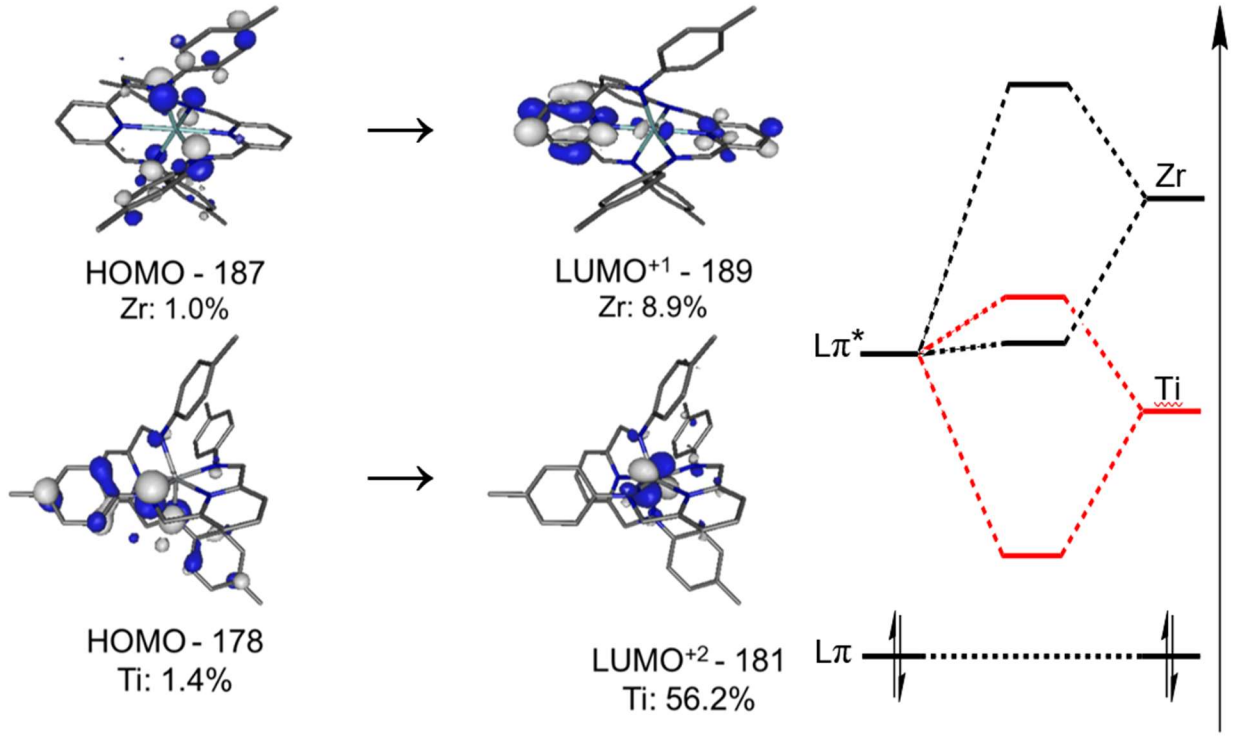

Figure 5.30: Left: Calculated lowest energy transitions of Zr(^{Tol}PDA)$_2$ and Ti(^{Tol}PDA)$_2$ with depictions of major molecular orbital contributions of each transition, as well as metal orbital contributions. Right: Qualitative MO diagram of metal orbital energy relative to PDA ligand.

These single electronic transitions can be composed of more than one orbital transition, and all relevant transitions that contributed were considered in this characterization. The major contributors are shown here as representatives of these data. With this in mind, calculations showed the dominant visible transition for the zirconium compound was primarily composed of a ligand-to-ligand charge transfer (LLCT), with very little density on the zirconium atom. The highest occupied orbital was roughly D_{2d} symmetric, with contributions from each anilido substituent. Considering the lack of ligand conjugation, however, these results were encouraging. Based on these data, the d^0 metal atom acts as a bridge for the donor/acceptor portions, while significantly red shifting the absorption spectrum. While these transitions were not the formal LMCT we anticipated, the metal center plays a central role. By comparison, the Zr(^{Mes}PDP^{Ph})$_2$

species showed new absorption bands as a result of LMCT pathways, but also a red shifting of the ligand centered absorption events. The blue shift (~100 nm) in the lowest energy absorption was anticipated in accordance with the structural change of the ligand. The lack of extended conjugation does not allow for lower accessible electronic transitions, as is accessible from the pyridine dipyrrole structure. This was observed in the characterization of the free ligands as well, as previously discussed. This compiled optical and computational data also suggests is that the Zr^{IV} ion is energetically inaccessible to the PDA ligand scaffold (Figure 5.30).

As for the titanium analogue, Ti(^{Tol}PDA)$_2$, the observed calculated orbitals showed what appeared to be a proper LMCT event. While this was a desirable outcome, this may further give explanation to the lack of luminescent events in the case of first row early metals. With these potentially significantly different charge transfer pathways in mind, it was not surprising that there was complete loss of emissive behavior for the Group 4 compounds at room temperature. It is reasonable to assume that while the methylene units between the aryl and the amide provide ready access to non-radiative decay pathways, the crystal structure and calculated optimized geometries both show a buckled, non-planar backbone, where the amide donors reside above and below the plane of the ring. This observation, in contrast to the D_{2d} symmetric NMR spectra that was observed for both the zirconium and titanium complexes, makes it is easy to envision an equalized rapid wagging of four symmetry related units where the benzylic protons are accounted for within a single unsplit resonance.

The redox properties of these Group 4 bis-PDA complexes were also probed via cyclic voltammetry. Samples were prepared in anhydrous tetrahydrofuran with tetrabutylammonium hexafluorophosphate as an electrolyte. While the titanium compound showed no reversible electrochemistry, Zr(^{Tol}PDA)$_2$ showed only a quasi-reversible couple with maxima at -0.103 V

and -1.312 V vs Fc/Fc^+, centered on -0.708 V (Figure 5.31). The observed reduction event is much too positive for a typical Zr^{III}/Zr^{IV} couple and is likely a ligand-centered electrochemical (EC) process.

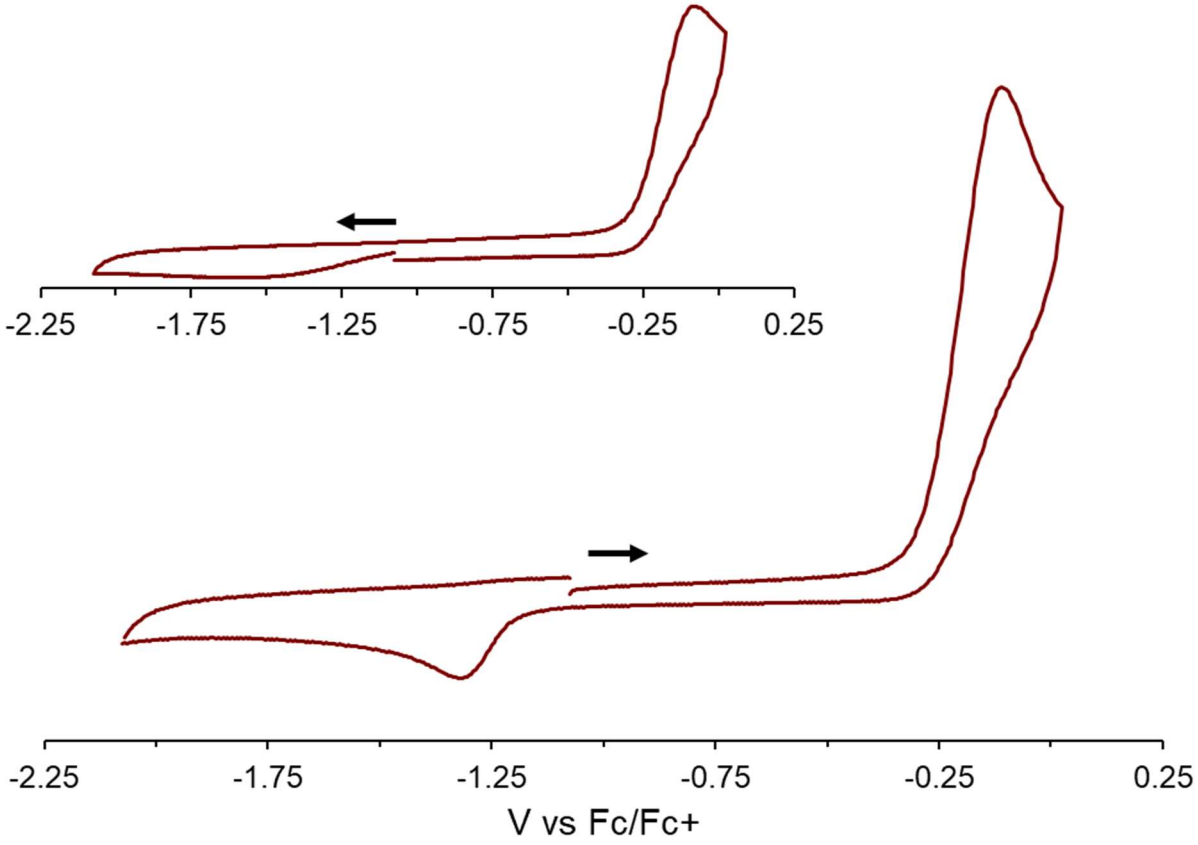

Figure 5.31: Cyclic voltammogram of $Zr(^{Tol}PDA)_2$ in anhydrous THF with NBu_4PF_6 as an electrolyte depicting a quasi-reversible electrochemical process.

Further evidence for this hypothesis can be shown when the same window is taken first reductively, as the peak at -1.312 V is not observed. A single oxidation of one of the ligands would likely lead to a cationic triamido-imino intermediate, which quickly decomposes. This is evidenced by the limited reverse wave after initial oxidation. Further evidence for this hypothesis will be presented in the next section of this Chapter, where the proposed intermediate structure was isolated in effort to synthesize a related complex.

5.4 Synthesis and Characterization of Group 5 PDA Complexes

The lack of reversible redox chemistry, in combination with the larger orbital energy mismatch with zirconium, made moving to Group 5 metals an attractive alternative for a photosensitizer. In particular, the Nb^{V}/Nb^{IV} redox couple is usually fairly accessible,[48] as the orbital energies for niobium(V) ions are lower than those of zirconium(IV) ions,[12] thus bringing them closer in energy to the highest occupied molecular orbital of the PDA ligand system. This diminished energy gap would result in lower energy absorption at longer wavelengths, as is known with the comparable $Nb^{IV/V}(^{Me}PDP^{Ph})_2$ system.[49] Also, as discussed, when comparing the optical properties of the bis-PDA complexes to bis-PDP complexes of zirconium, it was observed that the HOMO of the PDA system is demonstrably higher than that of the PDP. We would expect to see a similar outcome with respect to comparisons between PDP/PDA complexes of vanadium, niobium, or tantalum.

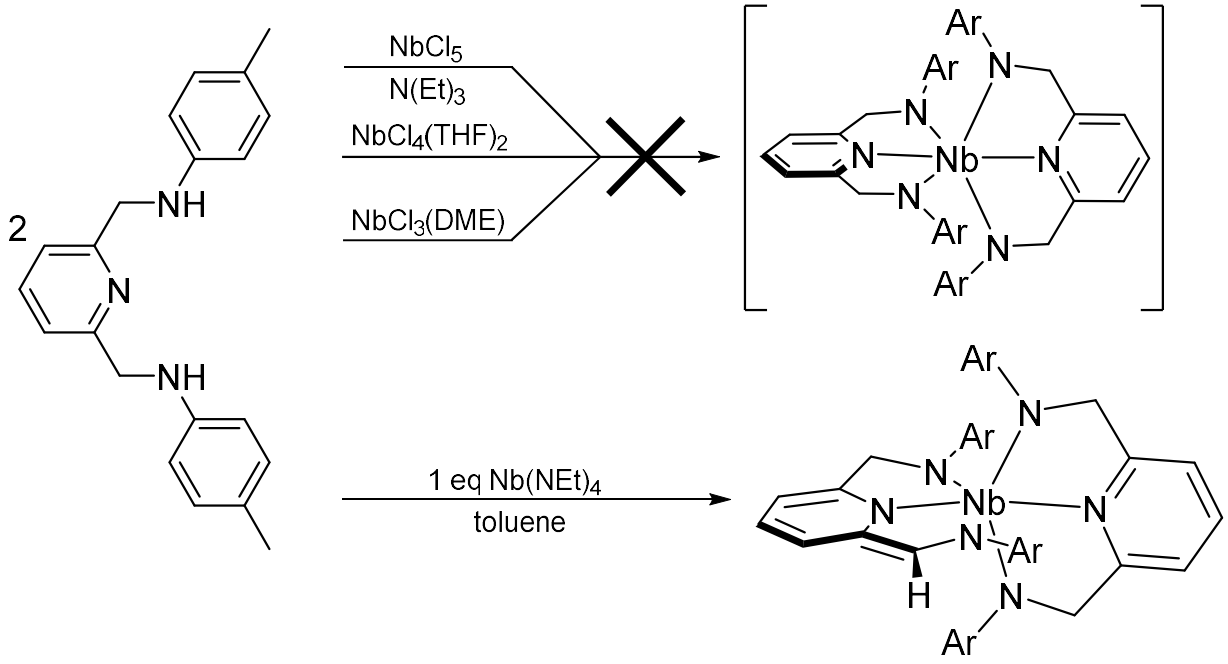

Scheme 5.8: Reaction of ^{Tol}PDA with niobium(III, IV, V) starting materials.

In effort to justify this hypothesis experimentally, attempts to prepare an analogous niobium bis-PDA complex were made. However, there has been no success with niobium starting materials in any oxidation state. An interesting failure (Scheme 5.8), 2.5 equivalents of ^{Tol}PDA were added to a Schlenk tube with $Nb^{IV}(NEt_2)_4$ in tetrahydrofuran. After refluxing at 80 ˚C overnight, all volatiles were removed under vacuum. The solids were reconstituted in minimal toluene, filtered with Celite, and layered with pentane to yield an asymmetric diamagnetic product (29% yield) with a denatured PDA ligand. This result was unexpected but gives insight into the properties of compounds bearing these PDA ligands.

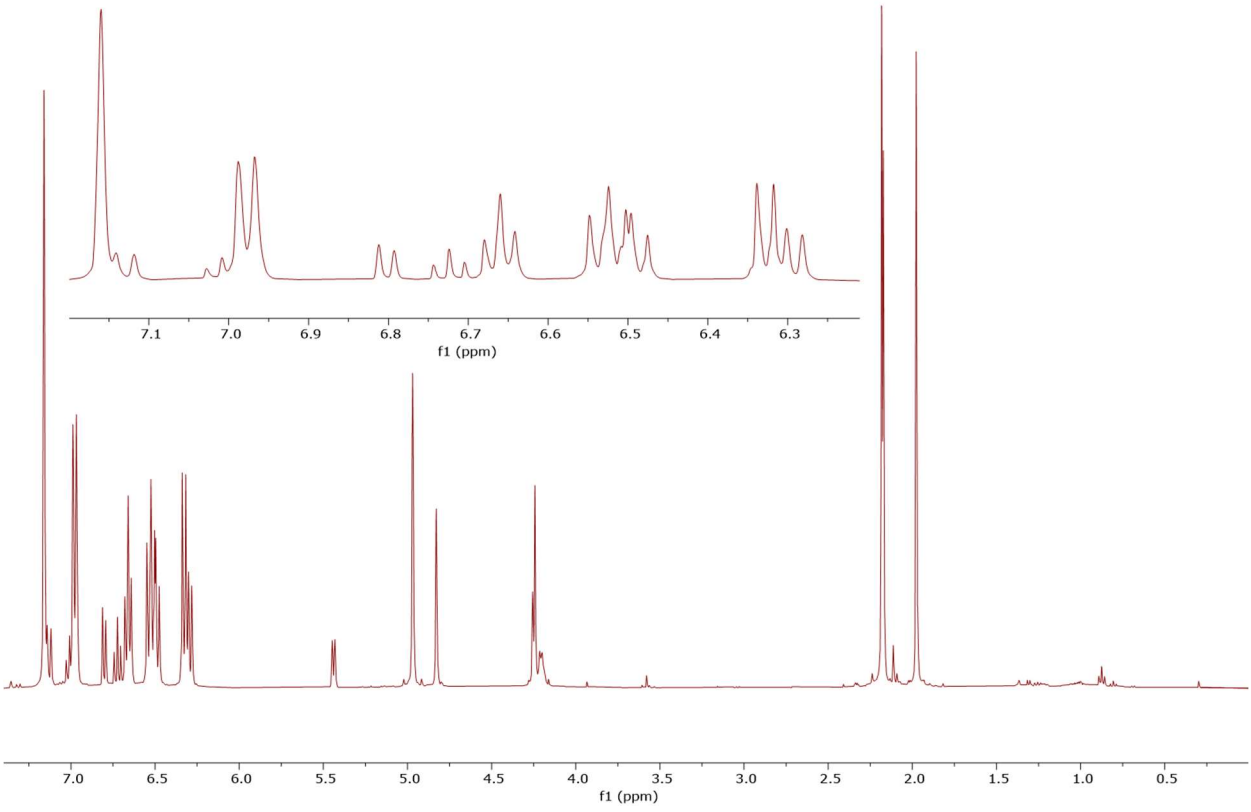

Figure 5.32: ^{1}H NMR spectrum of (^{Tol}PDA)Nb(NNN) in benzene-d_6. Inset: the region between δ 7.2 ppm – 6.2 ppm expanded for clarity.

As shown in Figure 5.32, the diamagnetic product of this reaction is not symmetric. Further, no paramagnetic products were detected. Due to the relatively few peaks observed in the ^{1}H NMR spectrum, correlated NMR spectroscopy was performed to illuminate coupling between overlapping signals.

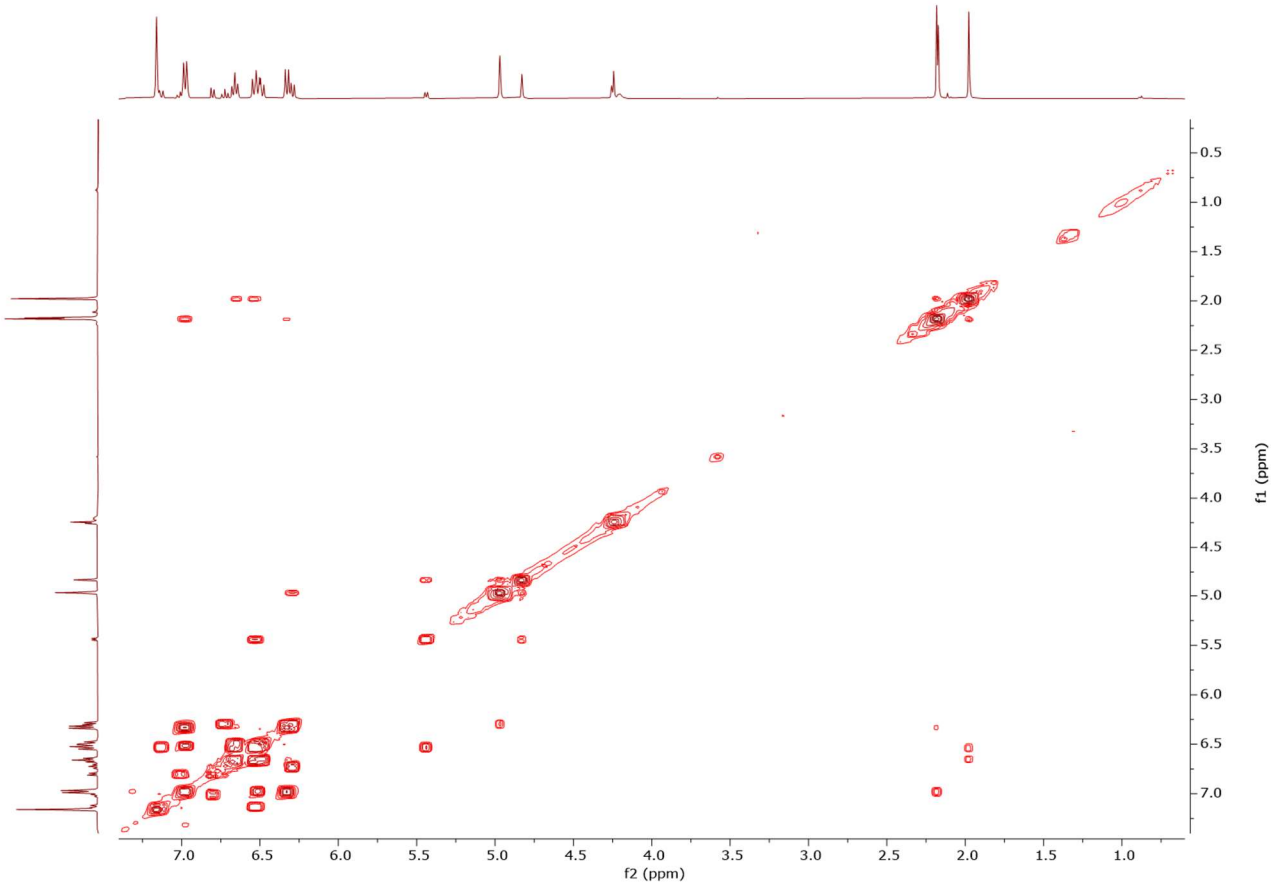

Figure 5.33: (HH) COSY NMR spectrum of (^{Tol}PDA)Nb(NNN) in benzene-d_6.

The first indication of overlap is shown in the region δ 1.5 – 2.5 ppm, where the three observed peaks in the ^{1}H NMR spectrum yield four resonances in the off-diagonal. Specifically, the peak at δ 1.98 ppm appears to comprise two chemically independent features, each coupled to a separate aryl peak (δ 6.65 ppm, δ 6.53 ppm).

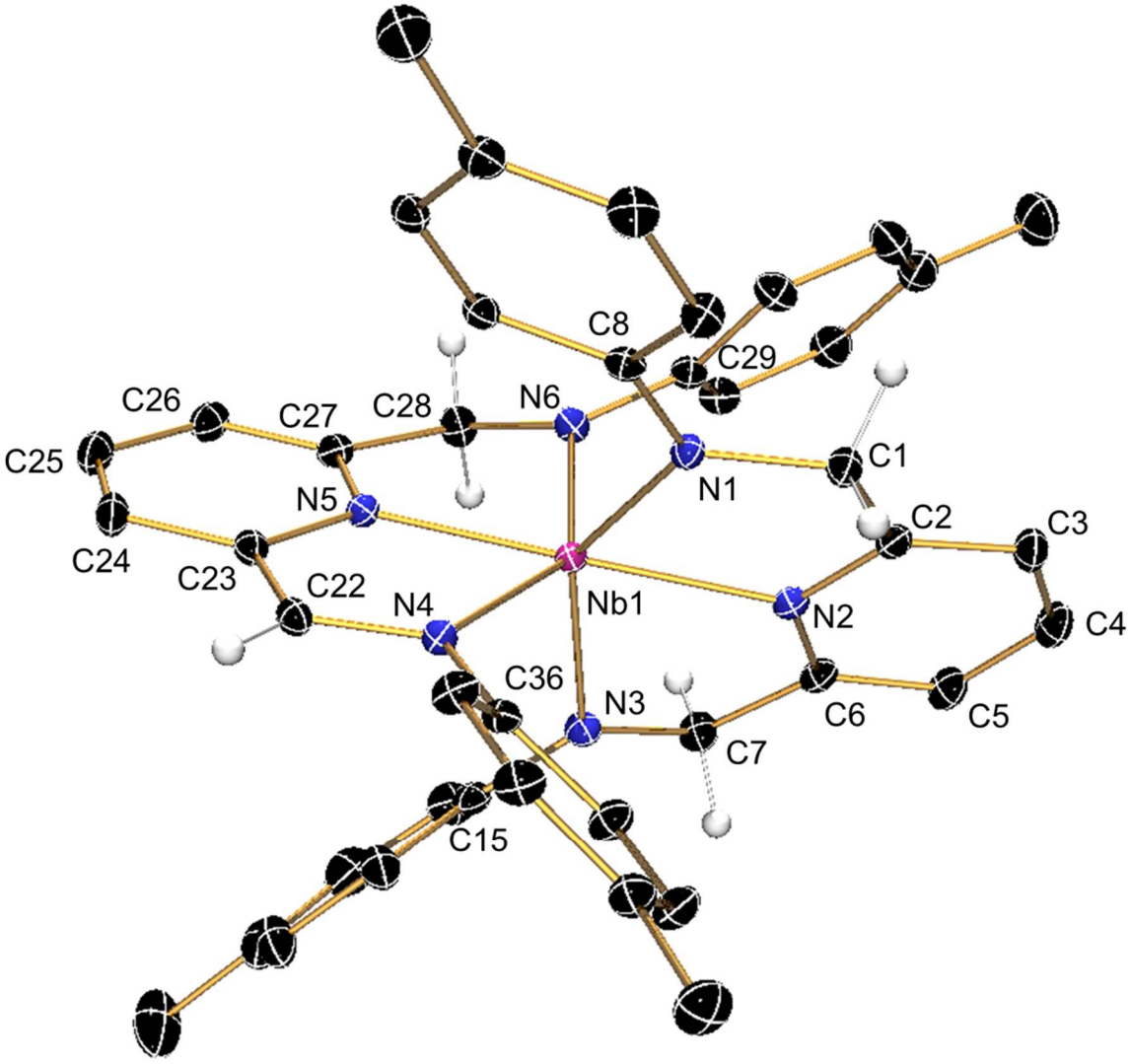

Figure 5.34: ORTEP depiction of (^{Tol}PDA)Nb(NNN) at 50% ellipsoid probability. Solvent of crystallization and hydrogen atoms were omitted for clarity, except about the methylene carbons between the aryl and anilido moieties.

The structure was further confirmed by X-ray crystallography. Because these proton positions are riding, a careful analysis of the structure was considered in order to validate these results. Notably, the geometry about N4 and its associated bond lengths are indicative of a sp^2 hybridized nitrogen atom, which is neatly situated in the plane of the associated pyridine ring. The pyridine ring also shows evidence of dearomatization with alternating double and single bonds

(Table 5.4). The bonds between C27-N5 and N5-C23 are roughly equivalent, suggesting some delocalization. These data are in contrast with the other ligand, where the pyridine ring is more certainly aromatic (1.373 Å $_{avg}$), and the pincer arms are buckled above and below the ligand plane.

Table 5.4: Comparison of bond lengths and angles between distinct ligands on (^{Tol}PDA)Nb(NNN).

(NNN)		^{Tol}PDA		bond and torsion angles (˚)	
length (Å)					
N5-C23	1.396(2)	N2-C2	1.3451(18)	Nb1-N4-C22	122.73(10)
C23-C24	1.426(2)	C2-C3	1.389(2)	Nb1-N4-C36	119.36(10)
C24-C25	1.357(2)	C3-C4	1.386(3)	C36-N4-C22	117.87(13)
C25-C26	1.428(3)	C4-C5	1.396(2)	Nb1-C36-N4-C22	~2.1
C26-C27	1.362(2)	C5-C6	1.381(2)		
C27-N5	1.3761(18)	C6-N2	1.342(2)	Nb1-N6-C28	118.07(10)
N4-C22	1.364(2)	N1-C1	1.4597(19)	Nb1-N6-C29	123.21(9)
N4-C36	1.4215(17)	N1-C8	1.4044(19)	C28-N6-C29	114.83(12)
C22-C23	1.374(2)	C1-C2	1.490(2)	Nb1-C29-N6-C28	~22.69
N6-C28	1.4524(18)	N3-C7	1.465(2)		
N6-C29	1.416(2)	N3-C15	1.412(2)		
C27-C28	1.495(2)	C6-C7	1.492(2)		

The oxidation of the niobium starting material is ambiguous and is still not understood with the conclusion of this work. However, the deprotonation of the benzylic protons of the methylene linker is precedented in the literature. The electrochemistry of this product was elucidated via cyclic voltammetry in order to probe the reversibility of this process. When probing a large voltage window, where over-reduction occurred first, many single electron waves were observed in the decomposition product well into oxidative potentials, none of which came back. When oxidized first, two initial waves gave way to no coherent phenomena with no reversible events.

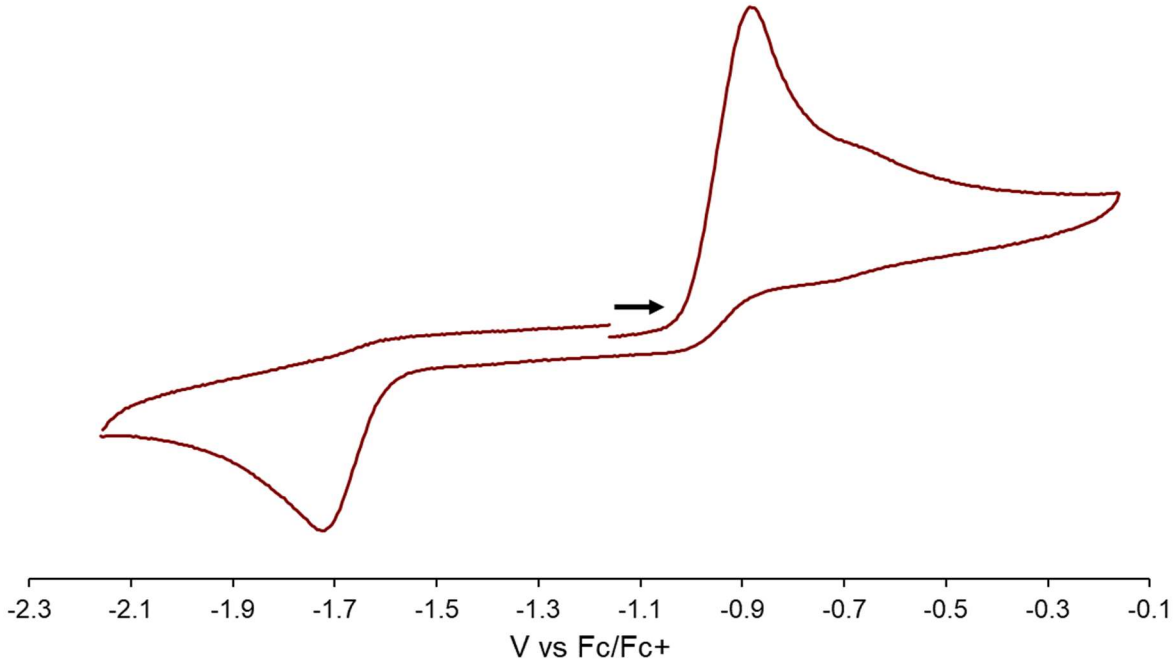

Figure 5.35: Cyclic voltammogram of (^{Tol}PDA)Nb(NNN) in THF with NBu_4PF_6 as an electrolyte depicting a reversible electrochemical process.

Isolation of the first oxidative event showed a quasi-reversible EC process with maxima at -0.87 V and -1.72 V, centered on -1.30 V (Figure 5.35). This process was probed further by applying current first in the negative direction over the same window. The result was a flat "curve" before the more oxidative event and showed that the reverse wave is dependent upon the electrochemical product of this oxidation.

At more reducing potentials, a nicely reversible event is isolable, independent of the direction of the applied current (Figure 5.36). This result was compared to the LUMO plot calculated by TD-DFT, where an added electron is likely to reside. This orbital is primarily composed of the niobium d_{xy} orbital (23.5%) mixed with the conjugated pyridine of the PDA ligand, suggesting a metal centered reduction event from $Nb^{V} \rightarrow Nb^{IV}$.

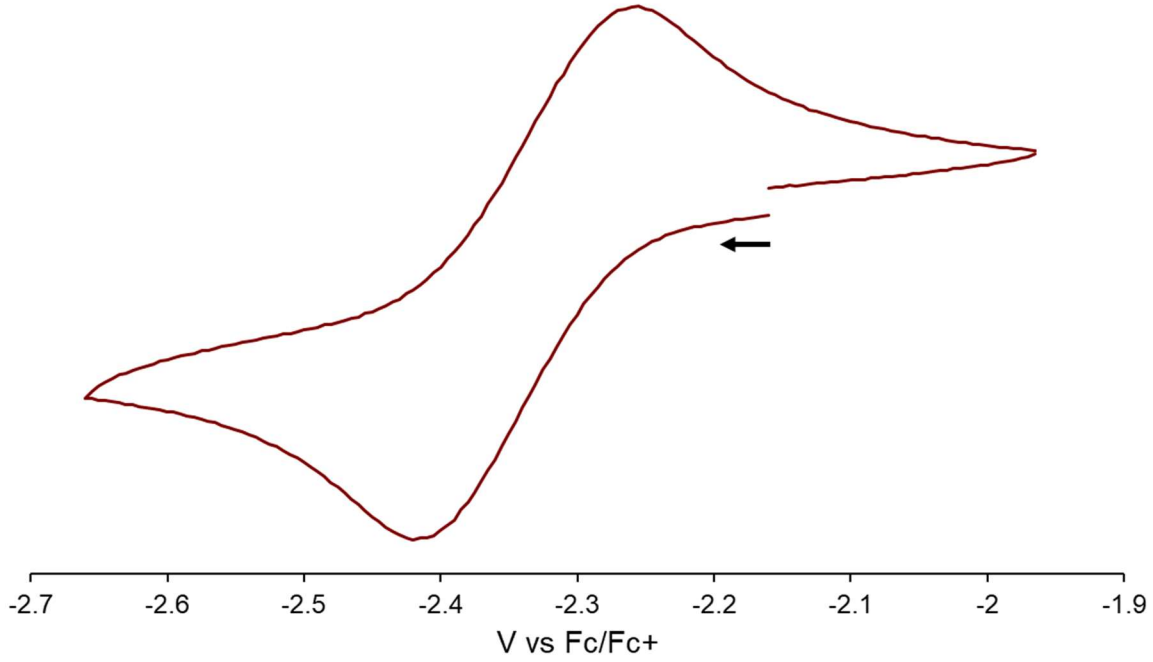

Figure 5.36: Cyclic voltammogram of (^{Tol}PDA)Nb(NNN) in THF with NBu_4PF_6 as an electrolyte depicting a reversible redox event at -2.34 V.

To infer whether the unexpected divergent reactivity which generated this asymmetric species was specific to niobium, or more generally applicable to Group 5 complexes, attempts were made to synthesize a bis-ligand vanadium complex. The tetrakis(diethylamido)vanadium(IV) starting material was prepared by literature methods[50] and refluxed in the presence of two equivalents of ^{Tol}PDA. If the reaction proceeds via aminolysis as intended with titanium and zirconium, the characterization of these products should not be amenable to NMR spectroscopy. The neutral species would be vanadium(IV), d^1, which is expected to be paramagnetic.

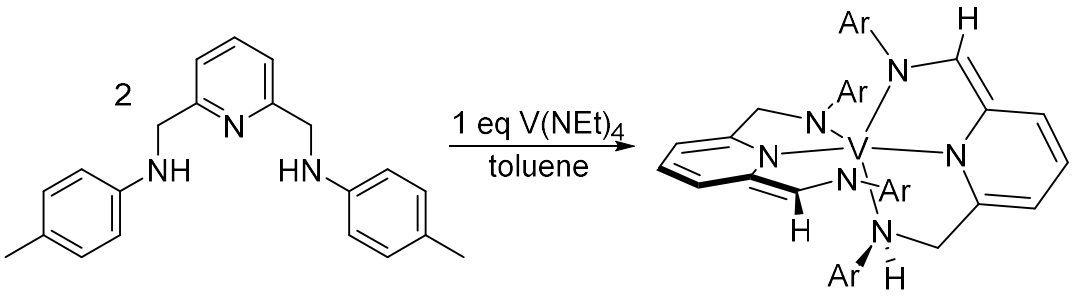

Scheme 5.9: Reaction of ^{Tol}PDA and tetrakis(diethylamido)vanadium(IV).

Recrystallization of the reaction mixture yielded the product (86% yield) shown in Scheme 5.9, another altogether separate product than anticipated. If the mechanism of this reaction is analogous to the niobium derivative, one might expect the product to be diamagnetic (V^{5+}, d^0) with a single denatured ^{Tol}PDA ligand. However, while diamagnetic, the ^{1}H NMR spectrum of this species show some marked structural differences than its predecessor. The spectrum was more asymmetric, with two distinct ligands, neither of which resembled the starting material (Figure 5.37).

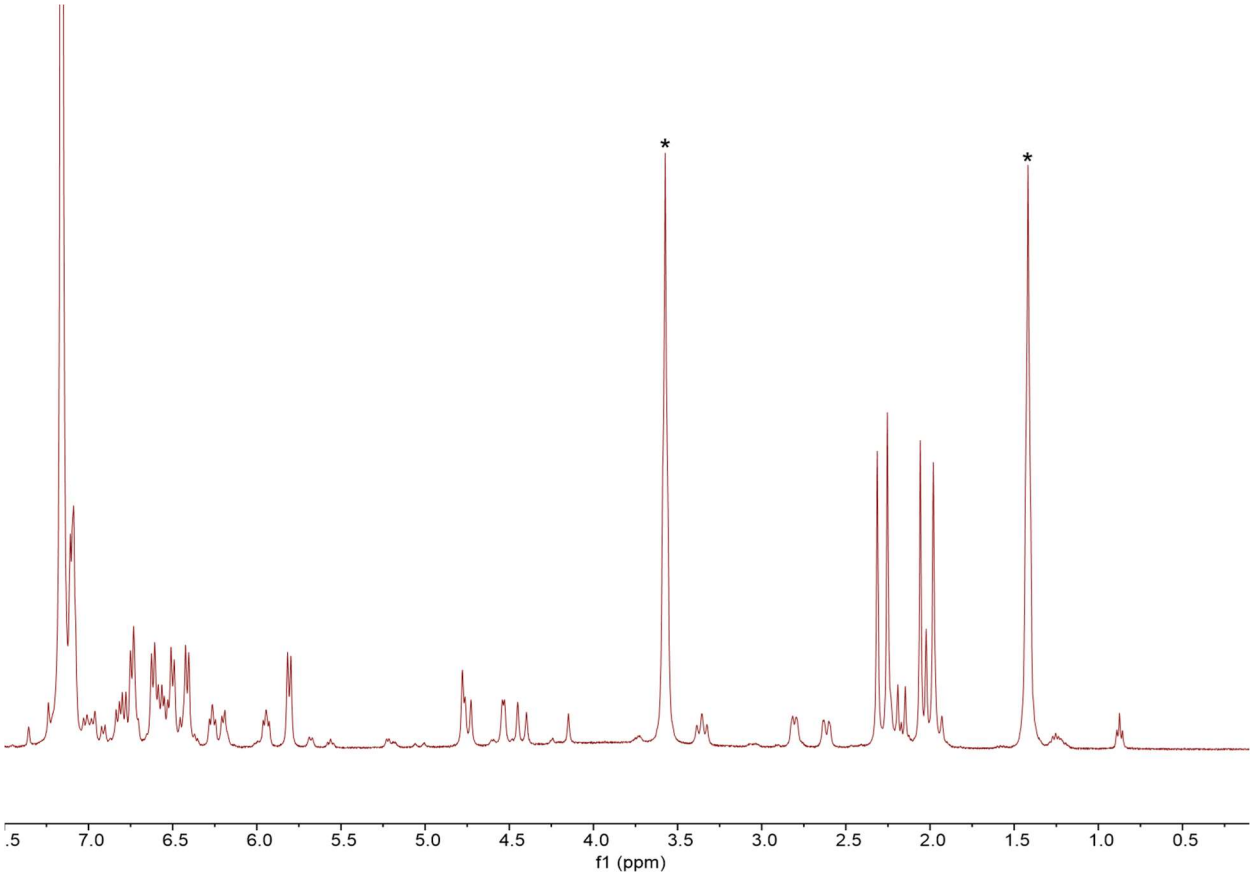

Figure 5.37: ^{1}H NMR spectrum of (NNN)V(NNNH) in benzene-d_6. Residual solvent of crystallization (THF) is marked with *.

Indeed, the product of this reaction gave a complicated spectrum which was heavily convoluted with overlapping peaks. The four singlets (δ 1.8 - 2.4 ppm) in the aliphatic region gave indication of a bis-ligated vanadium species where the aryl substituents on each anilido nitrogen were not chemically equivalent. This would render every proton on the molecule chemically inequivalent with low integrations, making the assignment of the overlapping signals incredibly difficult. To address this challenge, the correlated proton COSY NMR spectrum was measured.

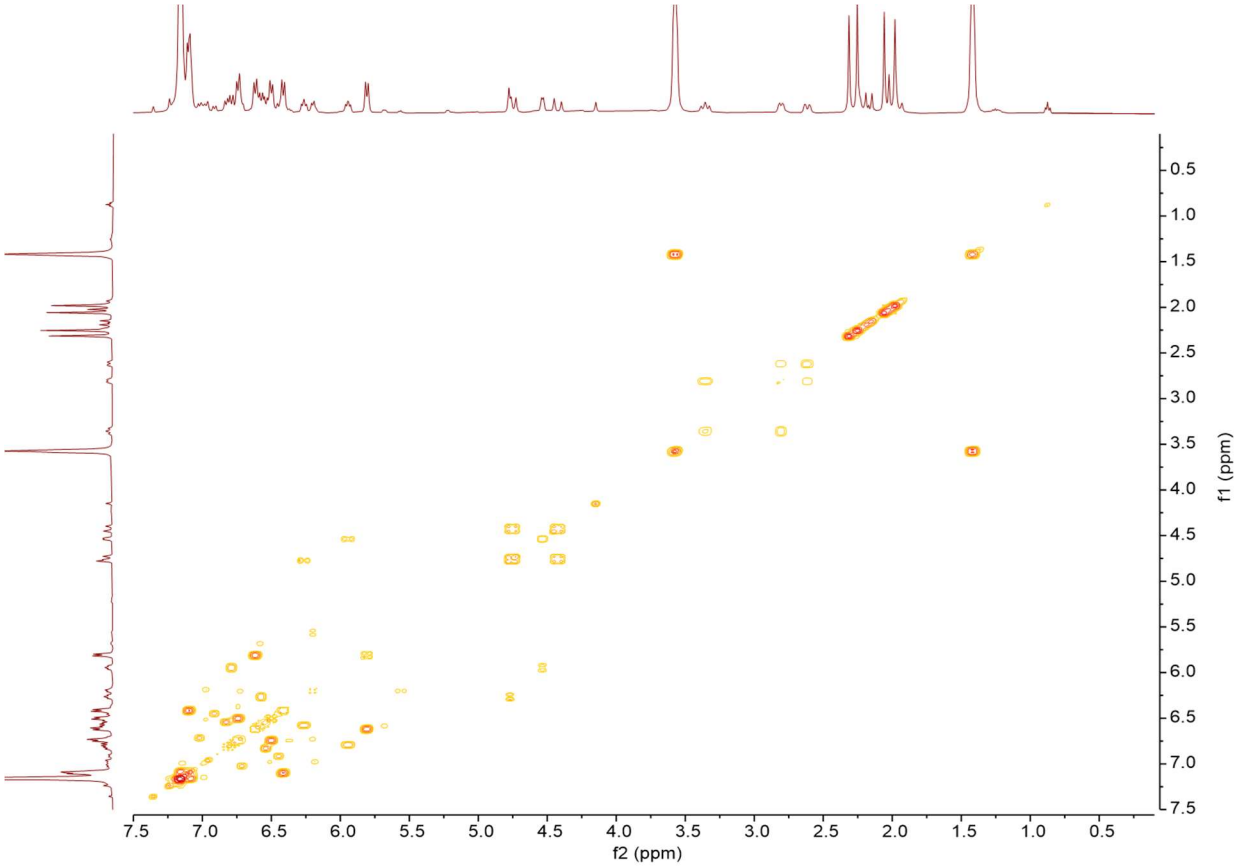

Figure 5.38: (HH) COSY NMR spectrum of (NNN)V(NNNH) in benzene-d_6.

The analysis of the COSY spectrum was further complicated by the many overlapping coupling patterns in the aromatic region. Though this spectrum was taken from crystalline material, the sheer crowding of signals makes the assignment of protons from what may be an impure material harrowing. However, the region between δ 5 – 4 ppm, where we would anticipate benzylic resonances, is relatively clear with reasonably visible coupling information.

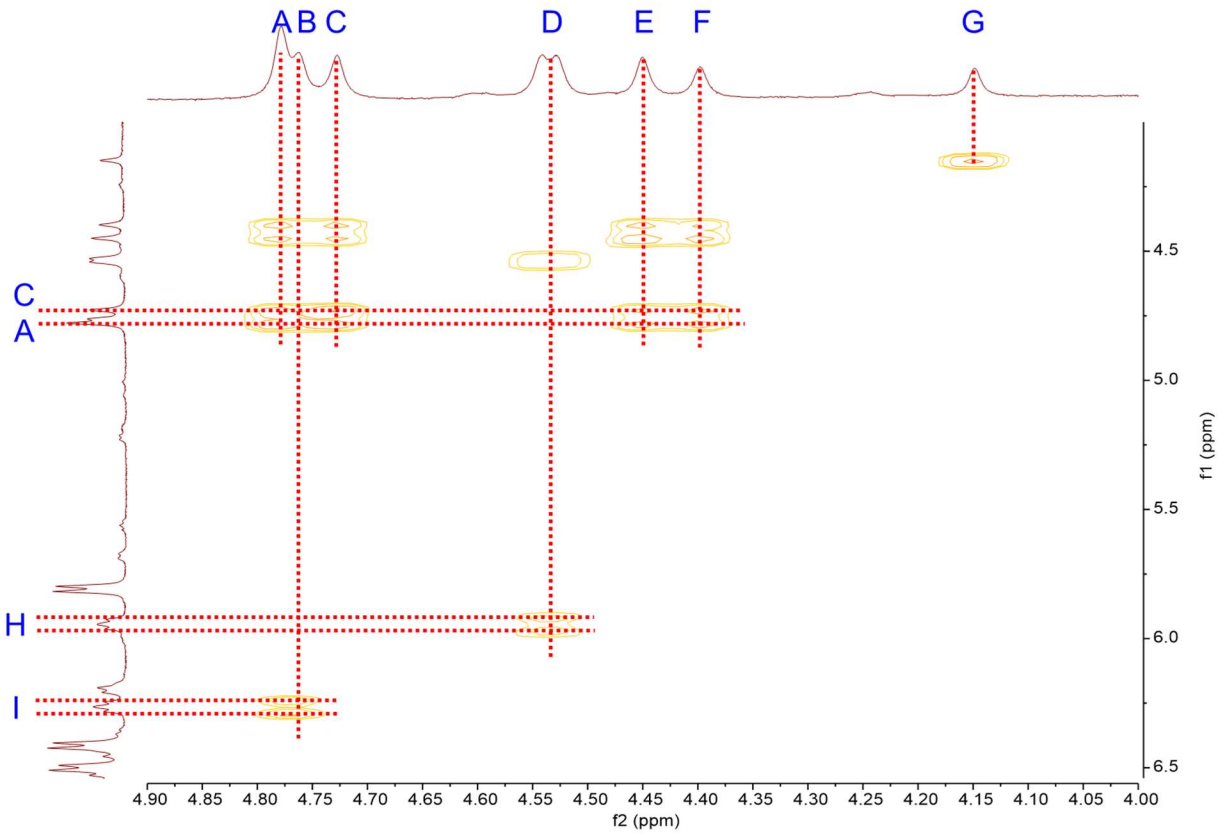

Figure 5.39: Expanded region (δ 5 – 4 ppm) of (HH) COSY NMR spectrum of (NNN)V(NNNH) in benzene-d_6.

Focusing on this region of the COSY spectrum (Figure 5.39), we can see three distinct kinds of signals: those that couple strongly to each other (A/C, E/F), those that couple strongly to the aromatic region (B/I, D/H), and one which couple with neither (G). While the integrations of these signals are not reliable due to the overlap of A, B, and C, the coupling habits of some diastereotopic benzylic protons[51] give some insight into the structure of couples A/C and E/F, where it has been observed that the restricted geometry in bound benzylic species often leads to chemical inequivalence in geminal protons.[52] The coupling of B/I and D/H can be rationalized from the de-aromatization of the pyridine ring, where the formerly methylene units are now a part of an extended π system. This is further evidenced by the close doublet of doublet pattern observed for signals H and I, which exhibits further coupling in the aromatic region. While these limited

data are inconclusive toward the structure of this asymmetric molecule, these inferences were confirmed by an X-ray structural analysis (Figure 5.40).

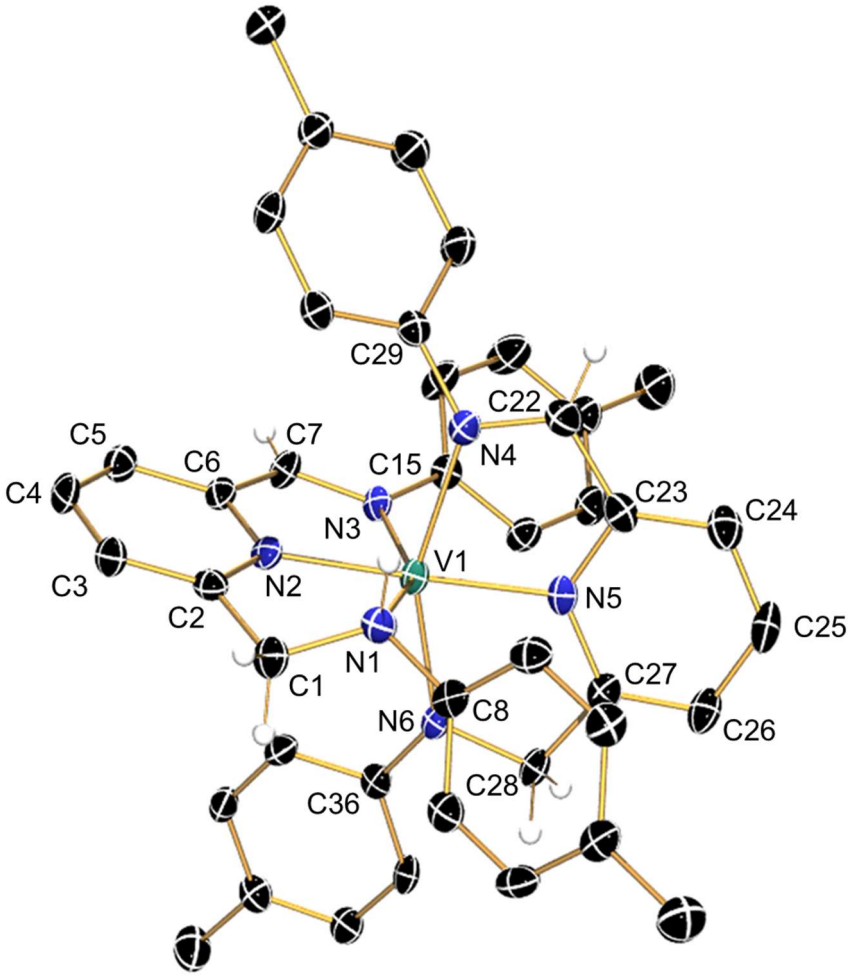

Figure 5.40: ORTEP depiction of (NNN)V(NNNH) at 50% ellipsoid probability. Solvent of crystallization and hydrogen atoms were omitted for clarity, except about the methylene carbons between the aryl and anilido moieties, as well as the proton associate with N1.

Single crystals were grown from the vapor diffusion of pentane into a solution of tetrahydrofuran at -45 ˚C. The structure resolved in a triclinic $P\bar{1}$ cell with a single molecule in the asymmetric unit, as well as three molecules of tetrahydrofuran. Over the course of the refinement of the diffraction data, the proton riding the N1 atom was calculated by the crystallography program (Olex2) as a result of the geometry and bond lengths about the N1 center. Further, a

molecule of THF was oriented in a hydrogen bonding interaction (2.16(5) Å) toward this position. Because its absolute position could not be reliably modeled under our conditions (Mo Kα = 0.71073 Å), these parameters were carefully evaluated in order to investigate the connectivity and hybridization of this nitrogen atom (Table 5.5)

Table 5.5: Relevant bond lengths and angles of (NNN)V(NNNH).

(NNN)		(NNNH)		bond and torsion angles (˚)	
length (Å)					
N4-V1	2.079(4)	N1-V1	2.217(4)	C1-N1-H_N	111(3)
N5-V1	2.014(4)	N2-V1	2.008(4)	V1-N1-H_N	99(3)
N6-V1	2.012(4)	N3-V1	2.037(4)	C8-N1-H_N	104(3)
N5-C23	1.370(5)	N2-C2	1.375(5)	C1-N1-C8	115.7(4)
C23-C24	1.415(7)	C2-C3	1.361(6)		
C24-C25	1.369(7)	C3-C4	1.413(6)		
C25-C26	1.397(7)	C4-C5	1.373(6)		
C26-C27	1.378(6)	C5-C6	1.413(6)		
C27-N5	1.361(6)	C6-N2	1.385(5)		
N4-C22	1.349(6)	N1-C1	1.461(6)		
N4-C29	1.426(6)	N1-C8	1.448(6)		
C22-C23	1.405(7)	C1-C2	1.484(6)		
N6-C28	1.467(5)	N3-C7	1.351(6)		
N6-C36	1.396(5)	N3-C15	1.420(5)		
C27-C28	1.479(6)	C6-C7	1.391(6)		

From these data, it is observed that the N1-V1 bond length is significantly elongated compared to the rest of the chelating ligands Specifically, the V1-N6 bond length of 2.012(2) Å, which is consistent with a proper anilido N donor, is approximately 0.2 Å shorter than the V1- N1 bond. Further, the N1-C1 bond length is roughly equivalent to the N6-C28 bond length, which are

both ~0.1 Å longer than the sp^2 hybridized imido donors (N3-C7; N4-C22). Finally, the bond angles about the N1 atom (Table 5.5) indicate a roughly tetrahedral coordination environment, restricted by the chelation angle of the ligand (N1-V1-N2 = 75.48(14)˚). These data collectively confirm that the assignment of the proton to N1 is reasonable, and that N1 is an sp^3 hybridized nitrogen atom acting as an L type donor to vanadium.

With the structural assignment resolved, the mechanism for this transformation remains ambiguous. Deprotonation of the methylene linkages by amide base provided by the starting material has been considered for both the niobium and now vanadium complexes of this type, however, this would not account for the proton migration to the anilido ligand. It is possible that the base could act as a proton shuttle from a deprotonated methylene bridge to an unrelated anilido nitrogen, though this would be entropically unfavorable. An experiment that could possibly probe this mechanism would involve the use of deuterium labeling of the methylene linkers to attempt to observe transfer to the anilido nitrogen. Further investigation of this reaction mechanism for this ligand transformation is not being pursued at this time.

5.5 Conclusions

The synthesis and characterization of pyridine diamine (PDA) derivatives was performed in order to study their early metal complexes as potential photosensitizers. This study was proceeded by a comparison between these ligands and the previously reported pyridine dipyrrole (PDP) ligands. The electronic structures of different conformations of the PDP derivative were studied in order to better understand their dynamic behavior in relation to the properties of the metalated species. The results of this study provide evidence to an equilibrium between monomeric and dimeric pairs depending on the polarity of the solution. As such, the electronic transitions associated with the extremes of these structures could not be reliably determined, where a distribution of geometries is more likely, especially in the case of the non-polar solvent.

Regardless of the solvent, no dimerization was observed with respect to the PDA ligands. Further, there were no remarkable optically or electrochemical properties intrinsic to the neutral molecule, in stark contrast to the PDP system. While this is not entirely surprising, considering the limited conjugation and increased degrees of freedom, these data are an important baseline for the properties of the metalated products. A mono-ligand species, (^{Mes}PDA)Zr(Bn)$_2$, was prepared in pursuit of this project. Our inability to isolate the bis-ligand species of the mesityl moiety was treated as defining the limit to the degree of steric encumberment that is allowed in these systems. It was also by the isolation of this complex that the idea of an aliphatic "tag" be placed on the aryl substituents of the ligand as a reporter for ^{1}H NMR spectroscopy. Preparation and utilization of ^{Tol}PDA followed these experiments, where the 2- and 6- positions of the amide aryl are no longer substituted.

Succinctly, bis-pyridine diamide complexes with tolyl substituents containing titanium and zirconium are not luminescent. This is likely due to the unrestricted vibrational modes associated

with the sp^3 hybridized methylene bridging unit, as was noted in the free ligand. This hypothesis is reinforced by a combination of structural data in the solution and solid states. In the crystal structure, significant buckling of the ligand backbone is observed about the pincer-metal plane. However, this structural feature contrasts with the NMR data, which gives a D_{2d} symmetric molecule on the NMR timescale, where both ligands are chemically equivalent to each other. These data suggest a good deal of unrestricted vibrational modes intrinsic to these molecules.

Further, the lack of aromaticity in the ligand backbone contributes to this lack of photoactivity by increasing the energy of the ground state HOMO relative to zirconium. The absorption profile of these molecules shows that excitation to the lowest excited state requires near violet light (~420 nm, 2.95 eV/photon), in contrast to the PDP complexes which only require green light (525 nm, 2.36 eV/photon). This suggests a larger energy gap between the ligand HOMO and the metal LUMO, preventing good mixing for ligand-to-metal charge transfer. This hypothesis is supported by calculations of these excited state transitions.

As noted previously, the pyridine diamine ligand has been shown to be redox innocent and undergo chemical electrochemical oxidation that is largely irreversible, making it unsuitable for applications as a scaffold for a photosensitizer. This was evidenced by cyclic voltammogram of $Zr(^{Tol}PDA)_2$, where electrochemical changes were observed over a span of nearly 1.2 V, centered around -0.7 V. This observation was replicated following the synthesis and characterization of the Group 5 derivatives.

While isolation of either the Nb^{IV} or Nb^{V} bis-PDA was not possible under our conditions, a singly deprotonated and dearomatized species was characterized. The cyclic voltammogram also had an interesting, more reversible, EC process with maxima at -0.87 V and -1.72 V, centered on 1.30 V. This event is likely analogous to the redox couple observed in the $Zr(^{Tol}PDA)_2$ species. An

unusual denatured ligand form was observed following the aminolysis of $V(NEt_2)_4$, where a proton was shuttled to an anilido nitrogen. The mechanisms of these transformations are not completely understood, but presumably a byproduct of the intended reaction in the presence of base.

5.6 Experimental Procedures

General Considerations. All air- and moisture-sensitive manipulations were carried out using standard Schlenk line and cannula techniques or in an MBraun inert atmosphere drybox containing an atmosphere of purified nitrogen. Solvents for air- and moisture- sensitive manipulations were dried and deoxygenated using a Glass Contour Solvent Purification System and stored over 4 Å molecular sieves. All solids were dried under high vacuum in oven-dried glassware in order to bring into the glovebox. Deuterated benzene (C_6D_6) for NMR spectroscopy was distilled from sodium. Deuterated methylene chloride (CD_2Cl_2) for NMR spectroscopy was distilled from CaH_2. All solids that were prepared in outside of the box were dried under high vacuum in oven-dried glassware before use in inert atmosphere. Metal halides were purchased and used without further purification. Tetrabenzylzirconium,[53] tetrakis(diethylamido)niobium,[54] tetrakis(diethylamido)vanadium,[50] and 2,6-pyridinedicarboxaldehyde[55] were prepared according to literature methods.

Physical and Computational Measurements. Nuclear magnetic resonance (NMR) experiments were performed at 400 MHz on a 400-MR DD2 Agilent instrument. All chemical shifts are reported relative to tetramethylsilane with residual solvent proton signal as a secondary standard. Deuterated benzene was distilled from sodium metal and stored over 4 Å molecular sieves. Deuterated methylene chloride was distilled from CaH_2 and stored of 4 Å molecular sieves. Splitting in ^1H NMR studies is notated by: s = singlet, d = doublet, t = triplet, sept = septet, b = broad, m = multiplet or combinations thereof.

Single crystals were prepared for X-ray diffraction in the glovebox by coating with previously degassed polyisobutylene oil (Sigma-Aldrich). These were then picked with a nylon

loop (MiTeGen) and mounted to the goniometer head of a Bruker AXS D8 Venture fixed-chi X-ray diffractometer in a cold stream of dry nitrogen. The instrument features a Triumph monochromator, a Mo Kα radiation source (λ = 0.71073 Å), and a PHOTON 100 CMOS detector. Utilizing the APEX3[56] software package, data was collected, processed with SAINT+, and subjected to absorption correction via SADABS/TWINABS. The space group were determined with XPREP and solved using intrinsic phasing (SHELXL[57]) before refinement with Olex2.[58] Structures are represented at 50% probability thermal ellipsoids via ORTEP-3.

Cyclic voltammetry was recorded under nitrogen atmosphere in anhydrous tetrahydrofuran using NBu_4PF_6 as an electrolyte and referenced to ferrocene/ferrocenium$^+$. Set up included a Gamry Interface 1000 electrochemical workstation in a single compartment cell utilizing a three-electrode system: a glassy carbon working electrode, platinum sheet as the counter electrode, and coiled silver wire as a quasi-reference electrode. All spectra were taken at a rate of 200 mVs^{-1} in 5 mV steps unless otherwise indicated.

UV-visible and emission spectra were acquired via Shimadzu UV-1800 spectrophotometer and RF-5301 PC spectrofluorophotometer, respectively. Samples were prepared in the glove box under nitrogen in either dry benzene or tetrahydrofuran in J-Young adapted quartz cuvettes.

Density functional theory (DFT) and time-dependent density functional theory (TD-DFT) calculations were performed with the ORCA[43,44] program package. Each were carried out at the B3LYP level of theory. Calculated orbitals were plotted using the program Gabedit.[59]

Preparation of ^{Tol}PDA – To a 250 mL round bottom flask, 3.003 g (22.22 mmol) of 2,6-pyridinedicarboxaldehyde was added with 4.818 g (44.96 mmol) of p-toluidine. The solids were dissolved in methanol with vigorous stirring before 3 drops of glacial acetic acid were added and

the reaction mixture refluxed overnight. The following morning, the reaction mixture was cooled to room temperature before excess $NaBH_4$ (3.41 g, 90.14 mmol) was carefully added, and the reaction mixture refluxed another 2 hours. The mixture was reduced to dryness via rotovap, and the solids extracted with diethyl ether. The solvent was removed under vacuum and the product obtained as a tan powder (7.00 g, 22.19 mmol, 99%). ^{1}H NMR (400 MHz, C_6D_6): δ 7.01 (t, 1H, J = 7.6 Hz), 6.97 (bd, 4 H, J = 8.0 Hz), 6.81 (d, 2H, J = 7.7 Hz), 6.51 (m, 4 H, 8.4 Hz), 4.25 (b, 6H, NH+CH_2), 2.17 (s, 6H). ^{13}C{^{1}H } NMR (400 MHz, C_6D_6): δ 158.96, 146.33, 136.84, 130.11, 126.53, 119.63, 113.52, 49.82, 20.62.

Preparation of ^{Mes}PDA – To a 100 mL round bottom flask, 1.232 g (9.12 mmol) of 2,6-pyridinedicarboxaldehyde was added with 3.70 g (27.36 mmol) of mesityl aniline. The solids were dissolved in ethanol with vigorous stirring before 3 drops of glacial acetic acid were added and the reaction mixture refluxed overnight. The following morning, the reaction mixture was cooled to room temperature before excess $NaBH_3(CN)$ (1.722 g, 27.40 mmol) was carefully added, and the reaction mixture refluxed another 5 hours. The mixture was reduced to a green sludge via rotovap and passed through a deep plug of silica gel with a 3:1 Hexane/EtOAc eluent. The first band was collected and reduced to dryness under vacuum. The product was isolated from the orange, oily residue by rigorous drying under high vacuum overnight, with gentle heating. Recrystallization from hexanes gave a tan powder (0.853 g, 2.27 mmol, 25%). ^{1}H NMR (400 MHz, C_6D_6): δ 7.00 (t, 1H, J = 7.9 Hz), 6.81 (s, 4H), 6.73 (d, 2H, J = 7.6 Hz), 4.18 (s, 4H), 4.15 (b, 2H), 2.28 (s, 12H), 2.19 (s, 6H). ^{13}C{^{1}H} NMR (400 MHz, C_6D_6): δ 159.37, 144.33, 136.69, 131.18, 129.93, 129.89, 120.30, 54.41, 20.81, 18.72.

Preparation of (^{Mes}PDA)Zr(Bn)$_2$ – A 20 mL scintillation vial, blacked out with vinyl tape, was charged with 65 mg (0.14 mmol) Zr(Bn)$_4$ and dissolved in benzene. A separate vial containing 52 mg (0.14 mmol) ^{Mes}PDA was also dissolved in benzene and added to the metal solution, dropwise. The reaction was left to stir for 3 hours at room temperature. It was then concentrated under vacuum and precipitated with pentane at -45 ˚C. The bright yellow solids (38 g, 0.05 mmol, 38 %) were triturated with pentane and dried under vacuum. ^{1}H NMR (400 MHz, C_6D_6): δ 7.02 (d, 2H, J = 7.6 Hz), 6.95 (s, 4H), 6.91 (t, 4H, J = 7.4 Hz) 6.85 (t, 1H, J = 7.7 Hz), 6.44 (d, 4H, J = 6.9 Hz), 6.37 (d, 2H, J = 7.6 Hz), 4.50 (s, 4H), 2.41 (s, 12H), 2.19 (s, 6H), 2.11 (s, 4H). Crystals suitable for X-ray diffraction were grown from vapor diffusion of pentane into toluene at -45 ˚C.

Preparation of Zr(^{Tol}PDA)$_2$ – A 20 mL scintillation vial, blacked out with vinyl tape, was charged with 68 mg (0.15 mmol) Zr(Bn)$_4$ and dissolved in toluene. A separate vial containing 101 mg (0.32 mmol) ^{Tol}PDA was also dissolved in toluene and added to the metal solution. The reaction was left to stir for 24 hours. It was then concentrated under vacuum, passed through a plug of Celite, and layered with pentane at -30℃. The resulting precipitate was again recrystallized by slow diffusion of pentane into toluene (111 mg, 0.14 mmol, 96%). ^{1}H NMR (400 MHz, C_6D_6): δ 6.93 (t, 2H, J = 7.7 Hz), 6.81 (d, 8H, J = 8.5 Hz), 6.90 (d, 8H, J = 8.32 Hz), 6.48 (d, 4H, 7.7 Hz), 4.61 (s, 8H), 2.16 (s, 12H). Yellow, transparent, rhomboidal crystals were collected by filtration, suitable for X-ray diffraction.

Preparation of Ti(^{Tol}PDA)$_2$ – In a 20 mL scintillation vial, 188 mg (0.60 mmol) of ^{Tol}PDA was dissolved in tetrahydrofuran and deprotonated with 478 mL (1.12 mmol) 2.5 M n-BuLi in hexanes. After stirring a few minutes, the blackened solution was added dropwise to a stirring slurry of

$TiCl_4(thf)_2$ (97 mg, 0.29 mmol). After the addition was complete, the reaction mixture was allowed to stir overnight before reduction to dryness under vacuum. The residue was taken in toluene to precipitate dissolved salts and filtered with Celite. The solution was dried under vacuum and triturated with pentane to yield a sparkly black powder (154 mg, 0.23 mmol, 78 %). ^{1}H NMR (400 MHz, C_6D_6): δ 6.85 (t, 2H, J = 7.7 Hz), 6.79 (d, 8H, J = 8.1 Hz), 6.68 (d, 8H, 8.4 Hz), 6.51 (d, 4H, J = 7.7 Hz), 4.88 (s, 8H), 2.14 (s, 12H). Dark red/black parallelopipeds were collected by filtration, suitable for X-ray diffraction.

Preparation of (^{Tol}PDA)Nb(NNN) – Tetrakis(diethylamido)niobium (44 mg, 0.12 mmol) was weighed in a vial and transferred to a bomb tube in toluene. Similarly, 100 mg (0.32 mmol) ^{Tol}PDA was weighed and added in toluene. The reaction vessel was sealed under nitrogen and refluxed overnight at 110℃. The resulting mixture was then reduced to dryness and triturated with pentane to remove any volatile amines. The solid residues were reconstituted in minimal toluene, filtered through Celite, and layered with pentane at -30℃. The red precipitate was collected by decanting the mother liquor (24 mg, 0.03 mmol, 29%). ^{1}H NMR (400 MHz, C_6D_6): δ 7.13 (d, 1H, J = 9.0 Hz), 6.98 (d, 4H, J = 8.2 Hz), 6.72 (t, 1H, J = 7.7 Hz), 6.66 (t, 4H, J = 8.5 Hz), 6.51 (m, 6H), 6.33 (d, 4H, J = 8.5 Hz), 6.29 (d, 2H, J = 7.8 Hz), 5.44 (dd, 1H, J = 6.3, 1.3 Hz), 4.97 (s, 4H), 4.83 (s, 2H), 2.18 (s, 6H), 1.98 (s, 6H). X-ray quality crystals were grown from by vapor diffusion of pentane into a solution of toluene at -30℃.

Preparation of (NNN)V(HNNN) – Tetrakis(diethylamido)vanadium (195 mg, 0.57 mmol) was weighed in a vial and transferred to a bomb tube in tetrahydrofuran. Similarly, 365 mg (1.16 mmol) ^{Tol}PDA was weighed and added in THF. The reaction vessel was sealed under nitrogen and

refluxed overnight at 110℃. The resulting mixture was then reduced to dryness and triturated with pentane to remove and volatile amines. The residue was reconstituted in THF, filtered through Celite, and reduced to dryness. Collected 336 mg (0.49 mmol, 86%) blue/black powder. Crystals suitable for X-ray diffraction were grown from vapor diffusion of pentane into tetrahydrofuran at -45 ˚C.

5.7 References

(1) Lewis, N. S. Solar Energy Use. *Science* **2007**, *798* (1), 798–802.

(2) Bora, L. V.; Mewada, R. K. Visible/Solar Light Active Photocatalysts for Organic Effluent Treatment: Fundamentals, Mechanisms and Parametric Review. *Renew. Sustain. Energy Rev.* **2017**, *76* (November 2015), 1393–1421.

(3) Liu, W.; Ma, H.; Walsh, A. Advance in Photonic Crystal Solar Cells. *Renew. Sustain. Energy Rev.* **2019**, *116* (April), 109436.

(4) Orona-Navar, A.; Aguilar-Hernández, I.; López-Luke, T.; Pacheco, A.; Ornelas-Soto, N. Dye Sensitized Solar Cell (DSSC) by Using a Natural Pigment from Microalgae. *Int. J. Chem. Eng. Appl.* **2020**, *11* (1), 14–17.

(5) Malviya, A.; Solanki, P. P. Photogalvanics: A Sustainable and Promising Device for Solar Energy Conversion and Storage. *Renew. Sustain. Energy Rev.* **2016**, *59*, 662–691.

(6) Sengupta, D.; Das, P.; Mondal, B.; Mukherjee, K. Effects of Doping, Morphology and Film-Thickness of Photo-Anode Materials for Dye Sensitized Solar Cell Application - A Review. *Renew. Sustain. Energy Rev.* **2016**, *60*, 356–376.

(7) Glunz, S. W.; Preu, R.; Biro, D. *Crystalline Silicon Solar Cells. State-of-the-Art and Future Developments*; 2012; Vol. 1.

(8) Blanco, J.; Malato, S.; Fernández-Ibañez, P.; Alarcón, D.; Gernjak, W.; Maldonado, M. I. Review of Feasible Solar Energy Applications to Water Processes. *Renew. Sustain. Energy Rev.* **2009**, *13* (6–7), 1437–1445.

(9) UNDP. *World Energy Assessment Update*; 2004.

(10) Photonique, L. D. E.; Interfaces, E. T. Dynamics of Electron Transfer Processes at the Surface of Dye-Sensitized Mesoporous Semiconductor Films. *Sci. York* **2010**, *4731*.

(11) Nazeeruddin, M. K.; Baranoff, E.; Grätzel, M. Dye-Sensitized Solar Cells: A Brief Overview. *Sol. Energy* **2011**, *85* (6), 1172–1178.

(12) Zeitler, K. Photoredox Catalysis with Visible Light. *Angew. Chemie Int. Ed.* **2009**, *48* (52), 9785–9789.

(13) Tucker, J. W.; Stephenson, C. R. J. Shining Light on Photoredox Catalysis: Theory and Synthetic Applications. *J. Org. Chem.* **2012**, *77* (4), 1617–1622.

(14) Xuan, J.; Xiao, W. J. Visible-Light Photoredox Catalysis. *Angew. Chemie Int. Ed.* **2012**, *51* (28), 6828–6838.

(15) Yoon, T. P.; Ischay, M. A.; Du, J. Visible Light Photocatalysis as a Greener Approach to Photochemical Synthesis. *Nat. Chem.* **2010**, *2* (7), 527–532.

(16) Prier, C. K.; Rankic, D. A.; MacMillan, D. W. C. Visible Light Photoredox Catalysis with Transition Metal Complexes: Applications in Organic Synthesis. *Chem. Rev.* **2013**, *113* (7), 5322–5363.

(17) Larsen, C. B.; Wenger, O. S. Photoredox Catalysis with Metal Complexes Made from Earth-Abundant Elements. *Chem. Eur. J.* **2018**, *24* (9), 2039–2058.

(18) Lees, A. J. Luminescence Properties of Organometallic Complexes. *Chem. Rev.* **1987**, *87* (4), 711–743.

(19) McCusker, J. K. Femtosecond Absorption Spectroscopy of Transition Metal Charge-Transfer Complexes. *Acc. Chem. Res.* **2003**, *36* (12), 876–887.

(20) Chergui, M. Ultrafast Photophysics of Transition Metal Complexes. *Acc. Chem. Res.* **2015**, *48* (3), 801–808.

(21) Yeh, A. T.; Shank, C. V.; McCusker, J. K. Ultrafast Electron Localization Dynamics Following Photo-Induced Charge Transfer. *Science* **2000**, *289* (5481), 935–938.

(22) Demadis, K. D.; Hartshorn, C. M.; Meyer, T. J. The Localized-to-Delocalized Transition in Mixed-Valence Chemistry. *Chem. Rev.* **2001**, *101* (9), 2655–2685.

(23) Baryshnikov, G.; Minaev, B.; Ågren, H. Theory and Calculation of the Phosphorescence Phenomenon. *Chem. Rev.* **2017**, *117* (9), 6500–6537.

(24) Penfold, T. J.; Gindensperger, E.; Daniel, C.; Marian, C. M.; J. Penfold, T.; Gindensperger, E.; Daniel, C.; M. Marian, C. Spin-Vibronic Mechanism for Intersystem Crossing. *Chem. Rev.* **2018**, *118* (15), 6975–7025.

(25) Grätzel, M. Dye-Sensitized Solar Cells. *J. Photochem. Photobiol. C Photochem. Rev.* **2003**, *4* (2), 145–153.

(26) Du, P.; Eisenberg, R. Energy Upconversion Sensitized by a Platinum(II) Terpyridyl Acetylide Complex †. *Chem. Sci.* **2010**, *1*, 502–506.

(27) Yakutkin, V.; Aleshchenkov, S.; Chernov, S.; Miteva, T.; Nelles, G.; Cheprakov, A.; Baluschev, S. Towards the IR Limit of the Triplet Triplet Annihilation-Supported Up-Conversion: Tetraanthraporphyrin. *Chem. Eur.J* **2008**, No. 14, 9846–9850.

(28) Baluschev, S.; Yakutkin, V.; Miteva, T.; Avlasevich, Y.; Chernov, S.; Aleshchenkov, S.; Nelles, G.; Cheprakov, A.; Yasuda, A.; Mullen, K.; Wegner, G. Blue-Green Up-Conversion Noncoherent Excitation by NIR Light. *Angew Chem. lni. Ed.* **2007**, No. 46, 7693–7996.

(29) Zhang, Y.; Lee, T. S.; Favale, J. M.; Leary, D. C.; Petersen, J. L.; Scholes, G. D.; Castellano, F. N.; Milsmann, C. Delayed Fluorescence from a Zirconium(Iv) Photosensitizer with Ligand-to-Metal Charge-Transfer Excited States. *Nat. Chem.* **2020**, *12* (4), 345–352.

(30) Metzger, R. M. Unimolecular Electronics. *Chem. Rev.* **2015**, *115* (11), 5056–5115.

(31) Dorn, M.; Kalmbach, J.; Boden, P.; Päpcke, A.; Gómez, S.; Förster, C.; Kuczelinis, F.; M. Carrella, L.; A. Büldt, L.; H. Bings, N.; Rentschler, E.; Lochbrunner, S.; González, L.; Gerhards, M.; Seitz, M.; Heinze, K. A Vanadium(III) Complex with Blue and NIR-II Spin-Flip Luminescence in Solution. *J. Am. Chem. Soc.* **2020**, *142* (17), 7947–7955.

(32) Rehm, D.; Weller, A. Kinetics of Fluorescence Quenching by Electron and H-Atom Transfer. *Isr. J. Chem.* **1970**, *8*, 259–271.

(33) Arias-Rotondo, D. M.; McCusker, J. K. The Photophysics of Photoredox Catalysis: A Roadmap for Catalyst Design. *Chem. Soc. Rev.* **2016**, *45* (21), 5803–5820.

(34) King, K. A.; Spellane, P. J.; Watts, R. J. Excited-State Properties of Triply Ortho-Metalated Iridium(III) Complex. *J. Am. Chem. Soc.* **1985**, No. 107, 1431–1432.

(35) Ando, K. Ligand-to-Metal Charge-Transfer Dynamics in a Blue Copper Protein Plastocyanin: A Molecular Dynamics Study. *J. Phys. Chem. B* **2008**, *112* (2), 250–256.

(36) N. Choing, S.; J. Francis, A.; Clendenning, G.; S. Schuurman, M.; D. Sommer, R.; Tamblyn, I.; W. Weare, W.; Cuk, T. Long-Lived LMCT in a D0 Vanadium(V) Complex by Internal Conversion to a State of $3d_{xy}$ Character. *J. Phys. Chem. C* **2015**, *119* (30), 17029–17038.

(37) Mandal, M.; Oppelt, K.; List, M.; Teasdale, I.; Chakraborty, D.; Monkowius, U. Copper(II) Complexes with Imino Phenoxide Ligands: Synthesis, Characterization, and Their Application as Catalysts for the Ring-Opening Polymerization of Rac-Lactide. *Monatshefte fur Chemie* **2016**, *147* (11), 1883–1892.

(38) Ghannam, J.; Al Assil, T.; C. Pankratz, T.; L. Lord, R.; Zeller, M.; Lee, W.-T. A Series of 4- and 5-Coordinate Ni(II) Complexes: Synthesis, Characterization, Spectroscopic, and DFT Studies. *Inorg. Chem.* **2018**, *57* (14), 8307–8316.

(39) Minh, P.; Đô˜, N. Đ.; Akhmedov, N. G.; Petersen, J. L.; Dolinar, B. S.; Milsmann, C.; Bennett, C. E.; Li, R.; Chemcomm, /; Communication, C. Photochemical Synthesis of a Zirconium Cyclobutadienyl Complex †. *Chem. Commun* **2020**, *56*, 5397.

(40) Li, C.; Kong, X. Y.; Tan, Z. H.; Yang, C. T.; Soo, H. Sen. Emergence of Ligand-to-Metal Charge Transfer in Homogeneous Photocatalysis and Photosensitization. *Chem. Phys. Rev.* **2022**, *3* (2), 021303.

(41) Zhang, Y.; Petersen, J. L.; Milsmann, C. A Luminescent Zirconium(IV) Complex as a Molecular Photosensitizer for Visible Light Photoredox Catalysis. *J. Am. Chem. Soc.* **2016**, *138* (40), 13115–13118.

(42) Zhang, Y.; Lee, T. S.; Petersen, J. L.; Milsmann, C. A Zirconium Photosensitizer with a Long-Lived Excited State: Mechanistic Insight into Photoinduced Single-Electron Transfer. *J. Am. Chem. Soc.* **2018**, *140* (18), 5934–5947.

(43) Neese, F. The ORCA Program System. *Wiley Interdiscip. Rev. Comput. Mol. Sci.* **2012**, *2* (1), 73–78.

(44) Neese, F. Software Update: The ORCA Program System, Version 4.0. *Wiley Interdiscip. Rev. Comput. Mol. Sci.* **2017**, *8* (1), e1327.

(45) Tantardini, C.; Oganov, A. R. Thermochemical Electronegativities of the Elements. *Nat. Commun.* **2021**, *12* (1), 1–9.

(46) Arnaiz, A.; Cuevas, J. V.; Garcia-Herbosa, G.; Carbayo, A.; Casares, J. A.; Gutierrez-Puebla, E. Revealing the Diastereomeric Nature of Pincer Terdentate Nitrogen Ligands 2,6-Bis(Arylaminomethyl)Pyridine through Coordination to Palladium. *J. Chem. Soc. Dalt. Trans.* **2002**, *12*, 2581–2586.

(47) Estler, F.; Eickerling, G.; Herdtweck, E.; Anwander, R. Organo-Rare-Earth Complexes

Supported by Chelating Diamide Ligands. *Organometallics* **2003**, *22* (6), 1212–1222.

(48) Weast, R. C.; Lide, D. R. *CRC Handbook of Chemistry and Physics: 70th Ed*.

(49) Unpublished Work.

(50) Bradley, D. C.; Mehta, M. L. Alkoxides of Vanadium (IV). *Can. J. Chem.* **1962**, *40* (6), 1183–1188.

(51) Guérin, F. Synthesis, Structure, and Reactivity of Zirconium Alkyl Complexes Bearing Ancillary Pyridine Diamide Ligands. *Organometallics* **1998**, *17* (23), 5172–5177.

(52) E. O'Reilly, M.; Ghiviriga, I.; A. Abboud, K.; S. Veige, A. A New ONO3- Trianionic Pincer-Type Ligand for Generating Highly Nucleophilic Metal–Carbon Multiple Bonds. *J. Am. Chem. Soc.* **2012**, *134* (27), 11185–11195.

(53) Rong, Y.; Al-Harbi, A.; Parkin, G. Highly Variable Zr-CH2-Ph Bond Angles in Tetrabenzylzirconium: Analysis of Benzyl Ligand Coordination Modes. *Organometallics* **2012**, *31* (23), 8208–8217.

(54) Bradley, D. C.; Chisholm, M. H. Covalent Compounds of Quadrivalent Transition Metals. Part IV Niobium(Iv) DiaIkylamides. *J. Chem. Soc.* **1971**, *A*, 1511–1514.

(55) Peng, Y.; Li, Z.; Zeng, Y.; Xie, X.; Wang, H.; Li, L.; Liu, X. Solid Phase Extractors Derived by Functionalising Sub-Micro Silica Gel with Chelating Agents and Their PH-Tunable Adsorbing Capability towards Pb(II) and Ag(I). *Microchim. Acta 2010 1701* **2010**, *170* (1), 17–26.

(56) Bruker. *APEX3 User Manual*; 2016.

(57) Sheldrick, G. M. Crystal Structure Refinement with SHELXL. *Acta Crystallogr. Sect. C Struct. Chem.* **2015**, *71* (Md), 3–8.

(58) Dolomanov, O. V.; Bourhis, L. J.; Gildea, R. J.; Howard, J. A. K.; Puschmann, H.

OLEX2: A Complete Structure Solution, Refinement and Analysis Program. *J. Appl. Cryst.* **2009**, No. 42, 339–341.

(59) Allouche, A. R. Gabedit - A Graphical User Interface for Computational Chemistry Softwares. *J. Comput. Chem.* **2011**, No. 32, 174–182.

Appendix A2: Supplementary Information for Chapter 2

A2.1 ^{1}H NMR spectrum of (^{Mes}PDP^{Ph})VCl(thf)$_2$ in benzene-d_6.

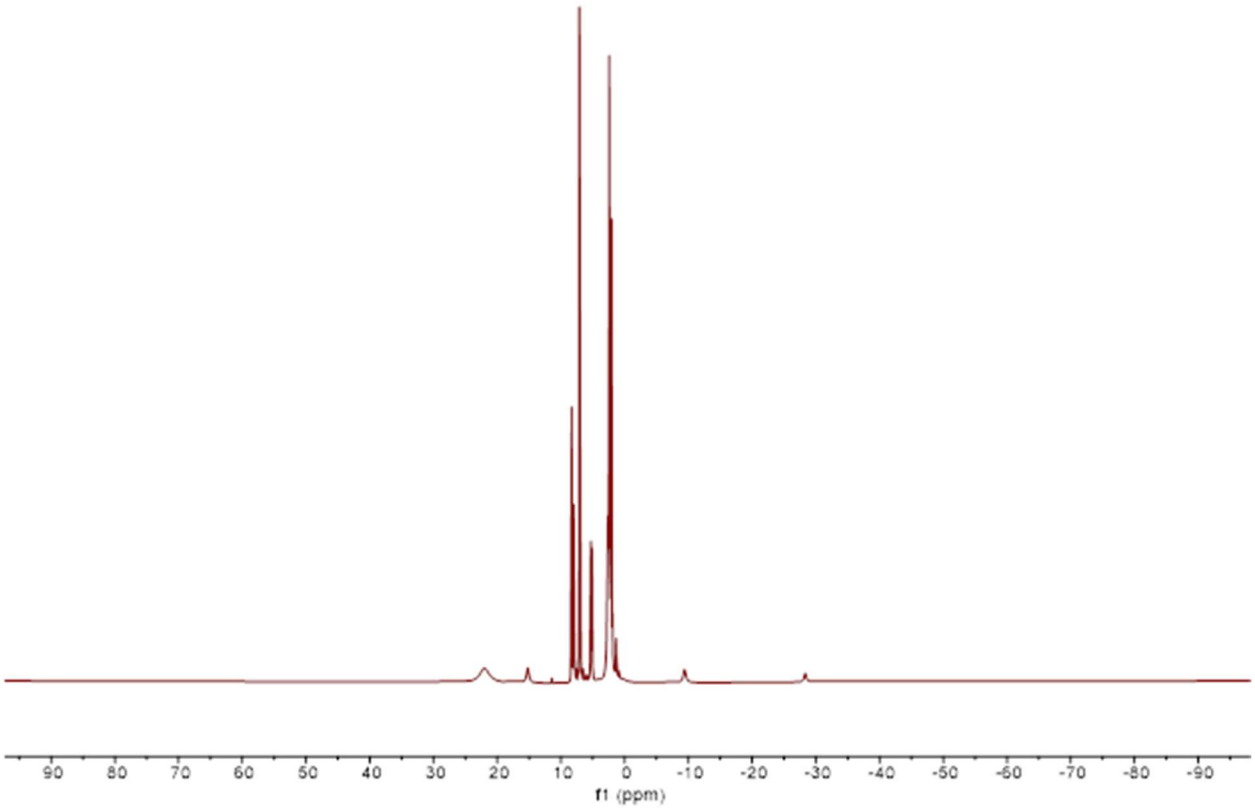

A2.2 IR spectrum of (^{Mes}PDP^{Ph})VCl(thf)$_2$ in KBr.

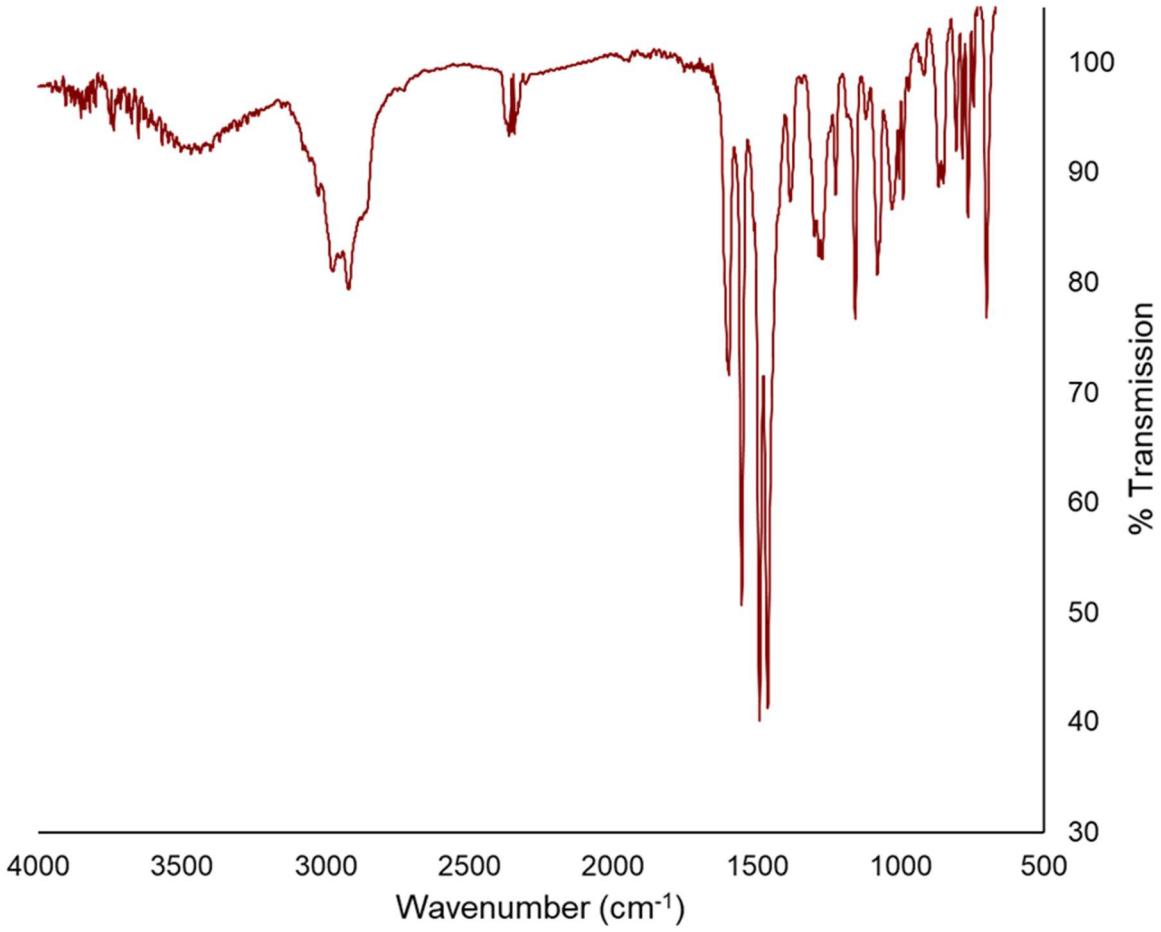

A2.3 ^{1}H of (^{Mes}PDP^{Ph})VCl(py)$_2$ in benzene-d_6.

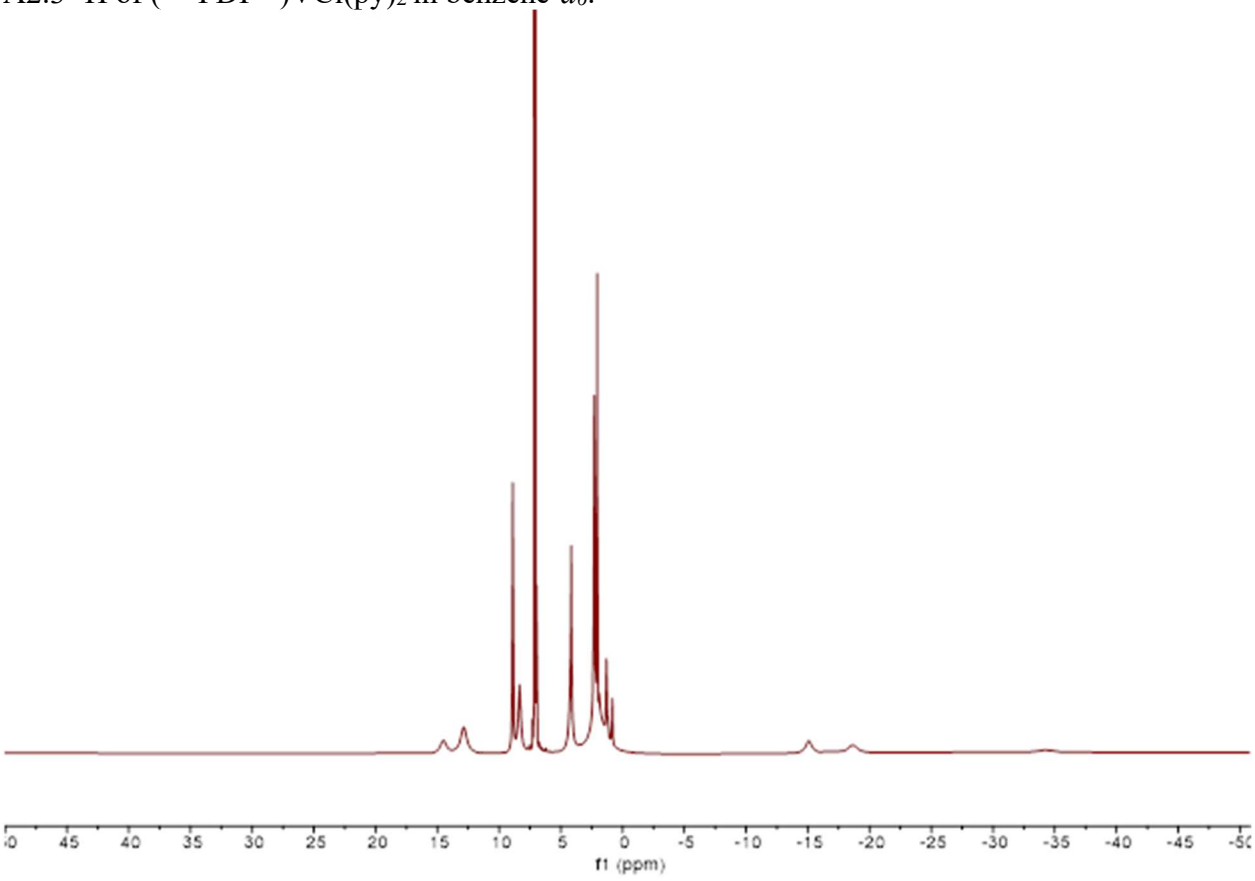

A2.4 ^{1}H NMR spectrum of (^{Mes}PDP^{Ph})V(thf)$_3$ in benzene-d_6 with residual toluene.

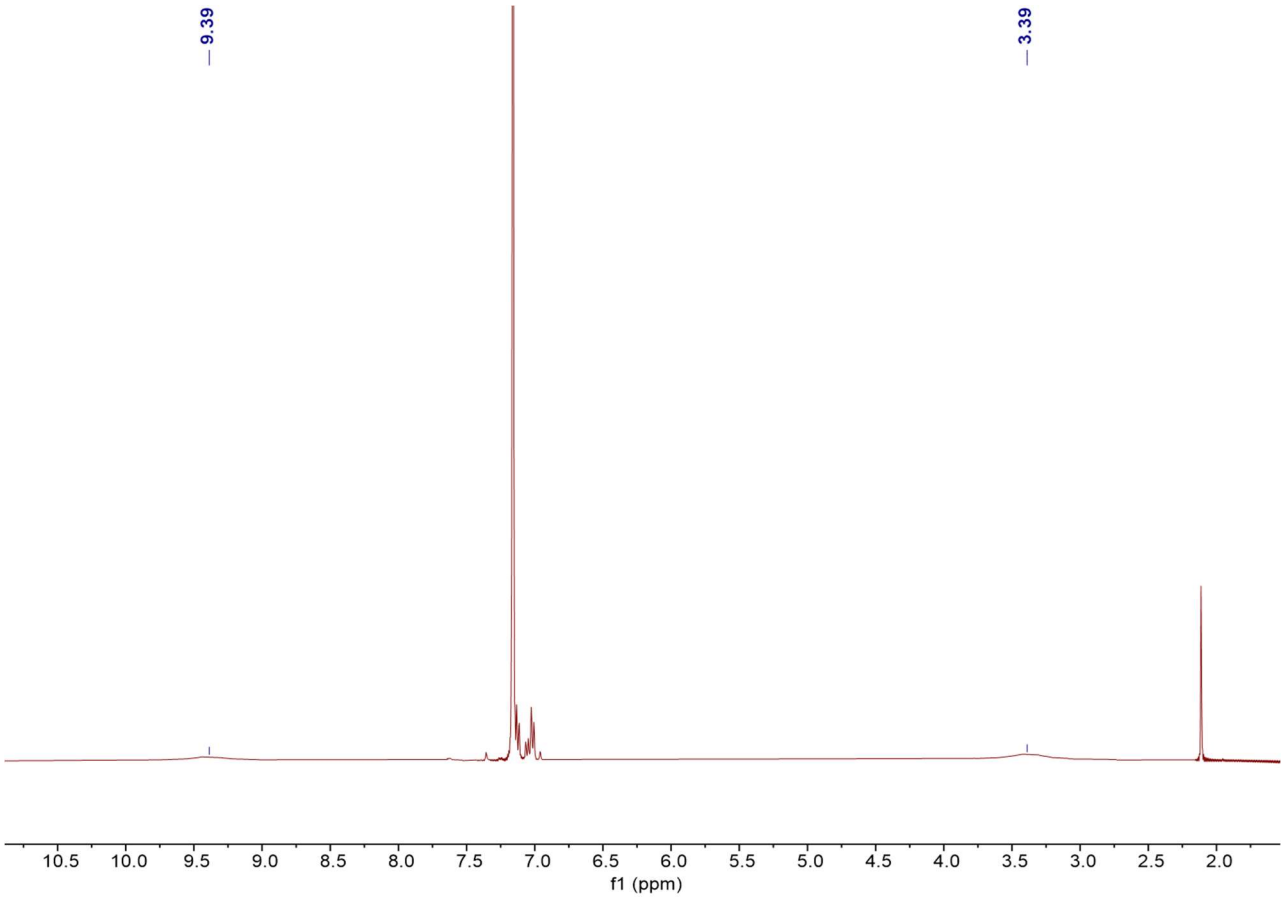

A2.5 ^{1}H NMR spectrum of (^{Mes}PDP^{Ph})V(terpy) in benzene-d_6.

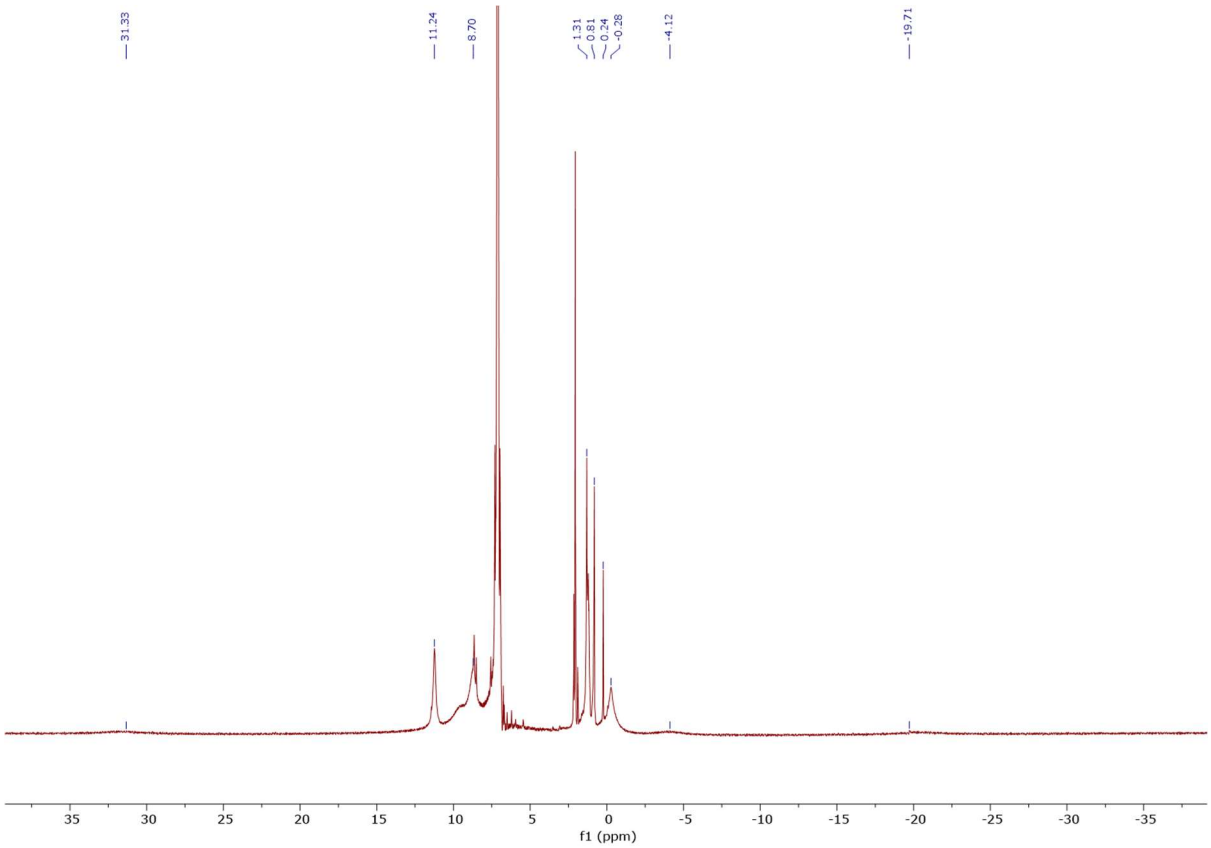

A2.6 UV-vis of (^{Mes}PDP^{Ph})V(terpy) in benzene.

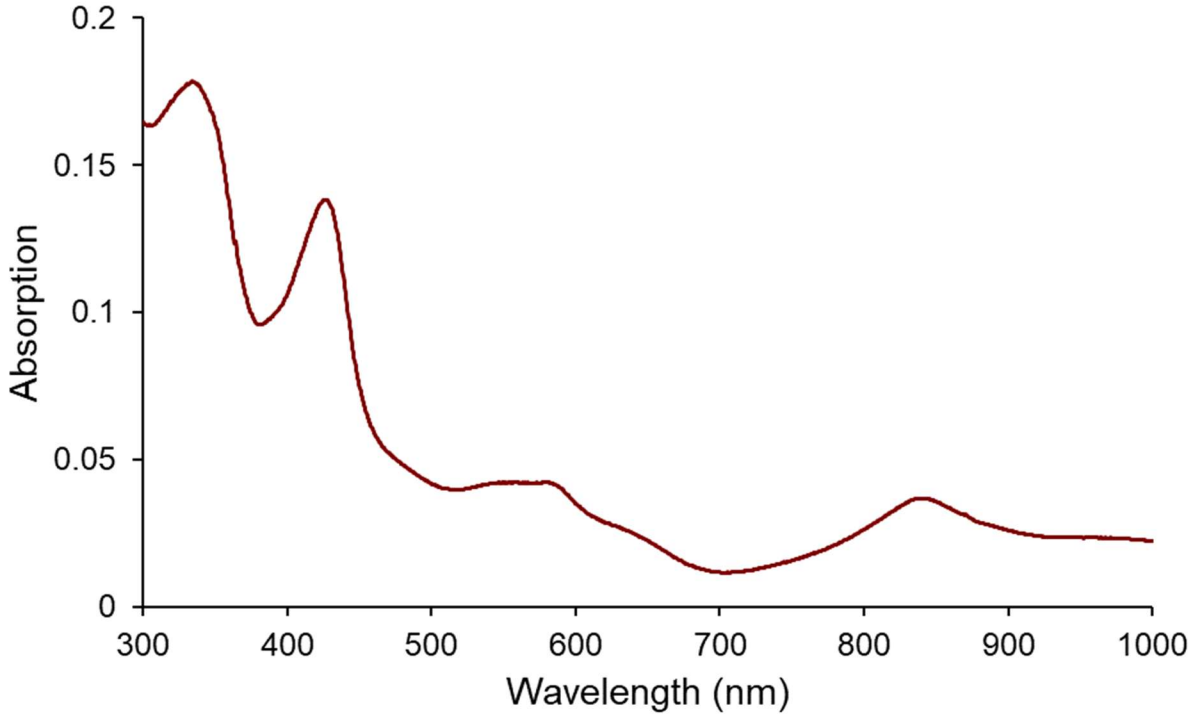

A2.7 ^{1}H NMR spectrum of [(^{Mes}PDP^{Ph})V(terpy)](BPh$_4$) in benzene-d_6.

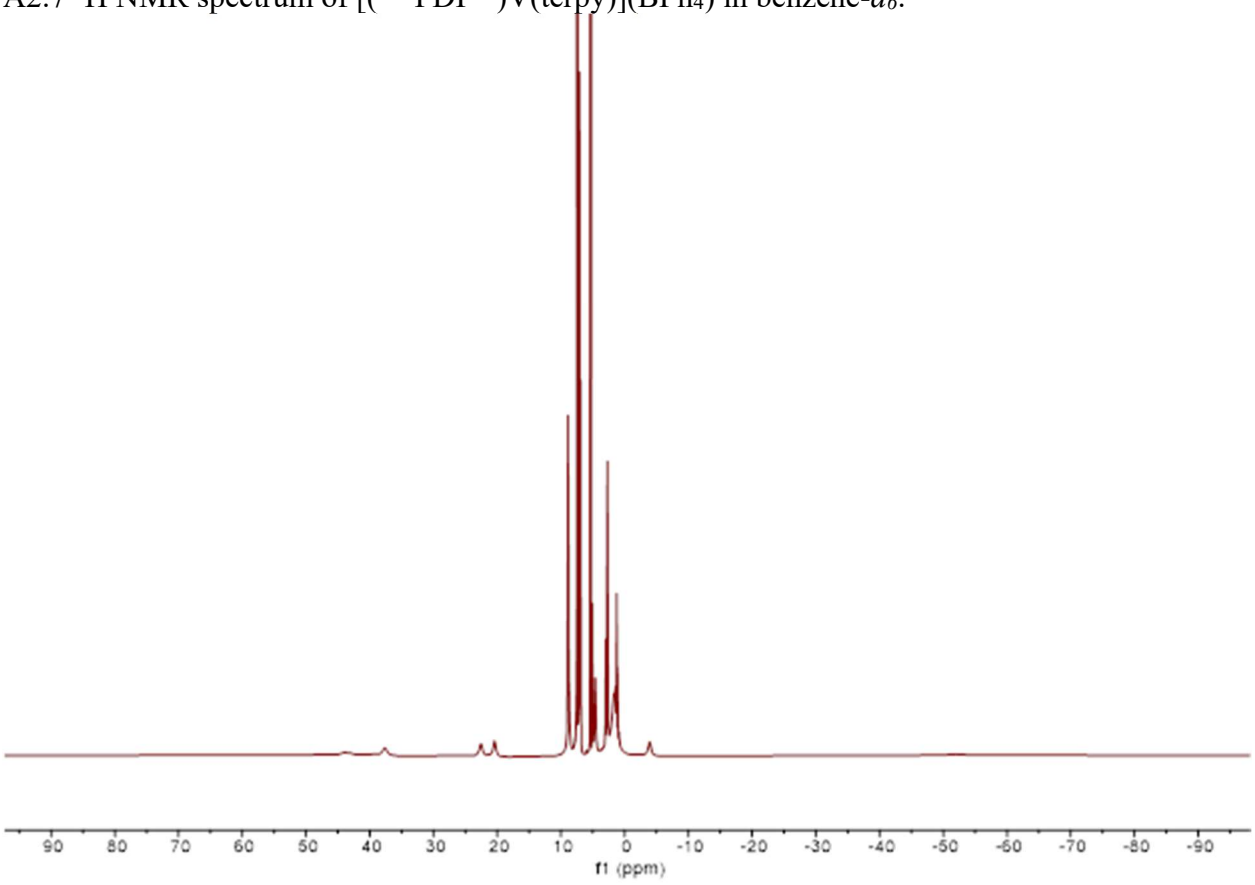

A2.8 ^{1}H NMR spectrum of Na[(^{Mes}PDP^{Ph})V(terpy)] in benzene-d_6.

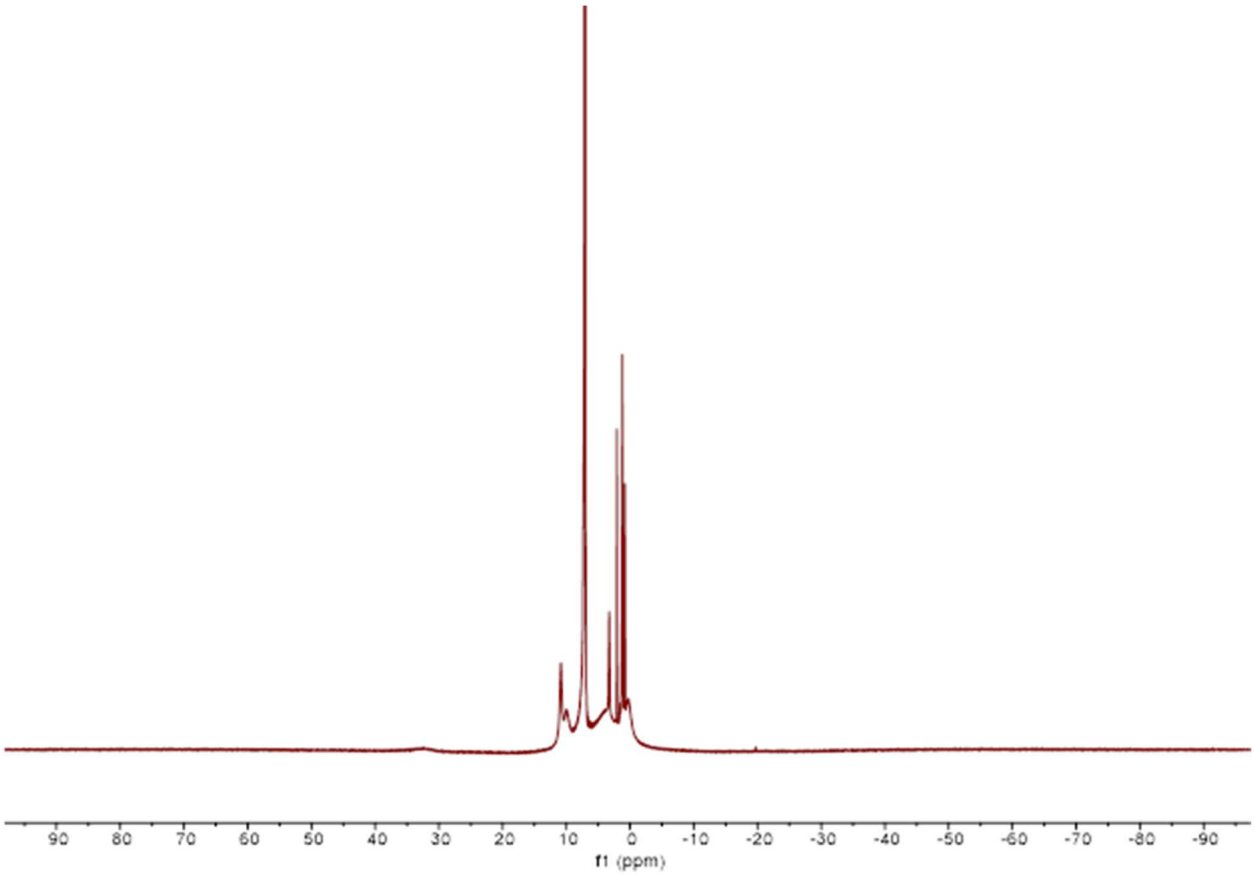

Appendix A3: Supplementary Information for Chapter 3

A3.1 ^{1}H NMR spectrum of [Na(18-crown-6)][(^{Mes}PDP^{Ph})V(N_3)$_2$(thf)] in benzene-d_6.

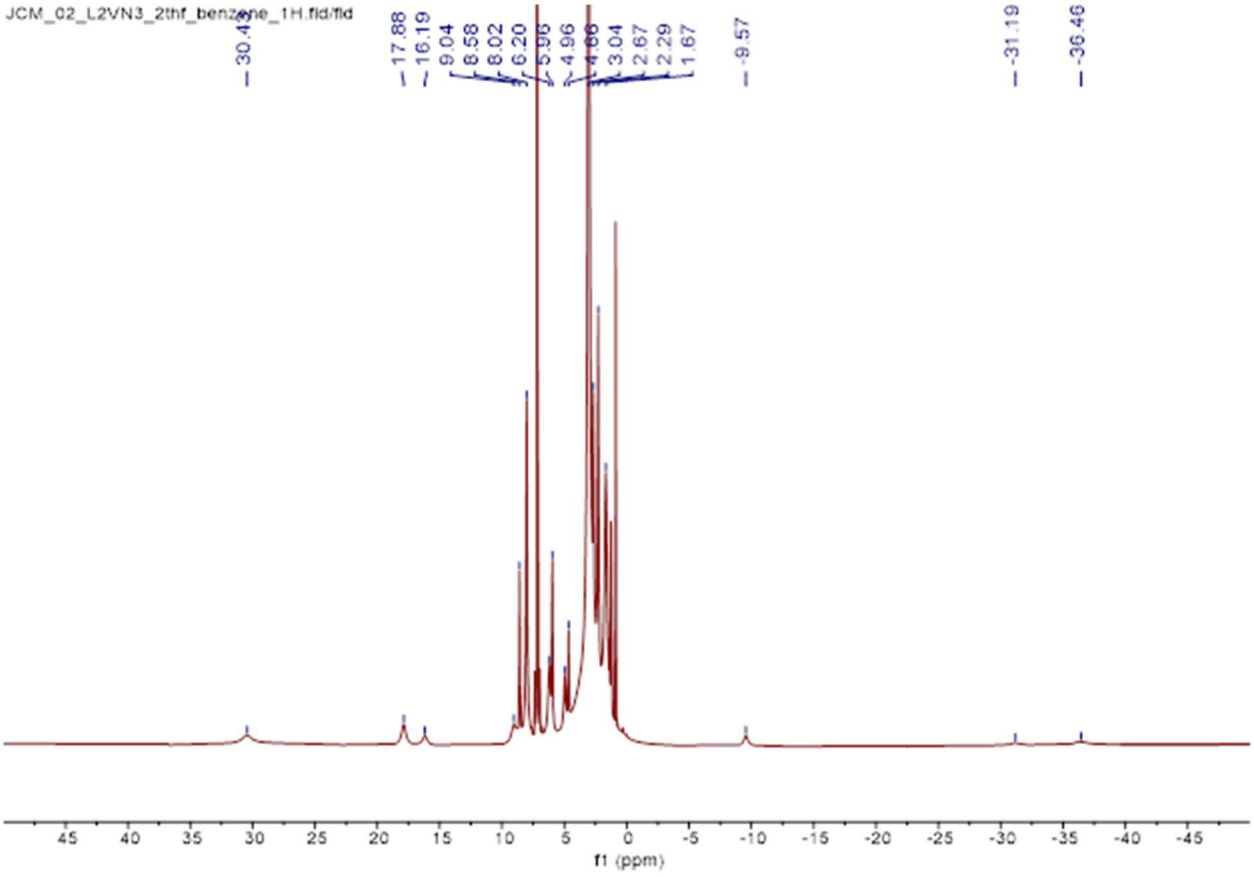

A3.2 ^{1}H NMR spectrum of [P(Ph)$_4$][(^{Mes}PDP^{Ph})V(N$_3$)$_2$(thf)] in benzene-*d*$_6$.

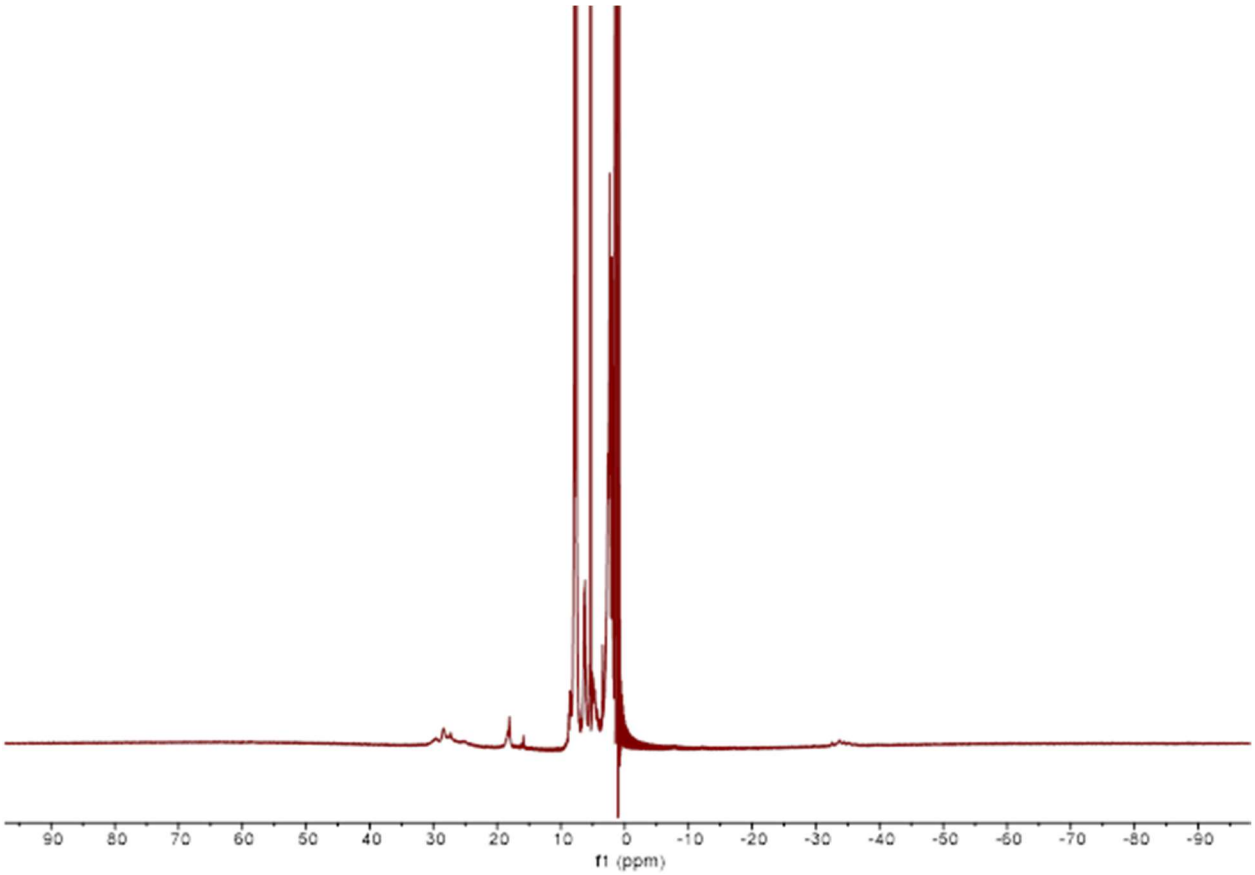

A3.3 ^{13}C NMR spectrum of [Na(18-crown-6)][($^{Mes}PDP^{Ph}$)VN(N_3)] in methylene chloride-d_2.

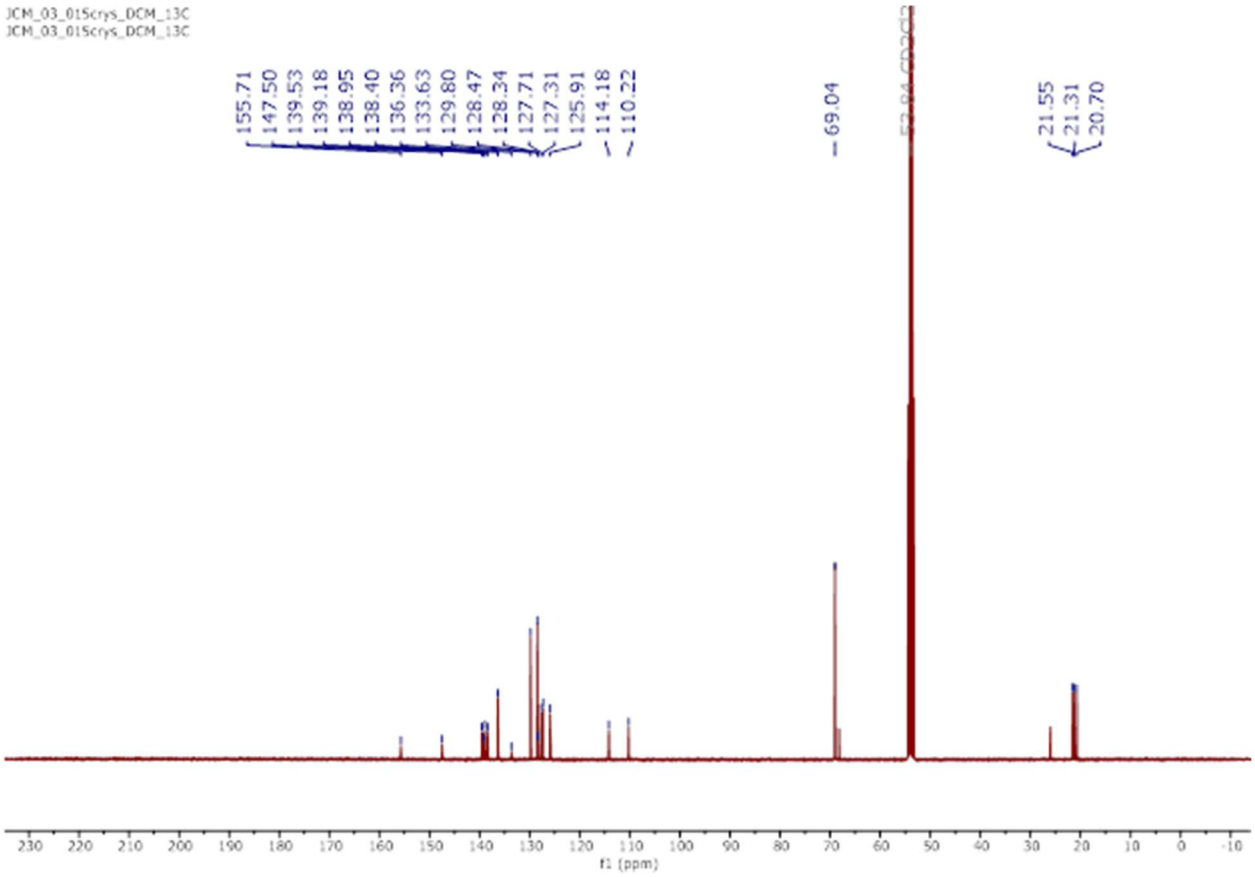

A3.4 ^{13}C NMR spectrum of ($^{Mes}PDP^{Ph}$)V(NTMS)(N_3) in benzene-d_6.

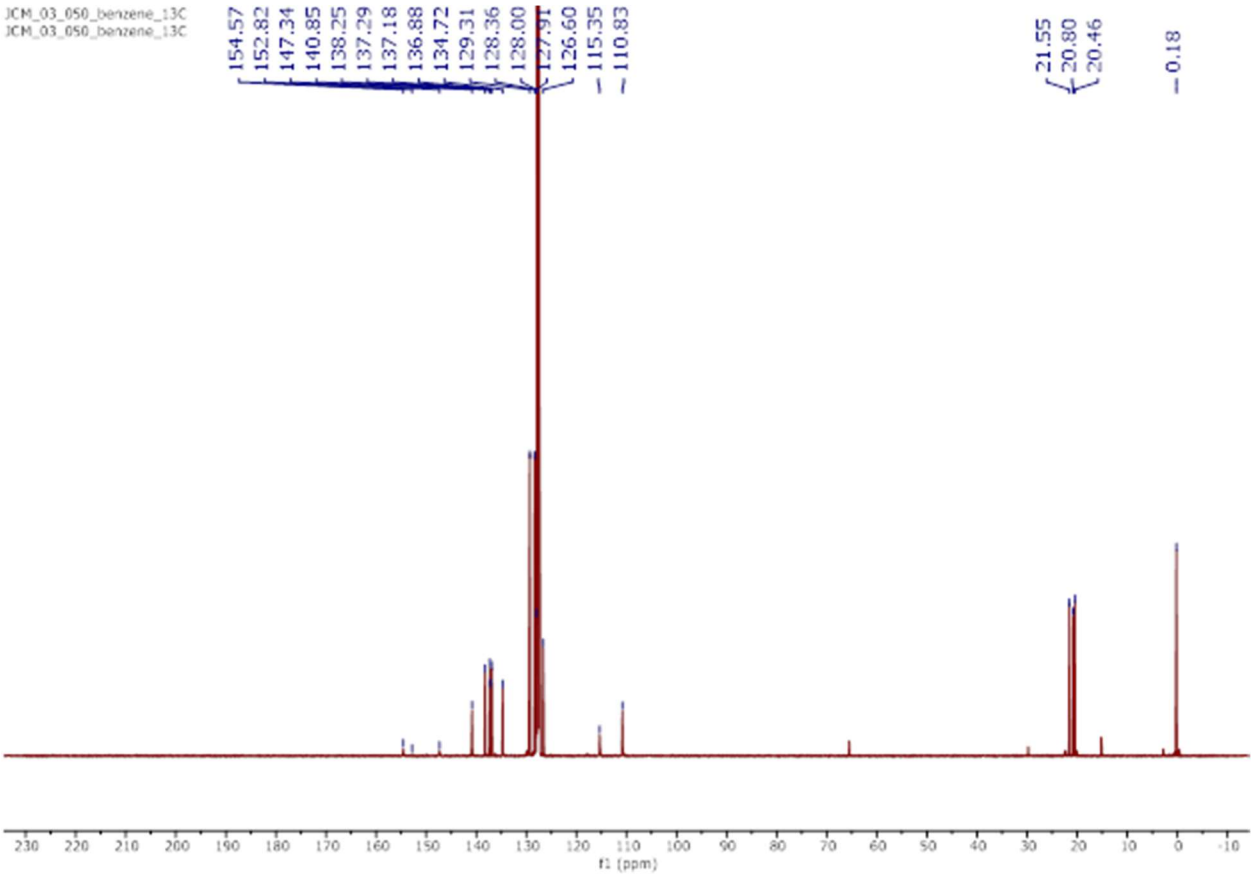

Appendix A4: Supplementary Information for Chapter 4

A4.1 ^{13}C NMR spectrum of (^{Mes}PDP^{Ph})V(N-^{1}Ad)(Cl) in benzene-d_6.

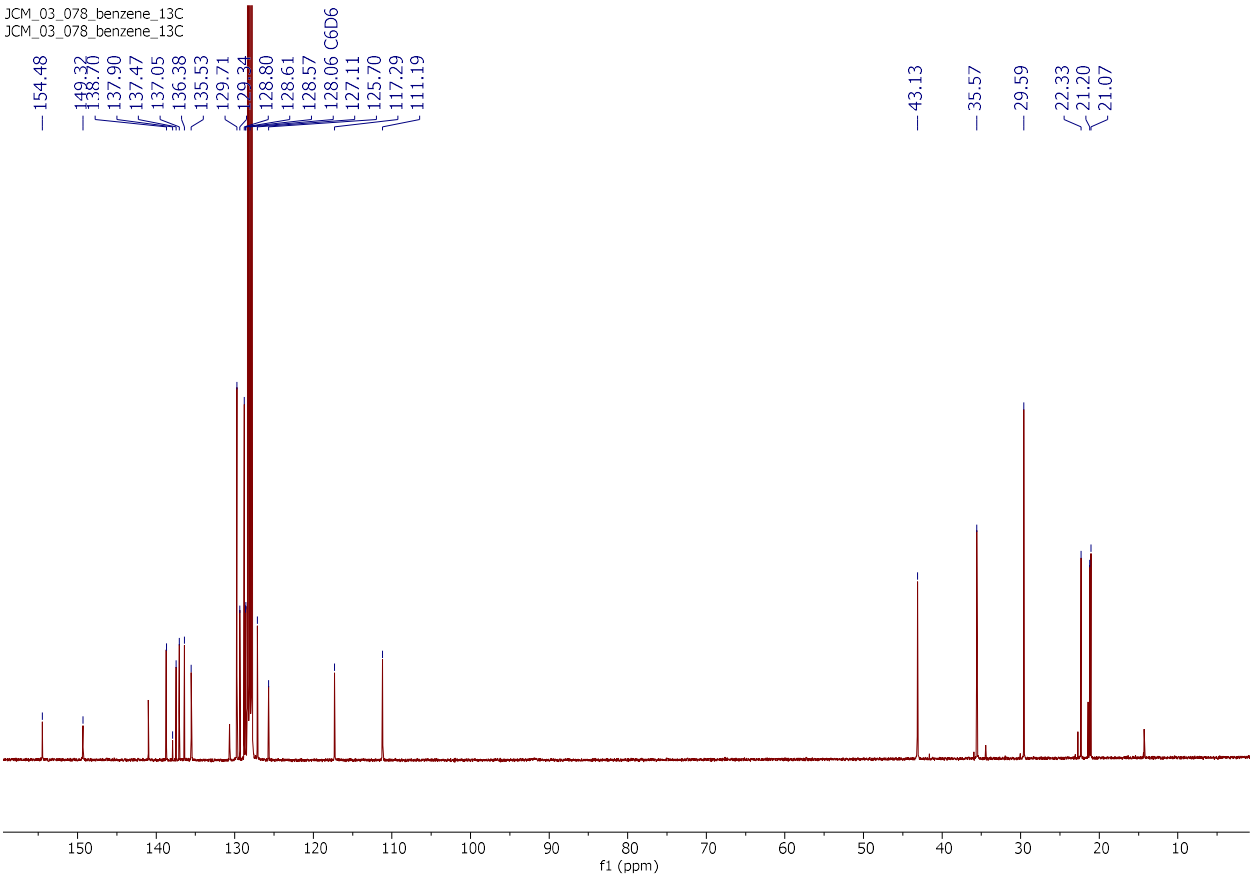

A4.2 UV-vis spectrum of (^{Mes}PDP^{Ph})V(N-^{1}Ad)(Cl) in benzene.

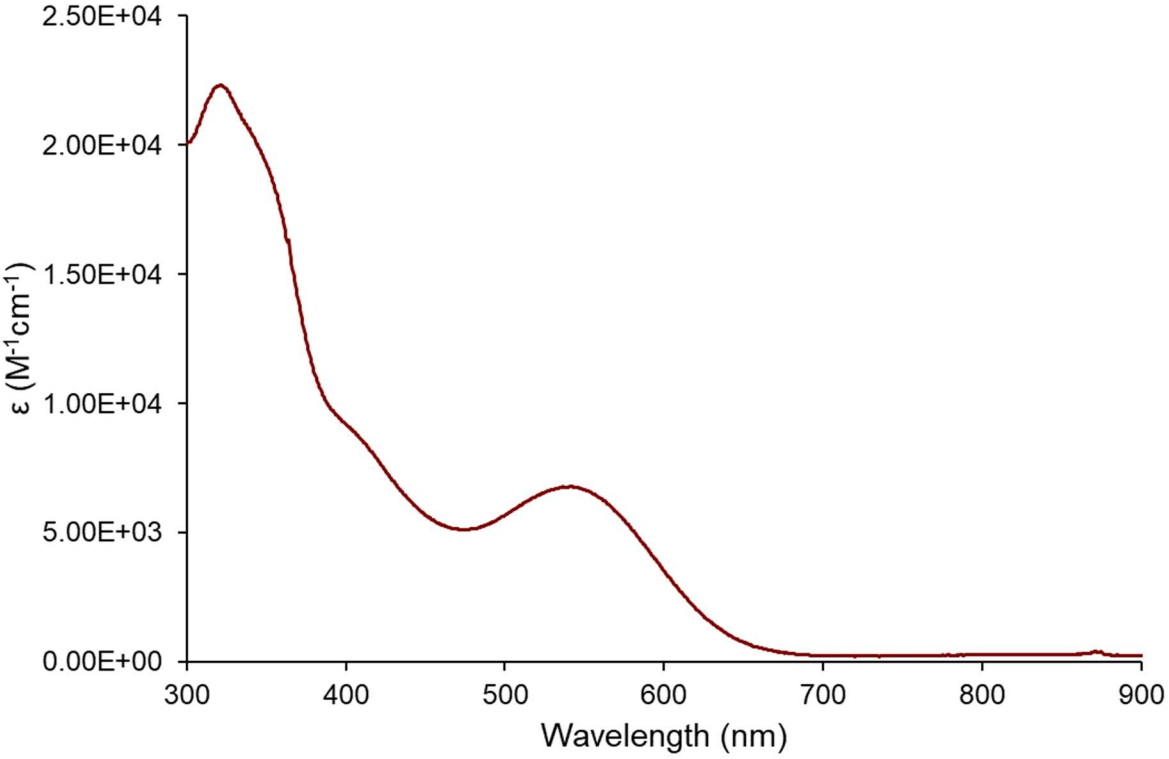

A4.3 ^{13}C NMR spectrum of ($^{Mes}PDP^{Ph}$)V(N-^{1}Ad)(N_3) in benzene-d_6.

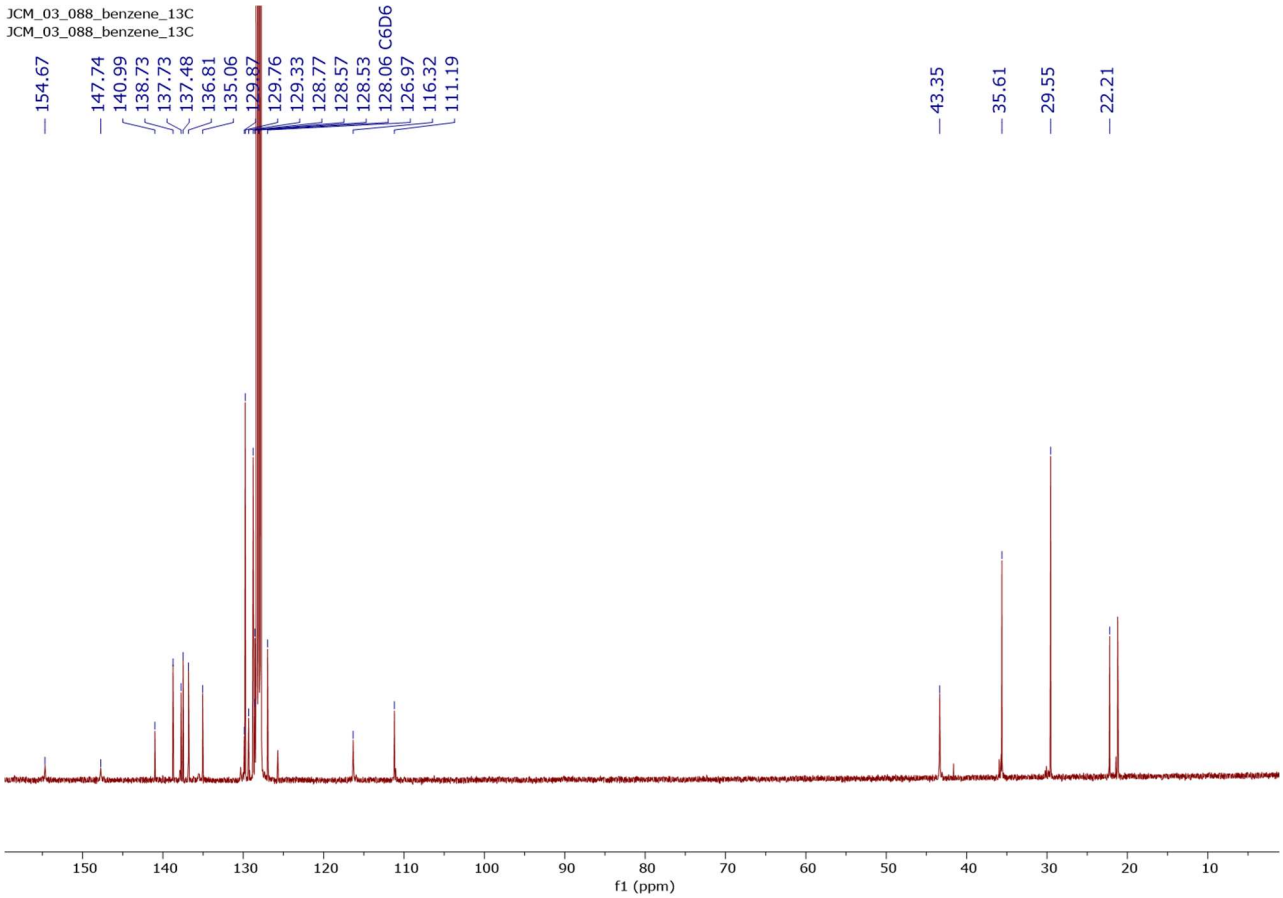

A4.4 (HH) COSY NMR spectrum of (^{Mes}PDP^{Ph})V(N-^{1}Ad)(N_3)

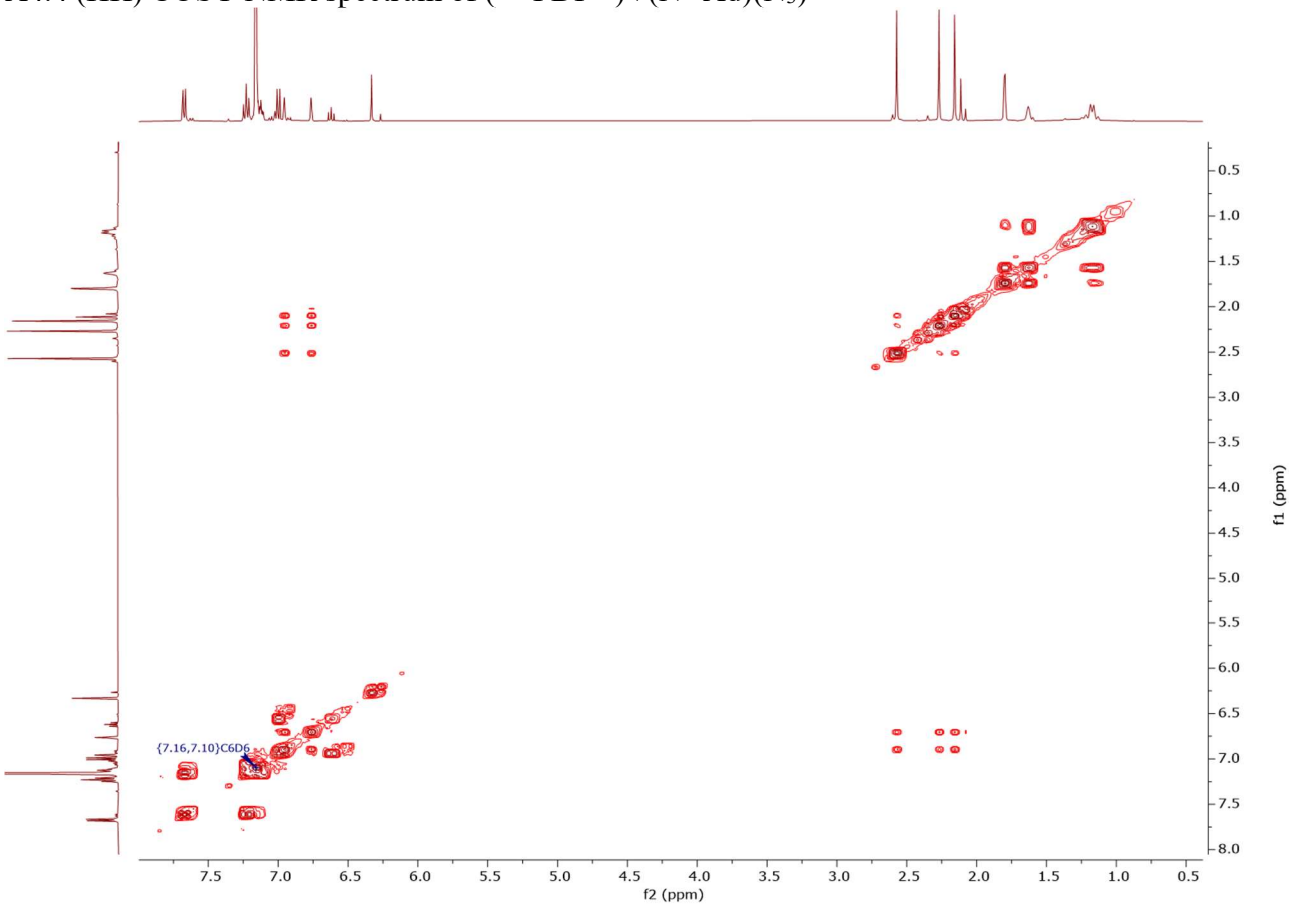

A4.5 ^{1}H NMR spectrum of [Na(18-crown-6)][(^{Mes}PDP^{Ph}-NH)VN] in tetrahydrofuran-d_8.

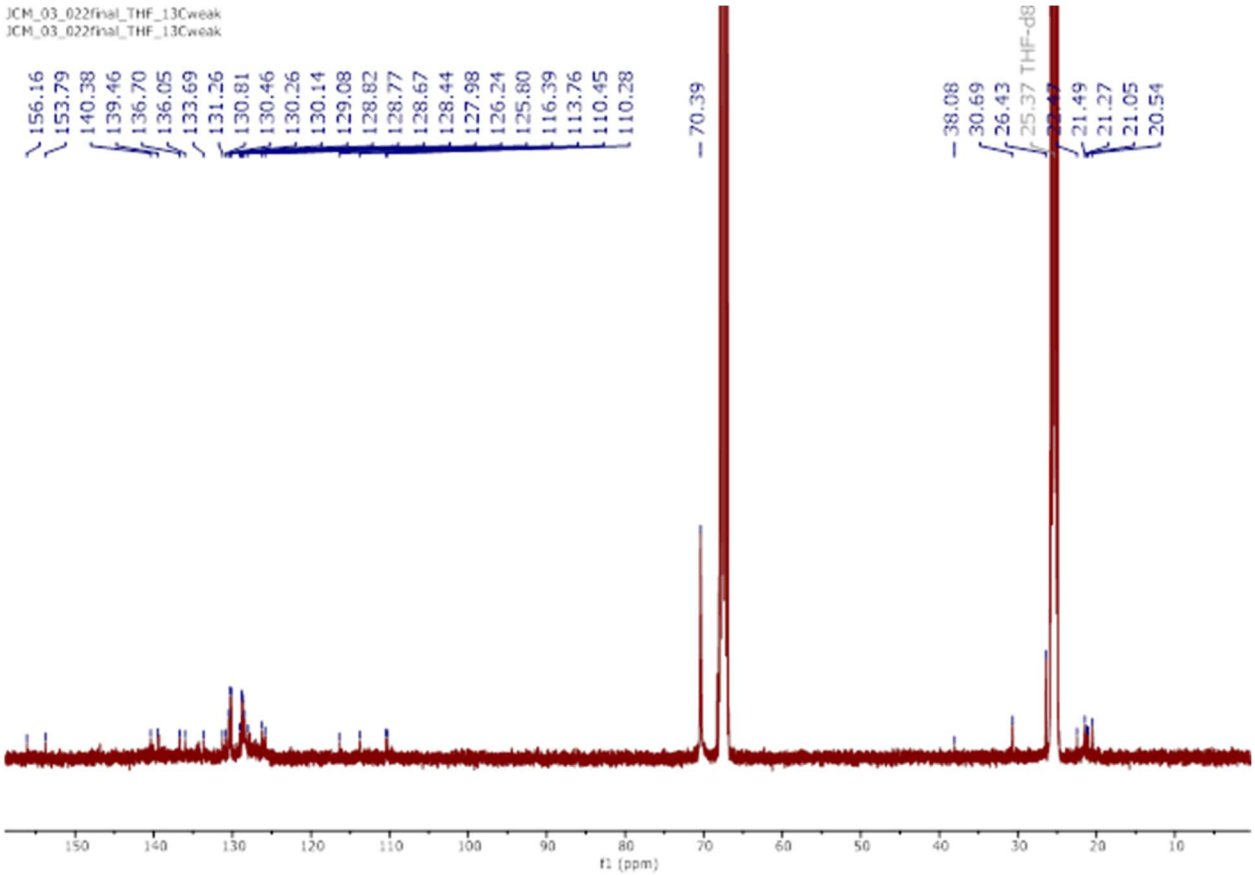

A4.6 ^{1}H NMR spectrum of (^{Mes}PDP^{Ph}-NH)V(NTMS) in benzene-d_6.

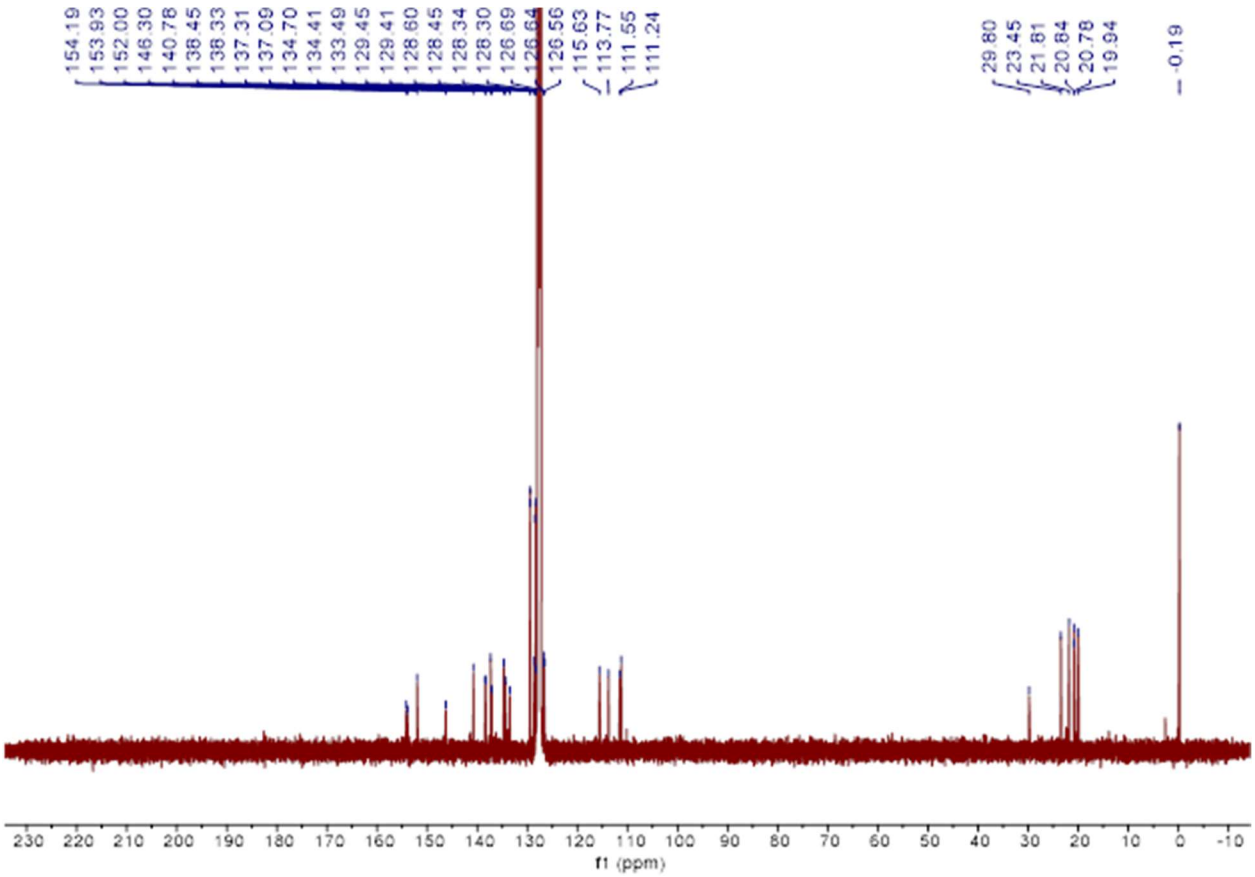

Appendix A5: Supplementary Information for Chapter 5

A5.1 ^{1}H NMR spectrum of ^{Mes}PDA in benzene-d_6.

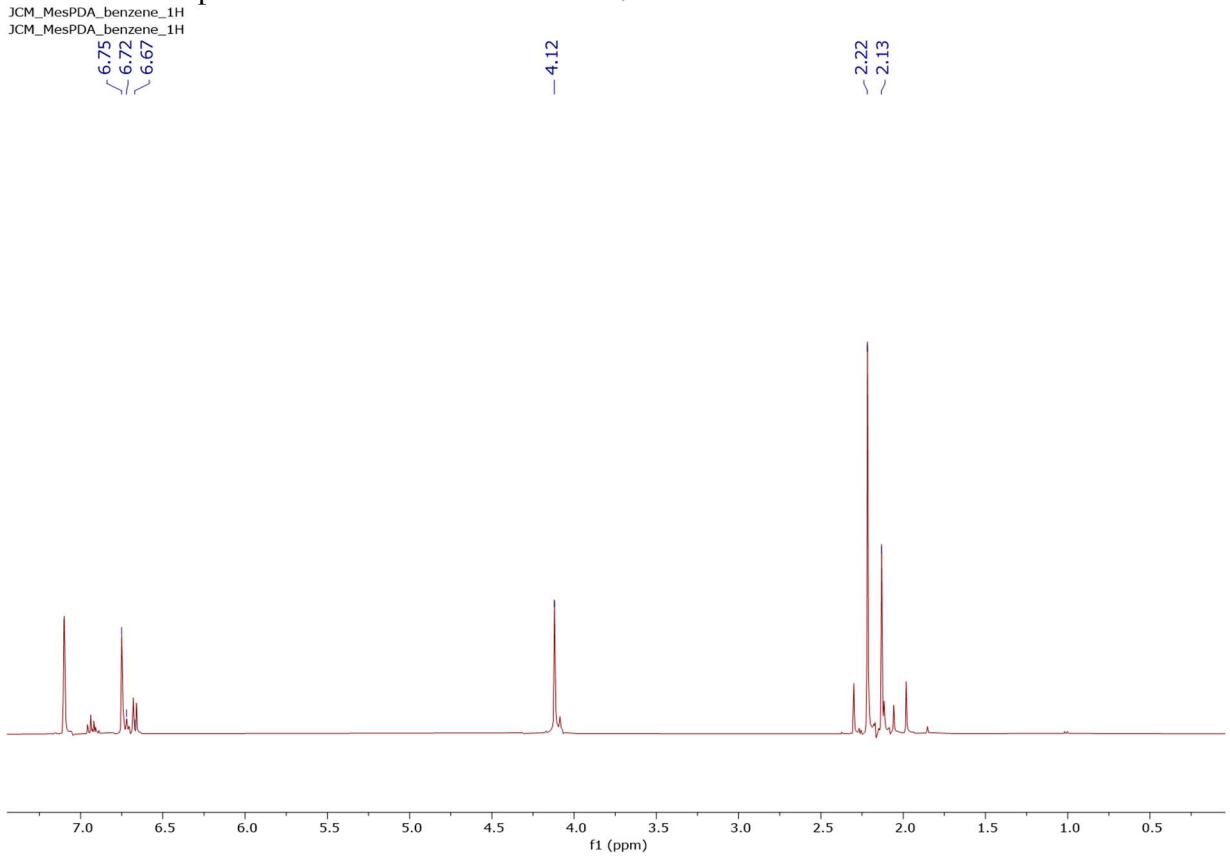

A5.2 ^{13}C NMR spectrum of ^{Mes}PDA in benzene-d_6.

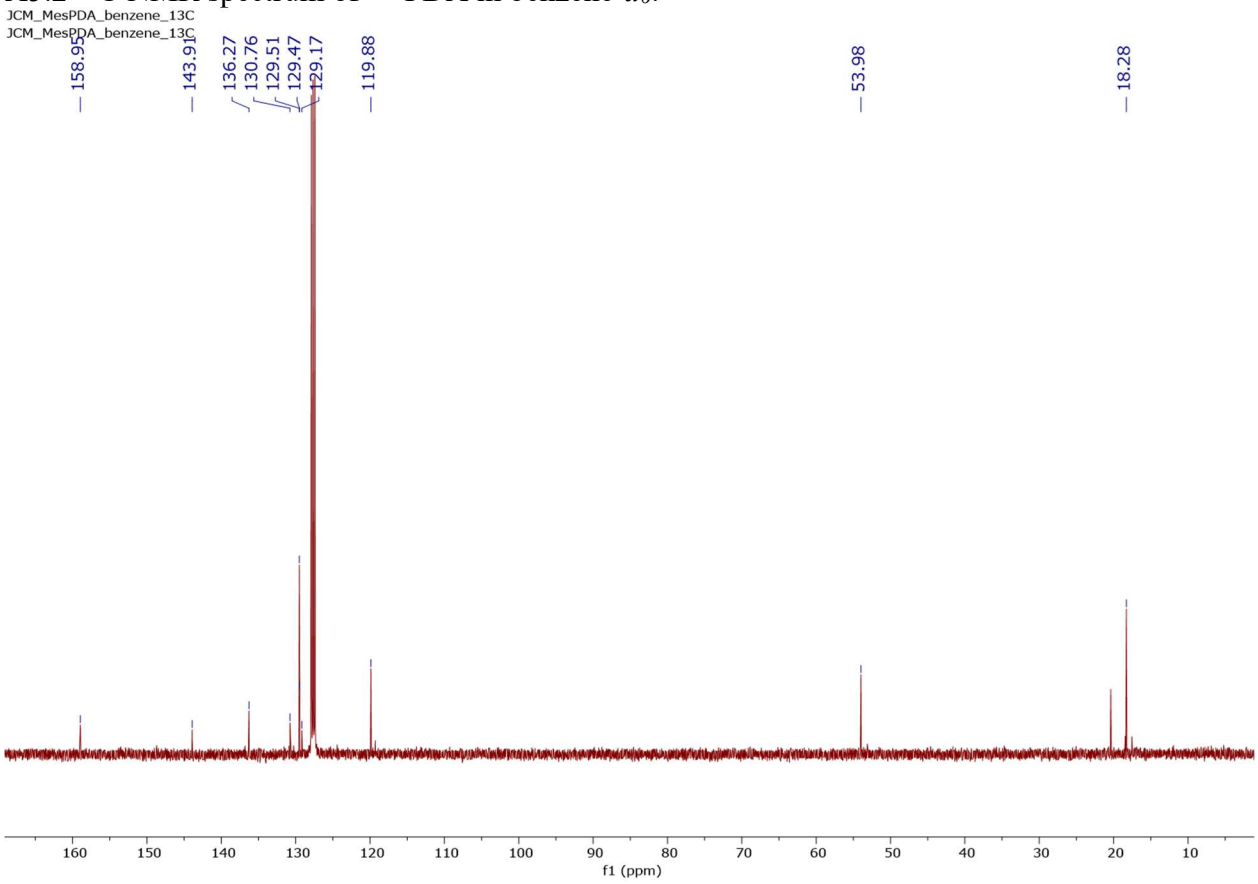

A5.3 ^{1}H NMR spectrum of ^{Tol}PDA in benzene-d_6.

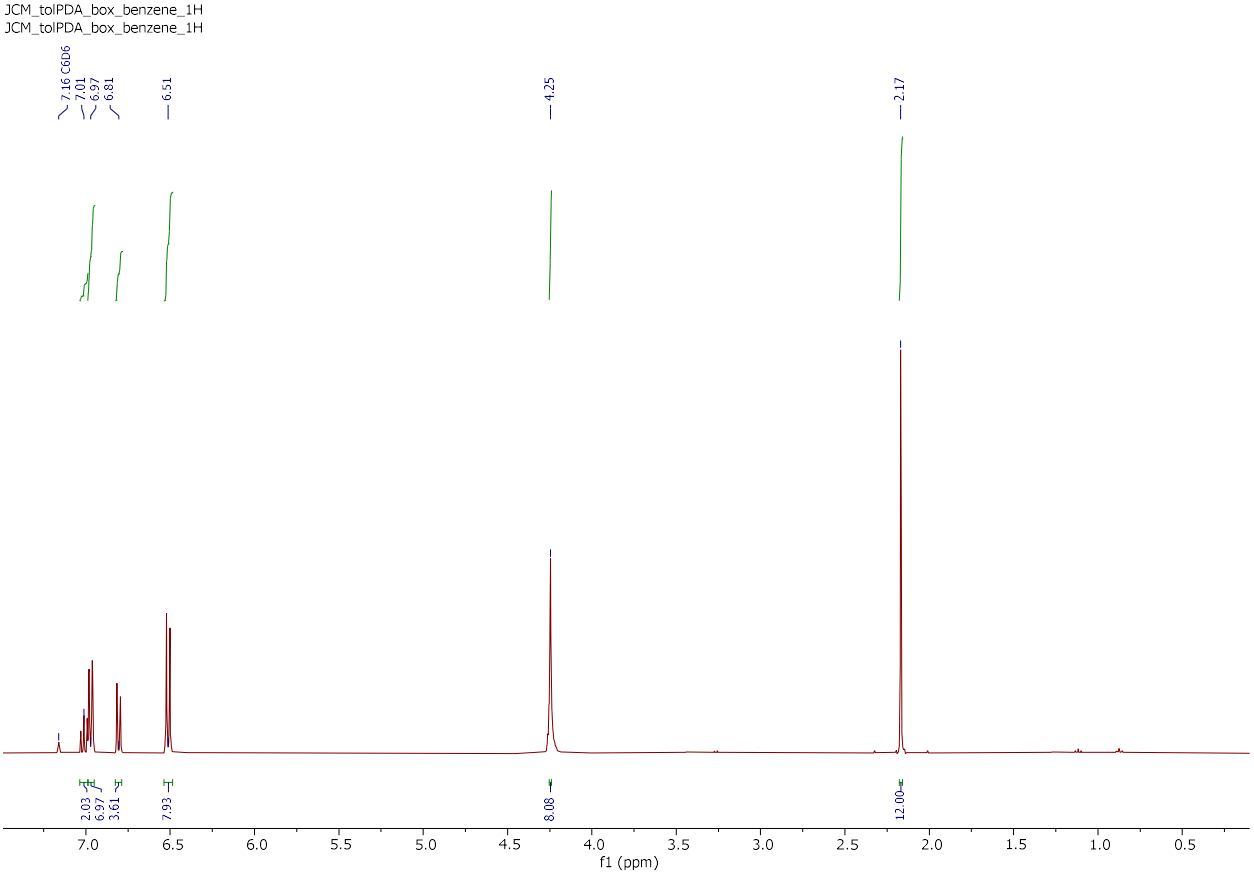

A5.4 ^{13}C NMR spectrum of ^{Tol}PDA in benzene-d_6.

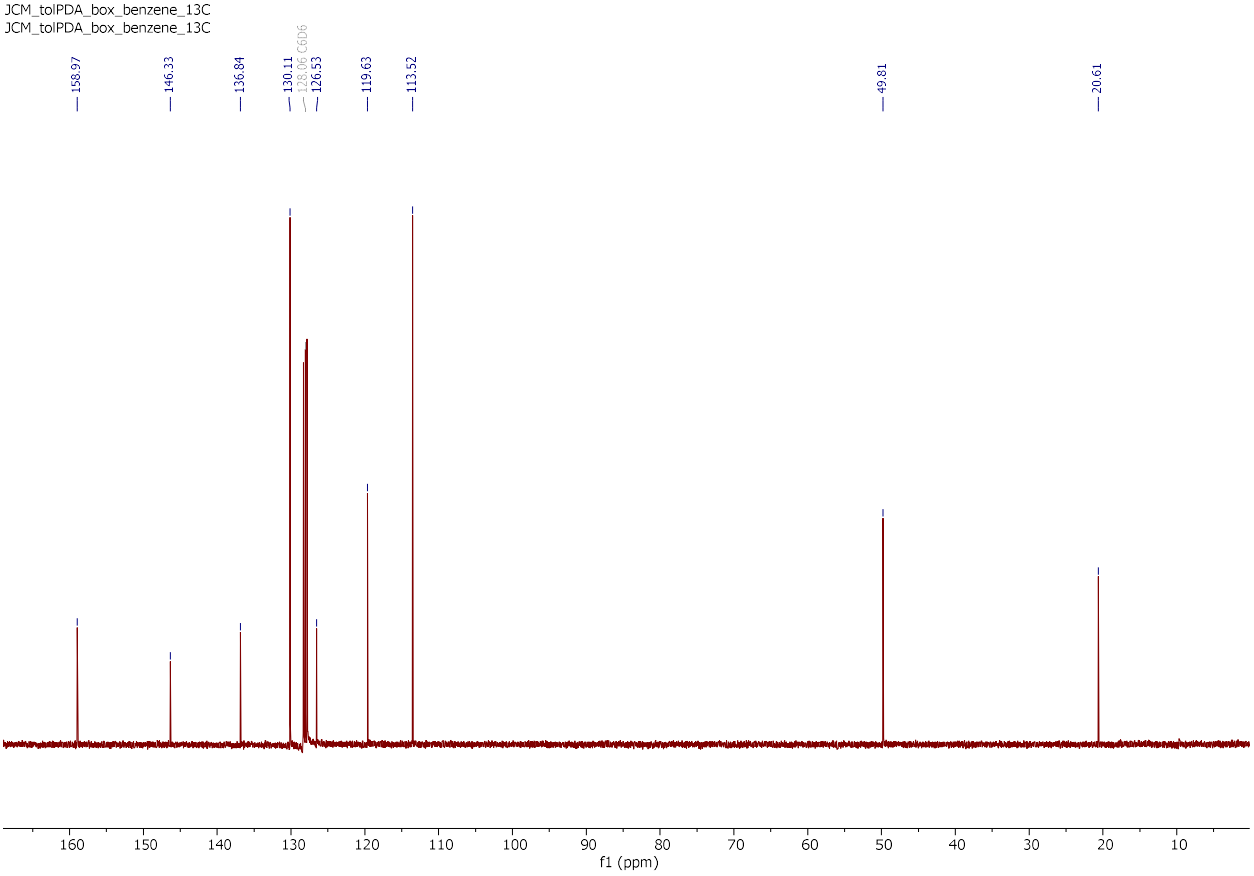

A5.5 ^{13}C NMR spectrum of (^{Mes}PDA)Zr(Bn)$_2$ in benzene-d_6.

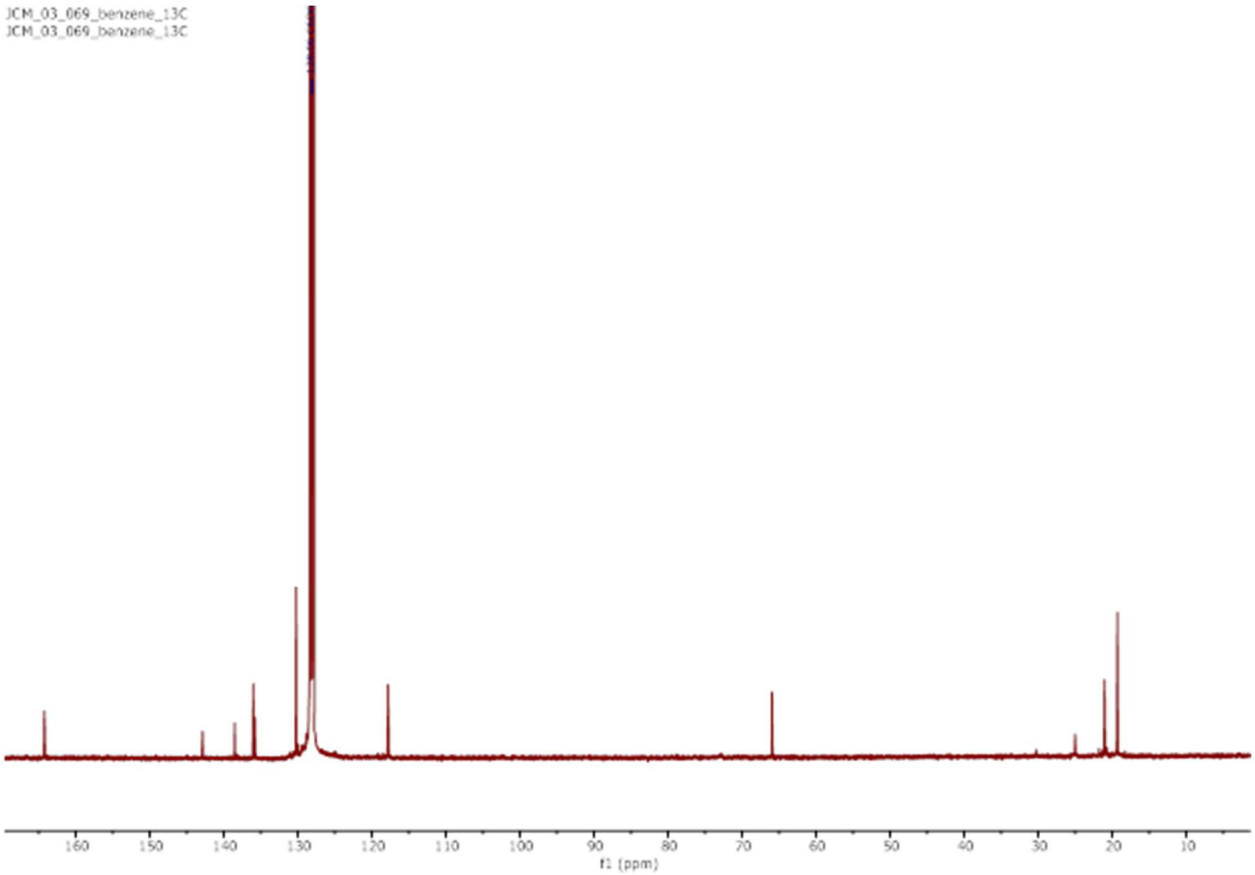

A5.6 ^{13}C NMR spectrum of Zr(^{Tol}PDA)$_2$ in benzene-d_6.

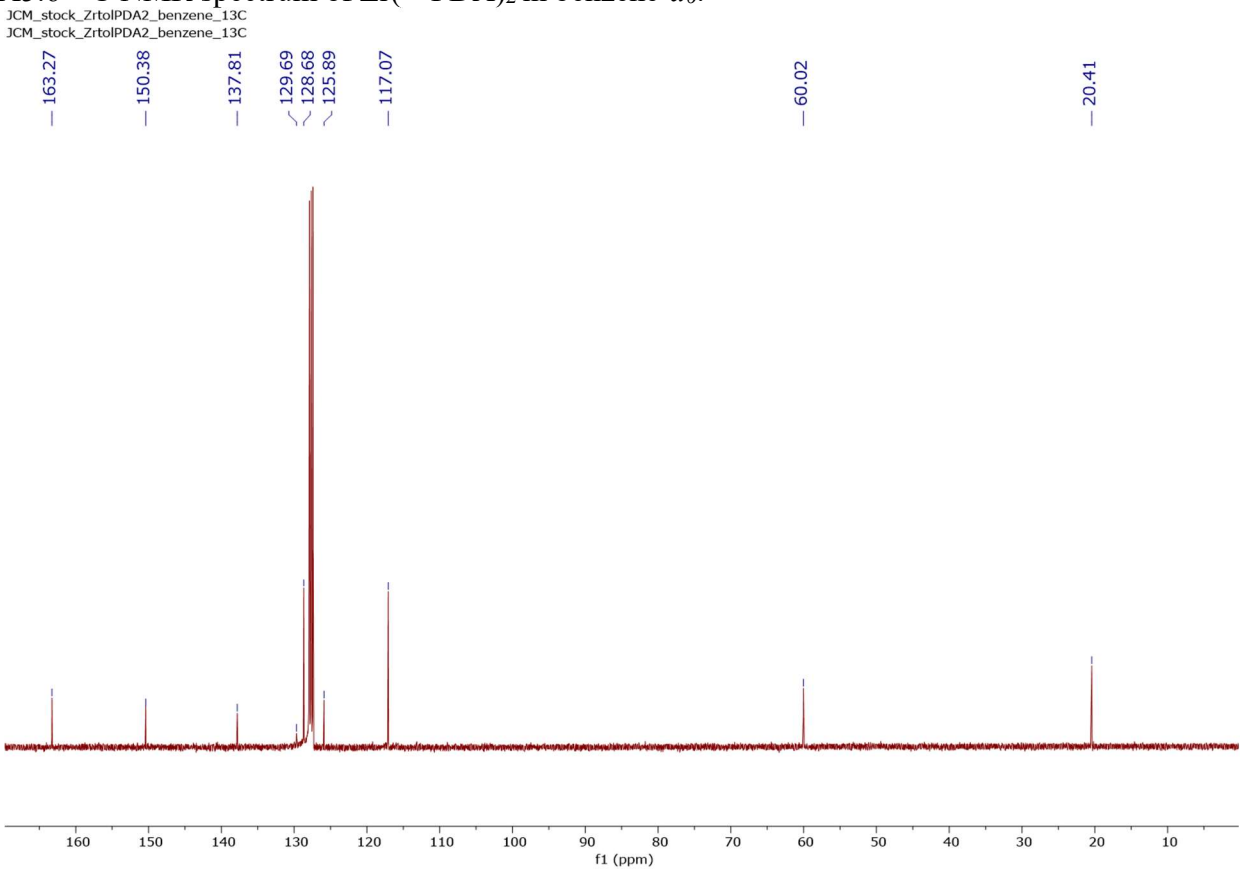

A5.7 ^{13}C NMR spectrum of Ti(^{Tol}PDA)$_2$ in benzene-d_6.

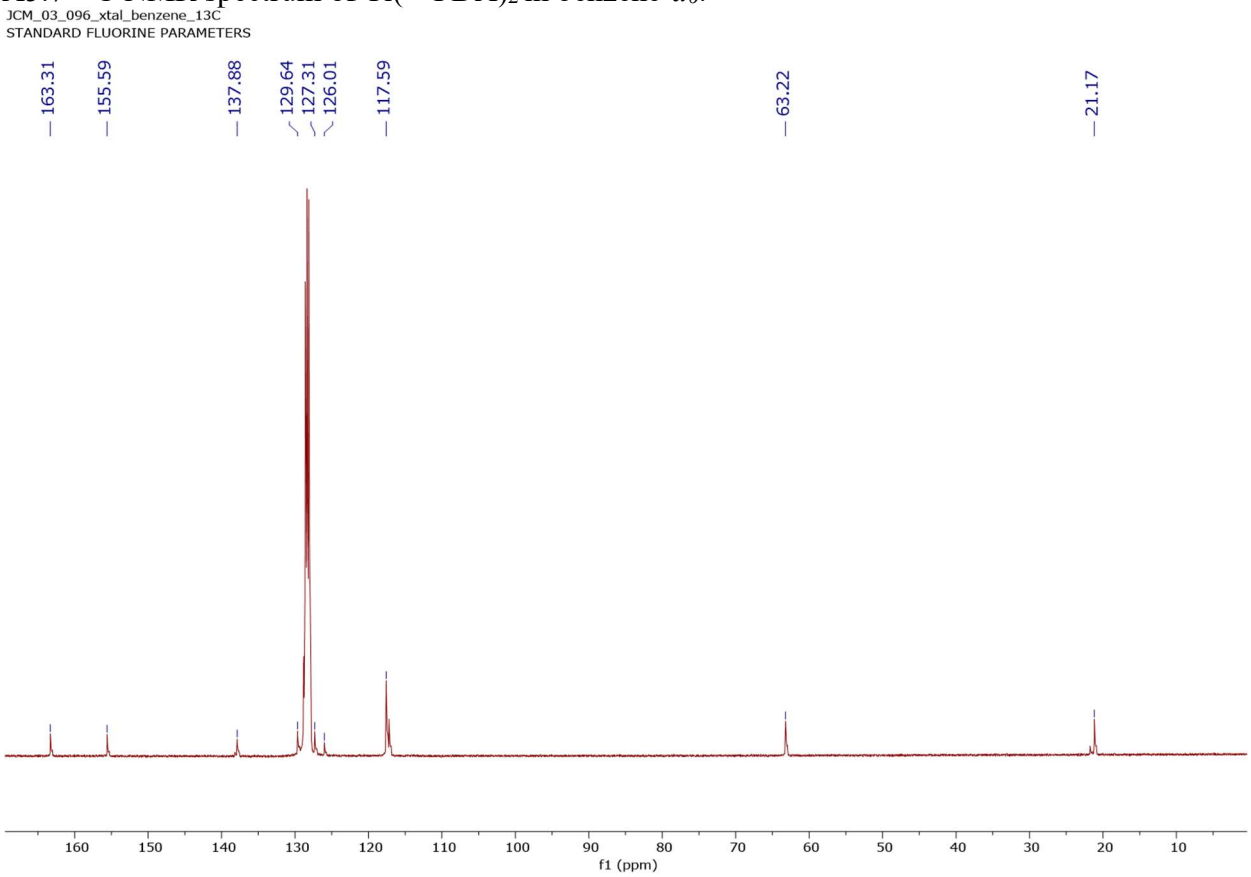

A5.8 ^{13}C NMR spectrum of (NNN)Nb(^{Tol}PDA) in benzene-d_6.

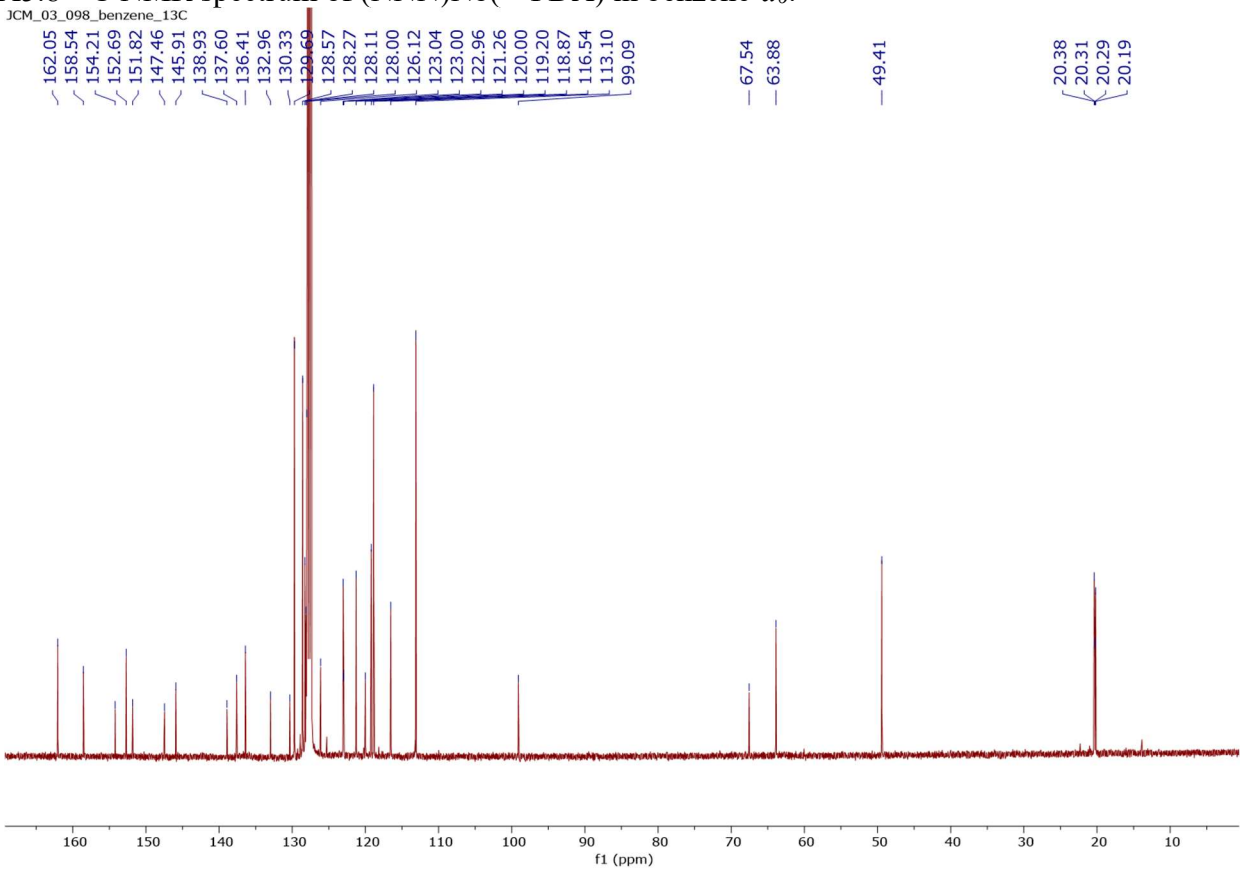

Appendix B: Miscellaneous Crystal Structures

Figure B.1 cm241cms - (^{Tol}PDA)$NbCl_2$(OMe)
Displayed at 50% probability ellipsoids. Solvent of crystallization and hydrogen atoms omitted for clarity.

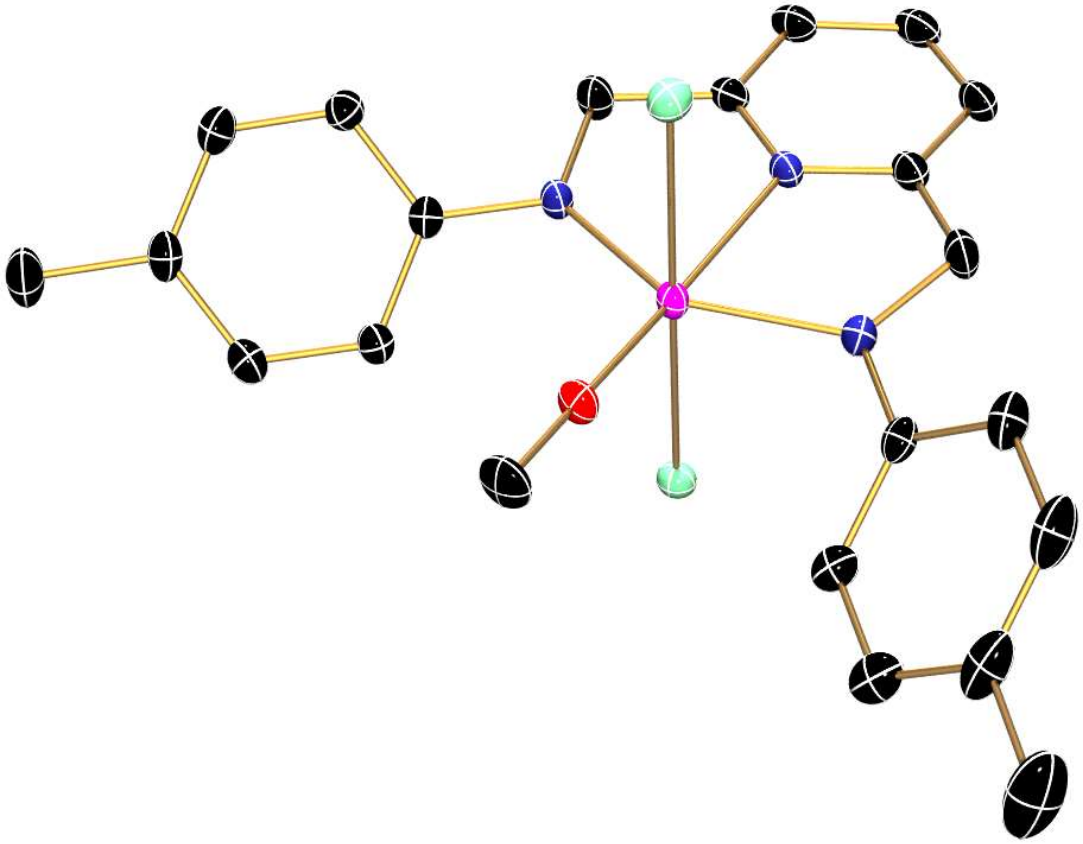

Figure B.2 cm249cms - (^{Mes}PDP^{Ph})NbCl$_3$
Displayed at 50% probability ellipsoids. Solvent of crystallization and hydrogen atoms omitted for clarity.

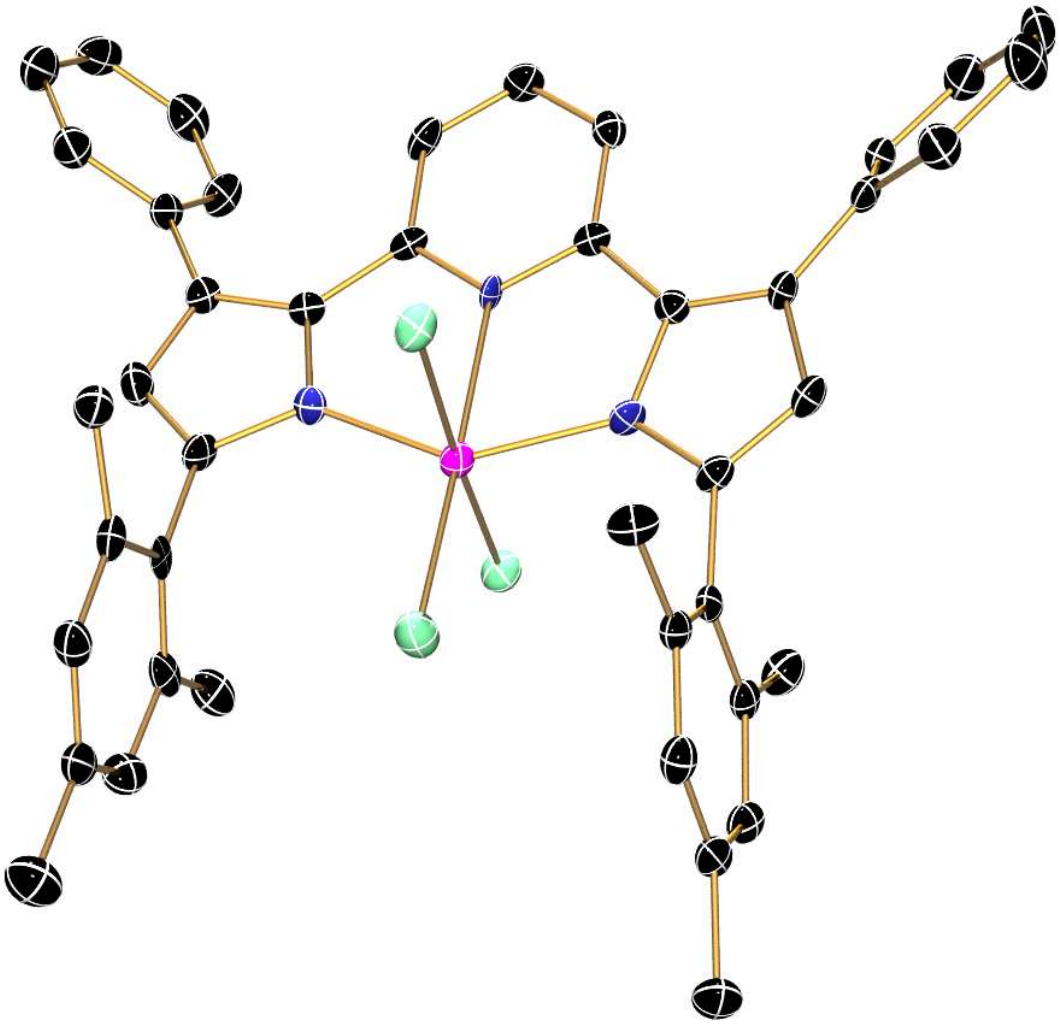

Figure B.3 cm257cms - (^{Me}PDP^{Ph})VCl(thf)$_2$
Displayed at 50% probability ellipsoids. Hydrogen atoms omitted for clarity.

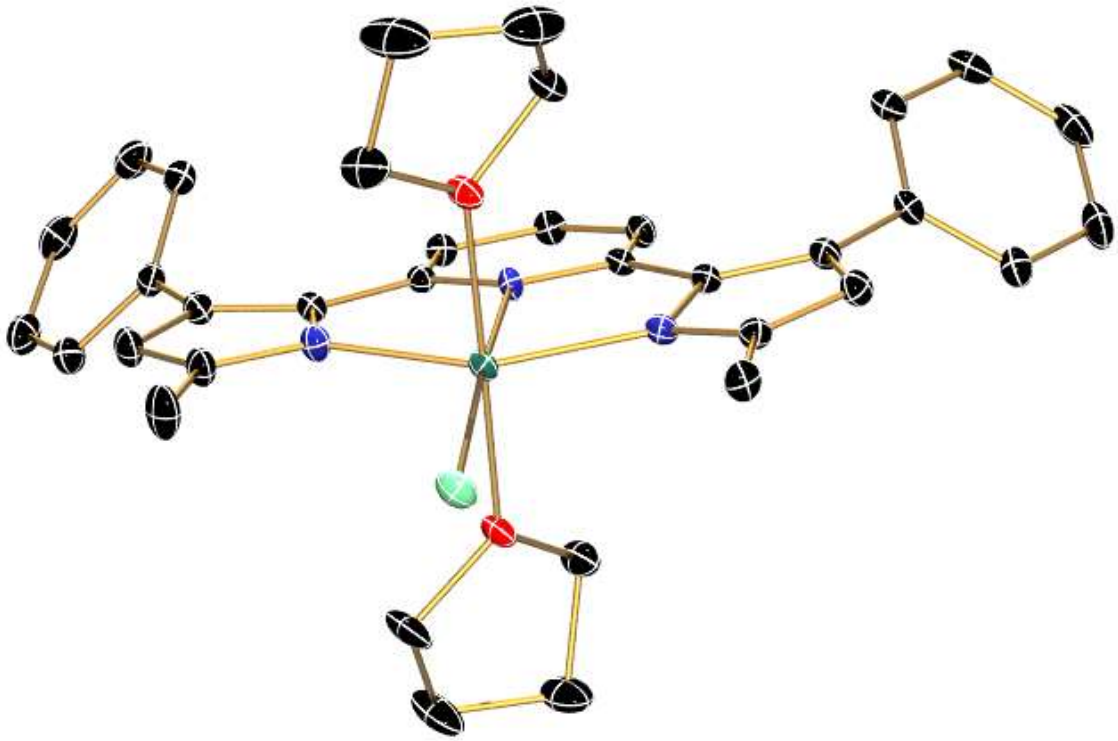

Figure B.4 cm259cms - $[(CoCp_2)][(^{Mes}PDP^{Ph})NbCl_3]$
Displayed at 50% probability ellipsoids. Hydrogen atoms omitted for clarity.

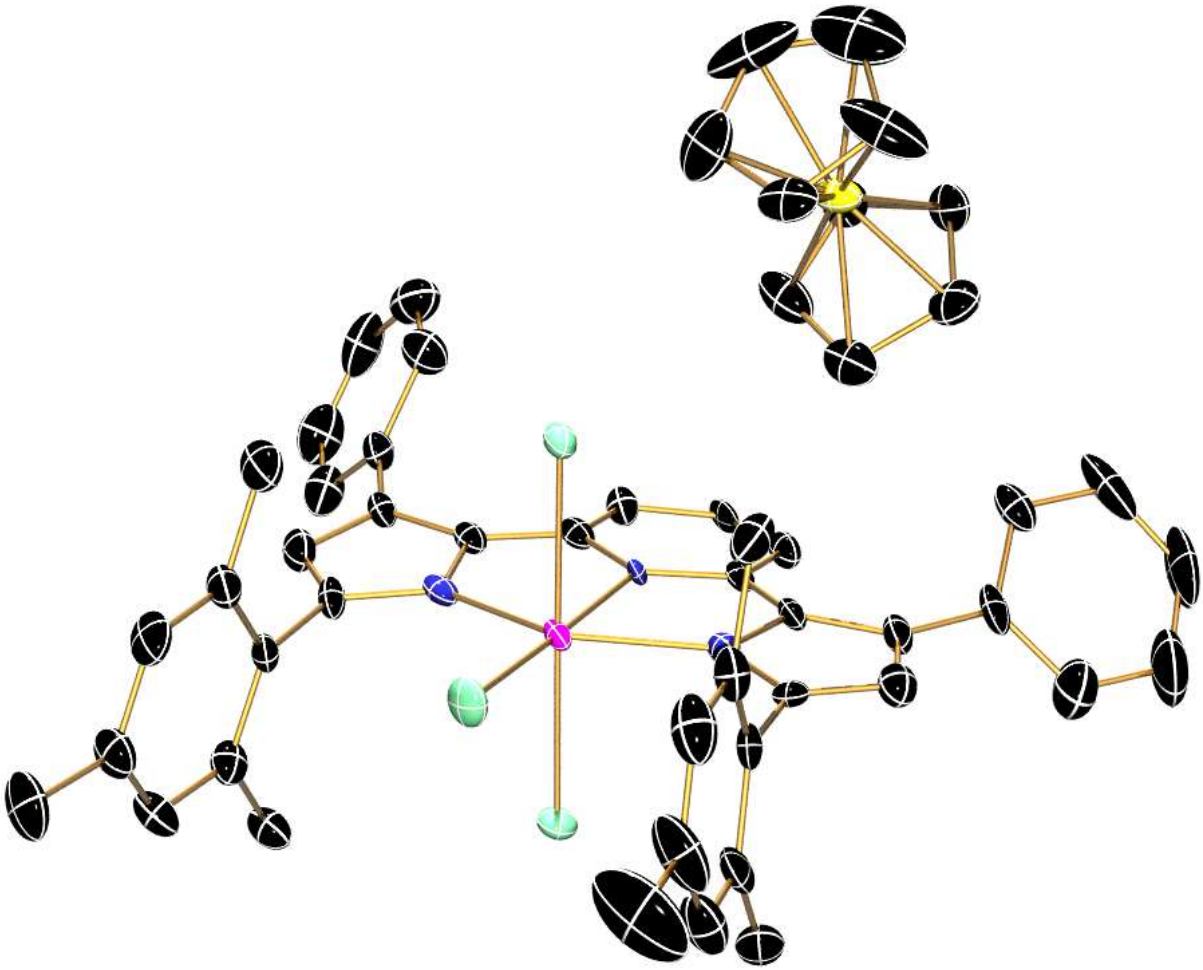

Figure B.5 cm279cms - (^{Mes}PDP^{Ph})V(N_3)(DMAP)$_2$
Displayed at 50% probability ellipsoids. Hydrogen atoms and disorder of back phenyl substituent omitted for clarity. One mesityl substituent truncated at the *ipso* carbon to better observe inner coordination sphere.

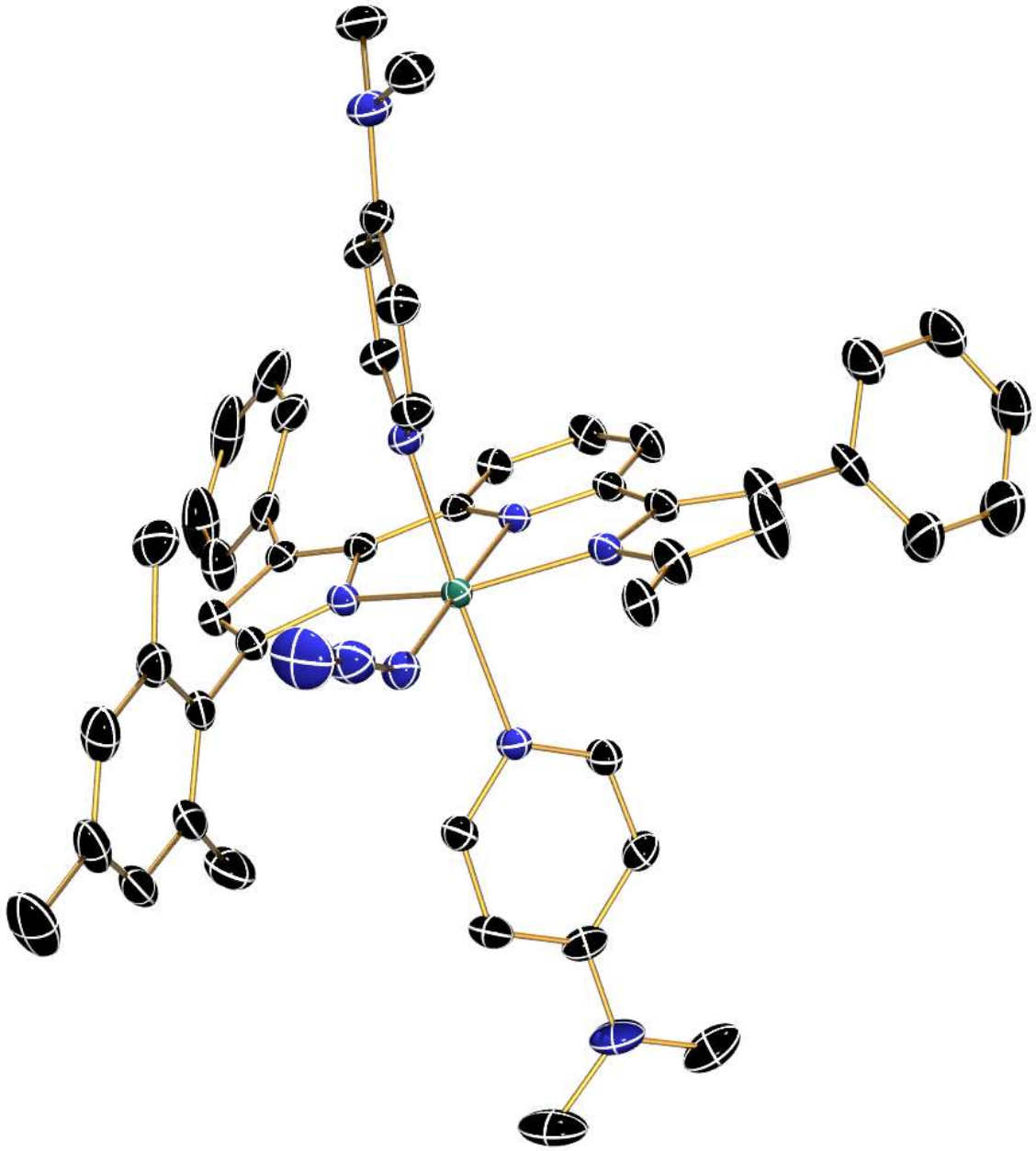

Figure B.6 cm295 - (^{Me}PDP^{Ph})NbCl$_3$
Displayed at 50% probability ellipsoids. Hydrogen atoms omitted for clarity.

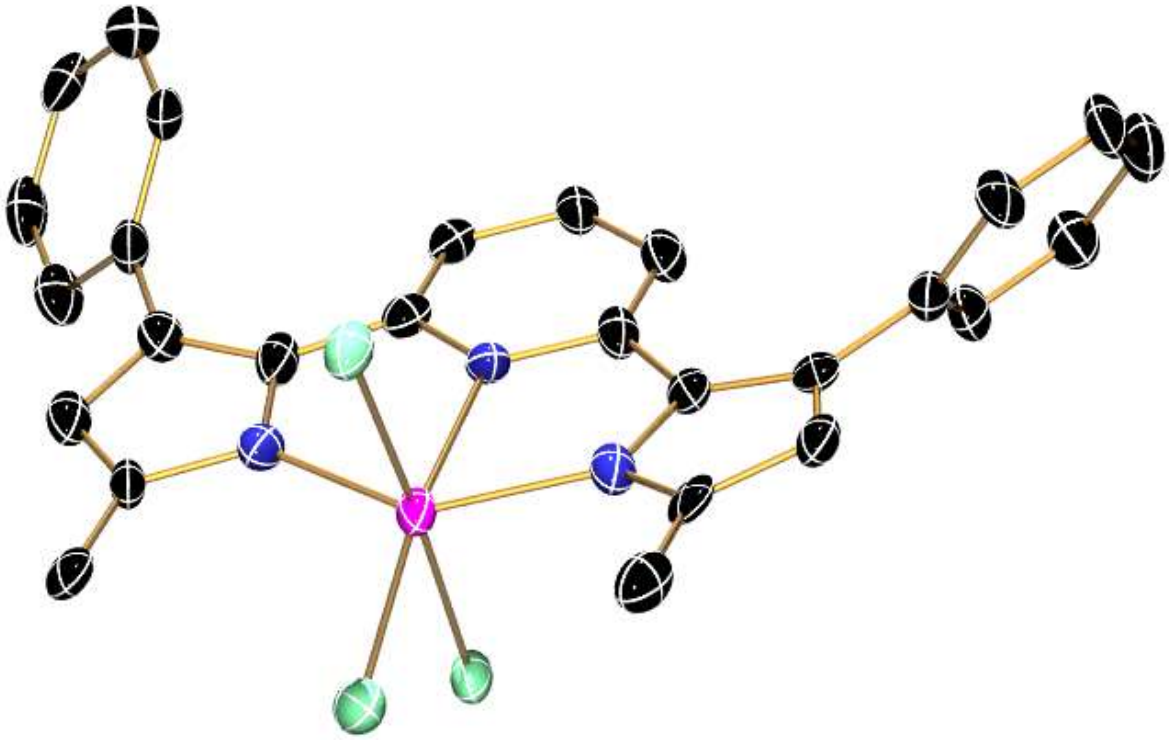

Figure B.7 cm304 - $[Co(Cp^*)_2][(^{Mes}PDP^{Ph})V{\equiv}O(NH_2)]$
Displayed at 50% probability ellipsoids. Solvent of crystallization and hydrogen atoms omitted for clarity. Disorder of a mesityl substituent, Cp* ring, and oxo ligand also omitted.

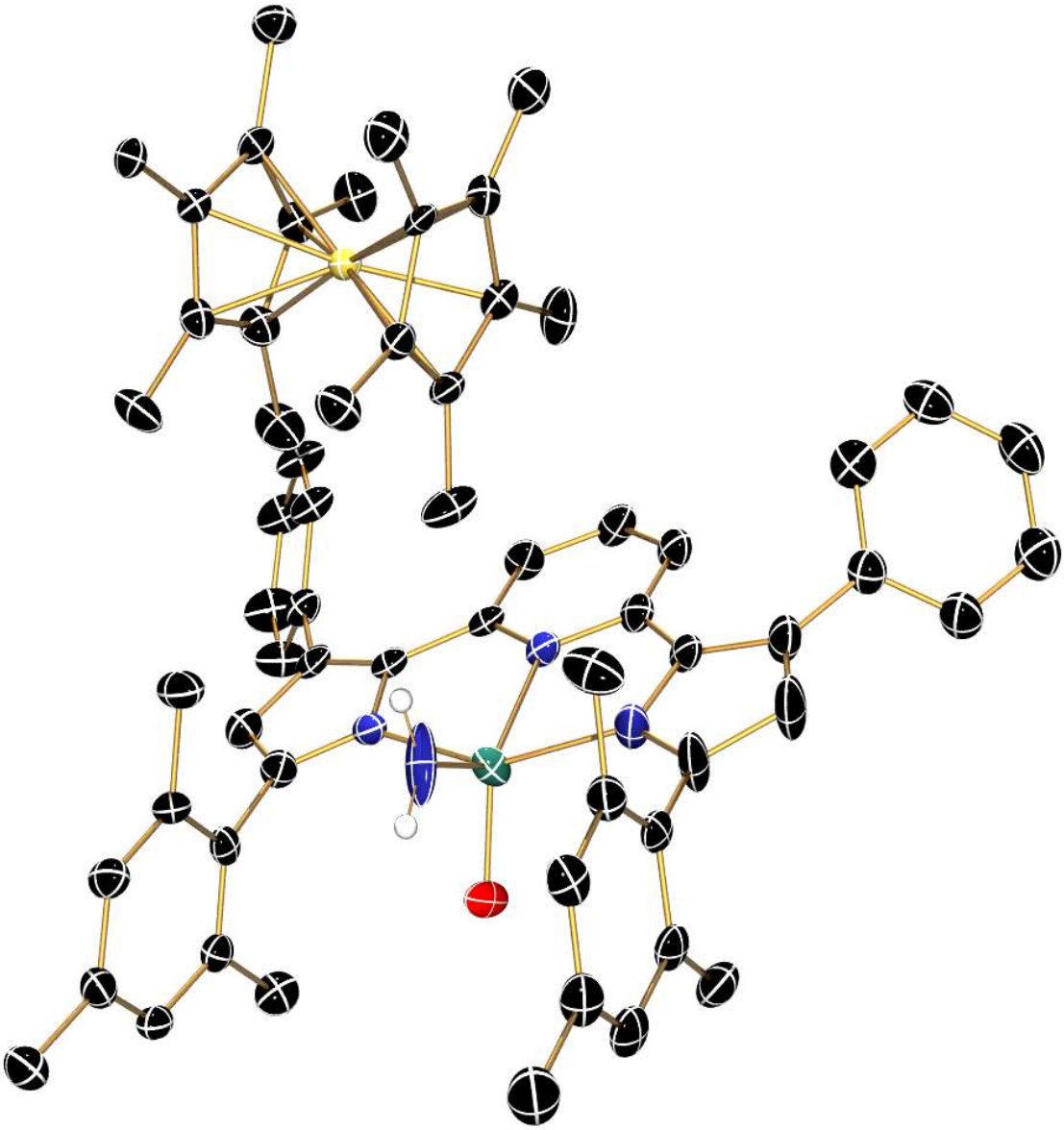

Figure B.8 cm309 - (^{Mes}PDP^{Ph})V≡N(DMAP)$_2$
Displayed at 50% probability ellipsoids. Hydrogen atoms omitted for clarity. One mesityl substituent truncated at the *ipso* carbon to better observe inner coordination sphere, as well as the opposite back phenyl group. Disorder of the back phenyls groups, mesityl substituents, and DMAP ligands are omitted for clarity.